Multiscale Analysis of Nanocomposites and Their Use in Structural Level Applications

by

Zeaid Hasan

A Dissertation Presented in Partial Fulfillment
of the Requirements for the Degree
Doctor of Philosophy

Approved July 2014 by the
Graduate Supervisory Committee:

Aditi Chattopadhyay (Chair)
Lenore Dai
Hanqing Jiang
John Rajadas
Yongming Liu

ARIZONA STATE UNIVERSITY

August 2014

ABSTRACT

This research focuses on the benefits of using nanocomposites in aerospace structural components to prevent or delay the onset of unique composite failure modes, such as delamination. Analytical, numerical, and experimental analyses were conducted to provide a comprehensive understanding of how carbon nanotubes (CNTs) can provide additional structural integrity when they are used in specific hot spots within a structure. A multiscale approach was implemented to determine the mechanical and thermal properties of the nanocomposites, which were used in detailed finite element models (FEMs) to analyze interlaminar failures in T and Hat section stringers. The delamination that first occurs between the tow filler and the bondline between the stringer and skin was of particular interest. Both locations are considered to be hot spots in such structural components, and failures tend to initiate from these areas. In this research, nanocomposite use was investigated as an alternative to traditional methods of suppressing delamination. The stringer was analyzed under different loading conditions and assuming different structural defects. Initial damage, defined as the first drop in the load displacement curve was considered to be a useful variable to compare the different behaviors in this study and was detected via the virtual crack closure technique (VCCT) implemented in the FE analysis.

Experiments were conducted to test T section skin/stringer specimens under pull-off loading, replicating those used in composite panels as stiffeners. Two types of designs were considered: one using pure epoxy to fill the tow region and another that used nanocomposite with 5 wt. % CNTs. The response variable in the tests was the initial damage. Detailed analyses were conducted using FEMs to correlate with the experimental data. The correlation between both the experiment and model was satisfactory. Finally, the effects of thermal cure and temperature variation on nanocomposite structure behavior were studied, and both variables were determined to influence the nanocomposite structure performance.

DEDICATION

To My Mother and Father

Yusra Hasan & Fouad Hasan

And the People of Gaza

ACKNOWLEDGMENTS

I would first and foremost like to express my sincerest gratitude to my advisor and the chair of my Ph.D. advisory committee, Dr. Aditi Chattopadhyay, for her guidance and support. In particular, I am most appreciative for the opportunities she provided me to work closely with other team members on different aspects of the research and her continuous encouragement throughout the years to pursue this degree, which was undoubtedly very challenging. Most of all I would like to thank Dr. Chattopadhyay for being my mentor both academically and professionally. I would also like to express my sincerest thanks to my graduate advisory committee, Dr. Lenore Dai, Dr. Hanqing Jiang, Dr. John Rajadas, and Dr. Yongming Liu, for their service in my educational process and their assistance in critiquing this work.

I would like to thank Dr. Yingtao Liu for his assistance during this work and for providing help in conducting the experiments that were essential in finalizing the studies presented in this dissertation. I would like to express my thanks to my dear friend Ghassan Atmeh for his help during this work and spending many nights writing and debugging codes. I would also like to thank my friends Angel Rodriguez, Phillip Pratt, Justen Leicht, Rafael Soto, Joel Johnston, Luke Borkowski, Christopher Heitland, and Masoud Yekani Fard for all their help with this research. Finally, I would like to show gratitude to my siblings Fatima, Eman, Fadia, Mohammed, Fedda, Bayan, and Obayda for their support and help throughout this journey.

TABLE OF CONTENTS

Page

CHAPTER

LIST OF TABLES

Table Page

LIST OF FIGURES

Figure Page

Figure Page

Figure Page

Figure Page

CHAPTER 1

INTRODUCTION

1.1. Background

The science and technology of controlling the structure of matter at the molecular level is known as nanotechnology. It is widely viewed as the most significant technological frontier currently being explored. Nanoparticles, nanotubes, and nanocomposites exhibit extremely high mechanical strength and are therefore of great interest to researchers.

The ideal formation of nano units and the ease by which the structural and functional units can be controlled helps identify interesting applications. To manipulate nanoscale systems, it is necessary to understand the mechanics involved. It is assumed that the atomic interactions are described by means of classical mechanics models at a molecular level. These interactions must be spatially scaled up to realize the cumulative effect. Analyses of different physical processes occurring at various scales of interest can be grouped as a multiscale analysis. Nanomechanics involves the mechanics at the nano scale, which are essential in understanding the local interactions, as well as phenomenological behaviors occurring on larger scales.

Carbon-based materials are ideally suited as molecular-level building blocks for nanoscale systems design, fabrication, and application because of their unique metallic, semi-conducting, and electromechanical properties, in addition to their light weight. There has been a great interest in studying carbon nanotubes (CNTs) from an engineering perspective as reinforcements in composites, even as replacements to high-strength carbon fibers. Because of their high axial strength and low weight, the resulting composite could be exceptionally light with enhanced strength. The computational and experimental analyses of nanocomposites are the primary focus of this research into nanocomposites.

CNTs are present mainly in three configurations (as shown in Figure 1): single-walled carbon nanotubes (SWCNTs), multi-walled carbon nanotubes (MWCNTs), and CNT bundles or ropes. It has been reported that CNTs are many orders of magnitude stronger, stiffer, conductive, and lighter than the best available carbon fibers (Baughman, R.H. et al. 2002) (Unnikrishnan, V.U. and Reddy, J.N. 2005). The perfect formation of nano-units and the ease by which the structural and functional units can be manipulated helps identify interesting applications.

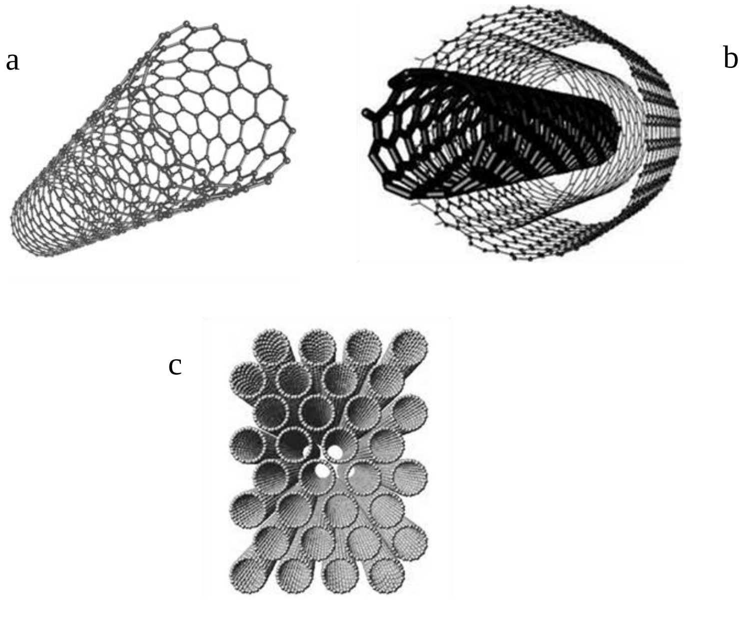

Figure 1. (a) Single-walled carbon nanotube (SWCNT), (b) multi-walled carbon nanotube (MWCNT), and (c) nanoropes and nanocomposites

There has been significant interest in the analysis of CNT-reinforced polymer composites under the application of various forces, as shown in

Figure 2. Many studies focused on fundamental understanding of the structure/size influence of CNTs on the elastic properties of nanotube-based composites, while others presented constitutive models for polymer composite systems reinforced with SWCNTs. It was found that the interaction at the polymer/nanotube interface is highly dependent on the local molecular structure and bonding (Thostenson, E.T. and Chou, T.W. 2003), (Dresselhaus, M.S. et al. 1996.), (Odegard, G.M. 2003). The CNTs, which are a few orders of nanometers, are randomly distributed and interact with the surrounding polymer matrix. The primary requirement to obtain the maximum effective property is that the reinforcements be homogeneously distributed in the matrix and aligned in specific orientations to obtain the desired effective properties in a composite material system (Camargo, P.H. et al. 2009).

Although the basic principles appear similar to conventional fiber-reinforced composites (Reddy, J.N. 2004), the scale of the conventional fibers is different from that of CNTs, which are on the order of a few nanometers. This discrepancy in scales brings a new set of challenges. To achieve the objective of transferring the exceptional properties of the CNTs into practical devices, one needs to understand how the processes that occur on the nanoscale affect those on macroscales (mm to cm to m). This can only be achieved through multiscale modeling. It must be noted that most of the computational work reported in the literature address the behavior of CNTs at the nanoscale, which is crucial to understanding material behavior. Limited knowledge is available on understanding their impact on structural-scale applications that primarily use composites. Part of this research is focused on the analysis of CNTs and CNT-reinforced composite structures in order to obtain the macroscale properties by means of an efficient multiscale modeling method. The information is then incorporated within a commercially available finite element (FE) analysis to analyze structural components reinforced with CNT-based composites.

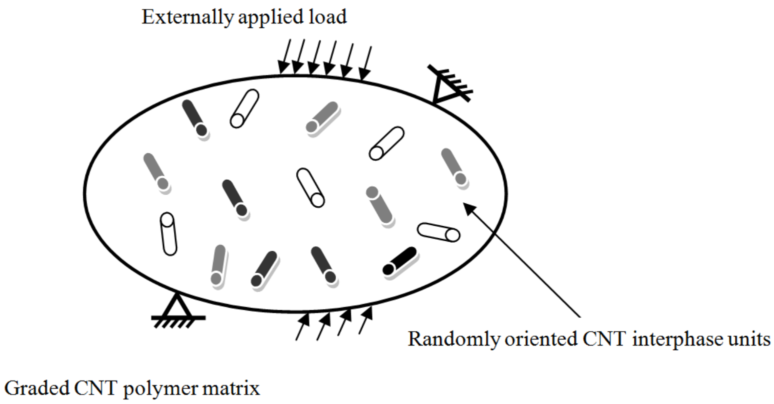

Figure 2. CNT-reinforced polymer nanocomposite

Research of composite properties is usually carried out using a bottom-up approach. The accuracy in predicting lower-order properties and the hierarchical transfer of the material properties to a larger scale is typically the main focus of multiscale modeling. In previous work on multiscale modeling, the response in the atomistic level was transferred to the meso- or microscale by the explicit use of equivalency in the response variables (Odegard, G.M. et al. 2002.). Figure 3 shows a schematic of a typical multiscale approach used in analyzing composite nanomaterials. The multiscale analysis can be carried out by the use of explicit modeling of various atomistic configurations, then simulating each of these configurations and subsequently relaying information to the higher scales. The various scales involved in a nanocomposite analysis are: atomistic level (a few orders of nanometers), mesoscale (which spans a couple of μm to ~10^{-7}), and finally the microlevel (a few μm to a few millimeters or higher).

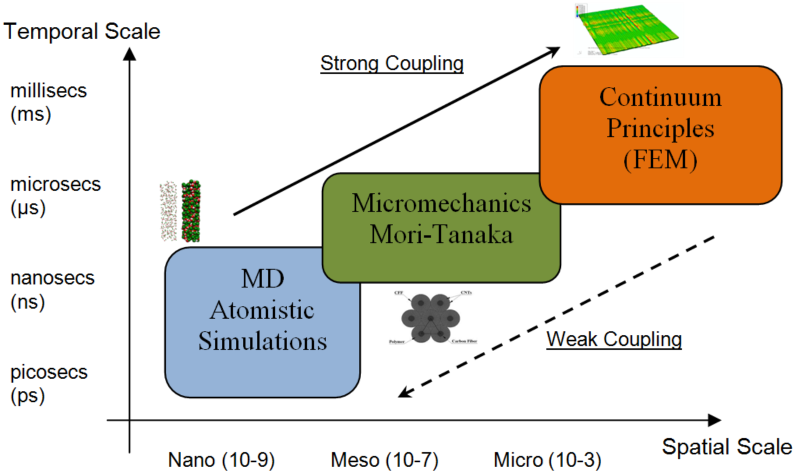

Figure 3. Multiscale analysis

At the atomistic level, the interactions exist in the molecular level and are modeled using pair potentials to respond to externally applied disturbances. The response variables in the lower scales are passed on to the higher scales, seeking change in the material properties. These properties are captured and passed on to the higher scales, which subsequently affects the macroscopic response. Once the atomistic material properties have been determined for the various morphologies of the fiber phase, the volume average over the ensemble would give the averaged material properties (Odegard, G.M. et al. 2002.), (Fisher, F.T. et al. 2003). The averaged volume properties are subsequently scaled to the mesolevel by applying Eshelby's equivalent eigenstrain method and the Mori-Tanaka formulation to obtain the effective material response in the mesolevel as shown in Figure 4. The advantage of this coupling method is the ultimate realization of an analysis and design philosophy based on the macroscopic structural behavior by predicting and enhancing the microstructural level.

1.2. Carbon Nanotubes

Since the discovery CNTs by Iijima (Iijima, S. 1991), they have become a subject of intense research across many disciplines. SWCNTs are made by the folding of a graphene sheet into a hollow cylinder, which is composed of hexagonal carbon ring units that are referred to as graphene units (Dereli, G. and Ozdogan, C. 2003.), as shown in Figure 5. Each of the carbon atoms forming the tubules has bonds with its three nearest neighbors. In a fully relaxed structure, the angles between these bonds depends on the radius of the cylinder, as well as the bonds' orientations (Baughman, R.H. et al. 2002). All three angles approach 120° (a perfect graphitic plane) with an increasing cylindrical radius.

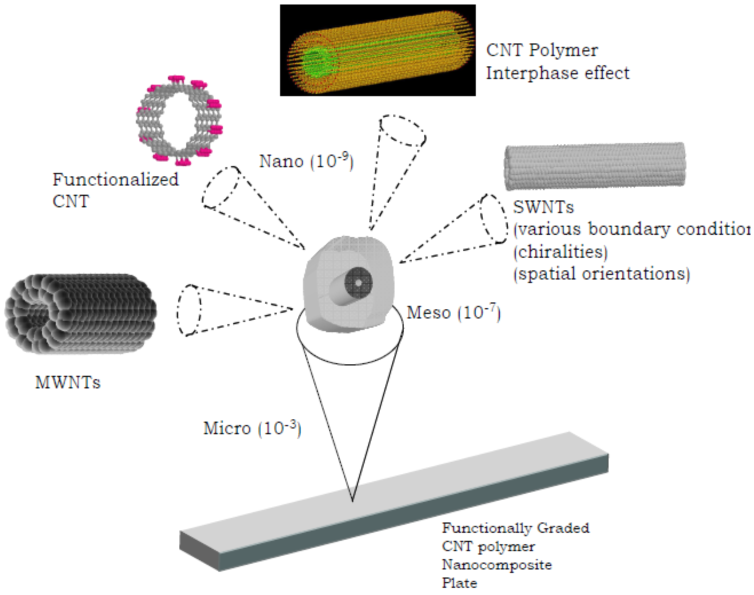

Figure 4. Relationships between nano-, meso-, and microscales

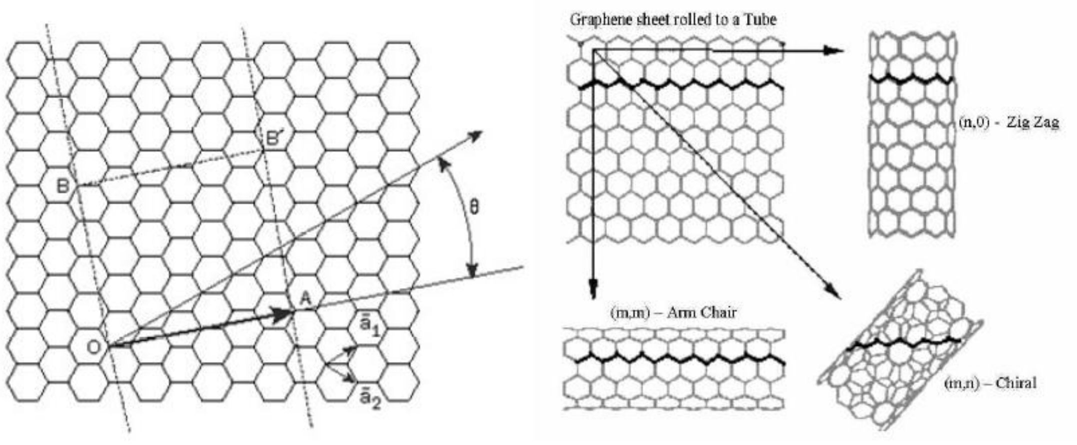

(a) (b)

Figure 5. (a) Graphene sheet representation and (b) Type of CNT: Chiral, Zig-Zag, and Armchair

The fundamental CNT structure can be classified into three categories in terms of their helicity: Armchair, Zig-Zag, and Chiral. One of the advantages of atomistic simulation is the ease with which various configurations can be studied, as shown in Figure 6. The experimental investigation of CNT is extremely difficult because the capability is limited by the availability of high-quality, defect-free CNTs of sufficient length and accurate measurement of nanoscale structures (Mukhopadhyay, P. et al. 2013). Studies of the mechanical, electrical, and thermal behavior of CNTs are focused primarily on the use of empirical potentials using Molecular Dynamics (MD) and continuum models using elasticity theory (Jin, Y. and Yuan, F.G. 2003), (Liao, K. and Li, S. 2001), (Yakobson, B.I. et al. 1996), (Zhao, Q.Z. et al. 2002), (Iijima, S. 1991). The application of continuum mechanic principles into nanomechanics demands the bridging of the two or more scales of interest. From a computational perspective, these techniques should be able to efficiently represent the processes on a fine scale and provide solutions to the analysis in the macroscale.

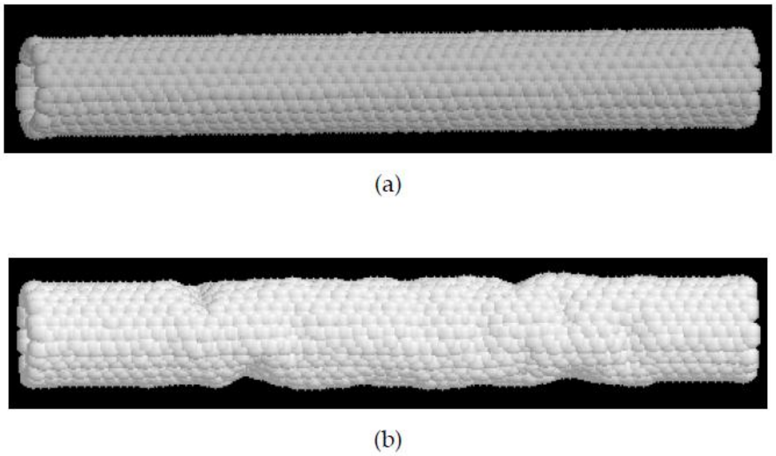

Figure 6. A CNT under (a) elastic axial tension and (b) elastic axial compression

1.3. Nanocomposites

Conventional composites are solid materials composed of two or more constituents combined to offer users the specific properties they require. They are usually composed of a matrix and different types of reinforcements. Nanocomposites are composites where at least one constituent has at least one dimension smaller than 100 nm (Ajayan, P.M. et al. 2003). Natural nanocomposites can be found in the structures of the abalone shell and bone. Nanocomposites can be classified based on the type of matrix, such as polymer matrix nanocomposites, metal matrix nanocomposites, and ceramic matrix nanocomposites. Compared to conventional composites, interphases in nanocomposites play a dominant role and affect the composites' macroscopic properties. The reinforcing material can be made up of nanomaterial in zero, one, or two dimensional forms (Mai, Y.W. et al. 2006.), (Knauth, P. and Schoonman, J. 2008). The area of the interface between the matrix and the reinforcement phase(s) is significantly larger than that of conventional composites. The applications of nanocomposites include structural materials with improved mechanical properties, electronic materials, magnetic materials, biomedical materials, photonics, high-performance coatings, and catalysts (Mukhopadhyay, P. et al. 2013), (Ahmed, J. and Ebrary, I. 2012). Figure 7 illustrates the usage of polymer nanocomposites in a Toyota motor vehicle as an example. The main advantages of using polymer nanocomposite parts in the automotive industry are reducing vehicle weight, improving engine efficiency, saving fuel, and increasing safety (nanowerk. 2014). Other commercial polymer nanocomposites that are currently available and their respective target markets are shown in Table 1.

Figure 7. Illustration of the usage of polymer nanocomposites parts (nanowerk. 2014)

Table 1. Polymer nanocomposites and applications

Supplier	**Matrix resin**	**Nano-filler**	**Target market**
Creanova (Vestamid)	Nylon 12	CNTs	Electrically conductive
GE Plastics (Noryl GTX)	PPO/Nylon	CNTs	Painted automotive parts
Honeywell	Nylon 6 Barrier Nylon	Organoclay	Multi-purpose
Hyperion	PETG, PBT, PPS	CNTs	Electrically conductive
Nanocor	Nylon 6 PP Nylon MDX6	Organoclay	Multi-purpose moulding
Showa Denko (Systemer)	Nylon 6 Acetal Clay	Mica	Flame retardancy Multi-purpose

1.4. Modeling Techniques to Determine the Effective Properties

Continuum micromechanics is an area of research that has the ability to determine the properties and behavior of inhomogeneous materials along various axial directions. A significant amount of research has been conducted to develop constitutive laws and micromechanical models to predict composite material properties (Aboudi, J. et al. 2012). In the analysis of composite structures, the choice of the micromechanical model is important both for predicting the properties and the local level stress analysis, which is important for understanding material failure.

1.4.1. Micromechanics

A combination of micromechanics and continuum mechanics is essential to synthesize a multi-constituent material. Continuum mechanics assumes homogeneity in material properties. Continuum mechanics' assumption of uniform material properties might not hold at the microlevel, thus, the continuum quantities associated with the microlevel constituents of the material are expressed with the help of micromechanics (Odegard, G.M. et al. 2005).

A widely used micromechanics model is the Mori-Tanaka method (Mori, T. and Tanaka, K. 1973), which entails the use of Eshelby's tensor to account for cylindrical inclusions. Fourth-order concentration tensors relate the average stress or average strain tensors in the inhomogeneity and matrix to the average macroscopic stress or strain tensor in the representative volume element (RVE) while accounting for phase interaction effects in a collective, approximate way. There are many other micromechanical methods, such as the self consistent method, which is based on the solution to an auxiliary inclusion problem where a single ellipsoidal inclusion is embedded in an infinite medium. In this method, it is assumed that the bond between inclusion and the infinite medium is perfect. Therefore, there is displacement and traction continuity across the interface of the two phases. Halpin-Tsai is another semi-empirical method that facilitates simple procedures implemented during the design phase. These relationships were developed by curve fitting to the results that are based on elasticity solution.

The principal advantage offered by the Mori-Tanaka method is that it directly computes the elastic properties of a composite in terms of its stiffness or compliance tensor, which can then be used to determine effective properties by simple arithmetic calculations. The averaging techniques used to compute the effective properties of composite materials are based on the calculation of Eshelby's tensor for the type of inclusion associated with each phase of the composite. The solution to the problem of ellipsoidal inclusions was formulated by Eshelby (Eshelby, J.D. 1957), and the determination of effective elastic constants using Eshelby's formulation depends on a fourth-order tensor that relates the average strain in the fibers to the average strain in the matrix, known as the Eshelby's tensor. The methodology for approximating these tensors is explained by Benveniste (Benveniste, Y., 1987). The use of the Eshelby tensor provides a direct formulation of the method to find effective moduli.

In this research, the fiber-interphase problem is modeled using a composite with cylindrical fiber inclusions. The transversely isotropic elastic phases consist of an inclusion phase of aligned or oriented ellipsoidal nanotubes. The concept of equivalent inclusion developed by Mori and Tanaka is used to compute the effective properties of the nanocomposites. The assumption is that the composite is being subjected to homogeneous boundary conditions.

1.4.2. Multiscale analysis

Multiscale models have been applied using both atomistic simulations and micromechanics to assess the constitutive properties of various functionalized nanotube materials (Odegard, G.M. et al. 2005), (Gao, X.L. and Li, K. 2005). Liu and Chen (Liu, Y. J. and Chen, X. L. 2003) studied the mechanical response in tension of a single CNT embedded in polymer using FE analysis. In a series of papers, Odegard et al. (Odegard, G.M. 2003), (Odegard, G. M. et al. 2001) modeled CNT composites using the equivalent continuum method in conjunction with the Mori-Tanaka micromechanics method. The objective was to obtain the effective elastic constants for both aligned and misaligned CNTs. They found the effective elastic moduli to be several times that of the matrix for aligned CNTs and almost 1.5 times the matrix value for misaligned CNTs at a volume fraction of 1% CNTs with a matrix consisting of a thermoplastic polyimide LaRC-SI.

Modeling of the thermal and electrical conductivities of nanocomposites has focused primarily on nanoscale effects, such as thermal interface resistance and low volume fraction percolation. Gang and Li (Zhang, G. and Li, B. 2005) studied the dependence of thermal conductivity of SWCNTs on chirality and isotope impurity using nonequilibrium molecular dynamics and found that, contrary to electronic conductivity, thermal conductivity is insensitive to chirality. As it is difficult to directly probe the interface between CNTs and the polymers in which they are embedded in the lab, some researchers (Huxtable, S.T. et al. 2003), (Clancy, T.C. and Gates, T.S. 2006) have used molecular dynamics simulations to estimate the interfacial thermal resistance. However, many others (Clancy, T.C. and Gates, T.S. 2006), (Bryning, M.B. et al. 2005), (Nan, C.W. et al. 2003) have used the effective medium approach (Nan, C.W. et al. 1997) or derivatives thereof (Song, P.C. et al. 2006) to estimate the thermal resistance by comparison with nanocomposite measurements. Others (Gojny, F.H. et al. 2006), (Chen, T.Y. et al. 2005) have employed a Mori-Tanaka approach proposed by Hatta and Taya to model the effective thermal conductivities of nanotubes and nanocomposites both with and without interfacial thermal resistance. Guthy et al. (Guthy, C. et al. 2007) applied the Nielsen model in comparisons with experimental observations of nanocomposite conductivity. A control volume FE method was employed by Song and Youn (Song, Y.S. and Youn, J.R. 2006) to obtain the effective thermal conductivity of nanocomposites.

1.5. Failure Analysis of Composite Structures

Fiber-reinforced polymer (FRP) composites are widely used in engineering applications, including aeronautical, marine, civil, and automotive industries. These materials have high strength-to-weight ratios, good corrosion resistance, superior fracture toughness, and can be engineered based on required strength or performance objectives for a given structure. To give few examples, leading aircraft manufacturers, such as Airbus and Boeing, have increased the application of FRP composites in their products from 3% to 20% in Airbus A380 and over 50% in Boeing 787 (Potluri, P. and Manan, A., 2007). Figure 8 depicts one of the largest aircraft wings, with a 42.4-m span, made of carbon FRP composites assembled for the Airbus Military A400M transport aircraft. In the construction industry, FRP composites have become a good alternative for innovative construction, and their applications have already been extended to upgrading and retrofitting existing structures, as well as constructing various types of off-shore platforms, buildings, and bridges. The Pontresina Bridge (Figure 8-d), with a span length of 12.5 m, was constructed in 1997 across the Flanz River in Switzerland. The structural truss system of the bridge is made of FRP composite (Keller, T., 2001).

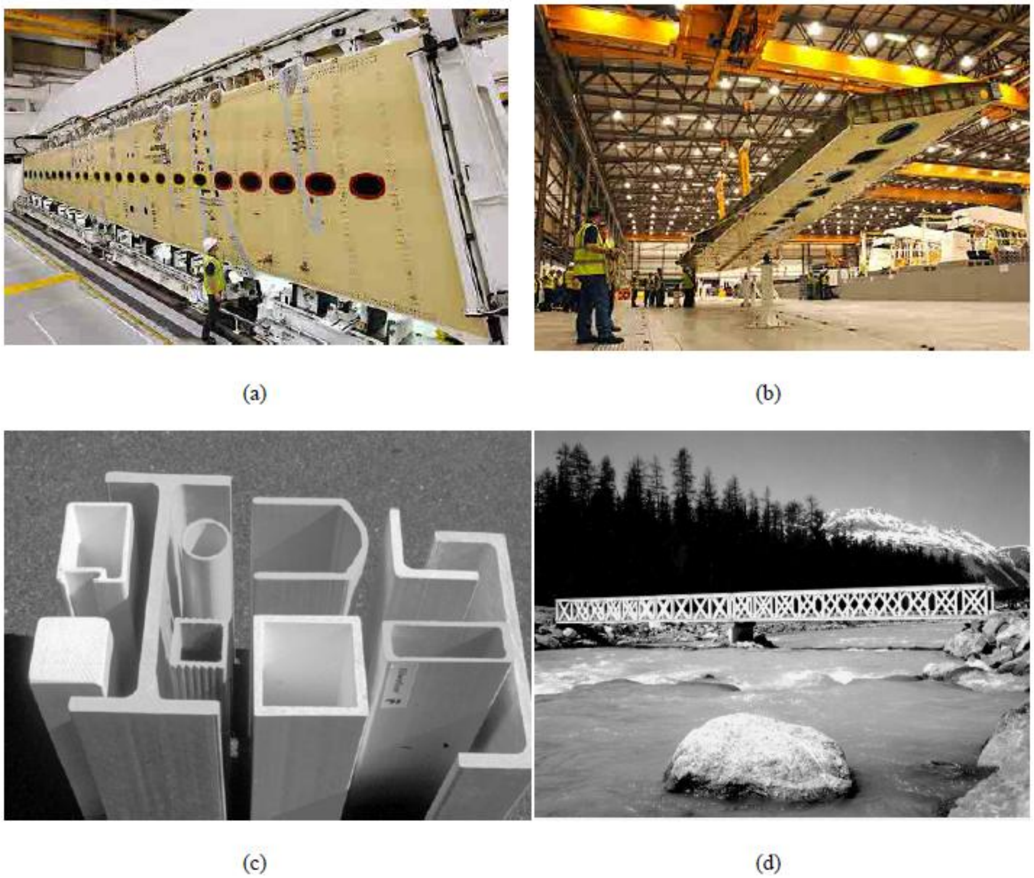

Figure 8. Sample applications of FRP composite materials in different industries: (a) & (b) Airbus Military A400M aircraft CFRP wing (Martin Chainey/Airbus Military), (c) cross-sections of glass fiber reinforced polymer (GFRP) structural members used, and (d) Pontresina Bridge made of FRP (Zhang, T.F. et al. 2011)

Although FRP composite structures offer numerous advantages, crack initiation and propagation in these materials can drastically affect their mechanical properties. The various damage modes include fiber breakage, fiber-pull out, matrix cracking, and interlaminar delamination, as depicted in Figure 9. Fiber breakage failure in FRP composites depends on the fiber strength distribution. This failure mode occurs when the subjected tensile stress in the FRP increases and leads to failure of low-strength fibers in the laminate while the high-strength fibers are still carrying the external load. For a better understanding of fiber breakage, distribution of the fiber strength in FRP has been investigated by several researchers, and it was determined that the strength of glass fibers follows the Rayleigh distribution (Durham, S.D. and Padgett, W.J., 1997) while the strength of carbon fibers fits the Weibull and Gauss distributions (Zhang, T.F. et al. 2011). In the cases where fiber strength is greater than the interface bond between the fibers and the matrix, the fibers can be pulled out of the matrix due to the tensile loading. In many cases, the fiber pull-out occurs at the fiber end or at a fracture surface in the laminate. Another common failure mode in FRP composites attributed to the matrix material is called matrix cracking. Because matrix strength is commonly lower than the fibers, the first stage of failure normally starts with matrix deterioration. Matrix cracking usually takes place before the entire FRP laminate matches its failure point, and it demonstrates a ductile failure in comparison with brittle fiber failures. Among other failure modes, delamination is perhaps the most common and may occur because of weak bonding between composite layers, existing cracks in the matrix material, broken fibers, and fatigue or impact loadings. Delamination can drastically reduce the structural stiffness and weaken the tensile or shear capacity of the FRP structures under service loads (Owen, M.J. and Bishop, P.T. 1979).

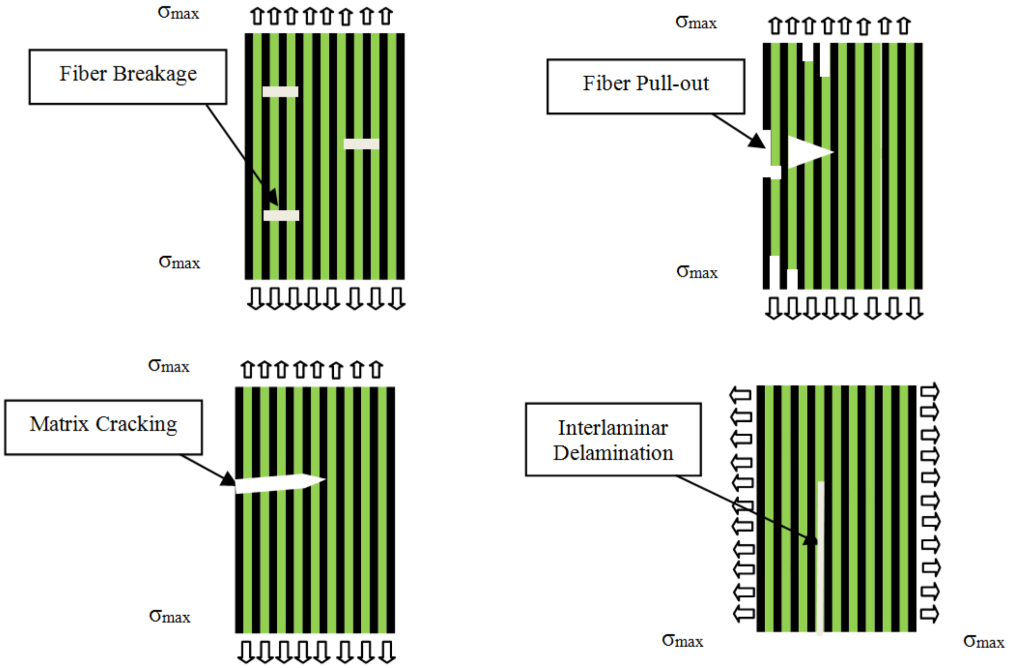

Figure 9. FRP composite materials common failure modes: (a) fiber breakage, (b) fiber pull-out, (c) matrix cracking, and (d) interlaminar delamination

In order to improve mechanical performance of FRP composite materials in the presence of process- or loading-induced cracks, extensive studies on the fracture properties of FRP composites have been performed, both experimentally and numerically. Owen and Bishop (Owen, M.J. and Bishop, P.T. 1979) applied the double edge-notched tensile test to measure the mode I critical stress intensity factor for varying orientations of ultra-low dispersion (UD) glass FRP composites. Gaggar and Broutman, (Gaggar, S. and Broutman, L.J. 1977) utilized both single and double edge-notched tensile tests, as well as a notched bend test, to extract the critical stress intensity factors.

The extensive investigation on the fracture phenomenon of test samples showed that delamination problems mainly consist of mixed mode fracture mechanics characteristics. Subsequently, the mixed mode bending (MMB) test was recently designed for mixed mode characterization (mode I and II interaction).

Numerous investigations have been performed over the past few decades regarding numerical modeling of delamination in FRP composites. Hillerborg et al. (Hillerborg, A. et al. 1976) introduced a combination of FE method and an analytical solution to simulate crack growth in concrete structures. This approach is often referred to as “fictitious crack modeling,” where a traction-separation law instead of the conventional stress-strain relationship is utilized in the crack-tip zone to capture the degradation of the material properties due to damage. Later Xu and Needleman (Xu, X.P. and Needleman, A., 1994) applied an energy potential function to implement the cohesive zone model (CZM) during the analysis of interface debonding. CZM application was extended to FRP composites by Camacho et al., Blackman et al., and others (Camacho, G.T. and Ortiz, M. 1996), (Camanho, P.P. et al. 2003), (Blackman, B.R. et al. 2003), (Gao, Y.F. and Bower, A.F. 2004), (Segurado, J. and Llorca, J. 2004), (Yang, Q.D. and Cox, B. 2005) and (Nishikawa, M. et al. 2007) while they have improved the cohesive interface models. Based on these studies, the CZM has proven to be capable of modeling delamination in FRP composites.

Despite the ability of the CZM to model progressive delamination, some serious disadvantages of applying a large process zone have been noted and require attention. These include numerical instability (elastic snap-back), reduction of stress intensity upon delamination initiation, and the fictitious softening of the original body in the process zone. In other investigations, a newly introduced feature of the FE method, known as the extended FE method (XFEM), has been more recently implemented for numerical modeling of progressive delamination in FRP composites. The original XFEM approach was first introduced by Belytschko and Black and enhanced by Moes (Moes, N., J. et al. 1999).

With considerable effort exerted regarding the problem of delamination in fiber-reinforced laminates, it is found that the factors that contribute most to delamination are the weak fiber/matrix interface and the brittle nature of the matrix resin. Several techniques have been developed to suppress or arrest delamination growth. Delamination may be suppressed by changing the architecture of the reinforcement through the introduction of thickness-reinforcing elements, such as three-dimensional (3D)-weaving (Tong, L. et al. 2002), stitching (Dransfield, K.A., et al. 1998), braiding (Brown, R.T. and Crow Jr, E.C. 1992), Z-pin anchoring (Mouritz, A.P. 2007), and the use of short fibers or microscale particles in the polymer matrix (Hojo, M. et al. 2006). These methods enhanced the interlaminar properties but at the cost of in-plane mechanical properties (Chang, P. et al. 2007). The weak interface and low matrix toughness should be addressed on the fundamental level of the composite structure that defines these properties (i.e., below the micro-structure on the nanolevel). This can be done through surface modification of the fibers and toughening of the matrix by embedding CNTs into the matrix material forming nanocomposites. Because the nanocomposite is on a macro continuum scale, challenges arise while attempting to model the nanocomposites analytically or numerically.

Many researchers performed experimental work that demonstrated that adding nanoparticles to epoxy has positive effects on the fracture toughness and the energy release rate (Sun, L.Y. et al. 2009), (Ragosta, G. et al. 2005), (Zhang, H. et al. 2006), (Fu, S.Y., et al. 2008), (Rosso, P. et al. 2006). Arai and colleagues (Arai, M. et al. 2008) reported respective 50% and 150% increases in the mode I and mode II fracture toughness of the epoxy/carbon fiber laminates modified by carbon nanofibers. Moreover, adding 5 wt. % CNT to epoxy increased the interlaminar fracture toughness up to 300% (Yokozeki, T. et al. 2009). In addition, a significant number of existing studies have focused on the stiffness and strength of CNT-reinforced composites (Montazeri, A. et al. 2010, 4202-4208), (Bal 2010), (Montazeri, A. et al. 2010). Qian et al. (Qian, D. et al. 2000) reported that when nanotubes of about 1 wt. % are homogenously dispersed into polystyrene matrices, the elastic modulus increased by 36–42%, and the tensile strength improved by about 25%.

Numerous studies have reported on the failure analysis of composite structures in aerospace applications; Ostergaard et al. (Ostergaard, M., et al., 2011) provided an overview on the general principles used in the process of virtual testing of both metallic and composite aircraft structures, which is achieved through the creation and execution of a detailed nonlinear FE analysis model of an aircraft structure that represents as accurately as possible the actual physical behavior when subjected to a wide range of loading scenarios. Martin (Martin, R.H. 1996) presented a global/local testing and analysis approach to evaluate the design of a composite stringer compression panel. The analysis investigated the variation of strain energy release rate G with debond length using a 2D plane strain FE analysis. Krueger and colleagues (Krueger, R. et al. 2000) presented a consistent step-wise approach to investigate the damage in composite-bonded skin/stringer construction under uni- and biaxial loading conditions. It was shown that the strain energy release rate exceeded the values obtained from a mixed-mode failure criteria in a certain location; hence, unstable propagation was likely to occur as predicted from experiments. Winzen (Winzen, A. 2006) studied the effect of several parameters on several subroutines in the commercial software Abaqus, which is mainly used in modeling the degradation of the adhesive layer between a skin and stringer in a composite panel. These types of studies enhance the capabilities of modeling complicated behaviors in composite laminates for future analysis development. Li (Li, J. 2002) presented an experimental study for several pull-off specimens required to identify the mechanism and associated crucial factors that control the failure mode of the frame to skin joint using angle clips stitched to the skin. The pull-off specimens were tested under both simply supported and clamped conditions. It was predicted that enormous savings of allowable development costs and greatly increased accuracy in analysis could be achieved by capturing the crucial factor governing the actual failure mode. Hoyt et al. (Hoyt, D.M. et al. 2002) presented a combined strength and fracture analysis applied to typical bonded composite joint configurations. Their analysis uses detailed 2D nonlinear FE models (FEMs) of the local bondline. A fracture mechanics-based approach is used to predict damage growth and failure under static and cyclic loads based on test data for static fracture toughness and crack growth rate. Li and colleagues. (Li, J.A. et al. 1997) performed pull-off tests on hat stringers to evaluate the delamination failure mechanisms in the flange region for a rod-reinforced hat stringer section. The test results indicated that the as-manufactured microstructure in the flange region has a strong influence on the delamination initiation and the associated pull-off loads. FEMs were created for each specimen with a detailed mesh based on micrographs of the critical location. A fracture mechanics approach and a mixed-mode delamination criterion were used to predict the onset of delamination and the pull-off load. By modeling the critical local details of each specimen from micrographs, the model was able to accurately predict the hat stringer pull-off loads and replicate the test result variability.

The work performed by Cope and Pipes (Cope, R.D. and Pipes, R.B. 1982) focused on various spar-skin joints that were designed with triangular and curved fillets to assess the most conservative tow profile. The delamination onset location was investigated through the Tsai-Wu and maximum stress failure criteria, and the analysis was carried out using plane stress FEMs. The authors demonstrated that design concepts with curved joints maximize the overall strength compared to triangular joints. The influence of different insert types placed within the resin-rich tow was investigated by Rispler et al. (Rispler, A.R. et al. 1997). By correlating experimental results and plane strain linear elastic FE analyses, it was shown that the FEMs accurately predict the failure initiation location on the majority of specimens, regardless of insert type and web thickness. According to Rispler and colleagues' findings, the interlaminar peel failure criterion provided the highest accuracy and was the most conservative in failure initiation load prediction. Kumari and Sinha (Kumari, S. and Sinha, P.K. 2002) conducted numerical parametric studies on wing T-joints with no filler inserts using FE analysis. By developing a thick composite shell FE, they showed that the failure mode is configuration dependent under pull-off loading and that the radius between two fixed points of arc length at the web/skin can increase the pull-off strength due to stress-concentration reduction. Ultra-thick composite joints (>60 mm) for the development of side stay fitting in a main landing gear were studied by Zimmerman (Zimmermann, K. et al. 2010). 3D linear elastic FE analysis with 8-noded stacked composite elements was chosen due to the presence of transverse shear and through-thickness stresses. Under tension, high-localized peeling stress concentrations were noticed at the free-edge of the joint. This was the main cause for failure at the upper tow tip through the web. Under bending, it was observed that high shear stresses in the fillet contribute to failure. For compressive loading, it was concluded that the use of stiffer gusset filler made of carbon instead of foam diverts the load, which significantly reduces the shear stresses and downward joint displacement. Hélénon et al. and Chen et al. (Helenon, F. et al. 2012), (Chen, J.Y. et al. 2009) presented a rigorous numerical investigation into the structural response of a composite laminate T-piece specimen subjected to a mechanical pull-off load case. They demonstrated that using realistic cohesive maximum strength values requires a very fine mesh. Reducing the values to ensure initiation occurs leads to conservative, mesh-independent predictions and that a suitable choice leads to good correlation with the experimental results. These studies also showed that T-piece failure was controlled by crack propagation.

Along with predicting delamination-induced damage, one important aspect of design and performance assessment is predicting failure initiation. Panigrahi and Pradhan (Panigrahi, S. and Pradhan, B. 2009) used 3D non-linear FE analysis to predict damage onset and growth in a composite spar-wing skin joint. Using the Tsai-Wu stress-based failure criterion and virtual crack closure technique (VCCT) to model delamination propagation, the authors arrived at the conclusion that delamination propagation initiating from the tow-ends caused complete joint failure. This result later motivated them to study the influence of different tow profiles, such as triangular, circular, elliptical, and modified elliptical load couplers on the strength of the composite spar-wing skin joint (Panigrahi,

S. and Pradhan, B. 2009). They presented several recommendations for the design of the studied structure based on their findings. Progressive delamination within a braided composite T-piece was studied by Chen and colleagues (Chen, J.Y. et al. 2009) using special-purpose cohesive elements in Abaqus/Standard; the modeling was performed under the plain strain assumption and was based on delamination failure as noticed from experimental observations. The prediction was in good agreement with their results. By independently varying the fracture toughness properties and strength, it was shown that the failure was dominated by mode II crack propagation rather than its initiation.

Based on the existing evidence, it can be observed that there is lack of published research on the use of nanocomposites as a means to prevent or delay such failures in composite structural components from occurring; therefore, this motivated an investigation which, to the best of the authors' knowledge, has not been explored previously. The main objective of the following research is to quantify the effect of nanocomposite use in the manufacturing of structural-level composite joints and determine their ability to improve the unique composite failure modes of those structures. This study focuses on delamination that exists around the tow filler of composite T and Hat section stringers, as well as the bondline between the skin and stringer. Two loading conditions will be taken into account: pull-off and combined axial/pull-off loading. The VCCT is used to determine the initial damage, which will be considered the dependent variable in this study to compare the results and determine the percent improvement achieved by using nanocomposites.

1.6. The Uniqueness of the Current Research

The uniqueness of this study lies in the premise that there is a lack of comprehensive research into the use of nanotubes at the structural level to understand the benefits of using CNTs in structural applications, particularly in complex aerospace applications. The developed integrated multiscale modeling technique will help reduce the number experiments necessary to conduct such an investigation. The application of the developed framework on complex composite structures, such as T-section stringers with integrated nanocomposite at selected hotspots, provides improved understanding of the benefit of using CNTs for delaying the onset of delamination and subsequent failure. The key elements of the developed methodology are shown in Figure 10.

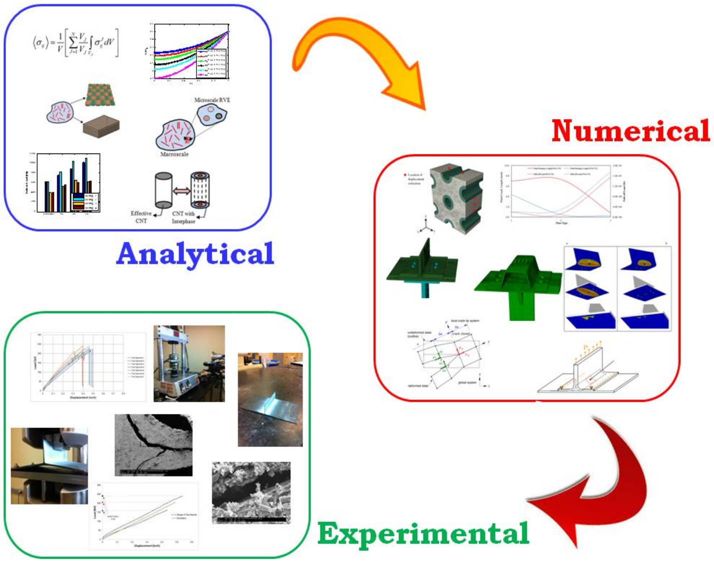

Figure 10. Schematic of the developed framework

1.6.1. Motivation of the Current Research

A comprehensive review of the recent state-of-the-art research in the field of nanocomposites revealed a lack of studies into the feasibility of using nanocomposites to overcome some of the weaknesses of conventional composites. This research is aimed at formulating a multiscale computational approach to quantify the use of nanocomposites at the structural level and its impact on the initial failure load for aerospace applications. The multiscale model is used to understand the effect of nanotubes on the mechanical properties of a nanocomposite system and to estimate the elastic properties of a complex polymeric nanofibrous structure. The properties estimated are used in detailed FEMs to understand the behavior of the structure under different typical service loadings. The effect of nanocomposites on improving delamination-related failure is also investigated. Experiments are conducted to help validate the numerical models.

The following are the specific contributions of this research:

1. Implemented several micromechanics techniques to obtain the effective mechanical and thermal properties of nanocomposites; extended this approach to obtain properties of unidirectional and woven lamina nanocomposites.
2. Investigated an alternative approach to estimate the effective mechanical properties using the Kalman filter framework
3. Determined the stress and displacement fields at the CNT/matrix interface, taking into consideration the time-dependent effect
4. Developed an integrated methodology, combining micromechanics models with FE analysis to quantify the effect of nanocomposites in complex structures

5. Conducted experimental investigation to validate the analysis methodology and tested a select set of complex structures to verify the hypothesis that the use of CNTs in the epoxy matrix helps prevent delamination and failure
6. Quantified the effect of thermal cure and operating temperature variation on nanocomposite structure performance; quantified the influence of nanotubes on crack propagation in structural composites

1.7. Outline of the Dissertation

The dissertation will be structured as follows:

Chapter 2 presents a description of the multiscale analysis and the micromechanics approaches used to determine the effective properties at the different length scales used in the numerical analysis. Parameter estimation is also presented, which estimates the mechanical properties of the nanocomposite based on a Kalman filter framework.

Chapter 3 discusses the stress and displacement field variation of the nanocomposite based on a perturbation approach. The analysis takes into account the time-dependent effects of the interface between the CNT and matrix by using the Kelvin-Voiget model. Results are presented based on the variation of the number of CNT walls, CNT aspect ratio, and the existence of interfacial layers between the CNT and matrix.

Chapter 4 describes the FEMs constructed for the purpose of this research. The analysis approach used to quantify the effect of using nanotubes is also presented, as well as validation by comparing the results with available experimental data in the literature.

The results from the analysis will then be presented for different loading conditions, namely pull-off and combined axial-pull-off, using different CNT weight percentages.

Chapter 5 presents the experimental work conducted in support of this research. Correlation with FEMs is also shown to validate the analytical solution presented in the previous chapters.

Chapter 6 highlights the thermo-mechanical analysis conducted. The effect of cure temperature is discussed, and the effect of operating temperature on the failure load is shown and quantified to be able to determine the influence of temperature on the failure load.

Chapter 7 presents conclusions and future work.

CHAPTER 2

EFFECTIVE MECHANICAL PROPERTIES OF NANOCOMPOSITES

Much attention has been focused on the modeling of composites containing CNTs. Because the nanocomposite is a macro, continuum scale composite and the individual phases can range from the continuum scale down to the nanometer scale, this creates challenges for analytical or numerical modeling. Throughout the literature, there are several models and techniques that address material behavior at the various length scales (Bouvard, J. L. et al. 2009), (Elliott, J. A., 2011), (Steinhauser, M. and Hiermaier, S. 2009).

Modeling of nanomaterials usually takes the form of a systematic procedure, which aids in transitioning from one scale to another. One example is the use of Schrödinger’s equation under a quantum mechanics framework at subnanometer scales. This allows the generation of the CNTs electronic structure. This approach is often avoided due to its large computational cost. One solution lies in the application of periodic boundary conditions, where models limited to a few hundred atoms yield acceptable results. Minimization of atomic conformations using Newton’s second law allows for the modeling of CNTs and their interaction with a polymer matrix, such as the approach of molecular dynamic (MD) simulations, which also requires high computational cost. Traditional continuum mechanics approaches can be efficiently used at larger scales in which engineering loads are applied with sufficient information about the submicron scale inhomogeneity. At the macroscale, continuum modeling methods, such as FE modeling, are utilized at scales of the order of millimeters or larger to design composite structures based on loading conditions.

Mechanical properties of nanostructured materials can be determined by a select set of computational methods. As discussed in Chapter 1 section 1.4, one of the most widely used approaches for determining the stress or strain concentration tensors (used to determine the effective properties of composite materials) is the Mori-Tanaka method, which was originally developed in 1973 (Mori, T. and Tanaka, K. 1973). This method focuses on calculating the average internal stress in matrix materials with inclusions. It use has attracted research in composite materials based on the idea of equivalent inclusions by Eshelby.

Introduced by Hashin and Rosen in 1964, the composite cylinder method is another technique used to determine the bounds and expressions for the effective elastic moduli of materials reinforced by parallel hollow circular fibers (Hashin, Z. and Rosen, B. 1964). The model utilized the direct strain energy equivalency between the response of concentric circular fiber cylinders embedded in a matrix (representing aligned fibers randomly dispersed in the matrix) and effective material response. The method can be used to determine the longitudinal Young's modulus, the longitudinal stiffness, the plane strain bulk modulus, the longitudinal shear, and the transverse shear for the effective material. This was accomplished by applying five sets of traction and displacement boundary conditions to the composite cylinder assemblage. Similar expressions for the effective properties were derived for all but one case: the transverse shear modulus G_{23}. Christensen and Lo (Christensen, R. and Lo, K. 1979) proposed the generalized self-consistent approach that yielded an expression for the shear modulus of spherical particles in a matrix.

This chapter presents the method adopted in this research to obtain effective mechanical properties. A combination of both the Mori-Tanaka and the composite cylinder method are used in a unique three-scale approach. Other special consideration will also be discussed throughout the chapter.

2.1. The Governing Equations

The linearized elasticity equations govern the macro- and microscales of the RVE for linear elastic composites. These can be related through the definition of the effective stiffness tensor C_{ijkl}^{eff}. At the macroscale, the static equilibrium equations are

$$\bar{\sigma}_{ji,j} + f_i \tag{1}$$

where $\bar{\sigma}_{ji}$ is the macroscale Cauchy stress, f_i is defined as the body force, and $\bar{\sigma}_{ji,j}$ is the divergence of the stress tensor in terms of the X_i coordinate system. The macroscale boundary conditions can be defined by specified tractions $(\bar{t}_i = \bar{\sigma}_{ji} n_j)$ or displacements $(\bar{u}_i = u_i)$. The macroscale kinematic relations are expressed in terms of the linearized strain-displacement equations given by

$$\bar{\varepsilon}_{ij} = \frac{1}{2}(\bar{u}_{i,j} + \bar{u}_{j,i}) \tag{2}$$

where $\bar{\varepsilon}_{ij}$ is the infinitesimal strain tensor in the macroscale, $\bar{u}_i$ is the displacement vector of a macroscale material point, and $\bar{u}_{i,j}$ is the gradient of the displacement vector in terms of the macroscale X_i coordinate system. Hence, the Cauchy stress tensor can be expressed as

$$\overline{\sigma}_{ij} = C_{ijkl}^{eff}\,\overline{\varepsilon}_{kl} \tag{3}$$

It should be noted that the effective stiffness tensor is obtained from the microscale; therefore, it is a function of the microscale x_i coordinate system.

Eq. (3) can be expressed as

$$\langle \sigma_{ij} \rangle = C_{ijkl}^{eff} \langle \varepsilon_{kl} \rangle$$

(4)

where

$$\langle \bullet \rangle = \frac{1}{V}\int_V \bullet\, dV \tag{5}$$

denotes the volume averages with V as the volume of the RVE in the microscale x_i coordinate system.

For the microscale RVE, the static equilibrium equations are expressed as

$$\sigma_{ij,j} = 0 \tag{6}$$

where σ_{ij} is the microscale Cauchy stress and $\sigma_{ij,j}$ denotes the divergence of the stress tensor in terms of the x_i coordinate system. It is noted that the body force is not included in Eq. (6) as it can be observed from the theory of multiple scale expansion that the body force need not be considered in the microscale equilibrium equations (Jansson, S. 1992). The microscale kinematic relations are expressed in terms of the linearized strain-displacement equations given by

$$\varepsilon_{ij} = \frac{1}{2}(u_{i,j} + u_{j,i}) \tag{7}$$

where ε_{ij} is the infinitesimal strain tensor on the microscale, u_i is the displacement vector of a material point, and $u_{i,j}$ denotes the gradient of the displacement vector in terms of the microscale x_i coordinate system. Assuming that all of the materials in the composite are linear elastic, the Cauchy stress is related to the infinitesimal strain tensor in the microscale through the constitutive relations given by

$$\sigma_{ij} = C_{ijkl}^{eff} \varepsilon_{kl} \tag{8}$$

where C_{ijkl}^{eff} is the fourth-order stiffness tensor, which varies in x_i depending on the microstructure of the composite. The inverse of the stiffness tensor is defined to be the compliance tensor O_{ijkl}^{eff}, so that Eq. (8) can alternatively be expressed as

$$\varepsilon_{ij} = O_{ijkl}^{eff} \sigma_{kl} \tag{9}$$

On the boundary of the microscale RVE, the traction or displacement conditions are homogeneous and consistent with the stress or strain at the macroscale (Jansson, S. 1992), i.e.

$$t_i = \sigma_{ji} n_j = \overline{\sigma}_{ji} n_j \tag{10}$$

$$u_i = \overline{\varepsilon}_{ij} x_j \tag{11}$$

where n_i is the unit outward normal on the RVE surface.

It can further be shown that, for linear materials the multiple scale expansion is synonymous with equating the strain energy of the RVE with that of the homogeneous effective material. For example, the volume-averaged strain energy density of the RVE is defined as

$$W^{RVE} = \frac{1}{2}\left\langle \sigma_{ij} \right\rangle \left\langle \varepsilon_{ij} \right\rangle \tag{12}$$

Similarly, the volume-averaged strain energy of the effective homogeneous material is defined as

$$W^{eff} = \frac{1}{2}\left\langle \sigma_{ij}{}^{eff} \right\rangle \left\langle \varepsilon_{ij}{}^{eff} \right\rangle \tag{13}$$

where σ_{ij}^{eff} and ε_{ij}^{eff} are the stress and strain in the effective homogeneous material having stiffness C_{ijkl}^{eff} and assumed applied displacements also given by Eq. (11), so that

$$W^{eff} = \frac{1}{2} C_{ijkl}^{eff} \bar{\varepsilon}_{kl} \bar{\varepsilon}_{ij} \tag{14}$$

Equating the volume-averaged strain energy of the RVE with that of its effective homogeneous material as

$$W^{RVE} = W^{eff} \tag{15}$$

we obtain

$$\left\langle \sigma_{ij} \right\rangle = C_{ijkl}^{eff} \bar{\varepsilon}_{kl} = C_{ijkl}^{eff} \left\langle \varepsilon_{kl} \right\rangle \tag{16}$$

which is equivalent to Eq.(4).

It must be noted that the effective properties are not dependent on the variation of the macroscale stresses or displacements. Therefore, considering the linear constitutive response of the composite (assuming no damage evolution at the microscale), the effective properties are independent of the macroscale boundary conditions and geometry. Hence, the effective properties are computed using the microscale RVE. Within the microscale RVE, subsets of volume (V_J) of the total volume (V) corresponding to the separate phases identified in the RVE are used to define a volume fraction for that phase as

$$c_J = \frac{V_J}{V} \tag{17}$$

such that for *N* phases

$$1 = \sum_{J=1}^{N} c_J \tag{18}$$

It is assumed that each inhomogeneity in the RVE and matrix are all considered to be separate phases. Thus, the volume averages of the stress and strain in the RVE can be expressed in terms of the volume averages of these quantities in each phase as follows

$$\left\langle \sigma_{ij} \right\rangle = \frac{1}{V}\left[\sum_{J=1}^{N} \frac{V_J}{V_J} \int_{V_J} \sigma_{ij}^{J} dV \right] \tag{19}$$

$$\left\langle \varepsilon_{ij} \right\rangle = \frac{1}{V}\left[\sum_{J=1}^{N} \frac{V_J}{V_J} \int_{V_J} \varepsilon_{ij}^{J} dV \right] \tag{20}$$

where the superscript *J* denotes value of the quantity within the J^{th} phase. Eqns. (19) and Eq. (20) can be written as

$$\left\langle \sigma_{ij} \right\rangle = \sum_{J=1}^{N} c_J \left\langle \sigma_{ij}^{J} \right\rangle \tag{21}$$

$$\left\langle \varepsilon_{ij} \right\rangle = \sum_{J=1}^{N} c_J \left\langle \varepsilon_{ij}^{J} \right\rangle \tag{22}$$

Applying the constitutive relations in Eq. (8) and Eq. (9), the volume averages of these quantities in the RVE given in Eq. (21) and Eq. (22) (assuming each phase is homogeneous) can be written as

$$\left\langle \sigma_{ij} \right\rangle = \sum_{J=1}^{N} c_J C_{ijkl}^{J} \left\langle \varepsilon_{ij}^{J} \right\rangle \tag{23}$$

$$\left\langle \varepsilon_{ij} \right\rangle = \sum_{J=1}^{N} c_J O_{ijkl}^{J} \left\langle \sigma_{ij}^{J} \right\rangle \tag{24}$$

The concentration tensor is now defined as the tensor that transforms the average quantity (stress, strain) into a phase averaged quantity, i.e.

$$\left\langle \sigma_{ij}^{J} \right\rangle = B_{ijkl}^{J} \left\langle \sigma_{ij} \right\rangle \tag{25}$$

$$\left\langle \varepsilon_{ij}^{J} \right\rangle = A_{ijkl}^{J} \left\langle \varepsilon_{ij} \right\rangle \tag{26}$$

Substituting the definitions of the concentration tensors in Eq. (23) into Eq. (24), one can obtain

$$\left\langle \sigma_{ij} \right\rangle = \sum_{J=1}^{N} c_J C_{ijkl}^{J} A_{klmn}^{J} \left\langle \varepsilon_{mn} \right\rangle \tag{27}$$

$$\left\langle \varepsilon_{ij} \right\rangle = \sum_{J=1}^{N} c_J O_{ijkl}^{J} B_{klmn}^{J} \left\langle \sigma_{mn} \right\rangle \tag{28}$$

Therefore, from the definitions of the effective properties in Eq. (8) and Eq. (9), it is observed from Eq. (27) and Eq. (28) that the effective properties can be expressed as

$$C_{ijmn}^{eff} = \sum_{J=1}^{N} c_J C_{ijkl}^{J} A_{klmn}^{J} \tag{29}$$

$$O_{ijmn}^{eff} = \sum_{J=1}^{N} c_J O_{ijkl}^{J} B_{klmn}^{J} \tag{30}$$

One can rewrite the consistency conditions as

$$c_N A_{ijkl}^{N} = I_{ijkl} = \sum_{J=1}^{N-1} c_J A_{ijkl}^{J} \tag{31}$$

$$c_N B_{ijkl}^{N} = I_{ijkl} = \sum_{J=1}^{N-1} c_J B_{ijkl}^{J} \tag{32}$$

where I_{ijkl} is the fourth-order identity tensors. Substituting Eq. (31) and Eq. (32) into Eq. (29) and Eq. (30)

$$C_{ijmn}^{eff} = \frac{c_N}{c_N} C_{ijkl}^{J} \left(I_{klmn} - \sum_{J=1}^{N-1} c_J A_{klmn}^{J} \right) + \sum_{J=1}^{N-1} c_J C_{ijmn}^{J} A_{klmn}^{J} \tag{33}$$

and the effective properties can be written as

$$C_{ijmn}^{eff} = C_{ijmn}^{N} + \sum_{J=1}^{N-1} c_J \left(C_{ijkl}^{J} - C_{ijkl}^{N} \right) A_{klmn}^{J}$$

(34)

$$O_{ijmn}^{eff} = O_{ijmn}^{N} + \sum_{J=1}^{N-1} c_J \left(O_{ijkl}^{J} - O_{ijkl}^{N} \right) B_{klmn}^{J} \tag{35}$$

Based on Eq. (34) and Eq. (35), one can consider inhomogeneities as having the same material properties and concentration tensors in a given RVE as a single phase; therefore, the combination of their individual volumes can be used to determine the volume fraction of the phase. Factors such as the shape of the inhomogeneity, its relative geometric orientation in the RVE, and orientation of the material symmetry within the inhomogeneity constitute whether a set of inhomogeneities constitute a single phase in that RVE. The availability of material properties of each phase allows for the determination of the concentration tensor for each phase.

In cases where the RVE model becomes too computationally intensive, the inhomogeneities can be grouped into a single phase. By utilizing closed-form solutions or approximate solutions (i.e., FE modeling) the concentration tensors can be approximated for each phase and substituted into Eq. (34) and Eq. (35). Such approximations consider a single inhomogeneity or a collection (clusters and bundles) of them to determine concentration tensors for the phase. It is noted that when using such approximations, one must account for the interactions of the individual inhomogeneities with all other inhomogeneities within the RVE.

2.2. The Mori-Tanaka Method

In order to calculate the strain or stress concentration tensors for homogeneous ellipsoidal inhomogeneities in a linear elastic matrix, the Eshelby equivalence principal must be used. The Eshelby solution embeds the inhomogeneities into the matrix material subject to a far-field displacement or traction consistent with the ones applied to the boundary of the microscale RVE. This is graphically shown in Figure 11.

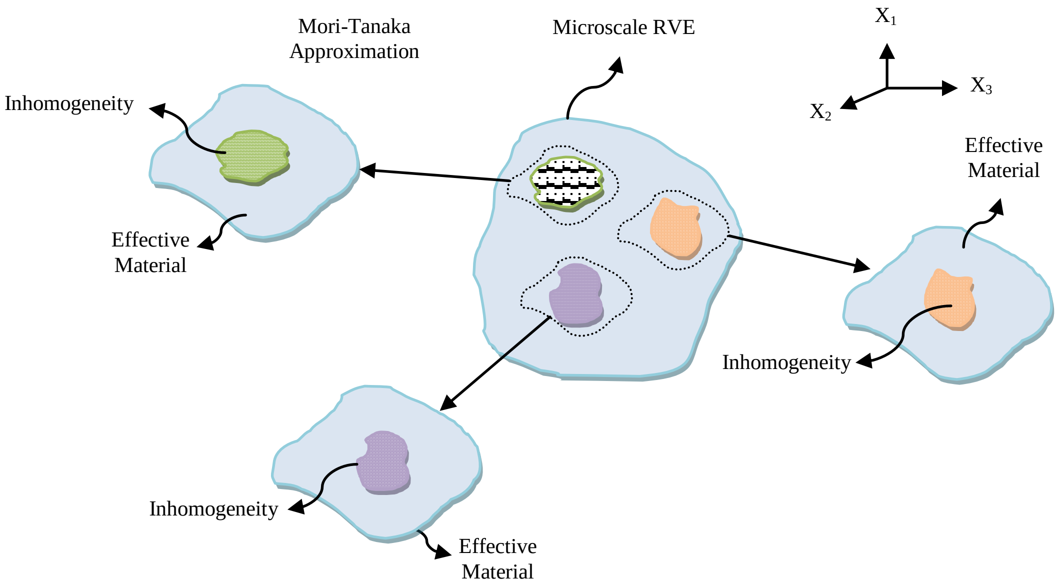

Figure 11. Graphical representation of the Mori-Tanaka approximations

These traction and displacement fields are representative of the average macroscale stress/strain with an additional perturbation added to account for interactions. The strain concentration tensor is given by applying the Mori-Tanaka method as follows

$$ {}^{MT}A^J_{ijmn} = T^J_{ijkl}\left[c_N I_{mnkl} + \sum_{J=1}^{N-1} c_J T^J_{mnkl}\right]^{-1} \tag{36} $$

with

$$ T^J_{pqij} = \left[I_{ijpq} + S_{ijkl} M^N_{klmn}\left(L^J_{mnpq} - L^N_{mnpq}\right)\right]^{-1} \tag{37} $$

where S_{ijkl} is the Eshelby tensor given by Eshelby (Eshelby, J.D. 1957) and Mura (Mura, T. 1987) and can be formulated using

Table 2. The stress concentration tensor in Eq. (25) is identified in the Mori-Tanaka method as

$$ {}^{MT}B^J_{ijmn} = P^J_{ijkl}\left[c_N I_{mnkl} + \sum_{J=1}^{N-1} c_J P^J_{mnkl}\right]^{-1} \tag{38} $$

where

$$ P^J_{ijpq} = L^J_{ijkl} T^J_{klmn} O^N_{mnpq} \tag{39} $$

2.3. The Composite Cylinder Method

The Mori-Tanaka method introduced in the previous section makes use of the Eshelby solution to approximate the concentration tensor. Therefore, it is intended for homogeneous ellipsoidal inhomogeneities. In this section, the generalized self-consistent composite cylinder method is introduced. This method surrounds inhomogeneities with a matrix shell for the purpose of estimating the concentration tensor; hence, the Eshelby tensor is no longer required for estimating the concentration tensors. This approximation is represented in Figure 12.

Table 2. The Eshelby tensor as a function of aspect ratio (Odegard,G. and Gates, T. 2002)

	Ellipsoid	Circular cylinder
S_{11}	$\frac{4p}{3}+RI_3+2s^2T$	0
S_{22} = S_{33}	$P+RI_1+\frac{3T}{4}$	$\frac{5-4\upsilon_m}{8(1-\upsilon_m)}$
S_{23} = S_{32}	$\frac{P}{3}-RI_1+\frac{4T}{3}$	$\frac{-1-4\upsilon_m}{8(1-\upsilon_m)}$
S_{21} = S_{31}	$-RI_1-s^2T$	$\frac{\upsilon_m}{2(1-\upsilon_m)}$
S_{12} = S_{13}	$-RI_3-T$	0
S_{44}	$\frac{P}{3}+RI_1+\frac{T}{4}$	$\frac{3-4\upsilon_m}{8(1-\upsilon_m)}$
S_{55} = S_{66}	$2R-\frac{RI_1}{2}-\frac{1-S^2}{2}T$	$\frac{1}{4}$
Other S_{ij}	0	0

$$I_1=\frac{2s}{\sqrt{\left(s^2-1\right)^3}}\left[s\sqrt{\left(s^2-1\right)}-\cosh^{-1}(s)\right], P=\frac{3}{8\left(1-\upsilon_m\right)}, \; T=\frac{4-3I_1}{3\left(s^2-1\right)}P, \; I_3=4-2I_1$$

with s and υ_m as the aspect ratio and matrix material Poisson's ratio.

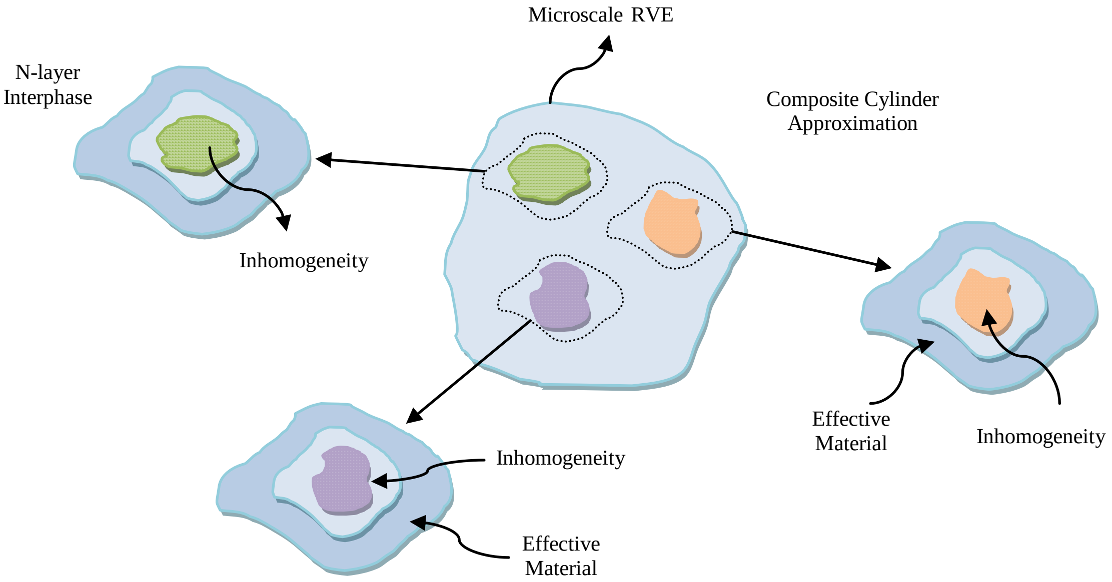

Figure 12. Graphical representation of the composite cylinder approximation

A calculation of the concentration tensors of homogenous cylinders using the self-consistent composite cylinder method can be achieved by formulating closed-form solutions for composite cylinders. This is done by embedding inhomogeneities into an effective medium and applying far-field displacement or traction boundary conditions, consistent with the ones applied to the boundary of the microscale RVE, which indicate the average macroscale strain/strain. This approximation is represented in Figure 13.

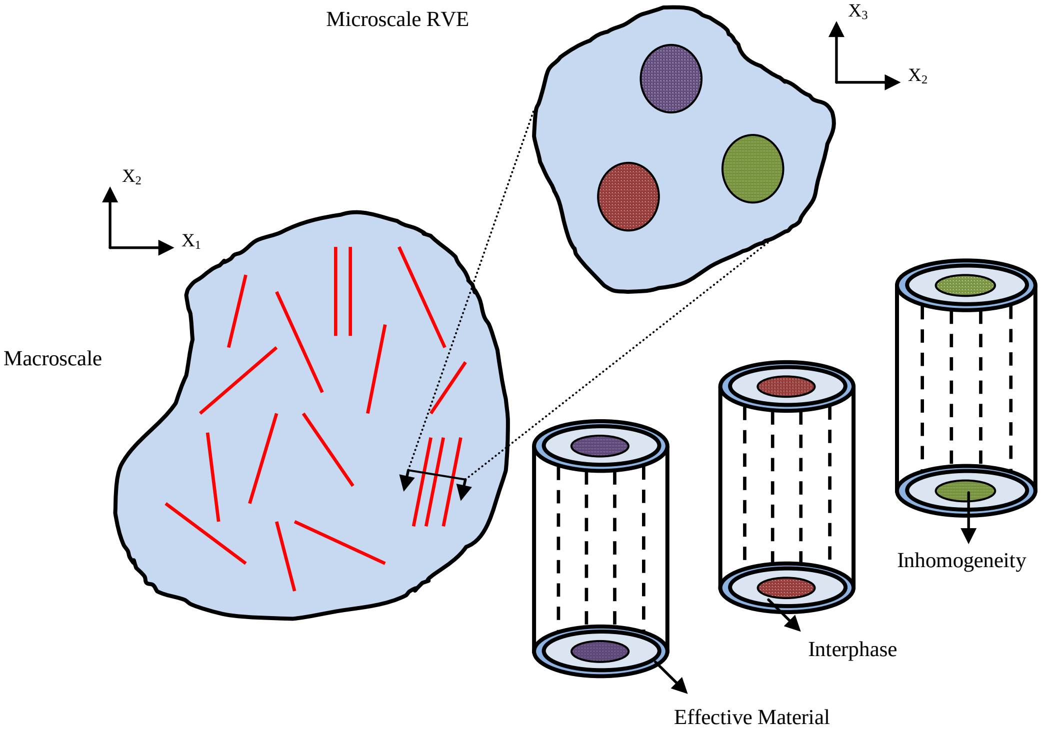

Figure 13. Graphical representation of the composite cylinder approximation

The multi-layered and generalized self-consistent composite cylinders method uses both energy equivalency and direct averaging methods. Consider the multi-layered composite cylinder assemblage shown in Figure 14; each layer is assumed to be subject to displacement fields, which satisfy the equilibrium equations. Another assumption is that each layer is a compatible phase in the configuration and does not include residual stresses or transformation strains. It is further assumed that each layer is subject to small deformations so that continuity of tractions and displacements can be applied across the boundary layers. The analogous homogeneous cylinder in Figure 15 is also subject to displacement fields, which satisfy the equilibrium equations. Using the strain displacement relations, the strains in each layer are determined by using the appropriate constitutive relation for each layer to calculate the stress.

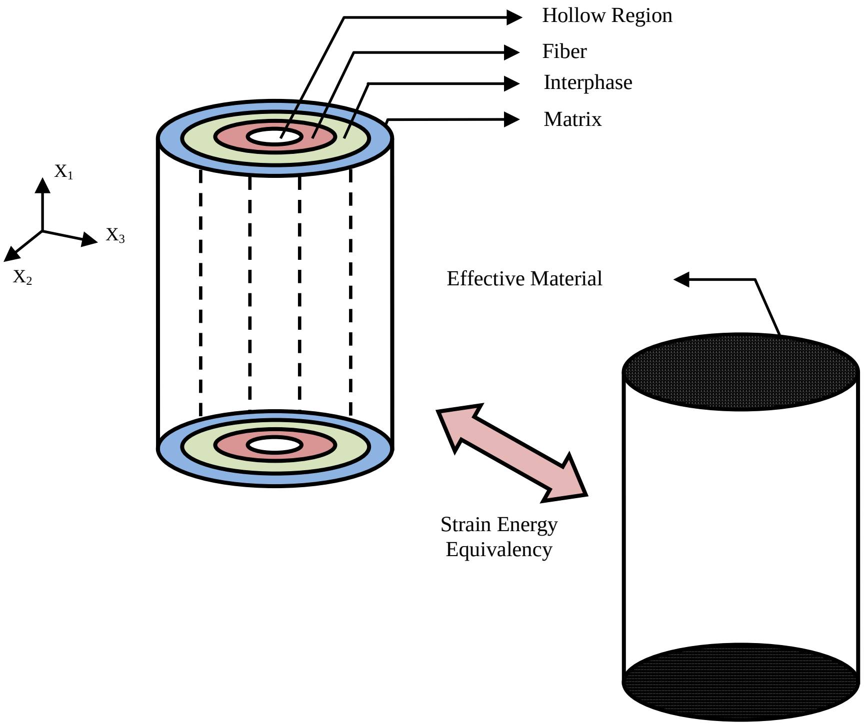

Figure 14. Graphical representation of the multi-layered and generalized self-consistent composite cylinders methods

Homogenous boundary conditions, depending on the number of independent effective material properties, are applied to the composite cylinder assemblage. The suitable interface matching conditions between the layers are also applied. Due to the transverse isotropic nature of the effective material, five sets of boundary conditions are required. To acquire the effective elastic properties of aligned fiber composites using the composite cylinders method, the volume-averaged strain energies of both the composite cylinder assemblage (W) and of the effective homogeneous cylinder (W^{eff}) are obtained from the volume average of the strain energy and are set equal to one another. Boundary value problems solved in the composite cylinder method are summarized in Table 3. The solution to these problems enables the calculations of the effective material in-plane bulk modulus, axial Young’s modulus, axial stiffness component, axial shear modulus, and in-plane shear modulus.

Table 3. Boundary value problems solved in the composite cylinder method*

Property	Boundary conditions
In-plane Bulk Modulus $\left(\kappa_{23}^{eff}\right)$	$u_z(r,\theta,L)=0, \quad u_z(r,\theta,-L)=0$ $\sigma_{rr}(r_0,\theta,z)=0, \quad u_r(r_N,\theta,z)=\varepsilon_0 r_N$
Axial Young’s Modulus $\left(E_{11}^{eff}\right)$	$u_z(r,\theta,L)=\varepsilon_0 L, \quad u_z(r,\theta,-L)=-\varepsilon_0 L$ $\sigma_{rr}(r_0,\theta,z)=0, \quad \sigma_{rr}(r_N,\theta,z)=\varepsilon_0 r_N$
Axial Stiffness Component $\left(C_{1111}^{eff}\right)$	$u_z(r,\theta,L)=\varepsilon_0 L, \quad u_z(r,\theta,-L)=-\varepsilon_0 L$ $\sigma_{rr}(r_0,\theta,z)=0, \quad u_r(r_N,\theta,z)=\varepsilon_0 r_N$
Axial Shear Modulus $\left(G_{12}^{eff}\right)$	$\sigma_{zz}(r,\theta,L)=0, \quad \sigma_{zz}(r,\theta,-L)=0$ $\sigma_{rz}(r_0,\theta,z)=0, \quad u_r(r_N,\theta,z)=2\varepsilon_0 r_N\cos(\theta)$
In-plane Shear Modulus $\left(G_{23}^{eff}\right)$	$\sigma_{rr}(r_0,\theta,z)=0, \quad \sigma_{r\theta}(r_0,\theta,z)=0$ $u_z(r,\theta,L)=0, \quad u_z(r,\theta,-L)=0$ $u_r(r_N,\theta,z)=\varepsilon_0 r_N\sin(2\theta)/2$ $u_\theta(r_N,\theta,z)=\varepsilon_0 r_N\sin(2\theta)/2$

*See Fig. 15 for coordinates and dimensions

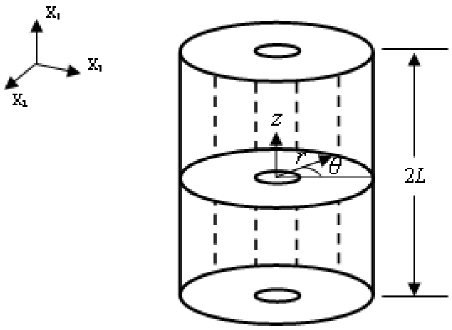

Figure 15. Coordinate system under which the boundary value problems solved in the composite cylinder method

The solutions to the equilibrium equations in cylindrical coordinates given in Eq. (40) provide the assumed displacement fields applied in each boundary value problem, where each phase of the composite cylinder assemblage is homogeneous.

$$\begin{aligned}
&\frac{\partial \sigma_{rr}}{\partial r}+\frac{1}{r}\frac{\partial \sigma_{r\theta}}{\partial \theta}+\frac{\partial \sigma_{rz}}{\partial z}+\frac{1}{r}\left(\sigma_{rr}-\sigma_{\theta\theta}\right)=0\\
&\frac{\partial \sigma_{r\theta}}{\partial r}+\frac{1}{r}\frac{\partial \sigma_{\theta\theta}}{\partial \theta}+\frac{\partial \sigma_{\theta z}}{\partial z}+\frac{2}{r}\sigma_{r\theta}=0\\
&\frac{\partial \sigma_{rz}}{\partial r}+\frac{1}{r}\frac{\partial \sigma_{\theta z}}{\partial \theta}+\frac{\partial \sigma_{zz}}{\partial z}+\frac{1}{r}\sigma_{rz}=0
\end{aligned} \tag{40}$$

The effective properties obtained from the multi-layered composite cylinders method can be summarized as follows (Christensen, R. and Lo, K. 1979) (Miloh, T. and Benveniste, Y. 1988) (Seidel, G. D. 2007) (Seidel, G. D. and Lagoudas, D. C. 2006).

Effective in-plane bulk modulus

$$\kappa_{23}^{eff}=\frac{\left(\mu_N+\lambda_N\right)r_N^2D_1^N-\mu_N D_2^N}{r_N^2D_1^N+D_2^N} \tag{41}$$

Effective axial Young's modulus

$$E_{11}^{eff}=\frac{\sum_{i=1}^{N}\left[2\left(\mu_i+\lambda_i\right)\varepsilon_0+2\lambda_i D_1^i\right]\left(r_i^2-r_{i-1}^2\right)}{\varepsilon_0 r_N^2} \tag{42}$$

Here it is noted that because the definition of the axial stiffness C_{1111}^{eff} and axial Young's modulus E_{11}^{eff} are identical and that the same displacement fields are used to calculate both properties, Eqn. (42) can also be used to calculate C_{1111}^{eff} with the only difference being the displacement constant D_1^i due to the difference in boundary conditions applied to the problem when solving for the axial stiffness component.

Effective axial shear modulus

$$G_{12}^{eff} = \frac{\mu_N \left(r_N^2 D_1^N - D_2^N \right)}{r_N^2 D_1^N + D_2^N} \tag{43}$$

In-plane shear modulus

The effective in-plane shear modulus cannot be estimated by the composite cylinder method (Odegard, G.M. et al. 2002.), which leads to the need to use the generalized self-consistent composite cylinders method. In this method, the composite cylinder assemblage shown in

Figure 16 is embedded in a (N + 1)th layer composed of material with properties similar to the material of the effective solid homogeneous cylinder of

Figure 16. By using the energy equivalency between the generalized self-consistent composite cylinder assemblage and a homogeneous solid cylinder, the effective in-plane shear modulus $\left(G_{23}^{eff} \right)$ can be calculated. It should be noted that the displacement field for the (N+1) layer is assumed to be a function of G_{23}^{eff}, and that is how the value is obtained after satisfying the boundary conditions.

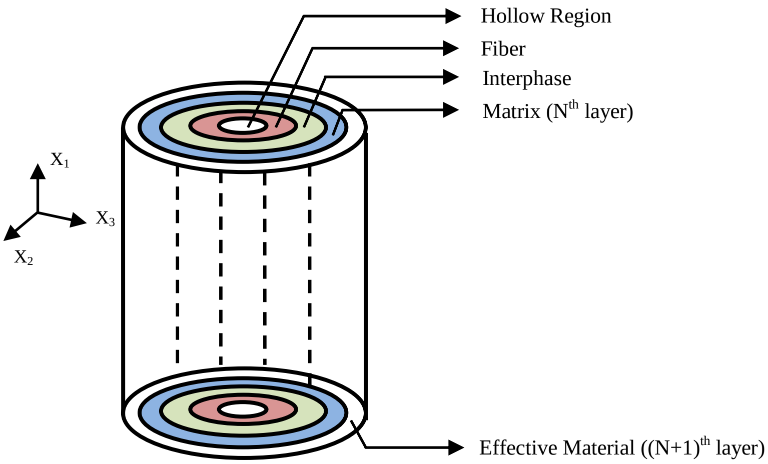

Figure 16. Graphical representation of a generalized self-consistent composite cylinders method – a multi-layer composite cylinder assemblage embedded into an (N+1)th layer of effective material

Axial Poisson's ratio

$$\upsilon_{12}^{eff} = -\frac{1}{\varepsilon_0}\left(D_1^n + D_2^n \frac{1}{r_N^2}\right) \tag{44}$$

Transverse Young's modulus

$$E_{22}^{eff} = \frac{4\mu_{23}^{eff}\kappa_{23}^{eff}}{\kappa_{23}^{eff} + \mu_{23}^{eff} + \dfrac{4\left(\upsilon_{12}^{eff}\right)^2 \mu_{23}^{eff}\kappa_{23}^{eff}}{E_{11}^{eff}}} \tag{45}$$

Poisson's ratio

$$\upsilon_{23}^{eff} = \frac{\kappa_{23}^{eff} - \mu_{23}^{eff} - \dfrac{4\left(\upsilon_{12}^{eff}\right)^2 \mu_{23}^{eff}\kappa_{23}^{eff}}{E_{11}^{eff}}}{\kappa_{23}^{eff} + \mu_{23}^{eff} + \dfrac{4\left(\upsilon_{12}^{eff}\right)^2 \mu_{23}^{eff}\kappa_{23}^{eff}}{E_{11}^{eff}}} \tag{46}$$

Prior to presenting the result obtained from the previous discussion, it should be noted that the CNTs are assumed to be randomly oriented within the matrix. The effective properties for randomly oriented CNTs within the RVE are determined using a set of transformations that take into account the different inhomogeneities at distinct orientations. In order to denote the orientations associated with each phase, the effective stiffness is written as (Marzari 1992) (Odegard, G.M. 2003).

$$C_{ijkl}^{eff} = C_{ijkl}^{N} + \sum_{J=1}^{M} c_J(\theta_J, \beta_J)\left(C_{ijmn}^{J}(\theta_J, \beta_J) - C_{ijmn}^{N}\right)A_{mnkl}^{J}(\theta_J, \beta_J) \tag{47}$$

where $c_J(\theta_J, \beta_J)$ is the volume fraction of a given orientation and where

$$C_{ijmn}^{J}(\theta_J, \beta_J) = Q_{ip}^{J} Q_{jq}^{J} \tilde{C}_{pqrs} Q_{mr}^{J} Q_{ns}^{J} \tag{48}$$

$$A_{ijmn}^{J}(\theta_J, \beta_J) = Q_{ip}^{J} Q_{jq}^{J} \tilde{A}_{pqrs} Q_{mr}^{J} Q_{ns}^{J} \tag{49}$$

$$c_J(\theta_J, \beta_J) = w_J \bar{c} \tag{50}$$

where the tilde denotes quantities expressed in the local inhomogeneity coordinate system and where w_J is the weight factor for the fraction of inhomogeneities with a given angle orientation (θ_J, β_J). The angle orientation relates the local inhomogeneity orientation to the microscale RVE coordinate system by a change of basis, which is determined from a series of single axis rotations, i.e. $Q_{ij}^{J} = Q_{ij}^{J,\theta} Q_{ij}^{J,\beta}$ such that in engineering notation

$$[Q^J] = \begin{bmatrix} \cos(\theta) & 0 & -\sin(\theta) \\ \sin(\beta)\sin(\theta) & \cos(\beta) & \sin(\beta)\cos(\theta) \\ \cos(\beta)\sin(\theta) & -\sin(\beta) & \cos(\beta)\cos(\theta) \end{bmatrix} \tag{51}$$

c is the total volume fraction of the inhomogeneity irrespective of orientation. It is also noted that $\tilde{C}_{pqrs}$ and $\tilde{A}_{pqrs}$ have been expressed without a superscript J in order to emphasize that the only difference between the inhomogeneities in all of the phases is the orientation.

2.4. Multiscale Approach – Effective Mechanical Properties

The main objective of the theory presented thus far is to lay the foundation for estimating the effective properties of nanocomposites over multiple scales. By starting out with the smallest constituent, the CNT, effective mechanical properties can be acquired based on the composite cylinder method. The composite cylinder method allows for calculating the effective properties of a single or multi-wall nanotube. Equations 41–46 allow for the calculation of the effective nanotube mechanical properties. Having acquired the properties of an effective nanotube, they can be used in tandem with matrix material isotropic properties to calculate the effective properties of the nanocomposite. This is done using the Mori-Tanaka method explained in section 2.2 for the effective mechanical properties. This will result in effective nanocomposite properties, which can then be used as a matrix material for composite laminates. This allows for calculating the mechanical properties of a unidirectional lamina composed of two constituents: AS4 carbon fiber and effective nanocomposite matrix. Figure 17 shows a flowchart of the multiscale approach adopted in this research.

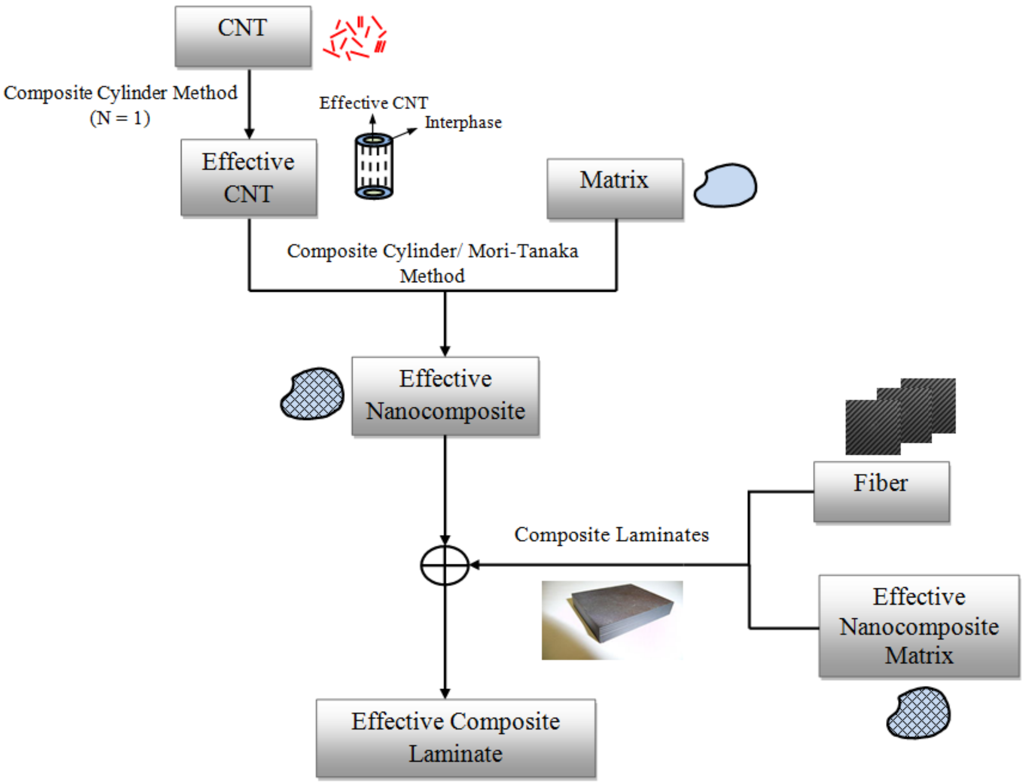

Figure 17. Flow chart of the multiscale analysis for acquiring unidirectional lamina mechanical and thermal properties

2.5. Numerical Results

The literature is rich with research into predicting the properties of nanocomposites that include CNTs embedded in polymer matrix (Gary D.S. and Dimitris C.L. 2006). However, the study of composites consisting of CNTs, fibers, and a matrix material has not received the same attention. The goal of the results presented here is to provide insight into the effect of adding CNTs on the mechanical properties, specifically those for the third length scale in our study, which represents the nano-unidirectional composite lamina. The fibers are assumed to be made of AS4 carbon. Table 4 shows the elastic and geometric properties of the CNTs used in the analysis. The effective properties obtained using the composite cylinder method for a three-wall CNT is shown in Table 5.

Table 4. Mechanical and geometrical properties of CNTs

Variable	**Value**
Young's Modulus	159.5 Msi
Poisson's ratio	0.14
Wall thickness	13.26 e^{-9} inch

Table 5. Effective CNT properties acquired through the composite cylinder method (N = 3)

Variables	**Effective CNT (inner radius = 19.89 e-9 inch)**
E_{11}^{eff}	128.8 Msi
E_{22}^{eff}	84 Msi
G_{12}^{eff}	48.245 Msi
G_{23}^{eff}	48.3 Msi
v_{12}^{eff}	0.19
v_{23}^{eff}	0.392

Figure 18 presents the variation of the nanocomposite mechanical properties as a function of CNT volume fraction. The results show an increase in the axial and lateral elastic moduli as the CNT volume fraction increases. The axial elastic modulus increases at an almost linear behavior as the volume fraction increases, while the lateral modulus exhibits such a trend up to 0.6 volume fraction and then increases in an exponential manner. The same behavior can be seen in the shear moduli after 0.6 volume fraction. Poisson’s ratio, in regards to the effect of axial displacement on lateral displacement (ν_{12}), decreases as the volume fraction increases. However, ν_{23} increases initially and then steadily decreases as the volume fraction increases.

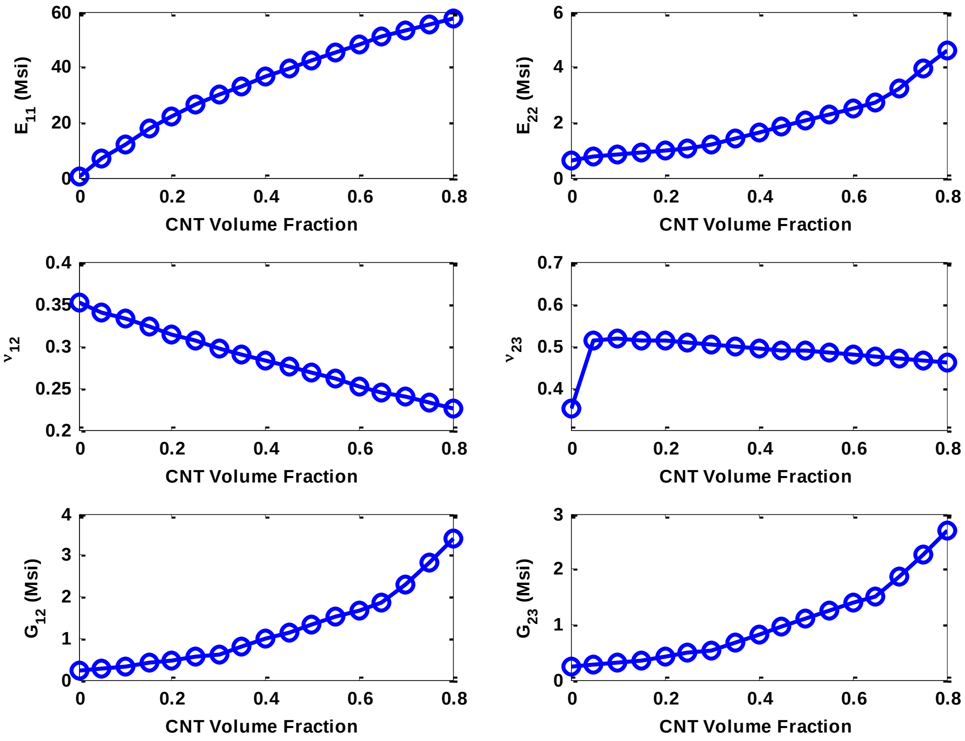

Figure 18. Effective mechanical properties of nanocomposite with three-walled CNT as a function of CNT volume fraction

In Figure 19, the variation of the nanocomposite mechanical properties as a function of CNT aspect ratio is shown. The results show that all the mechanical properties are affected by the change in aspect ratio. The axial elastic modulus increases substantially as the aspect ratio increases up until 100. The lateral modulus, however, exhibits a smaller increase with aspect ratio. The effect of aspect ratio on the shear moduli is subtle, where they both slightly decrease up until an aspect ratio of 50 and then remain constant. Poisson’s ratio, ν_{12}, decreases slightly as the aspect ratio increases, while ν_{23} increases up to 0.51 when the aspect ratio is 50 and then remains constant.

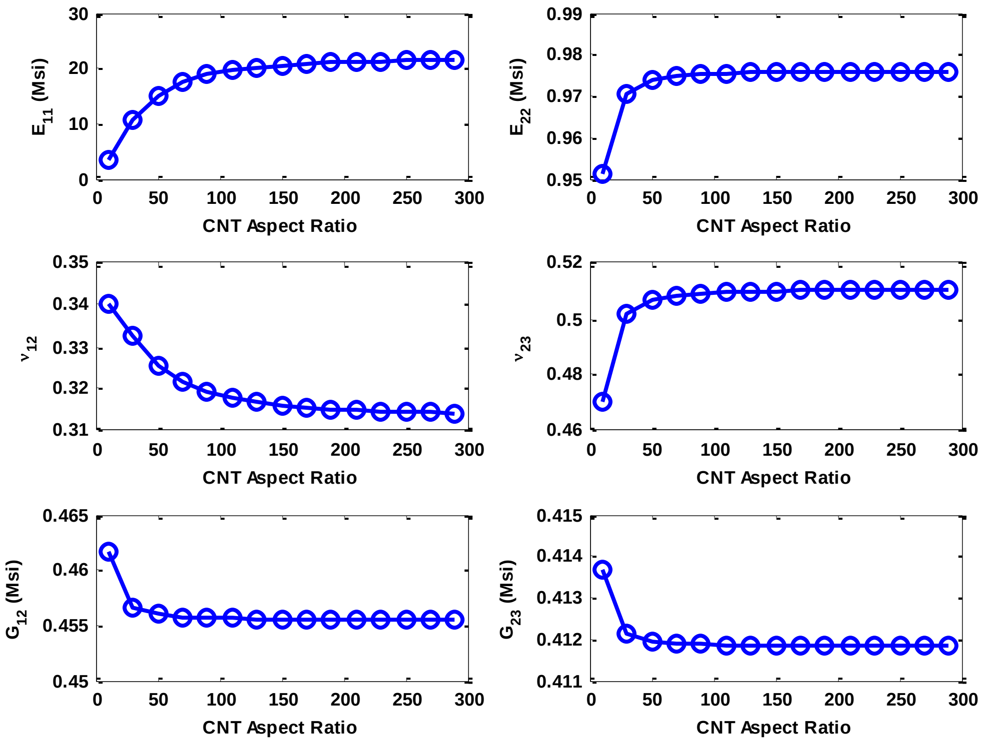

Figure 19. Effective mechanical properties of nanocomposite with three-walled CNT as a function of CNT aspect ratio

Figure 20 shows the mechanical properties variation as function of volume fraction but for N = 5. Moreover, Figure 21 shows the mechanical properties as function of aspect ratio also for N = 5. A similar conclusion with regard to N = 3 can be made, but the stiffness values are lower while the Poisson ratio behavior is similar.

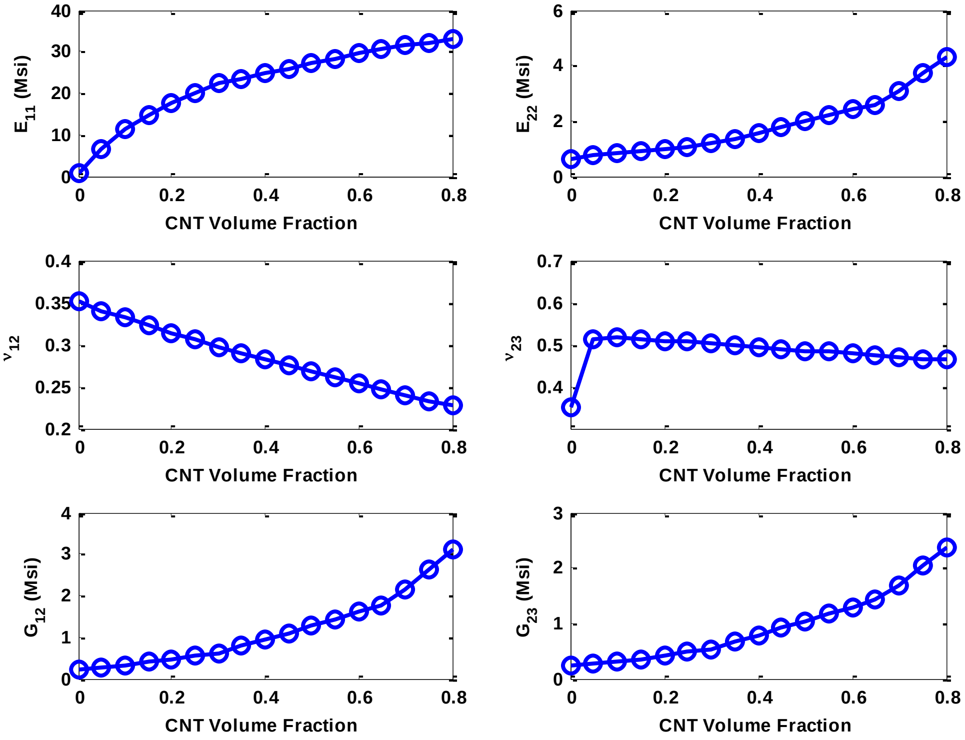

Figure 20. Effective mechanical properties of nanocomposite with five-walled CNT as a function of CNT volume fraction

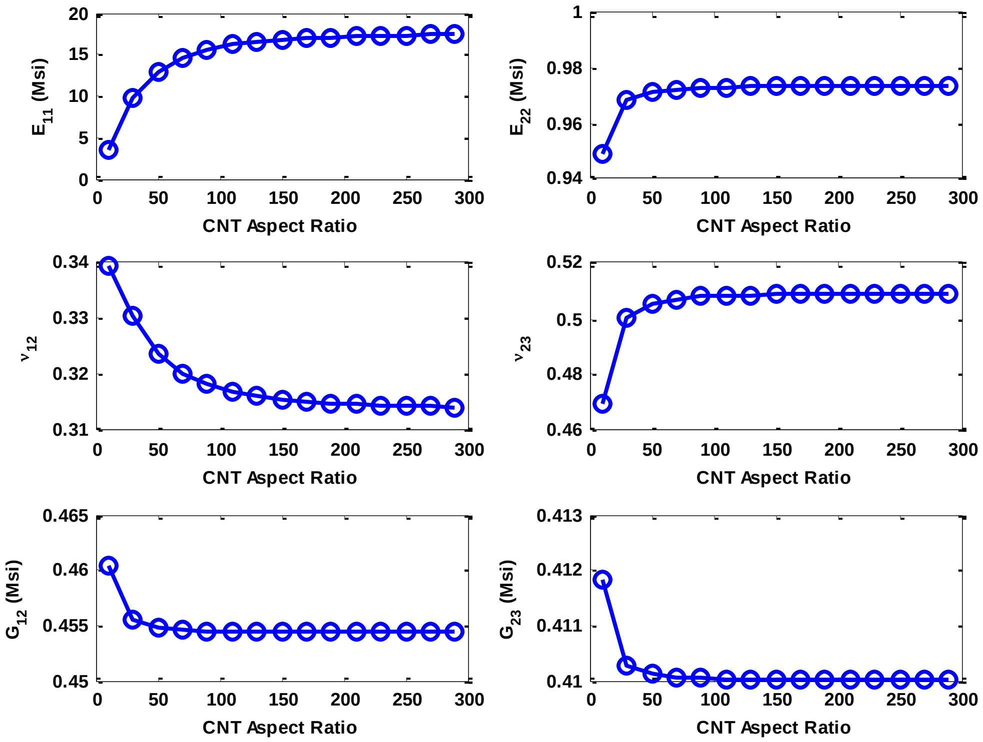

Figure 21. Effective mechanical properties of nanocomposite with five-walled CNT as a function of CNT aspect ratio

Figure 22 and Figure 23 show the results for a nanocomposite unidirectional lamina that have CNTs with three walls embedded in the matrix as function of volume fraction and aspect ratio, respectively. From Figure 22 it can be observed that as the CNT volume fraction increases the axial Young's modulus increases, while the lateral modulus is slightly reduced. Poisson's ratio, ν_{12}, decreases as the volume fraction increases, and a subtle change is observed in ν_{23}. The shear moduli undergo minimal changes. In Figure 23, the variation of the nanocomposite unidirectional lamina mechanical properties as a function of CNT aspect ratio is shown. The results demonstrate that all of the mechanical properties are affected by the change in aspect ratio. The axial elastic modulus increases substantially as the aspect ratio increases up until 100. The lateral modulus, however, exhibits a smaller increase with aspect ratio. The effect of aspect ratio on the shear moduli and does not affect either Poisson's ratio, ν_{12} and ν_{23}.

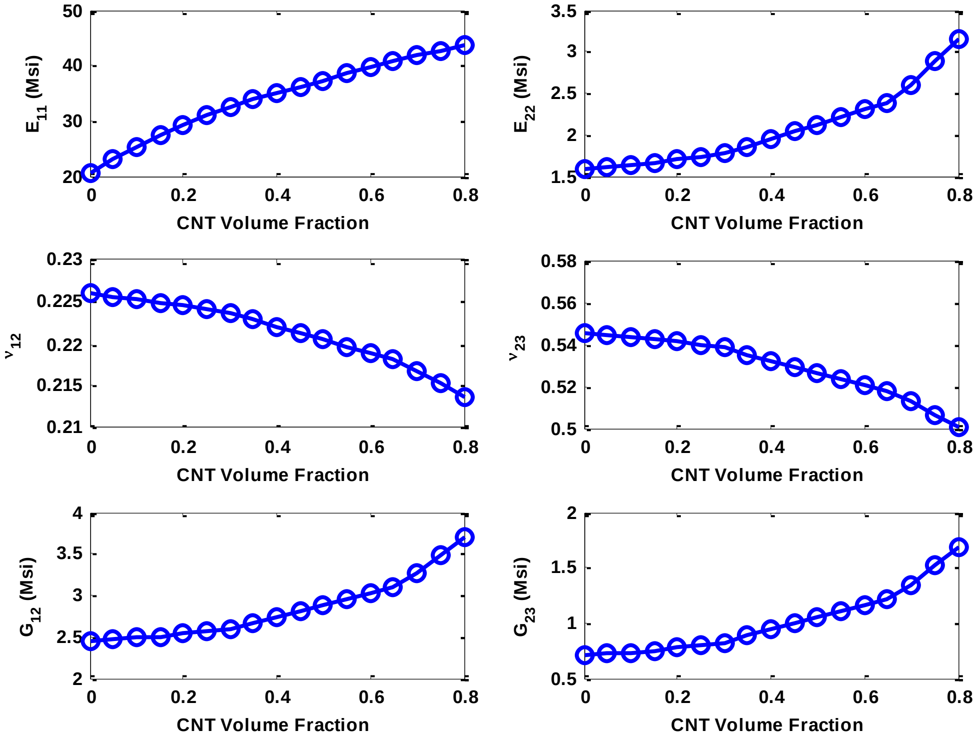

Figure 22. Effective mechanical properties of unidirectional lamina with three-walled CNT as a function of CNT volume fraction

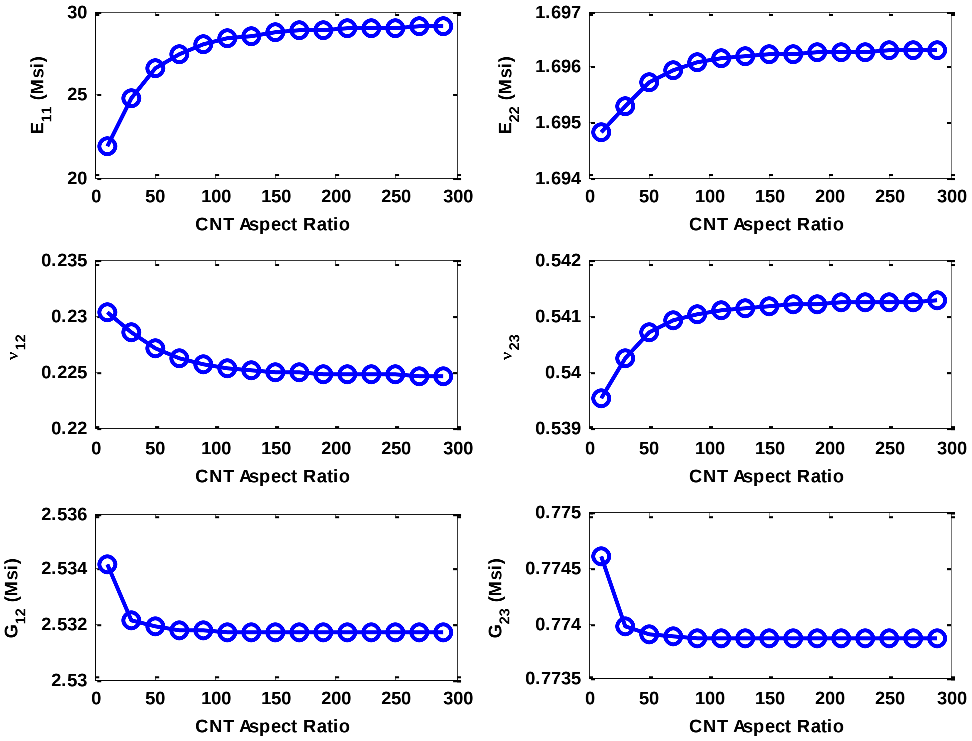

Figure 23. Effective mechanical properties of unidirectional lamina with three-walled CNT as a function of CNT aspect ratio

Figure 24 shows the mechanical properties variation as function of volume fraction for N = 5. Moreover, Figure 25 depicts the mechanical properties as a function of aspect ratio, as well as for N = 5. A similar conclusion can be reached as in the case of N = 3, but the stiffness values are lower while the behavior of Poisson's ratio are similar as was observed for the pure nanocomposite matrix.

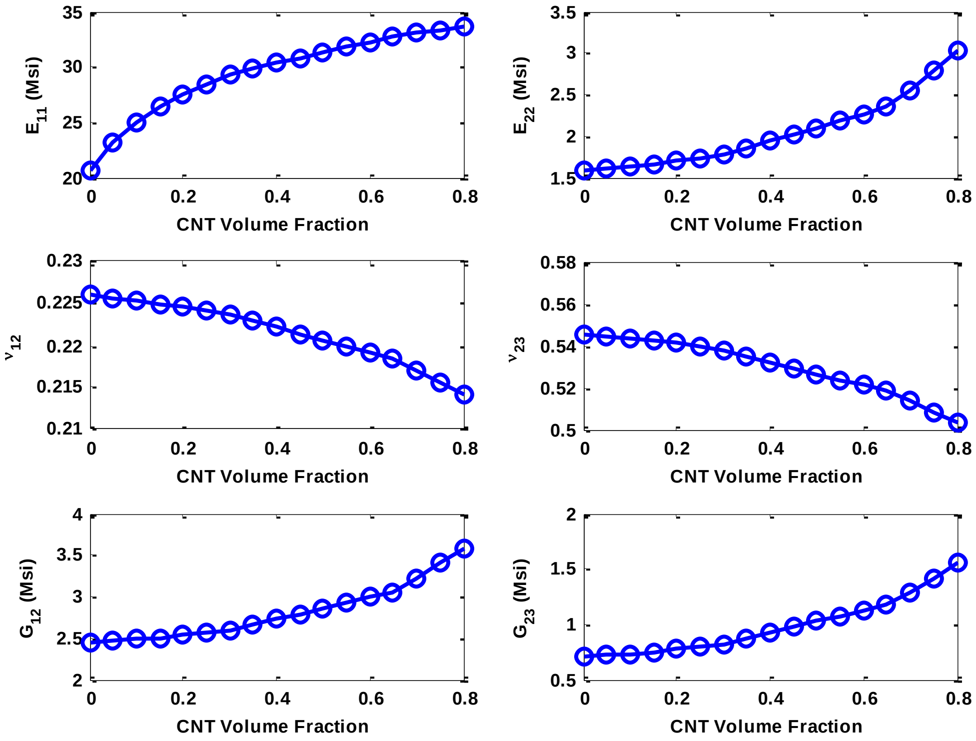

Figure 24. Effective mechanical properties of unidirectional lamina with five-walled CNT as a function of CNT volume fraction

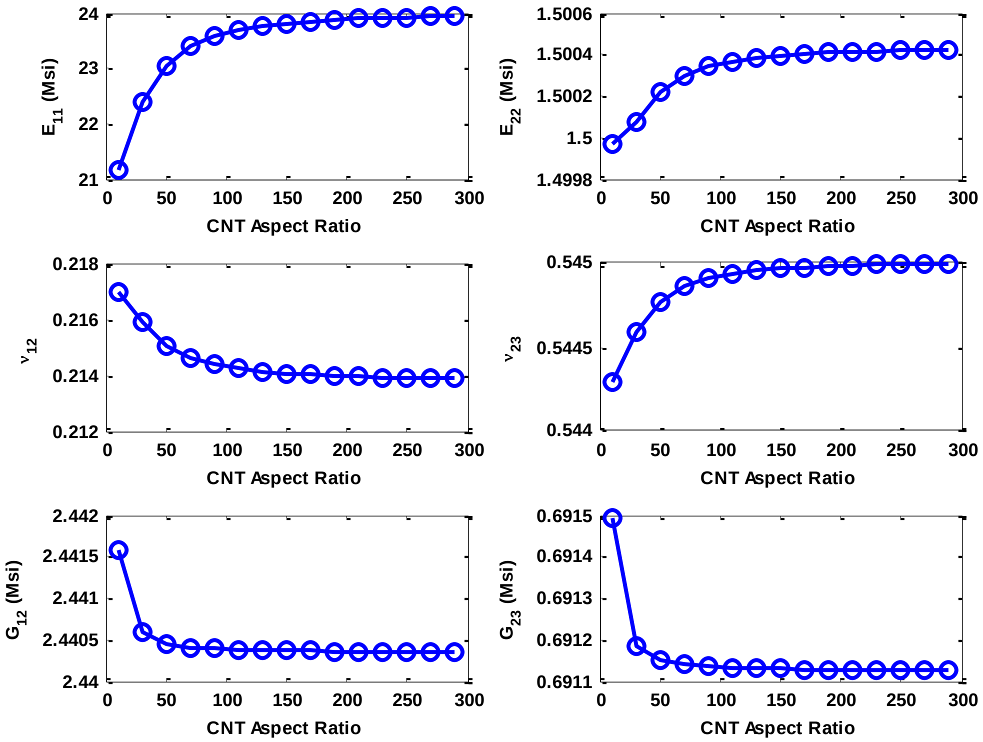

Figure 25. Effective mechanical properties of unidirectional lamina with five-walled CNT as a function of CNT aspect ratio

2.6. The Influence of Matrix/CNT Bonding on the Effective Mechanical Properties

This section investigates the effect of having a non-perfect interface between the CNT and the epoxy matrix on the effective mechanical properties. This is done using detailed FEMs. Micromechanical models for the nanocomposite are generated using the commercial FE software Abaqus. Several different CNT volume fractions are considered in this study (5%, 15%, 30%, and 40%). Figure 26 and Figure 27 show a schematic representation of unit-cell models of the CNT/epoxy (nanocomposite) for the perfect interface and non-perfect interface, respectively.

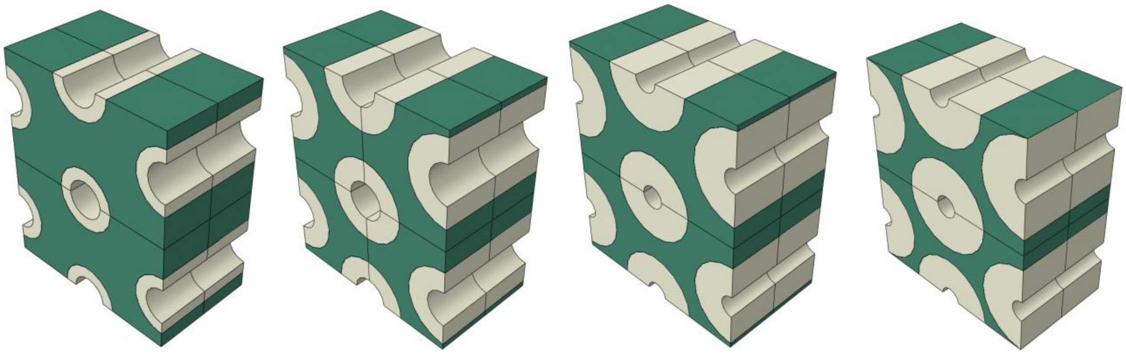

Figure 26. Micromechanical models for a perfect interface between CNT and epoxy

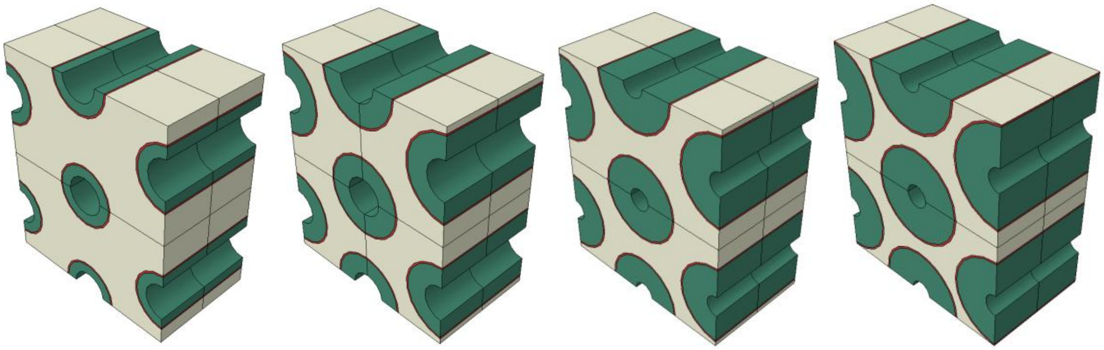

Figure 27. Micromechanical models for a non-perfect interface between CNT and epoxy

The models use approximately 20,000 3D eight-node continuum solid elements (C3D8R). The FE unit-cell models are presented in Figure 28.

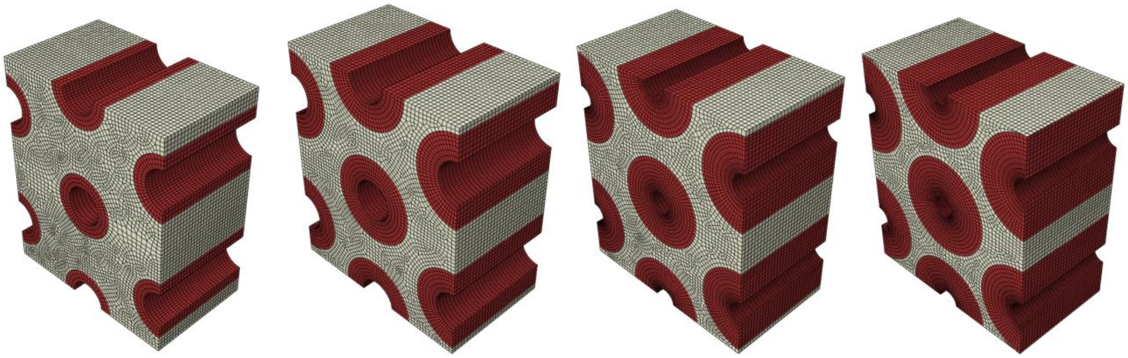

Figure 28. FEM of the nanocomposite

To determine the effective properties of the nanocomposite, specific prescribed boundary conditions are used. Figure 29 illustrates a cubic element with surface boundaries 1–6. Surfaces 1, 2, and 3 denote surfaces with a normal outward unit in the positive x_1, x_2, and x_3 directions, respectively. Surfaces 4, 5, and 6 indicate surfaces with a normal outward unit in the negative x_1, x_2, and x_3 directions, respectively.

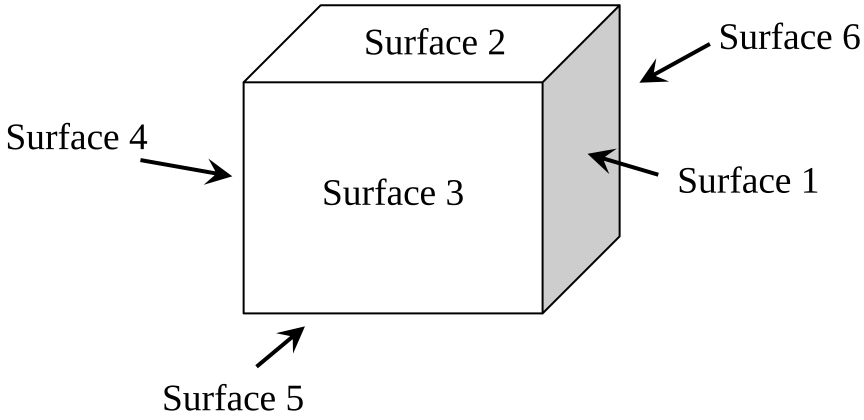

Figure 29:.Surface identification of the RVE

Different boundary conditions are prescribed to determine the effective mechanical properties, which are summarized in Table 6. Variable $u_1 = 0$ represents the displacement component in x_1 direction, and $\sigma_{11} = \sigma_o$ represents the stress applied to a surface whose outward normal is in the x_1 direction with a traction component in $-x_1$ direction. To characterize the moduli E_{11} and E_{33}, constant stresses $\sigma_{11} = \sigma_o$ and $\sigma_{33} = \sigma_o$ are applied, respectively. The strain responses ε_{11} and ε_{33} are extracted, and the elastic moduli are determined by

$$E_{11} = \frac{\sigma_{11}}{\varepsilon_{11}} \tag{52}$$

$$E_{33} = \frac{\sigma_{33}}{\varepsilon_{33}} \tag{53}$$

$$E_{22} = E_{33} \tag{54}$$

$$v_{12} = -\frac{\varepsilon_{22}}{\varepsilon_{11}} \tag{55}$$

$$v_{13} = -\frac{\varepsilon_{33}}{\varepsilon_{11}} \tag{56}$$

$$v_{23} = -\frac{\varepsilon_{33}}{\varepsilon_{22}} \tag{57}$$

For characterizing the shear moduli G_{12} and G_{13}, constant stresses $\sigma_{12} = \sigma_o$ and $\sigma_{13} = \sigma_o$ are applied, respectively. The shear strains γ_{11} and γ_{33} are computed and are used to determine the shear moduli as

$$G_{12} = \frac{\sigma_{12}}{\gamma_{12}} \tag{58}$$

$$G_{13} = G_{12} \tag{59}$$

$$G_{23} = \frac{\sigma_{13}}{\gamma_{13}} \tag{60}$$

Table 6. Boundary conditions applied on the FE of the nanocomposite to obtain the effective mechanical properties

Property / Surface	1	2	3	4	5	6
E11	$\sigma_{11}=\sigma_o$	--	--	$u_1=0$	$u_2=0$	$u_3=0$
E22 / E33	--	--	$\sigma_{33}=\sigma_o$	$u_1=0$	$u_2=0$	$u_3=0$
G12 / G13	$\sigma_{12}=\sigma_o$ $u_2=0$ $u_3=0$	$u_2=0$ $u_3=0$	$u_2=0$ $u_3=0$	$u_2=0$ $u_3=0$	$u_1=0$ $u_2=0$ $u_3=0$	$u_2=0$ $u_3=0$
G23	$u_2=0$ $u_3=0$	$u_2=0$ $u_3=0$	$\sigma_{13}=\sigma_o$ $u_2=0$ $u_3=0$	$u_2=0$ $u_3=0$	$u_2=0$ $u_3=0$	$u_1=0$ $u_2=0$ $u_3=0$

The effect of having a non-perfect interface on the effective mechanical properties between the CNT and the epoxy is shown in Figure 30–Figure 32 for the longitudinal elastic modulus, transverse elastic modulus, and Poisson's ratio, respectively. It can be noted that while the stiffness at the interface is lower, the values for the effective modulus decrease, resulting in the highest value for a perfect interface scenario. Poisson's ratio shows a similar trend, but the value for the perfect interface is smaller with an increase in the CNT volume fraction. The magnitude of the change is not as significant for Poisson's ratio compared to the elastic modulus. These values will be used to quantify the interface effect on the initial failure load discussed in Chapter 5.

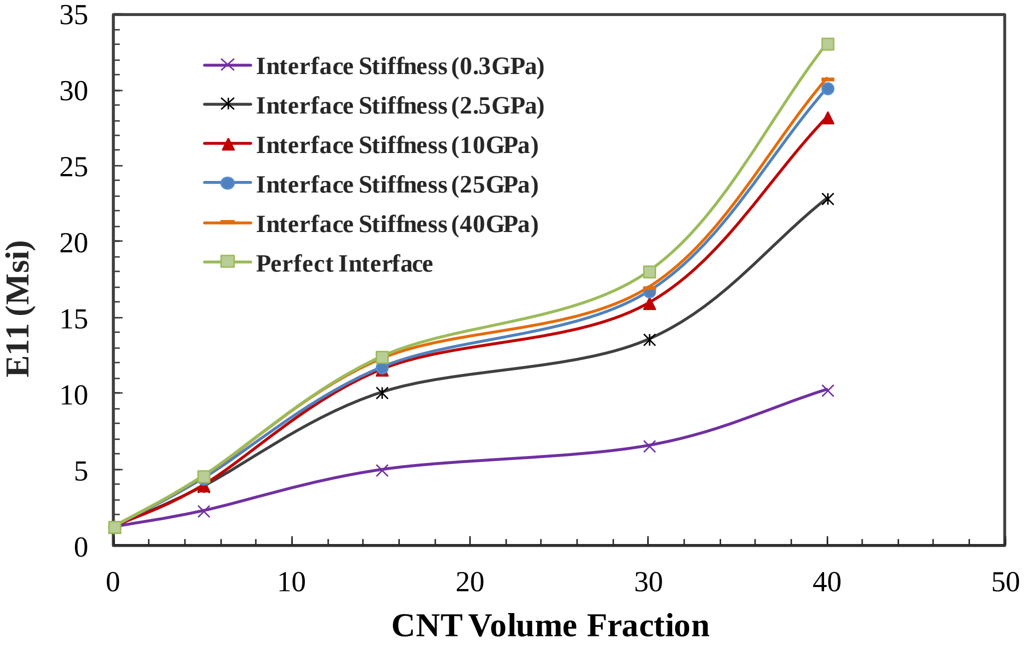

Figure 30. Effective longitudinal elastic moduli for different interface stiffnesses

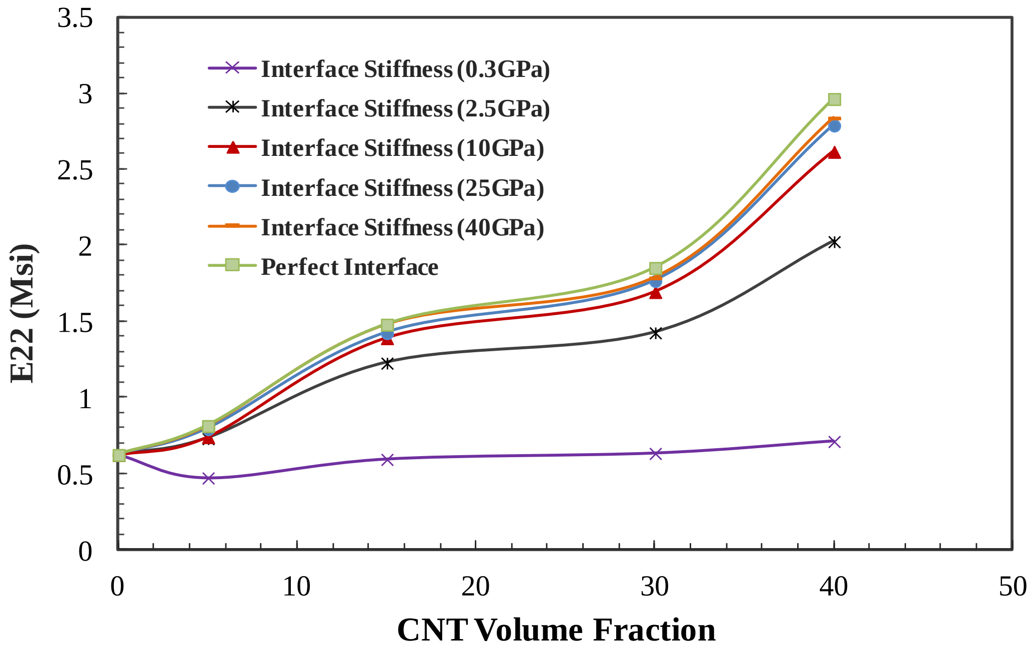

Figure 31. Effective transverse elastic moduli for different interface stiffnesses

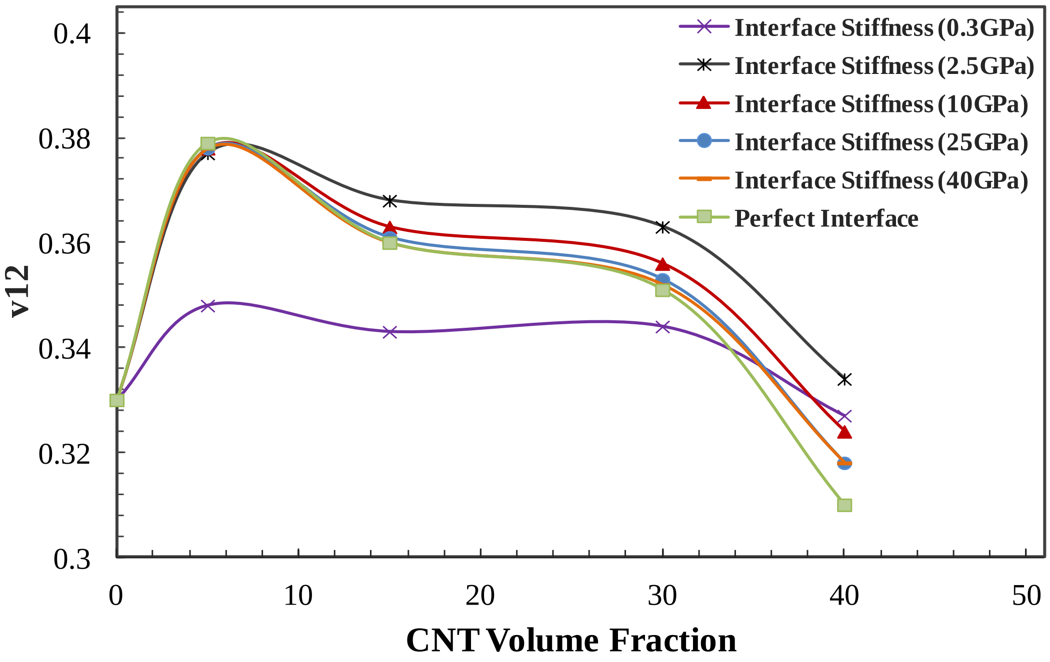

Figure 32. Effective Poisson’s ratios for different interface stiffnesses

2.7. Parameter Estimation

An alternative approach in determining the effective mechanical properties of the nanocomposites was also investigated in this study. It is based on an estimation framework that utilizes the Kalman filter algorithm. The Kalman filter employs a user-defined mathematical model of the phenomenon under study and measurements acquired by a practical experiment or an application to optimally estimate certain parameters (Courage, W. M. et al. 1990). These parameters can be measurable or non-measurable.

The motivation in presenting the following method to acquire the effective properties is to validate the results obtained from the micromechanics approach and to provide an alternative method to determine the effective properties. In this section, the procedure of how the Kalman filter can be combined with the micromechanic methods and FEA to estimate material properties is presented.

Consider a detailed FEM of a nanocomposite with hollow cylindrical CNTs, such as the one shown in Figure 33. When a certain load is applied to the model, the FE solution will output displacement values corresponding to the applied load. Such a model can be considered as an experimental procedure, and the displacement acquired from the FE solution can be considered as a measured value. This simulated measurement is synonymous to having a strain gauge attached to a specimen at different locations, which are represented by red dots in Figure 33. Now consider a homogenous solid FEM, as the one shown in Figure 34, with properties acquired by the analytical solution. This homogenous model is considered a mathematical representation of an actual nanocomposite, where at an applied load (equal to that applied to the detail FEM) a certain displacement is achieved. It is proposed that a displacement function be generated by varying the properties of the homogenous model and applying the same load every time to obtain a set of data points from which a mathematical function can be obtained. This displacement function acts as the mathematical model required for the Kalman filter.

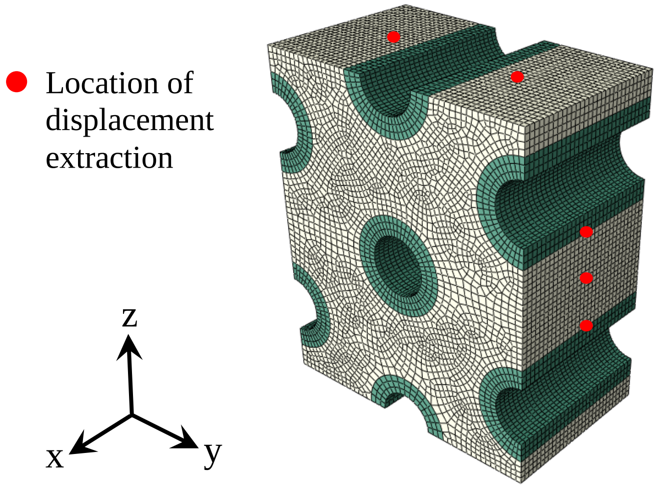

Figure 33. Detailed FEM of the nanocomposite RVE

The method is based on simulating an experiment using a detailed FEM of the specimen. The ability to estimate parameters of this simulated experiment is realized through a Kalman filter. This simulated experiment will generate a measured displacement of the specimen, which is stored and then passed to an extended Kalman filter. A second FEM, with the assumption of homogeneous material properties, is also created such that for a given set of homogenous material parameters the displacement can be calculated when the material is subject to the same boundary conditions and load as the detailed FEM (simulated experiment). The Kalman filter utilizes the measured displacement (experiment) and the calculated displacement (homogeneous model) to optimally estimate the material parameters. Below are the steps to execute the parameter estimation, which are shown in a block diagram in Figure 35.

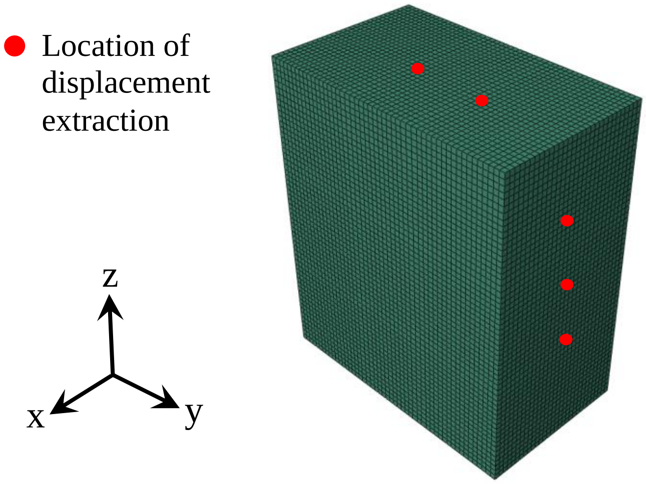

Figure 34. Homogenous FEM model of the nanocomposite RVE

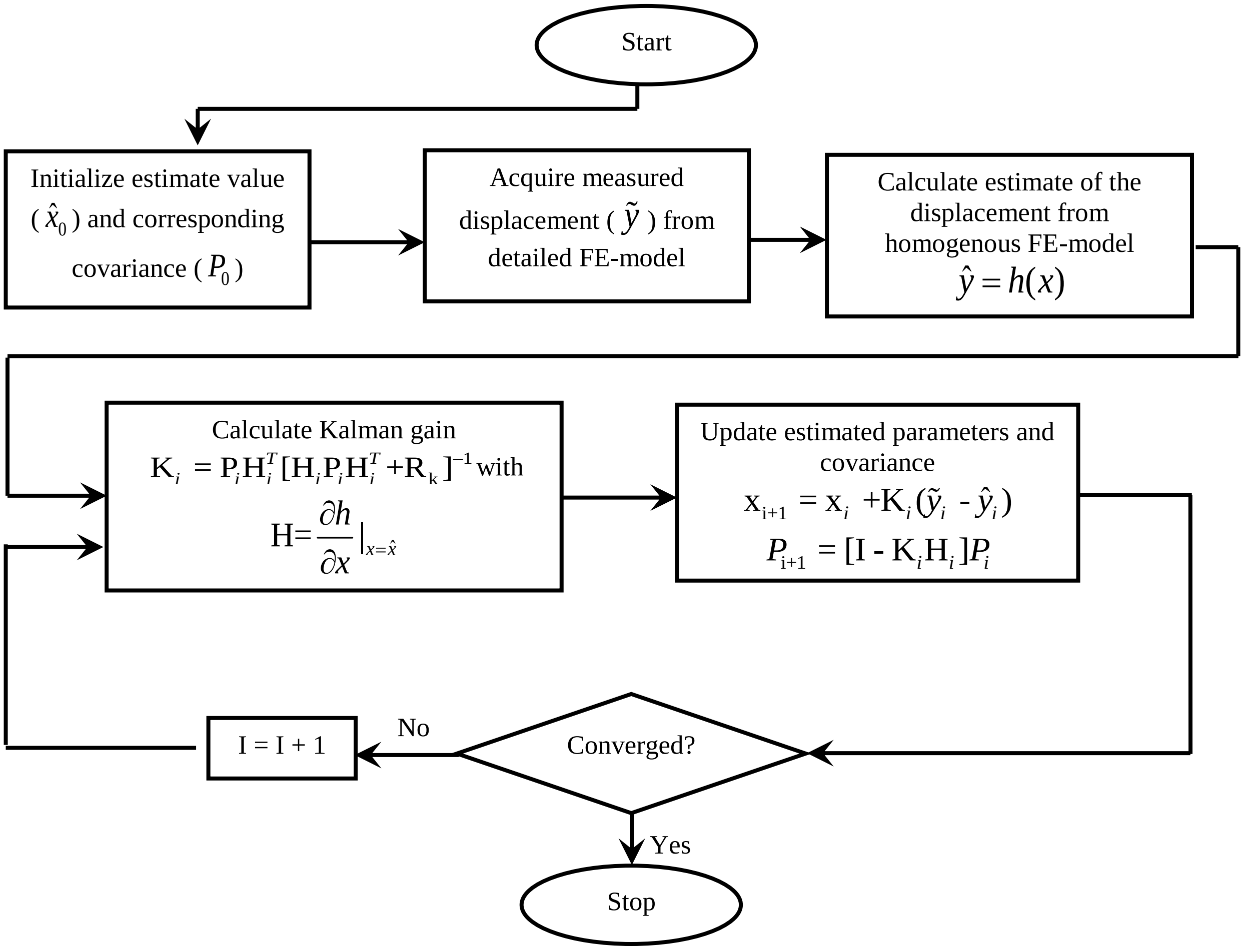

Figure 35. FEA-based Kalman filter algorithm block diagram for estimating effective nanocomposite material properties

A Kalman filter algorithm will utilize both the calculated displacement ($\hat{y}$) and measured displacement ($\tilde{y}$) to acquire an estimate of the material parameter ($\hat{x}$). The following steps show the general Kalman filter structure:

1. Initialize the estimate of the material parameter ($\hat{x}_0$)
2. Initialize the material parameter estimate covariance (P_0)
3. Acquire the measured displacement ($\tilde{y}$) from the detailed FEM model

4. Calculate an estimate of the displacement ($\hat{y}$) using the nonlinear function of material parameters ($\hat{y} = h(x)$) acquired from the homogeneous FEM and iterate the process until convergence using the Kalman filter equations summarized below

Calculate the Kalman gain

$$\mathrm{K}_i = \mathrm{P}_i \mathrm{H}_i^T [\mathrm{H}_i \mathrm{P}_i \mathrm{H}_i^T + \mathrm{R}_\mathrm{k}]^{-1}$$

where $\mathrm{H} = \frac{\partial h}{\partial x}|_{x=\hat{x}}$ and R is the measurement covariance.

Update the estimated parameter and covariance

$$\mathrm{x}_{\mathrm{i+1}} = \mathrm{x}_i + \mathrm{K}_i (\tilde{y}_i - \hat{y}_i)$$

$$P_{\mathrm{i+1}} = [\mathrm{I} - \mathrm{K}_i \mathrm{H}_i] P_i$$

where I is an identity matrix.

With the micromechanical information obtained so far, an actual displacement field in the composite RVE under a given load can provide estimates of the effective material parameters of that RVE. The Kalman filter allows for extensions to nonlinear material behavior based on such measurements (i.e., a general method for the system identification of the structures properties). It can be seen as a robust fitting procedure and it makes a direct estimation of the parameters without first optimizing a related quantity. Furthermore, in relation to the use of numerical solutions in determining the effective parameters, the use of the identification technique makes it possible to simultaneously estimate different parameters when a superposition of the different boundary conditions leads to a proper combined load case.

The results from applying this method are shown in Figure 36. While assuming the presence of a strain gauge at a certain point in Figure 34, displacements under a specified load are recorded for different CNT volume fractions. The results show that the properties estimated by the Kalman filter are in agreement with those calculated by the micromechanics approach described in previous sections. The only mechanical property with a large estimation error is ν_{23}, which might be attributed to the fact that not enough information was available in the measurement of displacement from one location. It might be necessary to obtain the displacement measurement from additional number of predefined points within the structure for a more accurate displacement prediction. Moreover, the initial estimate used in the prediction of that material parameter may have been the cause of the large error. The Kalman filter starts with initial values for the parameters and their covariances given by the user. Typically, good starting values can be taken, based on experience or physical background. Making the variance of the initial state estimate large makes sure that the estimate converges quickly and that the influence of the initial guess soon will be negligible. In order to overcome this issue, other mathematical and statistical approaches may be used to determine those initial values that might yield more accurate estimates as that published by Linderoth et al. (Linderoth, M. et al. 2011). Since this study is focused on composites with small values of CNT volume fraction (less than 0.1) and the correlation up to that point is accurate, no additional analysis has been conducted. The remaining of the mechanical properties are estimated in a manner that proves that the Kalman filter is a viable option for conducting system identification of nanocomposites by recording a minimal amount of displacement data.

Based on the approach and results presented in this section, the Kalman filter can easily be utilized as a first method of system identification for estimating material properties of a nanocomposite using minimal strain measurements. The results also highlight the validity of the micromechanics expressions derived earlier to calculate effective properties of nanocomposites because the estimates relied on set expressions and yielded acceptable results.

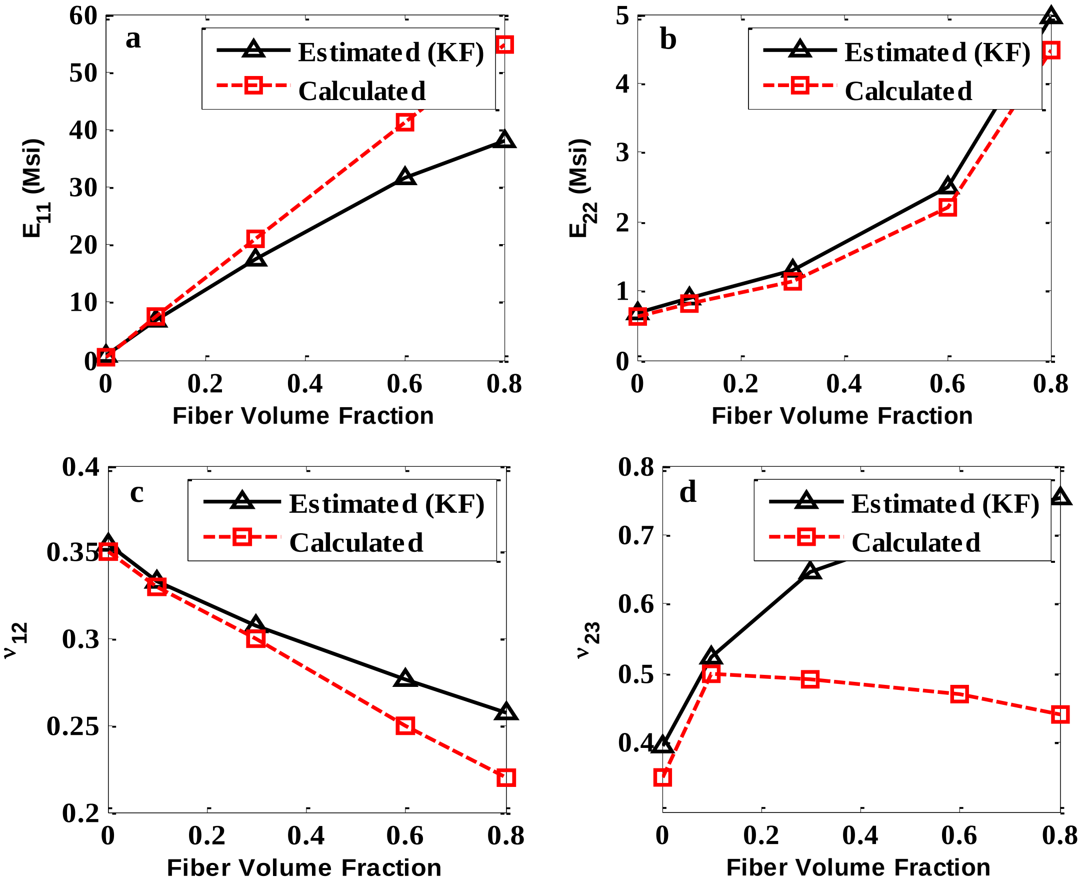

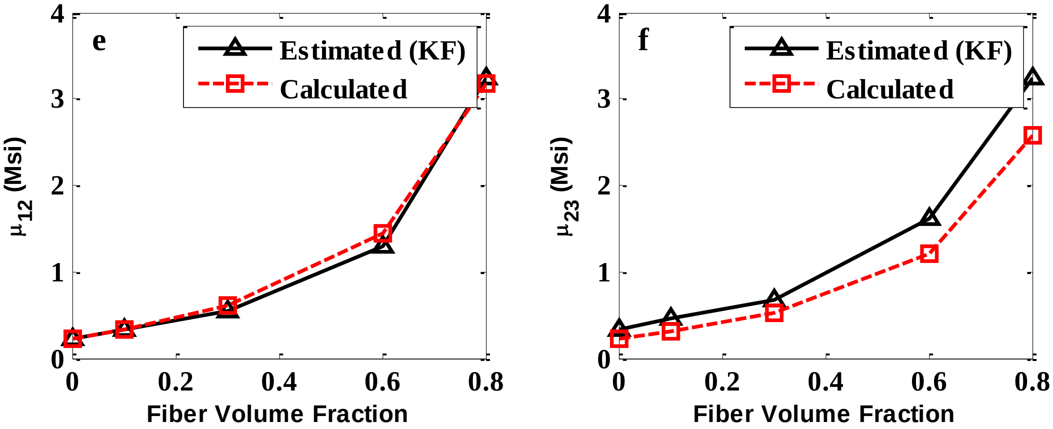

Figure 36. Effective properties of the nanocomposite as a function of CNT volume fraction – estimated and calculated

Chapter Summary

This chapter focused on the theoretical aspect of the multiscale approach used to obtain the effective mechanical properties of the nanocomposite. Numerical results were presented, and it was concluded that the use of CNTs at the different length scales improves nanocomposite mechanical properties.

Because the analytical approach assumes a perfect interface between the CNT and epoxy matrix, an investigation was initiated to determine the influence of a non-perfect interface. It was concluded that higher stiffness values at the interface provide us with higher values for the effective properties. In addition, an estimation approach based on the Kalman filter framework was discussed in an effort to provide an alternate method to compute the effective properties and validate the results from the analytical solution. The results obtained from this method showed good correlation with those from the micromechanics analysis and proved to be an effective alternative method to compute the effective mechanical properties.

CHAPTER 3

EFFECT OF VISCOELASTIC INTERFACE ON THE BEHAVIOUR OF NANOCOMPSOITES

This chapter focuses on the stress analysis of nanocomposites. The goal is to obtain the displacement and stress fields of a nanocomposite structure under uniaxial tension while accounting for the time-dependent behavior of the interface between the nanotube and the epoxy matrix. The effective properties of the CNTs are calculated using the composite cylinder micromechanics approach discussed in Chapter 2. A perturbation-type expansion is utilized to acquire the displacement and stress fields of the nanocomposite structure while the Kelvin–Voigt viscoelastic constitutive relation is adopted to model the time dependent effect. It is shown that time dependence can have an effect on the field distribution, which depends on the aspect ratio of the nanotube, number of CNT walls, and the CNT interface.

3.1. Displacement and Stress Fields of Nanocomposite Structures under Uniaxial Tension

A schematic illustration of several nanotubes randomly distributed inside an epoxy matrix creating a nanocomposite structure subject to tensile loading is shown in Figure 37-a. An RVE of consisting of two nanotubes (I and II) surrounded by the epoxy matrix is shown in Figure 37-b where L is the length of nanotube, t_1 is the thickness of nanotube, and t_2 is the thickness of epoxy matrix. The subscripts 1 and 2 stand for the nanotube and epoxy matrix respectively. A rectangular coordinate system (x, y, z) introduced in Figure 37 is such that the x-y plane coincides with the bottom surface of the

RVE, while the z axis is perpendicular to it. The problem can be regarded as a plane-stress problem since the width of the RVE is very thin and the load along the width stays invariant; that is, the nonzero stress components are σ_x, σ_z, and τ_{xz} only, which are independent of y. From the theory of elasticity the equilibrium equations for a 2D problem in the absence of body forces are given as

$$\frac{\partial \sigma_x}{\partial x} + \frac{\partial \tau_{xz}}{\partial z} = 0 \tag{61}$$

$$\frac{\partial \tau_{xz}}{\partial x} + \frac{\partial \sigma_z}{\partial z} = 0 \tag{62}$$

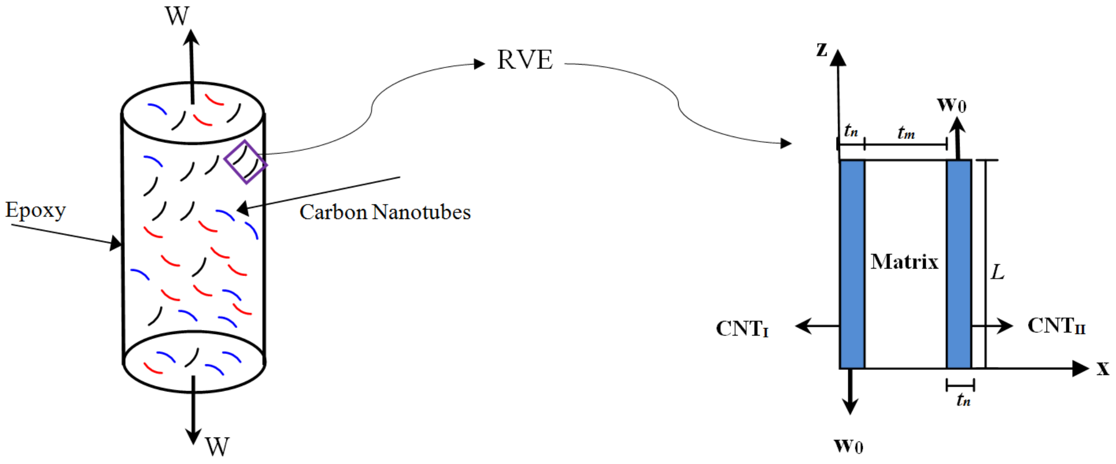

Figure 37. Schematic diagram of a nanocompsoite structure (a) Macroscale (b) Representative volume element

and Hooke’s law for the plane-stress problem is defined as

$$\varepsilon_{xx} = \frac{1}{E}(\sigma_{xx} - \upsilon\sigma_{zz}) \tag{63}$$

$$\varepsilon_{zz} = \frac{1}{E}(\sigma_{zz} - \upsilon\sigma_{xx}) \tag{64}$$

$$\varepsilon_{xz} = \frac{\tau_{xz}}{2G} \tag{65}$$

where *E, v, G* are Young's modulus, Poisson's ratio, and shear modulus respectively. The strain displacement relations are as follows;

$$\varepsilon_{xx} = \frac{\partial u}{\partial x} \tag{66}$$

$$\varepsilon_{zz} = \frac{\partial w}{\partial z} \tag{67}$$

$$\varepsilon_{xz} = \frac{1}{2}\left(\frac{\partial u}{\partial z} + \frac{\partial w}{\partial x}\right) \tag{68}$$

where *u* and *w* are the displacement in *x* and *z* directions respectively.

Following the work of He and Jiang (He, L. H. and Jiang, J. 2003) a perturbation based approach is used to solve the governing equations. In order to obtain the stress distribution in the nanocomposite, the following assumptions are made: i) the CNT is isotropic; ii) the elastic modulus of CNT is an order of magnitude higher than that of the matrix; iii) the load transfer relation between the CNT and matrix are equal in the transverse and shear directions but different in the longitudinal direction; i.e., ($\gamma_d \sigma_{zz}^n = \sigma_{zz}^m,\ \sigma_{xx}^n = \sigma_{xx}^m,\ \tau_{xz}^n = \tau_{xz}^m$) where $\gamma_d = \frac{L}{t_1}$ is the aspect ratio of the CNT. The expansions of the strain components can also be obtained in a similar manner by substitution in the constitutive relations. The perturbation expansion for the stress, strain, and displacement for the nanocomposite CNT can be expressed as follows

$$\sigma_{zz}^n = \sigma_{zz0}^n + \gamma_d \sigma_{zz1}^n \tag{69}$$

$$\sigma_{xx}^n = \gamma_d \sigma_{xx0}^n + \gamma_d{}^2 \sigma_{xx1}^n \tag{70}$$

$$\tau_{xz}^n = \sqrt{\gamma_d}\,\tau_{xz0}^n + \sqrt[3]{\gamma_d}\,\tau_{xz1}^n \tag{71}$$

$$\varepsilon_{zz}^n = \varepsilon_{zz0}^n + \gamma_d \varepsilon_{zz1}^n \tag{72}$$

$$\varepsilon_{xx}^{n} = \varepsilon_{xx0}^{n} + \gamma_d \ \varepsilon_{xx1}^{n} \tag{73}$$

$$\varepsilon_{xz}^{n} = \sqrt{\gamma_d}\,\varepsilon_{xz0}^{n} + \sqrt[3]{\gamma_d}\,\varepsilon_{xz1}^{n} \tag{74}$$

$$w^{n} = w^{n}{}_{0} + \gamma_d w^{n}{}_{1} \tag{75}$$

$$u^{n} = \sqrt{\gamma_d}\,u^{n}{}_{0} + \sqrt[3]{\gamma_d}\,u^{n}{}_{1} \tag{76}$$

and for the matrix as

$$\sigma_{zz}^{m} = \gamma_d \sigma_{zz0}^{m} + \gamma_d{}^{2} \sigma_{zz1}^{m} \tag{77}$$

$$\sigma_{xx}^{m} = \gamma_d \sigma_{xx0}^{m} + \gamma_d{}^{2} \sigma_{xx1}^{m} \tag{78}$$

$$\tau_{xz}^{m} = \sqrt{\gamma_d}\,\tau_{xz0}^{m} + \sqrt[3]{\gamma_d}\,\tau_{xz1}^{m} \tag{79}$$

$$\varepsilon_{zz}^{m} = \varepsilon_{zz0}^{m} + \gamma_d \varepsilon_{zz1}^{m} \tag{80}$$

$$\varepsilon_{xx}^{m} = \varepsilon_{xx0}^{m} + \gamma_d \ \varepsilon_{xx1}^{m} \tag{81}$$

$$\varepsilon_{xz}^{m} = \sqrt{\gamma_d}\,\varepsilon_{xz0}^{m} + \sqrt[3]{\gamma_d}\,\varepsilon_{xz1}^{m} \tag{82}$$

$$w^{m} = w^{m}{}_{0} + \gamma_d w^{m}{}_{1} \tag{83}$$

$$u^{m} = \sqrt{\gamma_d}\,u^{m}{}_{0} + \sqrt[3]{\gamma_d}\,u^{m}{}_{1} \tag{84}$$

Expansions of the constitutive and equilibrium equations for the CNT are obtained by substituting the expansions Eq. (69 – 76) into Eq. (63 – 68). Similarly, by substituting the expansions Eq. (77 – 84) into Eq. (63 – 68), the corresponding governing equations of the epoxy matrix are obtained.

3.2. Kelvin-Voiget Viscoelastic Interfacial Model

The boundary conditions associated with the nanocomposite are defined as symmetric boundary conditions on the free edges of the CNT ($x = 0$ and $x = 2t_1 + t_2$). The traction free boundary conditions are applied to the face CNT opposite to where the load is applied. The viscoelastic interface between the CNT and the matrix at $x = x_k$ can be mathematically expressed as follows

$$\sigma_z^{(k+1)} = \sigma_z^{(k)} \tag{85}$$

$$\tau_{xz}^{(k+1)} = \tau_{xz}^{(k)} \tag{86}$$

$$u^{(k+1)} = u^{(k)} \tag{87}$$

$$w^{(k+1)} = w^{(k)} + \Delta^{(k)} \tag{88}$$

where $\Delta^{(k)}$ is the relative sliding displacement at the k^{th} interface. The quantity $\Delta^{(k)}$ must satisfy the following differential equation

$$\tau_{xz}^{(k+1)} = \eta_0^{(k)}\Delta^{(k)} + \eta_1^{(k)}\dot{\Delta}^{(k)} \ at \ z = z_k \tag{89}$$

where $\dot{\Delta}^{(k)}$ is the sliding velocity, $\eta_0^{(k)}$ and $\eta_1^{(k)}$ are the elastic constant and viscous coefficient respectively of the elastic interface. The constitutive law in Eq. (84) is known as the Kelvin-Voigt viscoelastic relation (Fan, H., and Wang. G. 2003). It should be noted that if $\eta_0^{(k)}$ is zero, the results would correspond to the model in He and Jiang (He, L. H. and Jiang, J. 2003). On the other hand, if $\eta_1^{(k)}$ is zero, the result would correspond to a time-independent linear spring model with no viscous effects (Chen, W. et al. 2003), (Chen, J.Y. et al. 2009).

3.3. Analytical Solution

In this study, the main focus is on solving the first expansion terms in Eqs. (69) – (84) since the results of the initial solution are very close to those of the combination of the initial solution and the first order perturbation (Chen, W. et al. 2003). Therefore, the initial solution can appropriately describe the stress and displacement fields in the nanocomposite structure under tension or compression. By adopting the perturbation expansion described previously the governing equations for the first expansion term of the CNT are given as follows

$$\varepsilon^n_{zz0} = \frac{\sigma^n_{zz0}}{E_n} = \frac{\partial w^n{}_0}{\partial z} \qquad (90)$$

$$\varepsilon^n_{xx0} = -\frac{\upsilon_n \sigma^n_{zz0}}{E_n} = \frac{\partial u^n{}_0}{\partial x} \qquad (91)$$

$$\varepsilon^n_{xz0} = \frac{\sigma^n_{xz0}}{2G_n} \qquad (92)$$

and

$$\frac{\partial w^n{}_0}{\partial x} = 0 \qquad (93)$$

$$\frac{\partial \sigma_{zz}}{\partial z} + \frac{\partial \tau_{xz}}{\partial x} = 0 \qquad (94)$$

$$\frac{\partial \tau_{xz}}{\partial z} + \frac{\partial \sigma_{xx}}{\partial x} = 0 \qquad (95)$$

The initial analytical solution of the perturbation approximation can be obtained by solving Eq. (90 – 95), and yields the following

$$w^n{}_{0,i} = \Gamma_{0,i}(z) \qquad (96)$$

$$u^n{}_{0,i} = -\upsilon_n x \frac{\partial \Gamma_{0,i}(z)}{\partial z} + \mathrm{X}_{0,i}(z) \qquad (97)$$

$$\sigma^n_{zz0,i} = E_n \frac{\partial \Gamma_{0,i}(z)}{\partial z} \qquad (98)$$

$$\tau^n_{xz0,i} = -E_n x \frac{\partial^2 \Gamma_{0,i}(z)}{\partial z^2} + \Phi_{0,i}(z) \qquad (99)$$

$$\sigma^n_{xx0,i} = \frac{E_n}{2} x^2 \frac{\partial^3 \Gamma_{0,i}(z)}{\partial z^3} - x \frac{\partial \Phi_{0,i}(z)}{\partial z} + \psi_{0,i}(z) \qquad (100)$$

where the subscript i = I or II refers to the first or second nanotube, respectively.

Following a similar procedure, the solution to the matrix material can be obtained, which are expresses as

$$\varepsilon_{zz0}^{m} = R\left(\sigma_{zz0}^{m} - \upsilon_{m}\sigma_{xx0}^{m}\right) = \frac{\partial w^{m}{}_{0}}{\partial z} \tag{101}$$

$$\varepsilon_{xx0}^{m} = R\left(\sigma_{xx0}^{m} - \upsilon_{m}\sigma_{zz0}^{m}\right) = \frac{\partial u^{m}{}_{0}}{\partial x} \tag{102}$$

$$\varepsilon_{xz0}^{m} = \frac{S}{2}\tau^{m}_{xz0} = \frac{\partial w^{m}{}_{0}}{2\partial x} \tag{103}$$

$$\frac{\partial \tau_{xz0}^{m}}{\partial x} = 0 \tag{104}$$

$$\frac{\partial \tau_{xz0}^{m}}{\partial z} + \frac{\partial \sigma_{xx0}^{m}}{\partial x} = 0 \tag{105}$$

where *R*, *S* are constants that can be written as

$$R = \frac{1}{E_n C_E}, \qquad S = \frac{1}{G_n C_G}$$

with

$$C_E = \frac{E_m}{\gamma_d^2 E_n}, \qquad C_G = \frac{G_m}{\gamma_d^2 G_n}$$

The initial analytical solution of the perturbation approximation can be obtained by solving Eq. (101 – 105) for the matrix and are given as

$$w^{m}{}_{0,i} = Sx\beta_0\left(z\right) + T_0(z) \tag{106}$$

$$u^{m}{}_{0,i} = \frac{-(1+\upsilon_m)^2 R}{2}x^2\frac{\partial \beta_0\left(z\right)}{\partial z} - \upsilon_m x\frac{\partial T_0(z)}{\partial z} + Q_0\left(z\right) + R\left(1-\upsilon_m{}^2\right)xV_0(z) \tag{107}$$

$$\sigma_{zz0,i}^{m} = \left(2+\upsilon_m\right)x\frac{\partial \beta_0\left(z\right)}{\partial z} + \frac{1}{R}\frac{\partial T_0(z)}{\partial z} + \upsilon_m V_0(z) \tag{108}$$

$$\tau_{xz0,i}^{m} = \beta_0\left(z\right) \tag{109}$$

$$\sigma^m_{xx0,i} = -x\frac{\partial\beta_0(z)}{\partial z} + V_0(z) \tag{110}$$

The unknown functions $\Gamma_{0,i}(z)$, $\mathrm{X}_{0,i}(z)$, $\beta_0(z)$, $T_0(z)$, $Q_0(z)$, $V_0(z)$, and $\Phi_{0,i}(z)$, shown in Eq. (96 – 110) can be obtained by applying the continuity conditions at the CNT matrix interface $x = (t_1)$ for the first CNT and $x = (t_1 + t_2)$ at the second CNT.

$$w^n{}_0 = w^m{}_0 + \Delta^k$$

$$u^n{}_0 = u^m{}_0$$

$$\sigma^n_{xx0,i} = \sigma^m_{xx0,i}$$

$$\sigma^n_{xz0,i} = \sigma^m_{xz0,i}$$

Substitution of the value of x into Eq. (96), (97), (99), (100), (106), (107), (109), and (110), and the use of boundary and continuity conditions yield the following;

$$\Gamma_{0,I}(z) = S\frac{t_2}{2}\beta_0(z) + T_0(z) + \Delta^k \tag{111}$$

$$\begin{aligned} -\upsilon_n \frac{t_2}{2}\frac{\partial\Gamma_{0,I}(z)}{\partial z} + \mathrm{X}_{0,I}(z) = \frac{-(1+\upsilon_m)^2 R}{2}\frac{t_2}{2}^2\frac{\partial\beta_0(z)}{\partial z} - \upsilon_m\frac{t_2}{2}\frac{\partial T_0(z)}{\partial z} + Q_0(z)\ldots \\ +R\left(1-\upsilon_m{}^2\right)\frac{t_2}{2}V_0(z) \end{aligned} \tag{112}$$

$$-E_n\frac{t_2}{2}\frac{\partial^2\Gamma_{0,I}(z)}{\partial z^2} + \Phi_{0,I}(z) = \beta_0(z) \tag{113}$$

$$\frac{E_n}{2}\frac{t_2}{2}^2\frac{\partial^3\Gamma_{0,I}(z)}{\partial z^3} - \frac{t_2}{2}\frac{\partial\Phi_{0,I}(z)}{\partial z} + \psi_{0,I}(z) = -\frac{t_2}{2}\frac{\partial\beta_0(z)}{\partial z} + V_0(z) \tag{114}$$

and

$$\Gamma_{0,II}(z) = -S\frac{t_2}{2}\beta_0(z) + T_0(z) + \Delta^k \tag{115}$$

$$\upsilon_n \frac{t_2}{2}\frac{\partial \Gamma_{0,II}(z)}{\partial z} + \mathrm{X}_{0,II}(z) = -\frac{(1+\upsilon_m)^2 R}{2}{\frac{t_2}{2}}^2 \frac{\partial \beta_0(z)}{\partial z} + \upsilon_m \frac{t_2}{2}\frac{\partial T_0(z)}{\partial z} + Q_0(z)\ldots$$
$$-R\left(1-\upsilon_m{}^2\right)\frac{t_2}{2}V_0(z) \tag{116}$$

$$E_n \frac{t_2}{2}\frac{\partial^2 \Gamma_{0,II}(z)}{\partial z^2} + \Phi_{0,II}(z) = \beta_0(z) \tag{117}$$

$$\frac{E_n}{2}{\frac{t_2}{2}}^2 \frac{\partial^3 \Gamma_{0,II}(z)}{\partial z^3} + \frac{t_2}{2}\frac{\partial \Phi_{0,II}(z)}{\partial z} + \psi_{0,II}(z) = \frac{t_2}{2}\frac{\partial \beta_0(z)}{\partial z} + V_0(z) \tag{118}$$

The symmetric boundary conditions at the top surface of the CNT ($z = L$) are given as $u^n{}_0 = C_0$ and $\sigma^n_{xz0,i} = 0$, substitution of these values in Eq. (96) and Eq. (99) respectively along with the values of x gives

$$-\upsilon_n\left(\frac{t_2}{2}+t_1\right)\frac{\partial \Gamma_{0,I}(z)}{\partial z} + \mathrm{X}_{0,I}(z) = C_0 \tag{119}$$

$$-E_n\left(\frac{t_2}{2}+t_1\right)\frac{\partial^2 \Gamma_{0,I}(z)}{\partial z^2} + \Phi_{0,I}(z) = 0 \tag{120}$$

The symmetric boundary condition at the bottom surface of the CNT ($x = 0$) are given as $u^n{}_0 = -C_0$ and $\sigma^n_{xz0,i} = 0$. Substituting these values in Eq. (96) and Eq. (99) respectively along with the values of x gives

$$\upsilon_n\left(\frac{t_2}{2}+t_1\right)\frac{\partial \Gamma_{0,II}(z)}{\partial z} + \mathrm{X}_{0,II}(z) = C_0 \tag{121}$$

$$E_n\left(\frac{t_2}{2}+t_1\right)\frac{\partial^2 \Gamma_{0,II}(z)}{\partial z^2} + \Phi_{0,II}(z) = 0 \tag{122}$$

Combining Eq. (117) and Eq. (118) to obtain the following expression

$$-E_n \frac{t_2}{2}\frac{\partial^2 \Gamma_{0,I}(z)}{\partial z^2} + \Phi_{0,I}(z) - E_n \frac{t_2}{2}\frac{\partial^2 \Gamma_{0,II}(z)}{\partial z^2} - \Phi_{0,II}(z) = 0 \tag{123}$$

and by subtracting Eq. (122) from Eq. (120) we have

$$E_n\left(\frac{t_2}{2}+t_1\right)\frac{\partial^2\Gamma_{0,I}(z)}{\partial z^2}-E_n\left(\frac{t_2}{2}+t_1\right)\frac{\partial^2\Gamma_{0,II}(z)}{\partial z^2}+\Phi_{0,I}(z)-\Phi_{0,II}(z)=0 \tag{124}$$

Comparing Eq. (123) with Eq. (124)

$$\frac{\partial^2\Gamma_{0,I}(z)}{\partial z^2}=-\frac{\partial^2\Gamma_{0,II}(z)}{\partial z^2} \tag{125}$$

Note that the difference in Eq. (125) is the subscript which refers to the CNT that is considered. Substituting Eq. (125) into Eq. (120) and Eq. (122) provides the following result;

$$\Phi_{0,I}(z)=\Phi_{0,II}(z)=E_n\left(\frac{t_2}{2}+t_1\right)\frac{\partial^2\Gamma_{0,II}(z)}{\partial z^2} \tag{126}$$

Substituting Eq. (126) into Eq. (113), the value of β can be obtained as

$$\beta_0(z)=E_n t_1\frac{\partial^2\Gamma_{0,I}(z)}{\partial z^2} \tag{127}$$

The following expression is obtained by summing Eq. (111) and Eq. (115)

$$\Gamma_{0,I}(z)+\Gamma_{0,II}(z)=2\left(T_0(z)+\Delta^k\right) \tag{128}$$

Taking the second derivative of Eq. (128) with respect to *z* and substituting into Eq. (125) the following differential equation is obtained

$$T_0^{"}(z)=0 \tag{129}$$

which can be solved as follows

$$T_0(z)=C_{1,0}+C_{2,0}z$$
(130)

Substituting Eq. (127) and Eq. (130) into Eq. (111)

$$\frac{1}{\zeta^2}\frac{\partial^2\Gamma_{0,I}(z)}{\partial z^2}-\Gamma_{0,I}(z)=-C_{1,0}-C_{2,0}z-\Delta^k \tag{131}$$

where

$$\zeta = \sqrt{2E_m / \left(E_n t_1 t_2 \left(1+\upsilon_p\right)\right)}$$

Assuming $\Delta^k = \overline{\Delta}^k \cosh\left(\zeta z\right)$, the solution of Eq. (131) is given as

$$\Gamma_{0,I}\left(z\right) = \frac{\left(2\overline{\Delta}^k \cosh\left(\zeta z\right)\zeta^2 + 2\zeta^2\left(C_{1,0} + C_{2,0} z\right)\right)}{2\zeta^2} + C_{3,0}e^{\zeta z} + C_{4,0}e^{-\zeta z} \tag{132}$$

Substituting Eq. (132) into Eq. (126) and Eq. (127) respectively provides the following expression

$$\Phi_{0,I}\left(z\right) = \Phi_{0,II}\left(z\right) = E_n\left(\frac{t_2}{2} + t_1\right)\left(\zeta^2 e^{(-\zeta\ z)}C_{4,0} + \zeta^2 e^{(\zeta\ z)}C_{3,0} + \zeta^2\,\overline{\Delta}^{(k)} \cosh(\zeta z)\right) \tag{133}$$

By substituting Eq. (126) into Eq. (113) yields

$$\beta_0\left(z\right) = E_n t_1\left(\zeta^2 e^{(-\zeta\ z)}C_{4,0} + \zeta^2 e^{(\zeta\ z)}C_{3,0} + \zeta^2\,\overline{\Delta}^{(k)} \cosh(\zeta z)\right) \tag{134}$$

And substituting Eq. (130) and Eq. (134) into Eq. (115) gives

$$\Gamma_{0,II}\left(z\right) = -S\frac{t_2}{2}E_n t_1\left(\zeta^2 e^{(-\zeta\ z)}C_{4,0} + \zeta^2 e^{(\zeta\ z)}C_{3,0} + \zeta^2\,\overline{\Delta}^{(k)} \cosh(\zeta z)\right) + C_{1,0} + C_{2,0}z + \Delta^k \tag{135}$$

The values for the other unknown function is obtained in a similar maner. Substituting Eq. (132) into Eq. (119) gives

$$\mathrm{X}_{0,I}\left(z\right) = \upsilon_n\left(\frac{t_2}{2} + t_1\right)\left(\frac{\left(2\overline{\Delta}^k\zeta^3 \cosh\left(\zeta z\right) + 2\zeta^2 C_{2,0}\right)}{2\zeta^2} + \zeta C_{3,0}e^{\zeta z} - \zeta C_{4,0}e^{-\zeta z}\right) + C_0 \tag{136}$$

Substituting Eq. (135) into Eq. (121) yields

$$\mathrm{X}_{0,II}\left(z\right) = C_0 + \upsilon_n\left(\frac{t_2}{2} + t_1\right)\left(S\frac{t_2}{2}E_n t_1\left(-\zeta^3 e^{(-\zeta\ z)}C_{4,0} + \zeta^3 e^{(\zeta\ z)}C_{3,0} + \zeta^3\,\overline{\Delta}^{(k)} \sinh(\zeta z)\right) + C_{2,0}\right)$$

(137)

Subtracting Eq. (112) from Eq. (116) gives

$$V_0(z) = \frac{2}{R\left(1-\upsilon_m^{\ 2}\right)}\left[\upsilon_m C_{2,0} - \upsilon_n\frac{1}{2}\left(\frac{\partial\Gamma_{0,I}\left(z\right)}{\partial z} + \frac{\partial\Gamma_{0,II}\left(z\right)}{\partial z}\right)\right] \tag{138}$$

Adding Eq. (112) from Eq. (116) gives the following expression

$$Q_0\left(z\right)=\frac{Rt_2^2(1+\upsilon_m)^2}{2}\frac{\partial\beta_0\left(z\right)}{\partial z} \tag{139}$$

By substituting Eq. (127), Eq. (132), Eq. (133) and Eq. (138) into Eq. (118) and substituting Eq. (127), Eq. (132), Eq. (134), and Eq. (139) into Eq. (118) a solution for the unknown functions $\psi_{0,I}\left(z\right)$ and $\psi_{0,II}\left(z\right)$ can be obtained. After acquiring the values of all the required functions shown above, the stress and displacement fields can be calculated using Eq. (96 – 100) for the CNT and Eq. (106 – 110) for the matrix. The value of $\Delta^{(k)}$ can be computed by substituting the stress value into Eq. (89) and solving the differential equation for $\overline{\Delta}^{(k)}$ with a zero initial condition.

3.4. Numerical Results

FE analysis is conducted on a model of a nanocomposite similar to that shown in Figure 37. The stress and displacement field distribution along the interface are obtained via an FEM constructed using the commercial software Abaqus.

By setting $\eta_0=\eta_1=0$, E_n = 100 GPa, E_m = 0.1 GPa, $\upsilon_n=0.25$ and $\upsilon_m=0.35$ we obtain the results shown in Figure 38–Figure 40. The figures show a comparison between the results in Chen et al. (Chen, W. et al. 2003) and the FEA solution for the displacement, axial stress, and shear stress fields respectively. The results show good agreement between both, which provides confidence in the methodology that is further used to investigate the time dependence and effects of other variables on the overall behavior of the nanocomposite.

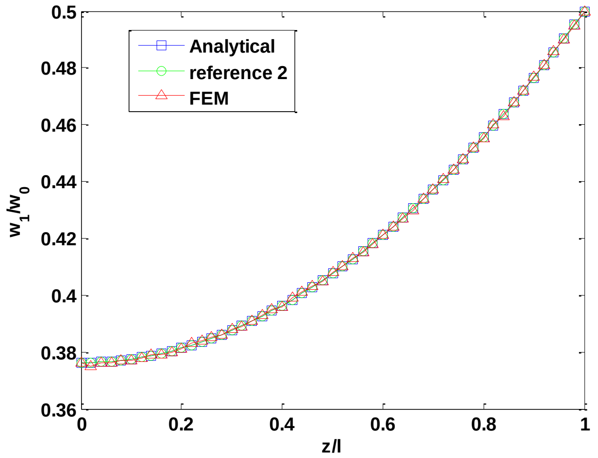

Figure 38. Displacement variation along CNT, matrix interface

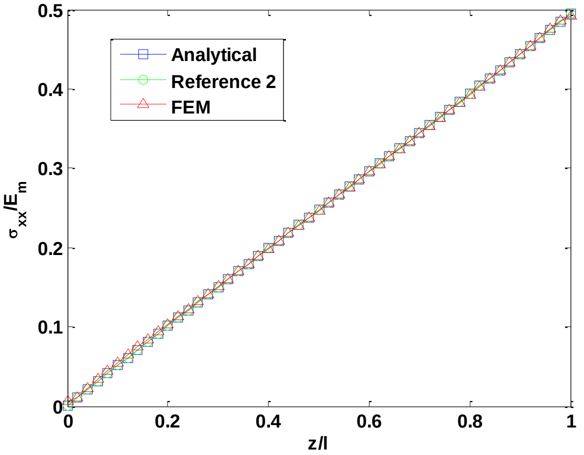

Figure 39. Axial stress variation along CNT, matrix interface

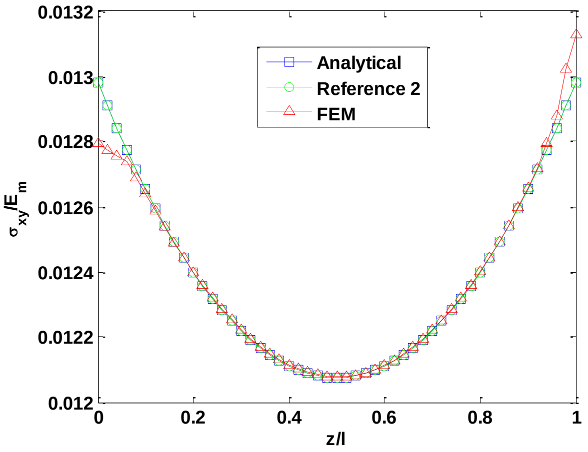

Figure 40. Shear stress variation along CNT, matrix interface

The properties of the CNT are obtained from the composite cylinder approach discussed in Chapter 2 for different aspect ratio values and the epoxy matrix properties are given as E = 4.3 GPa, v = 0.35. The solution for aspect ratio (γ_d = 20) can be seen in Figure 41–Figure 43. Similar results for different aspect ratios (γ_d = 30, 40, 50) are presented in Figure 44–Figure 52.

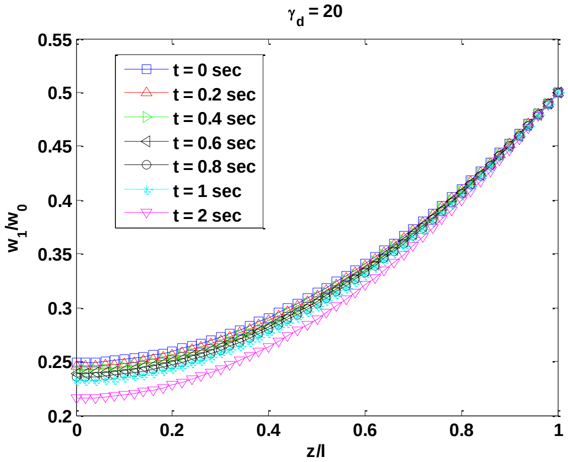

Figure 41. Displacement variation along CNT, matrix interface for 2 sec, aspect ratio 20

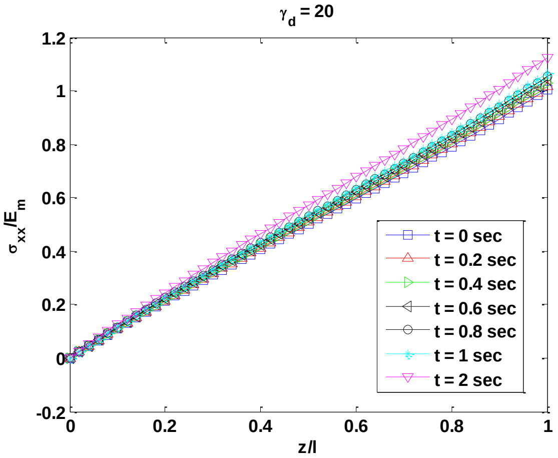

Figure 42. Axial stress variation along CNT, matrix interface for 2 sec, aspect ratio 20

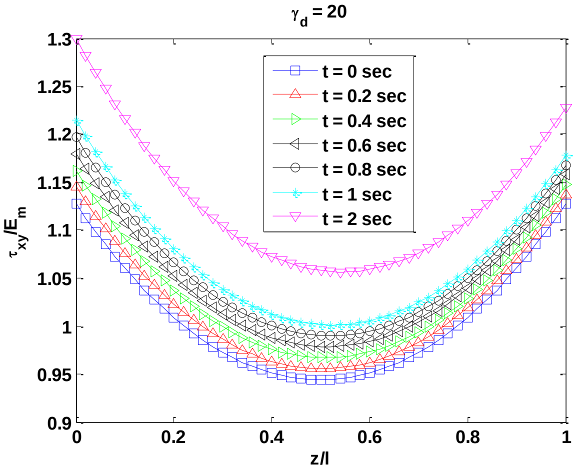

Figure 43. Shear stress variation along CNT, matrix interface for 2 sec, aspect ratio 20

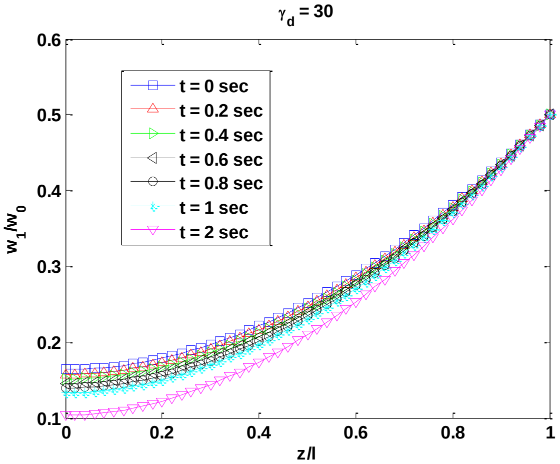

Figure 44. Displacement variation along CNT, matrix interface for 2 sec, aspect ratio 30

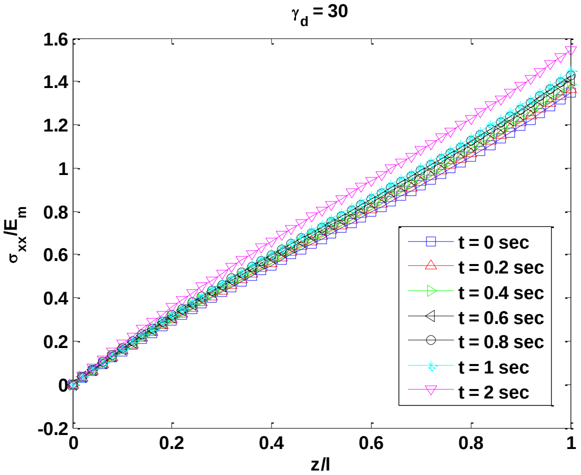

Figure 45. Axial stress variation along CNT, matrix interface for 2 sec, aspect ratio 30

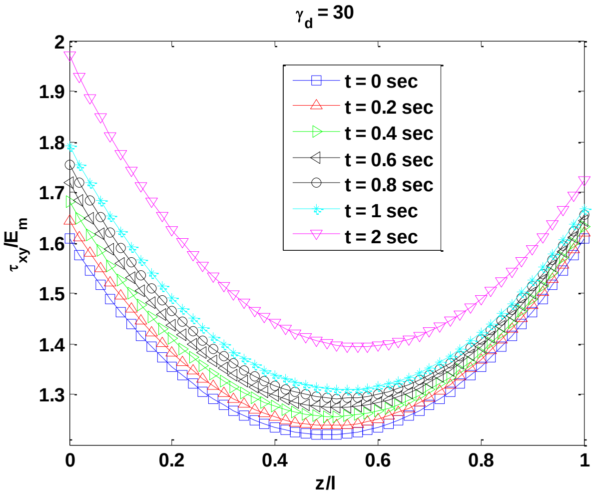

Figure 46. Shear stress variation along CNT, matrix interface for 2 sec, aspect ratio 30

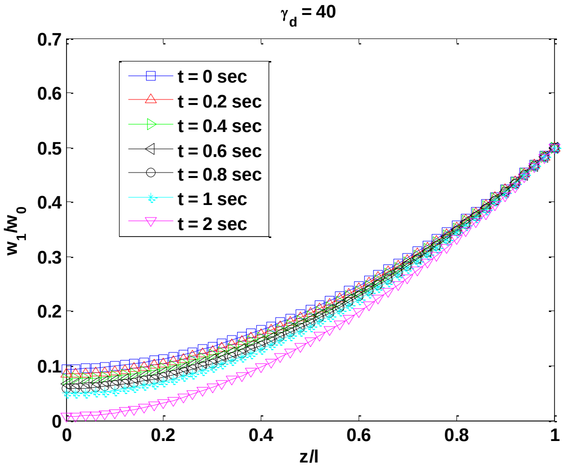

Figure 47. Displacement variation along CNT, matrix interface for 2 sec, aspect ratio 40

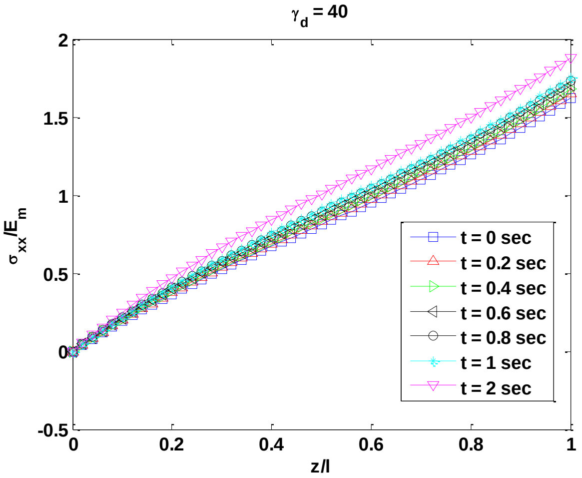

Figure 48. Axial stress variation along CNT, matrix interface for 2 sec, aspect ratio 40

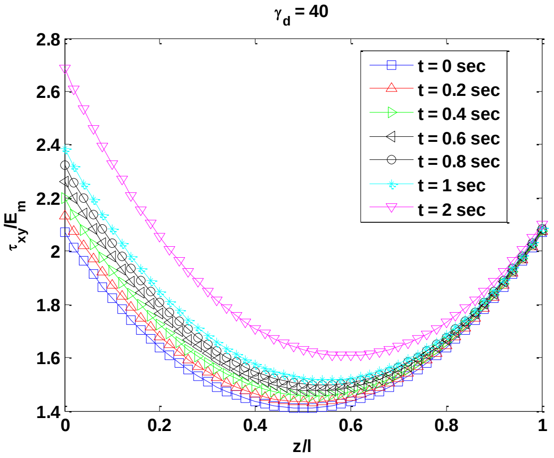

Figure 49. Shear stress variation along CNT, matrix interface for 2 sec, aspect ratio 40

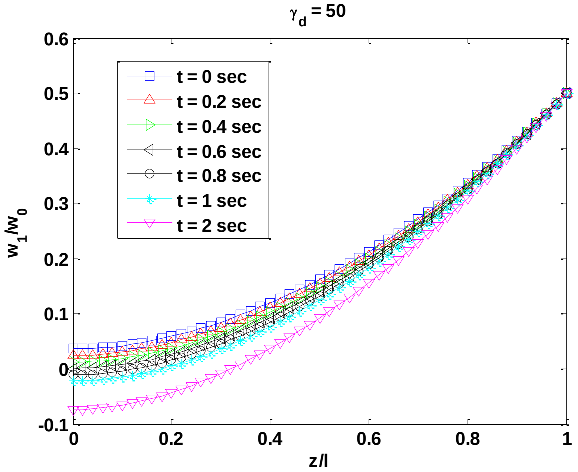

Figure 50. Displacement variation along CNT, matrix interface for 2 sec, aspect ratio 50

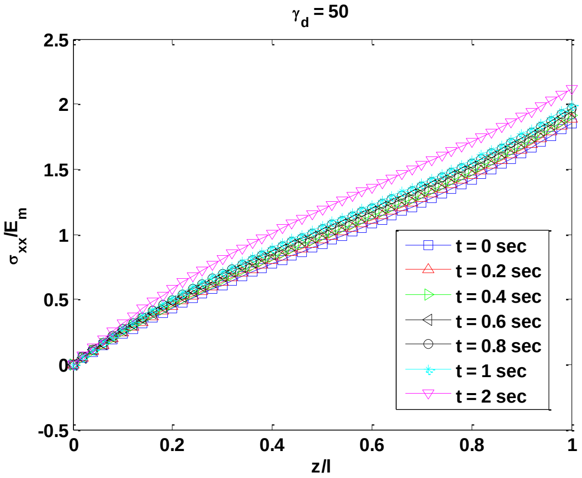

Figure 51. Axial stress variation along CNT, matrix for 2 sec, aspect ratio 50

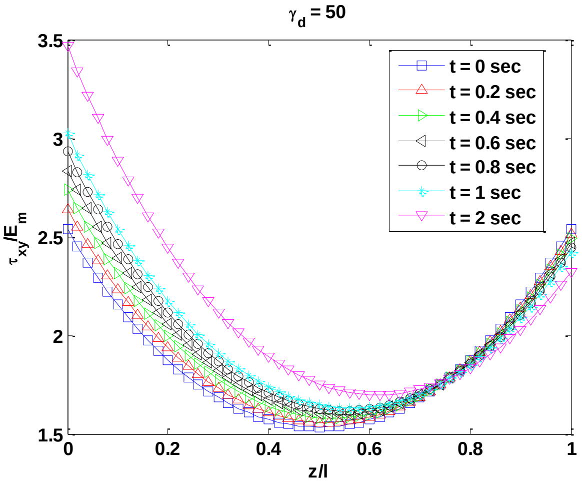

Figure 52. Shear stress variation along CNT, matrix interface for 2 sec, aspect ratio 50

The results presented indicate that the variation of the axial stress with time is more pronounced for larger aspect ratios and the magnitude of the stress is observed to increase as the aspect ratio increases as shown in Figures 42, 45, 48, and 51. Similar behavior can also be seen for the displacement field as shown in Figures 41, 44, 47, and 50. The shear stress distribution observes a more significant increase with an increase in aspect ratio along with time. Based on these results it can be concluded that the viscoelastic property of the interface should be taken into consideration when designing nanocomposites; this is particularly important in structural health monitoring applications since the nanotubes may disbond from the matrix due to the high shear stresses at the interface.

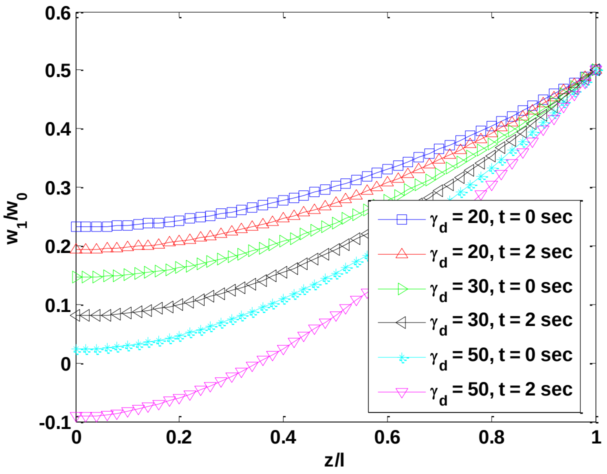

Figure 53. Displacement variation along CNT, matrix interface as a function of aspect ratio

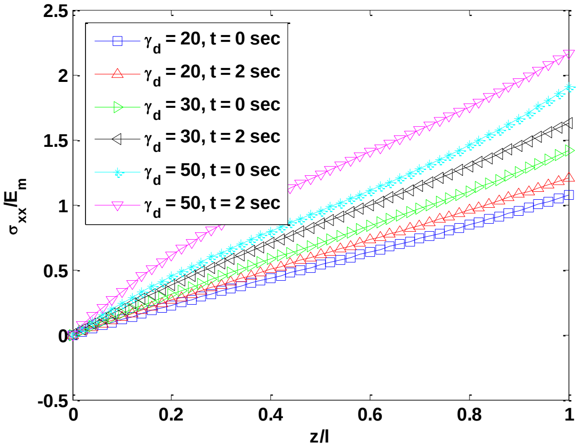

Figure 54. Axial stress variation along CNT, matrix interface as a function of aspect ratio

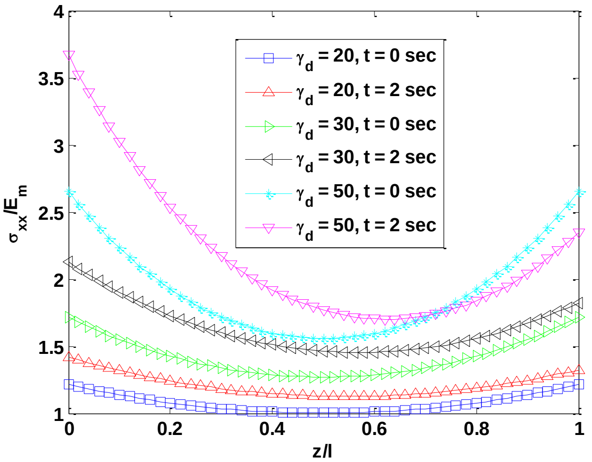

Figure 55. Shear stress variation along CNT, matrix interface as a function of aspect ratio

The effect of using multiwall CNTs is also investigated in this study. The effective properties of the nanotube for a single wall, two wall, three wall and five wall configurations are obtained from the composite cylinder method. Their effects on the overall performance of the nanocomposite are investigated using different aspect ratios. Figure 56–Figure 58 show the displacement, axial stress, and shear stress distribution for a CNT that has an aspect ratio of 10 with no time dependent effect. As observed, the change in the number of CNT walls has an impact on the overall performance, particularly on the shear stress distribution.

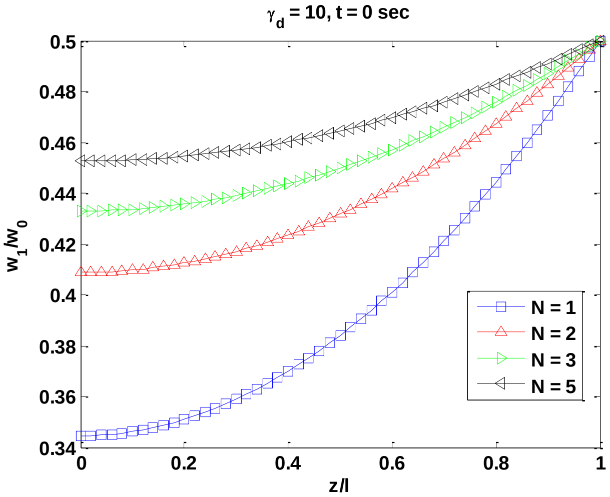

Figure 56. Displacement variation along CNT, matrix interface for different numbers of walls, aspect ratio of 10 time 0 sec

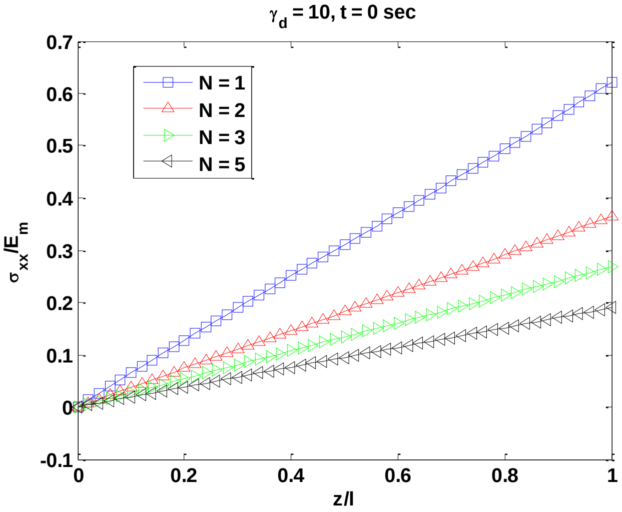

Figure 57. Axial stress variation along CNT, matrix interface for different numbers of walls, aspect ratio of 10 time 0 sec

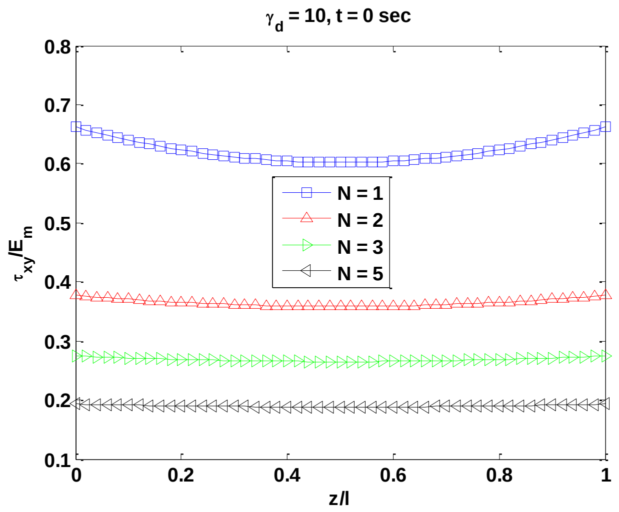

Figure 58. Shear stress variation along CNT, matrix interface for different numbers of walls, aspect ratio of 10 time 0 sec

Figure 59–Figure 61 compare the field distributions at time *t* = 2 seconds. The trends are similar to those observed at *t* = 0 although the quantitative values of the different fields are altered as expected due to the time dependence.

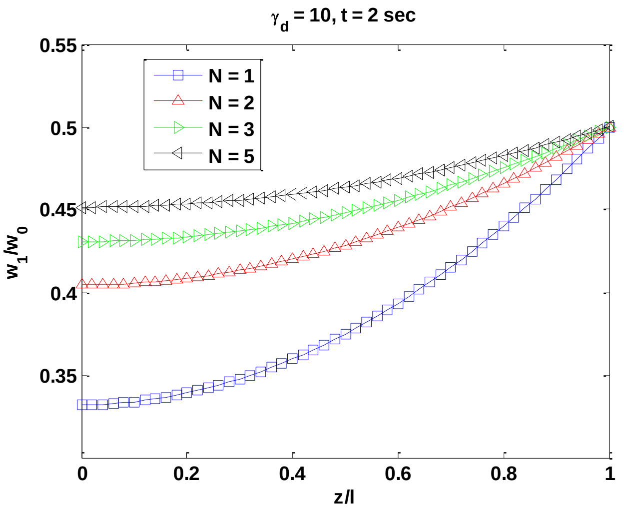

Figure 59. Displacement variation along CNT, matrix interface for different numbers of walls, aspect ratio of 10 time 2 sec

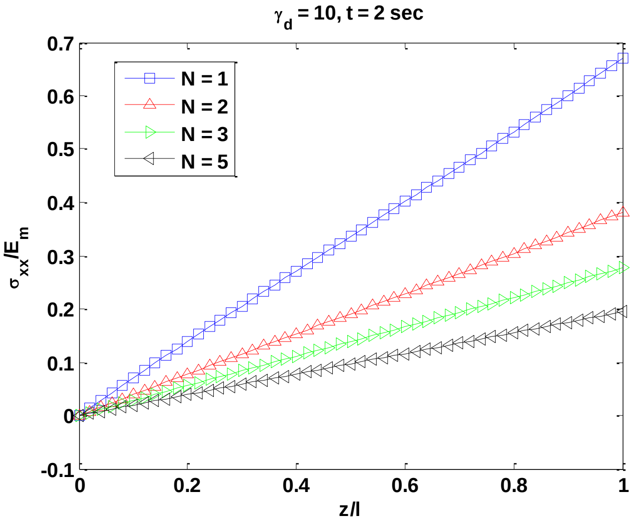

Figure 60. Axial stress variation along CNT, matrix interface for different numbers of walls, aspect ratio of 10 time 2 sec

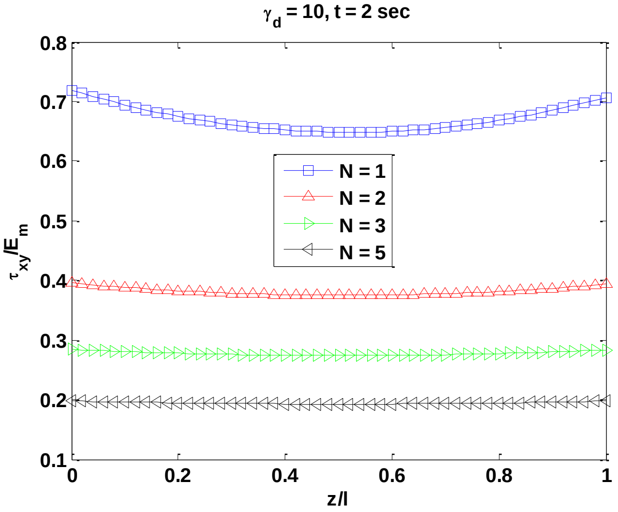

Figure 61. Shear stress variation along CNT, matrix interface for different numbers of walls, aspect ratio of 10 time 2 sec.

Finally, the effect of including an interface layer between the CNT and the epoxy matrix is considered. As shown in Figure 62–Figure 64, the change in the stress and displacement field is not altered and the variation is insignificant for different values of Interphase stiffness. The effect of time dependence was included and the results obtained are shown in Figure 65–Figure 67. The figures indicate that the interface layer does not affect the mechanical fields significantly; this observation is true for the different interface stiffness values.

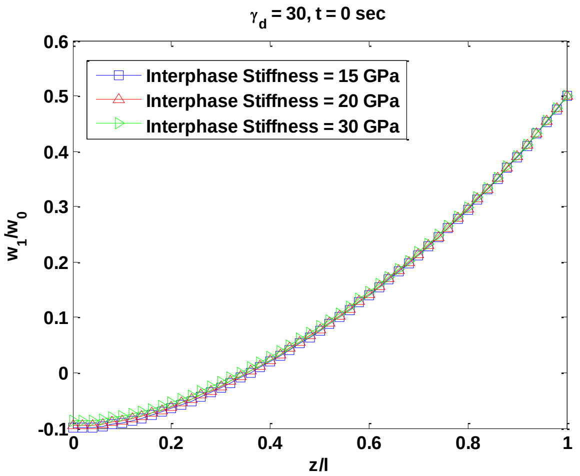

Figure 62. Displacement variation along CNT, matrix interface for different numbers of walls, aspect ratio of 30 time 0 sec

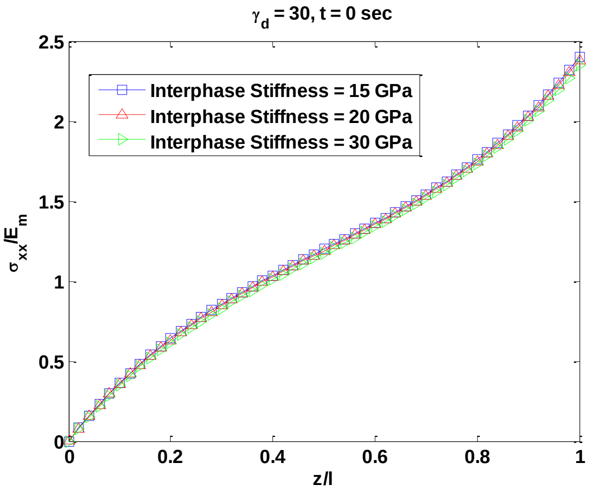

Figure 63. Axial stress variation along CNT, matrix interface for different number of walls, aspect ratio of 30 time 0 sec

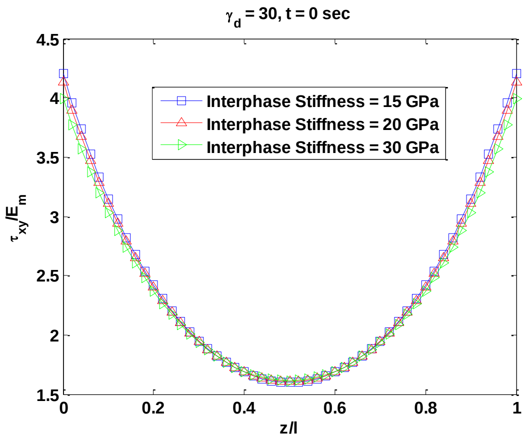

Figure 64. Shear stress variation along CNT, matrix interface for different numbers of walls, aspect ratio of 30 time 0 sec

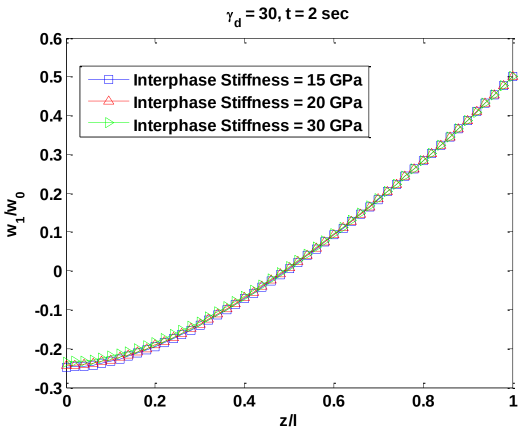

Figure 65: Displacement variation along CNT, matrix interface for different number of walls - aspect ratio of 30 time 2 sec.

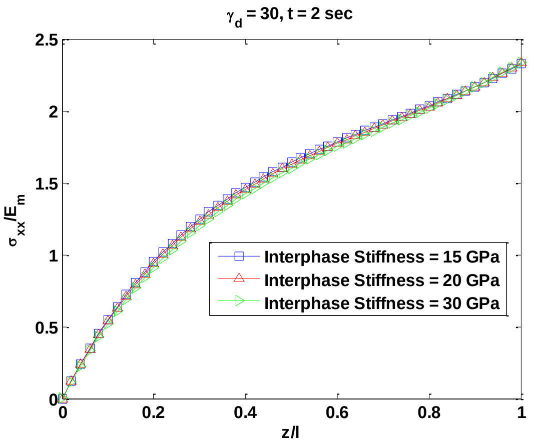

Figure 66. Axial stress variation along CNT, matrix interface for different numbers of walls, aspect ratio of 30 time 2 sec

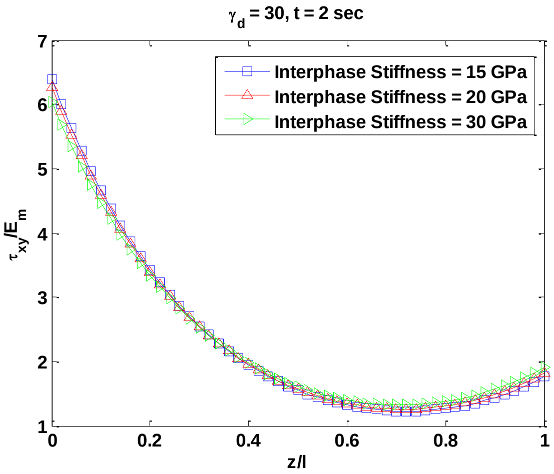

Figure 67. Shear stress variation along CNT, matrix interface for different numbers of walls, aspect ratio of 30 time 2 sec

Chapter Summary

The stress analysis of nanocomposites was presented in this chapter. The stress and displacement fields were obtained via an analytical method that adopted the Kelvin–Voigt viscoelastic constitutive relation in order to incorporate the time dependent behavior of the composite. The effective properties of the CNT were calculated using the composite cylinder micromechanics approach. It was concluded that the variation of axial stress with time is more pronounced for CNTs with larger aspect ratios and the magnitude of the stress increases as well. The shear stress distribution increases significantly with increased aspect ratio along with time. Results show that it is important to model the viscoelastic nature of the interface since the high shear stresses at the interface can lead to debonding of the CNT from the matrix and adversely affecting the structural performance.

CHAPTER 4

ANALYSIS OF COMPOSITE JOINTS INCORPORATING NANOCOMPOSITES

Delamination is a primary mode of failure in laminated composite structures, especially when there is no reinforcement in the thickness direction. In order to develop composite structures that are more damage tolerant and resistant to interlaminar failure, it is necessary to understand how delamination develops and how it can affect the performance. Residual thermal stresses, matrix-curing shrinkage, and manufacturing defects are all factors that determine how damage will initiate and grow in a composite structure. The high stress gradients that occur in specific hot spots in the structure, such as tow fillers and skin/stringer bondlines, promote damage initiation and may cause a significant loss of structural integrity. The use of nanocomposites in such critical locations may alleviate these problems and help improve overall structural performance. This chapter will investigate the applicability of using CNTs in structural level components as means to improve the interlaminar failure modes.

4.1. FE Modeling

In this section the FEMs used to analyze the nanocomposite structure are discussed. The computer software CATIA is used to create the CAD geometry, and the commercial software Abaqus is used for the analysis. Particular attention is paid to issues such as boundary conditions, mesh refinement, contact behaviors, and proper fastener modeling technique.

A brief description of the different type of structural elements considered in this research is presented here to provide the reader with a better understanding of the different parts that compose a typical composite I or T stringer and a Hat stringer. I section stringers (which are identical to the composition of T section stringers) are typically used as structural support members in aircraft wings and as fuselage panel stiffeners. The amount of tension or compression on the flanges and shear in the web of the I stringer vary depending on its connection. I stringers are fabricated by separately curing the flange and web components of the I-beam and then bonding them together using an adhesive with or without laminated angle corner pieces. Either an autoclave or a hot press is used to cure the I stringer. The radius fillet exists at the corners of the web/flange region to avoid the excessively high stresses that could be associated with a sharp corner. Two tow fillers are used to fill the triangular void that exists between the flange and web areas behind the fillet radii on the C-sections. A schematic diagram of a typical I stringer is shown in Figure 68.

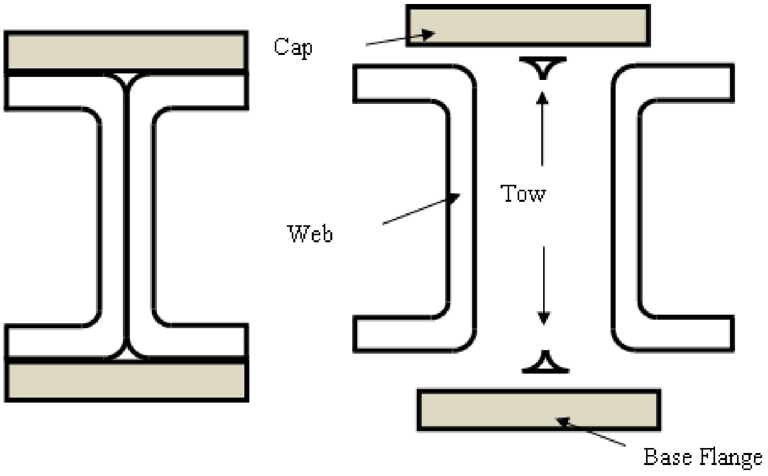

Figure 68. Schematic diagram of a composite I stringer

Similarly, a composite Hat stringer is manufactured by using pre-cured hats co-bonded on a flange and then bonded on a skin. The hat is lined with two fabric layers, which include an inner wrap ply. Two tow fillers are used for the hat-stiffeners as shown in Figure 69, which consist of rolled unidirectional tape plies or can be filled with adhesive.

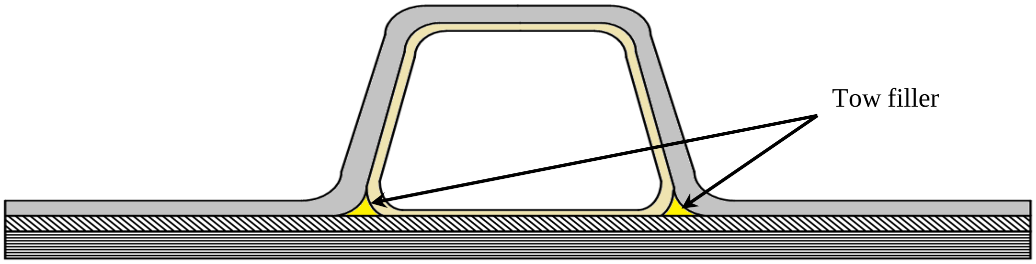

Figure 69. Schematic diagram of a composite hat stringer

The basic FEM used to simulate the test specimen (which in this case is either a T or Hat stringer) and loading fixture is shown in Figure 70. The aluminum fixture, carbon fiber-reinforced plastic (CFRP) stringer, and fasteners are modeled using continuum elements (continuum shells and/or solids). This simplified the specification of the numerous contact pairs and VCCT surfaces that will be discussed later in this chapter.

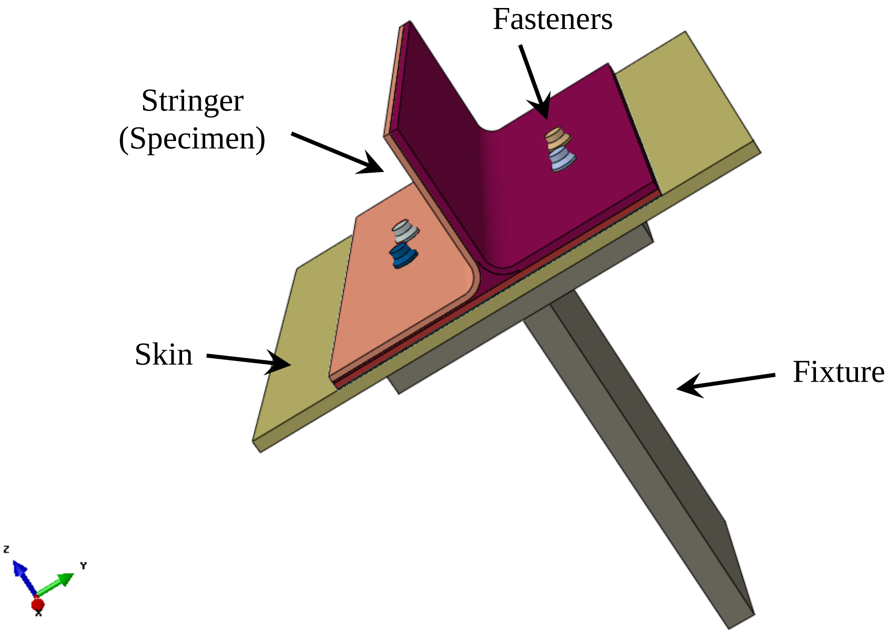

Figure 70. Typical FEM representation of Cap Pull-off Test

The aluminum fixture is modeled using C3D8Rs. These elements use a reduced integration scheme for computing their stiffness matrix, which reduces computation time with no appreciable loss in accuracy when using several elements through the thickness direction. However, such elements have a “zero energy displacement mode” that can result in false displacement patterns known as “hourglassing.” Hourglassing is usually triggered by local extreme strain gradients, which are often the result of placing a very large load on a single node. A drawback is that it can prevent solution convergence and/or compromise accuracy; however, it can be detected and controlled. Because the test fixtures were sized to keep strains and strain gradients low, the C3D8R elements reliably captured the component response. The material model for the fixtures is a simple homogeneous isotropic representation of 7075 aluminum.

The webs of the test specimens are also modeled using C3D8Rs. Several layers of elements are used for each cap, base flange, and web section, as shown in Figure 71. The number of plies used in the stack-up in each of those composite sections determines the thickness of the elements. Moreover, two surfaces are available for modeling contact, VCCT, or other interactions. The same precautions regarding hourglassing discussed earlier also apply here. “Ply-by-ply” composite properties are used for these sections, meaning that the orientation angle and orthotropic material properties for each lamina in the test specimen’s stacking sequences are specified. Local Abaqus/CAE cylindrical systems are used for the radius sections.

The unidirectional CFRP tow fillers of the specimens are modeled using continuum solid elements: C3D8I bricks and C3D6I prismatic wedges. These are first-order elements enhanced with incompatible modes, which eliminate excessive stiffness in bending behavior from “shear locking.” The mesh density around the tow region is shown in Figure 72, along with two stringer webs for reference.

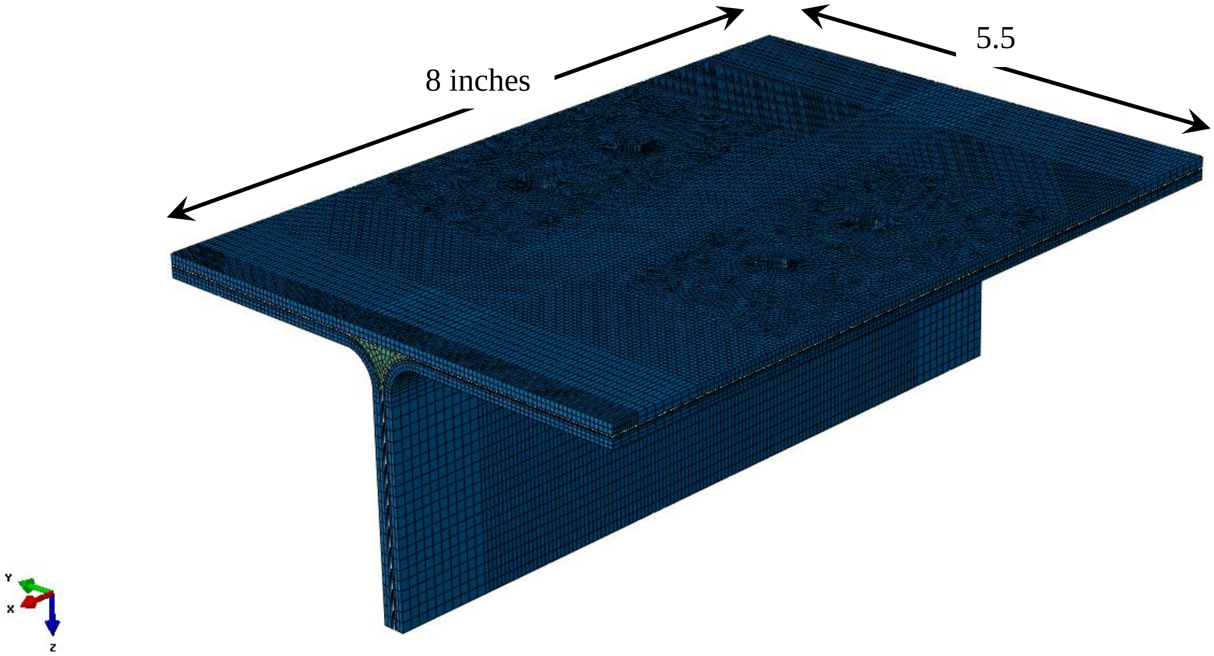

Figure 71. Typical size and mesh density of the models used in this study

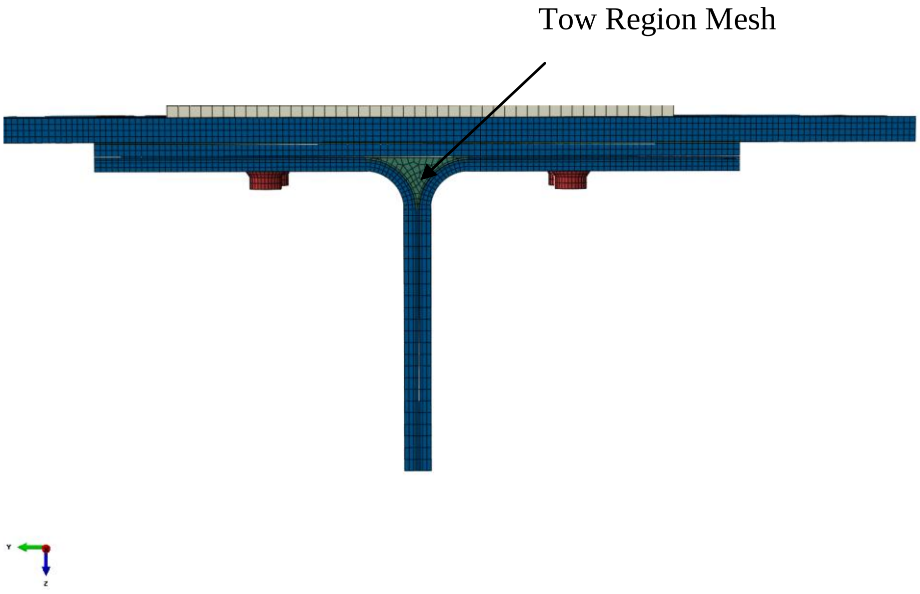

Figure 72. Tow region mesh density

In order to simulate delamination extending from an embedded manufacturing flaw, the stiffener is modeled to accommodate the VCCT analysis technique in Abaqus. This requires that a predefined crack path be included in the model definition at the interface between the elements. The crack path for the cap pull-off simulations is along the interior of one of the stiffener charges, as shown in Figure 73. The stiffener components are created in a way that resulted in matching meshes on both sides of the VCCT interface because non-matching meshes can produce erroneous delamination loads.

The two surfaces defining the crack paths are joined via the VCCT surface interaction, and a “bonded” node set is defined that excludes the nodes representing the embedded flaw. The cap pull-off models define an initially unbonded area that is centered in the spanwise direction around a fastener, and is centered radially around the tow radius. The flaw is made to be 0.5 in × 0.5 in or slightly larger if the mesh does not initially line up exactly with 0.5 in. An element size of 0.09 in or less was used for the entire delamination propagation region. At least nine elements are used around the stringer radius.

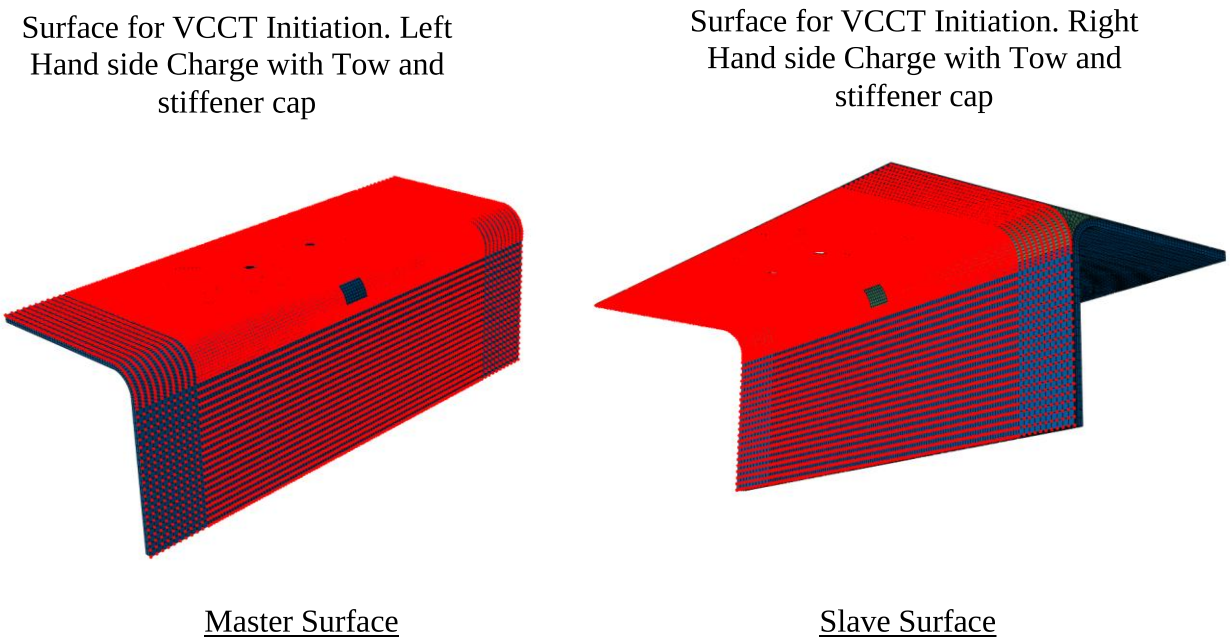

Surface for VCCT Initiation. Left Hand side Charge with Tow and stiffener cap

Surface for VCCT Initiation. Right Hand side Charge with Tow and stiffener cap

Master Surface

Slave Surface

Figure 73. Master and slave surfaces used in the fracture mechanics analysis

Fasteners and contact behaviors are used to assemble the parts in a manner that capture the physics of the mechanically fastened joint. The upper surface of the base flange and the lower surface of the fixture are defined as a “contact pair.” Small overclosures are removed in the contact definition (using the Adjust = 0 parameter in Abaqus) unless the contact caused slow convergence where in this case a contact clearance of $1e^{-6}$ is used. No friction is used between the fixture and the stringer, meaning that only compressive force is transmitted between their contact surfaces. A friction coefficient of 0.6 is used for the contact between the stringer and any radius or angle fillers, meaning that tangential forces are also transmitted between these contact surfaces. The tensile forces are transmitted from the fixture to the specimen via Abaqus (star-fasteners) in conjunction with elastic connectors. Abaqus uses distributing coupling constraints to attach the end points of the fasteners to the surfaces in a “mesh-independent” manner. The fasteners and connectivity used in a typical model is shown in Figure 74. The four fasteners common to the test fixture are only connected at the outermost surfaces of the test specimen (to the outermost surfaces of the fillers or the specimen) if no fillers are present. The “radius of influence” of the coupling constrains are specified to be twice the fastener shank radius.

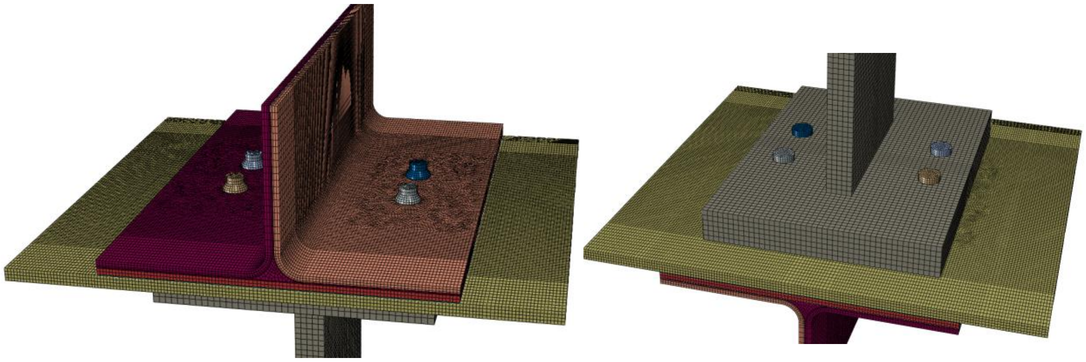

Figure 74. 3D solid fasteners used in the models

Solid continuum elements (C3D8I) are utilized to model the 3D fasteners. An Abaqus connector modeling routine (star-fastener) is used to represent the fasteners in the model. These connectors use multi-point constraints (MPCs) to constrain nodes on each surface in a fastener stackup with respect to a central reference point, which lies on the fastener axis centerline. Separate “axial” and “shear” connector definitions are used at each fastener location to provide both in-plane and through-thickness constraints to the surfaces in the fastener stackup. The connectors are shown in Figure 75, where *K* represents the fastener stiffness in the given direction. The aforementioned issues are considered contributors to the success of obtaining accurate structural behavior.

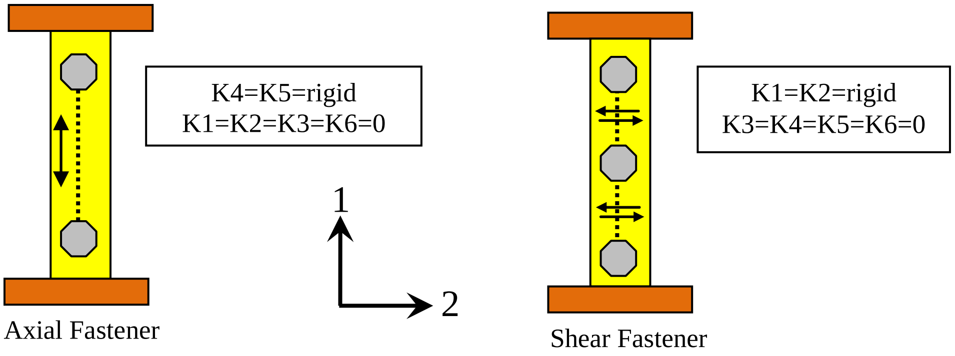

Figure 75. Axial and shear fastener representation used in the models

Connector elements are created from the fasteners to allow fastener flexibilities to be specified. The axial elasticity is calculated from the equation *EA/Li*, where *Li* is the length of the fastener segment. The rotational elasticity is calculated from the equation *EI/Li*. The *EI* is used for bending around the edge of the fastener rather than around the neutral axis. Note that the connector elasticity and preload generally have an effect on the VCCT results. Preload is used during the simulation, which is run with geometrical nonlinearity. A mechanical load step is used during each simulation. In addition, thermal load steps are considered, followed by a mechanical loading step. The thermal step simulated the internal residual strains induced when the stiffener cools from its glass transition temperature to room temperature. An initial condition of 350°F is assigned to the CFRP part and the thermal step cooled this part to 75°F, resulting in a -275°F temperature change. This will be highlighted in Chapter 6. The mechanical step simulated the pull-off loading through an applied displacement boundary condition. The boundary conditions for the analysis are shown in Figure 76.

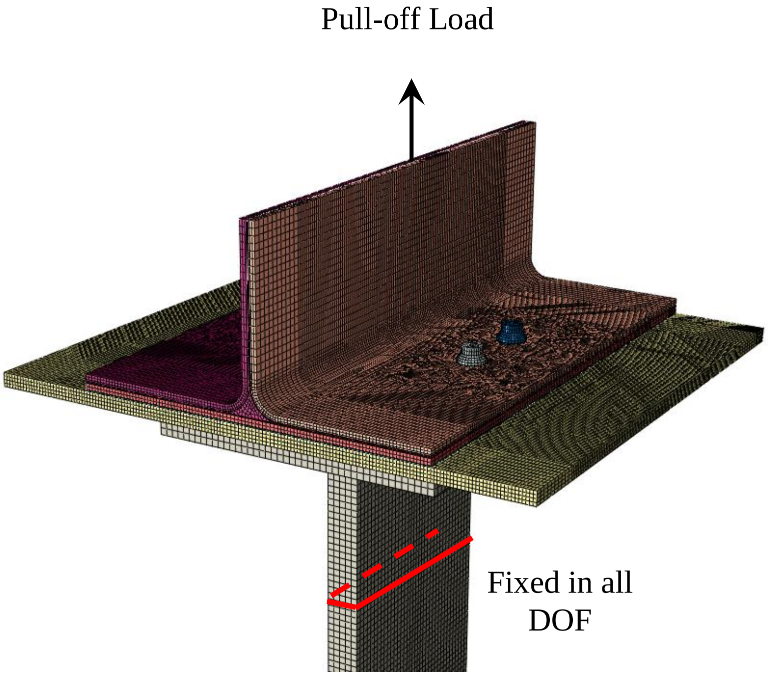

Figure 76. Loading and boundary condition (BC) applied to the detailed model

Default static stabilization is used in the models (dissipated energy fraction = 2 × 10^{-4}) to improve convergence. No contact stabilization is used on the VCCT interface. The "Power Law" VCCT mixed mode failure criterion is selected to represent the fracture of the material system:

$$\frac{G}{G_C} = \left(\frac{G}{G_{IC}}\right)^{am} + \left(\frac{G}{G_{IIC}}\right)^{an} + \left(\frac{G}{G_{IIIC}}\right)^{ao} \tag{140}$$

where *am*, *an*, *ao* = 1, and G_{Ic}, G_{IIc}, G_{IIIc} are the critical energy release rates for the three modes of fracture that will be discussed in more detail later in this chapter.

The choice of the power law is partially based on the absence of a well-defined mode mix relationship between G_{IIC} and G_{IIIC}. The power law is more conservative than the other mode mixity laws available in Abaqus (e.g., Benzeggagh-Kenane, and Reeder

Laws). In addition, the power law provides mode separation, which for the current application discussed in this study, may be more appropriate because the failure is mode specific and the interaction is not significant.

The VCCT calculation in Abaqus is made along the crack front, which is comprised of any bonded nodes that are adjacent to unbonded nodes. Any of these nodes along the boundary that meets the fracture criterion (i.e., $G/G_C \geq 1.0$) are removed from the bonded node set, meaning that they have been "released." Two separate static simulations are used in this study and explained below.

1. A simulation that predicts the initiation of fracture. For this type of simulation, the Abaqus VCCT release tolerance is set to 0.01, allowing virtually no "overshoot" of the time step beyond the critical effective energy release rate ratio ($G/G_C=1.0$). The simulation is terminated after the first VCCT node on the perimeter of the unbonded region reached the critical energy release rate.
2. Another simulation that is considered is identical in every way to the previous simulations (including the fracture toughness properties) except that the solution is allowed to propagate beyond onset in order to observe the crack propagation. This is achieved by increasing the Abaqus VCCT release tolerance to 0.40, the maximum number of cutbacks to 20, the maximum number of increments to 300, and decreasing the minimum permissible time increment to 1.0×10^{-20}. These changes are required to prevent the simulation from being terminated due to a time increment constraint. This will be implemented in Chapter 6.

The effective energy release rate ratio is tested along the entire crack front during every time increment. The crack can grow to a maximum of one node in the depth per increment, but Abaqus automatically adjusts the size of the time increment in order to propagate the crack at the appropriate rate. The size of the time increment following initiation can indicate the stability of the crack growth along the predefined VCCT interface. A time increment that is large enough for the load to increase indicates that the crack growth along this interface is relatively stable. On the other hand, very small time increments corresponded to a virtually constant displacement because the pull-off is applied as a displacement in these simulations. If the stiffness decreases from the crack growth that is dominating the response, then the pull-off load would actually drop. The propagation simulation uses load drop, which indicated unstable delamination as a key assessment for correlation. The field output requests include displacements and reaction forces for node points, as well as logarithmic strain, stress, and section forces for elements. Contact forces for the surfaces in contact are output. VCCT for Abaqus generates solution-dependent state variables at each node of the slave surface of the bonded pair. The following variables are used.

SDV10 Mode I strain energy release rate

SDV11 Mode II strain energy release rate

SDV12 Mode III strain energy release rate

SDV13 Bond State, 0 = fully bonded, 1 = unbonded

SDV14 Failure index or effective energy release rate ratio (G/G_C)

The history of output requests include the reaction force for the pull-off node (RF2), the total strain energy of the structural system (ALLSE), and the strain energy dissipated through damping (ALLSD). ALLSD is very useful in evaluating the first load drop.

4.2. Fracture Mechanics Approach

Delamination can be related to the initiation of fracture between two anisotropic layers (i.e., interlaminar damage). The principles of fracture mechanics can be utilized to study such damage in interlaminar regions on composites. To do so, the assumption must be made that delamination grows as a function of crack propagation. Every material has a set threshold level that, when exceeded by the amount of energy released for unit width and unit length of the crack surface, causes the crack to grow; this threshold is known as the fracture toughness (Moore, D.R. et al. 2001).

The delamination in a composite can be studied by monitoring strain energy release rates. The VCCT provides the capability to predict delamination and propagation from an initial crack in a laminated structure efficiently via an FEM of the CFRP structure. It assumes that an infinitesimally small crack releases certain amounts of strain energy, which are equal to the work required to close that crack. Two analyses can be conducted to find the magnitude of that work; the first evaluates the stress at the tip of the crack and the second evaluates the displacement at the crack front.

The total strain energy release rate G_T, the mode I component due to interlaminar tension G_I, the mode II component due to interlaminar sliding shear G_{II}, and the mode III component G_{III} due to interlaminar scissoring shear shown in Figure 77 are the components that need to be computed to evaluate the structural performance. In order to predict delamination onset or growth for two-dimensional (2D) problems, these calculated G components are compared to interlaminar fracture toughness properties measured over a range from pure mode I loading to pure mode II loading.

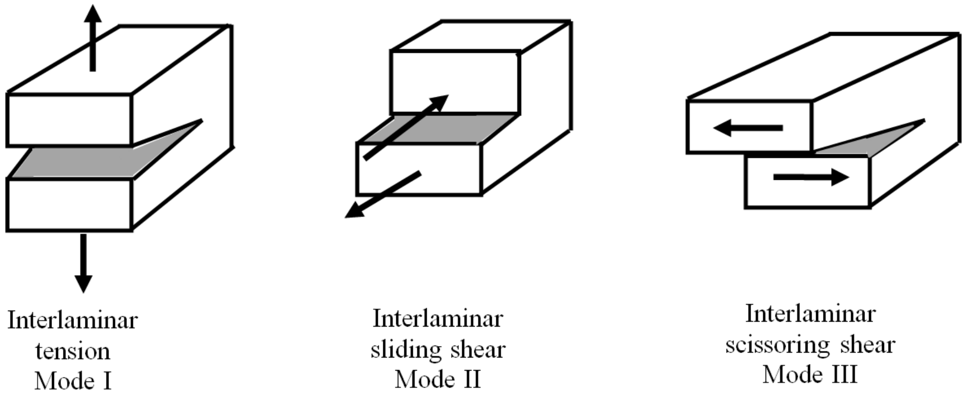

Figure 77. Schematic diagram of the 3 modes of fracture failure.

4.2.1. Methods used to compute the strain energy release rate

A variety of methods are used to compute the strain energy release rate based on the results obtained from the FE analysis. Several of them will be discusses here to provide the reader with insight into other available methods. The finite crack extension method (Doltsinis, J. et al. 1985), (Krüger, R. et al. 1993) requires two complete analyses. In the model, the crack is extended for a finite length prior to the second analysis. The method provides one global total energy release rate as global forces on a structural level are multiplied with global deformations to calculate the energy available for crack advancement. The virtual crack extension method (Hellen, T. K. 1975), (Parks, D. M., 1974), (Parks, D. M. 1977), (Parks, D. M. 1978), (Delorenzi, H. G. 1982), (Delorenzi, H. G. and Shih, C. D. 1983), (Delorenzi, H. G. 1985), (Lin, S. C. and Abel, J. F. 1988) (Claydon, P. W. 1992), (Hwang, C. G. et al. 1998) requires only one complete analysis of the structure to obtain the deformations. The total energy release rate or J-integral is computed locally at the crack front, and the calculation only involves an additional computation of the stiffness matrix of the elements affected by the virtual crack extension. The method yields the total energy release rate as a function of the direction in which the crack was virtually extended, yielding information on the most likely growth direction. Modifications of the method have been suggested in the literature to allow the mode separation for 2D analysis (Ishikawa, H. 1980), (Sha, G. T. 1984). An equivalent domain integral method, which can be applied to both linear and nonlinear problems and also allows for mode separation, was proposed in Shivakumar and Raju’s work (Shivakumar, K. N. and Raju, I. S. 1992), (Raju, I. S. and Shivakumar, K. N. 1990). A comprehensive overview of different methods used to compute energy release rates is given in Banks-Sills (Banks-Sills, L. 1991). Alternate approaches to compute the strain energy release rate based on results obtained from FE analysis have also been published (Chow, W. T. and Atluri, S. N. 1997), (Gosz, M. and Moran, B. 2002), (Park, O. and Sankar, B. V. 2002).

The VCCT (Rybicki, E. F. and Kanninen, M. F. 1977), (Raju, I. S. 1987), (Buchholz, F. G. 1988) is widely used for computing energy release rates based on the results from continuum (2D) and solid (3D) FE analyses. This is done in order to supply the mode of separation required when using the mixed-mode fracture criterion. In this method, the crack is physically extended, or closed, during two complete FE analyses as shown in Figure 78. The original crack closure method is based on Irwin’s crack closure integral (Irwin, G. R. 1958), (Broek, D. 1982). The method is based on the assumption that the energy E released when the crack is extended by a from a (Figure 78a) to $a + \Delta a$ (Figure 78b) is identical to the energy required to close the crack between location l and i (Figure 78a). Index “1” denotes the first step depicted in Figure 78a, and index “2” is the second step as shown in Figure 78b. For a crack modeled with 2D, four-noded elements as shown in Figure 78, the work required to close the crack along one element side can be calculated as

$$\Delta E = \frac{1}{2}\left[X_{1l} \cdot \Delta u_{2l} + Z_{1l} \cdot \Delta w_{2l}\right] \tag{141}$$

where X_1 and Z_1 are the shear and opening forces to close nodal point l (Figure 78a), and *u2* and *w2* are the differences in shear and opening nodal displacements at node l as shown in Figure 78b. The crack closure method establishes the original condition before the crack was extended. Therefore, the forces required to close the crack are identical to the forces acting on the upper and lower surfaces of the closed crack. The forces X_1 and Z_1 may be obtained from a first FE analysis, where the crack is closed. The displacements *u2* and *w2* are obtained from a second FE analysis where the crack has been extended to its full length $a + \Delta a$.

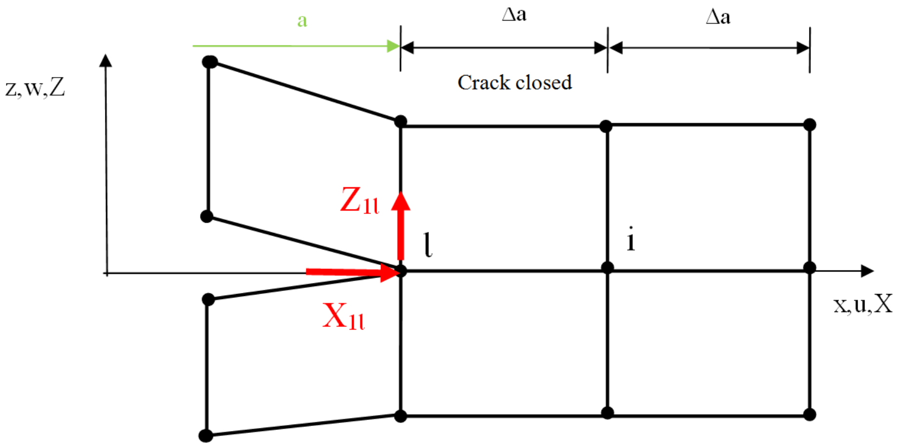

(a) *First Step - Crack closed*

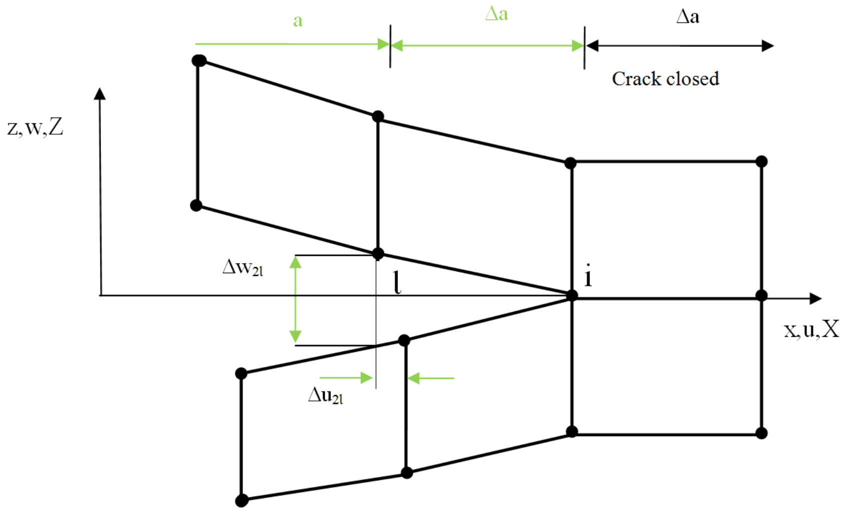

(b). *Second Step - Crack extended*

Figure 78. Crack closure method (two-step VCCT)

The modified, or virtual, crack closure method is based on the same assumptions as the crack closure method described above. However, it is assumed that a crack extension from $a + \Delta a$ (node i) to $a + 2\Delta a$ (node k) does not significantly alter the state at the crack tip (Figure 79). Therefore, the displacement behind the crack tip at node i is approximately equal to the displacement behind the original crack tip at node l. Furthermore, the energy E released when the crack is extended from $a + \Delta a$ to $a + 2\Delta a$ is identical to the energy required to close the crack between location i and k. For a crack modeled with 2D, four-noded elements, as shown in Figure 79, the work E required to close the crack along one element side and therefore can be calculated as

$$\Delta E = \frac{1}{2}\left[X_i \cdot \Delta u_l + Z_i \cdot \Delta w_l\right] \tag{142}$$

where X_i and Z_i are the shear and opening forces at nodal point i, and u and w are the shear and opening displacements at node l as shown in Figure 79. Thus, the forces and displacements required to calculate the energy E to close the crack may be obtained from a single FE analysis.

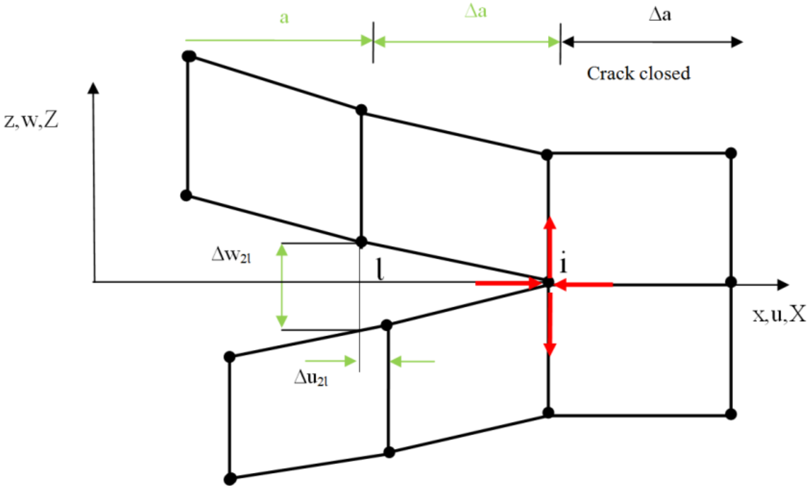

Figure 79. Modified Crack closure method (One-step VCCT)

In an FEM made of 3D solid elements as shown in Figure 80, the delamination of length a is represented as a 2D discontinuity in two surfaces. The additional dimension allows for calculating the distribution of the energy release rates along the delamination front and makes it possible to obtain G_{III}, which is identical to zero for 2D models. Nodes at the top and bottom surfaces have identical coordinates and are not connected with each other. The delamination front is represented by either a row of single nodes or two rows of nodes with identical coordinates that are coupled through multipoint constraints. The undamaged section where the delamination is closed, and the structure is intact is modeled using single nodes or two nodes with identical coordinates coupled through multi-point constraints if a delamination propagation analysis is desired.

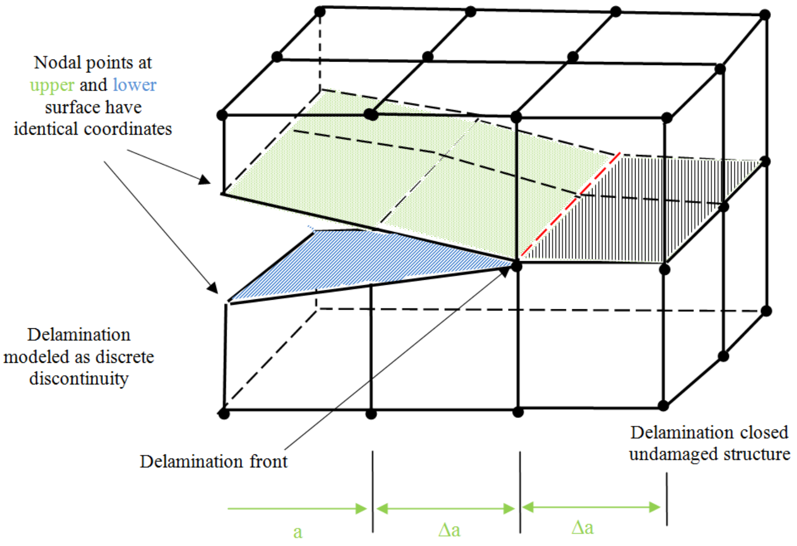

Figure 80. Delaminations modeled as 2D discontinuity

For convenience, only a section of the delaminated area, which is modeled with eight-noded 3D solid elements, is illustrated in Figure 81. The mode I, mode II, and mode III components of the strain energy release rate, G_I, G_{II}, and G_{III}, are calculated as

$$G_I = -\frac{1}{2\Delta A} \cdot Z_{Li} \cdot \left(w_{Ll} - w_{Ll^*}\right) \tag{143}$$

$$G_{II} = -\frac{1}{2\Delta A} \cdot X_{Li} \cdot \left(u_{Ll} - u_{Ll^*}\right) \tag{144}$$

$$G_{III} = -\frac{1}{2\Delta A} \cdot Y_{Li} \cdot \left(v_{Ll} - v_{Ll^*}\right) \tag{145}$$

with $A = a \times b$ as shown in Figure 81. Here A is the area virtually closed, a is the length of the elements at the delamination front, and b is the width of the elements. X_{Li}, Y_{Li}, and Z_{Li} denote the forces at the delamination front in column L row i. The corresponding displacements behind the delamination at the top face node row l are denoted u, v, and w, and at the lower face node row l* are denoted u^*, v^*, and w^*, respectively, as shown in Figure 81. All forces and displacements are obtained from the FE analysis with respect to the global system. A local crack tip coordinate system, (x`, y`, z`) defines the normal and tangential coordinate directions at the delamination front in the deformed configuration.

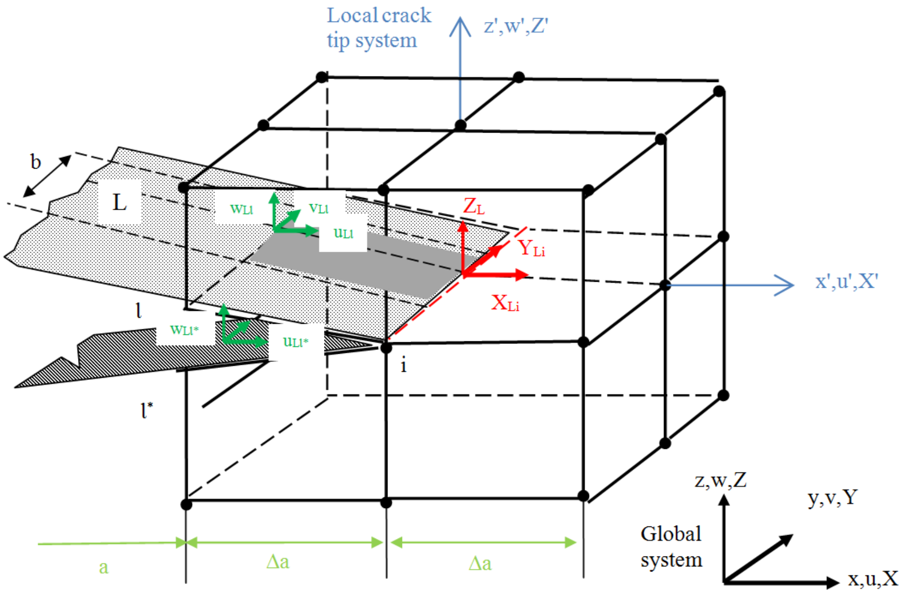

Figure 81. VCCT for four noded plate/shell and eight noded solid elements

In order to use the VCCT analysis technique in Abaqus, an initial flaw must be embedded in the model. The flaw is usually inserted in locations where delamination is most likely to occur. Because different flaws behave differently, three dissimilar flaw types will be considered in this study as will be shown later on in this chapter.

4.3. Validation

To validate both the modeling techniques and the method of analysis, the results are compared with available experimental data in the literature (Li, J. 2002). Two simulation models are constructed: one with simply supported boundary conditions and another clamped at the ends with fasteners. Figure 82 shows the 3D FEMs developed, as well as the actual specimen that was tested.

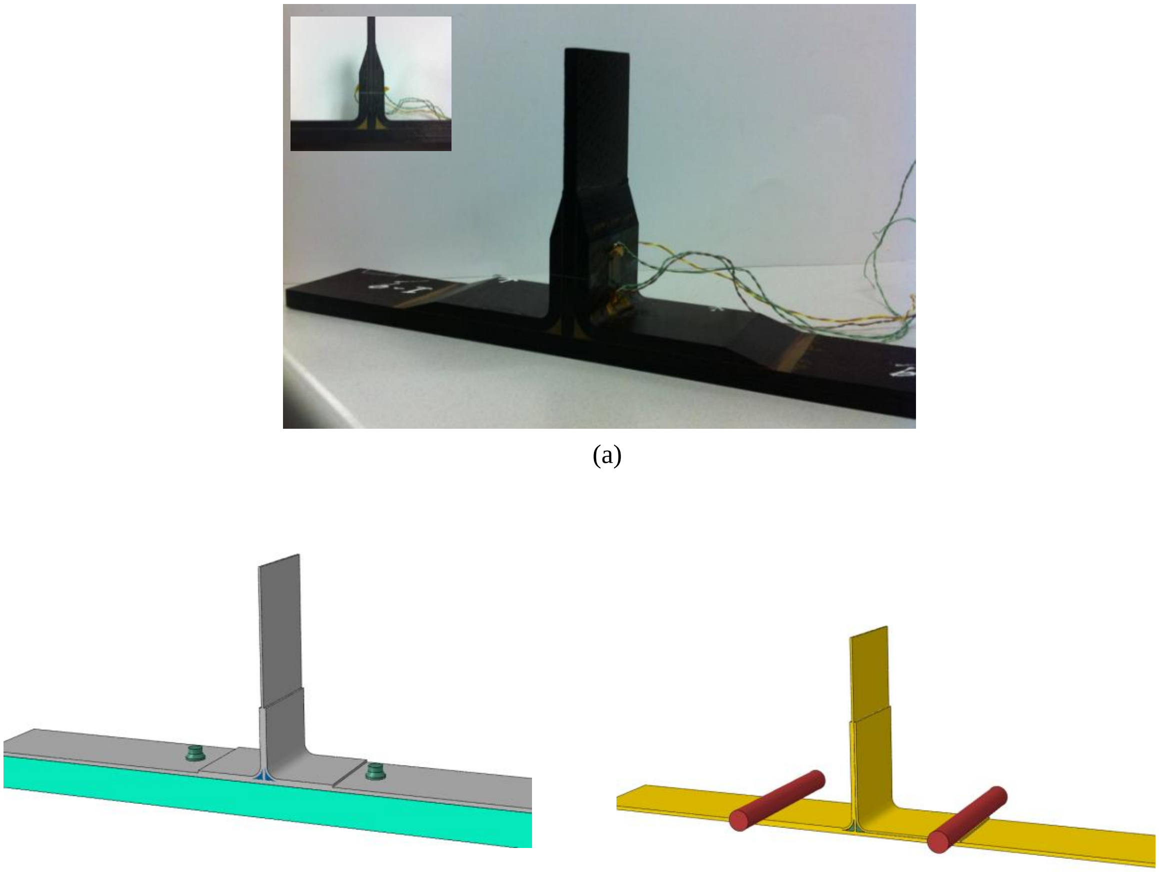

(a)

(b)

(c)

Figure 82. (a) Experimentally tested specimen (Li, J. 2000), (b) 3D CAD model with clamped BC, and (c) 3D CAD model with simply supported BC

In order to correlate to the available experimental data, a 0.5 in × 0.5 in flaw is inserted between the tow filler and the web midway along the stringer span where delamination was observed to initiate, as shown in Figure 83. It is important to mention that preload is applied to all of the fasteners in the model. It should also be noted that resin toughness values are used in the analysis to predict the initial damage.

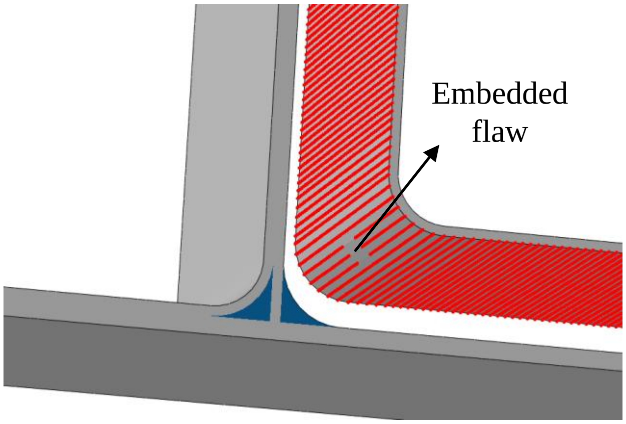

Figure 83. Embedded flaw used in the model

Figure 84 shows the value for mode I energy release rate around the embedded flaw. It is noted that the failure is usually dominated by this failure mode and the contributions of mode II and III are not significant. Figure 85 and Figure 86 show the correlation between the FEMs and the experimental data for both the simply supported and clamped models, respectively. Note that the correlation was performed to the initial damage load rather than the final failure load. A total of 20 specimens were tested (8 for the simply supported boundary condition case and 12 for the clamped boundary condition case) with dimensions 2 in wide and 14 in long (Li, J. 2002). It can be observed that the predicted initial damage from the FEMs is within 10% of the results obtained from testing. Note that the initial damage predicted by the models is lower, indicating that the models provide a more conservative estimate. This correlation provided confidence in both the analysis method and modeling techniques and therefore is used for the remaining analyses.

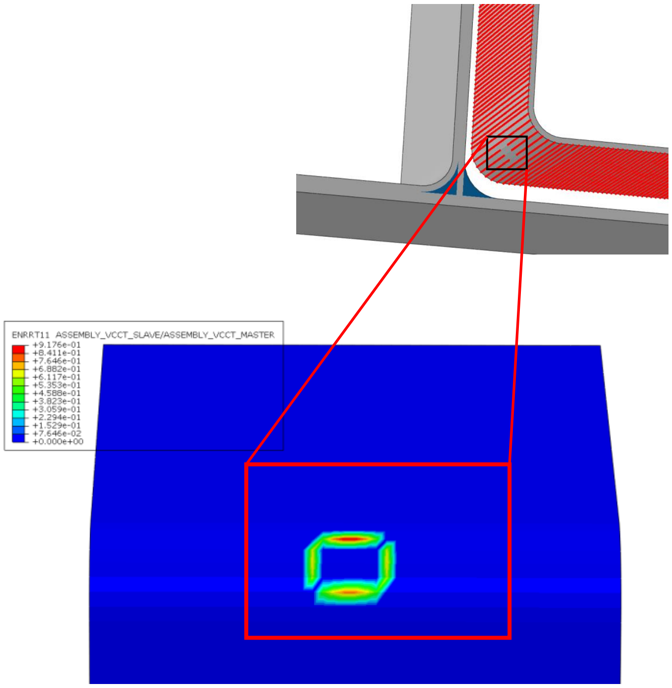

Figure 84. Mode I energy release rate around the embedded flaw used in the model

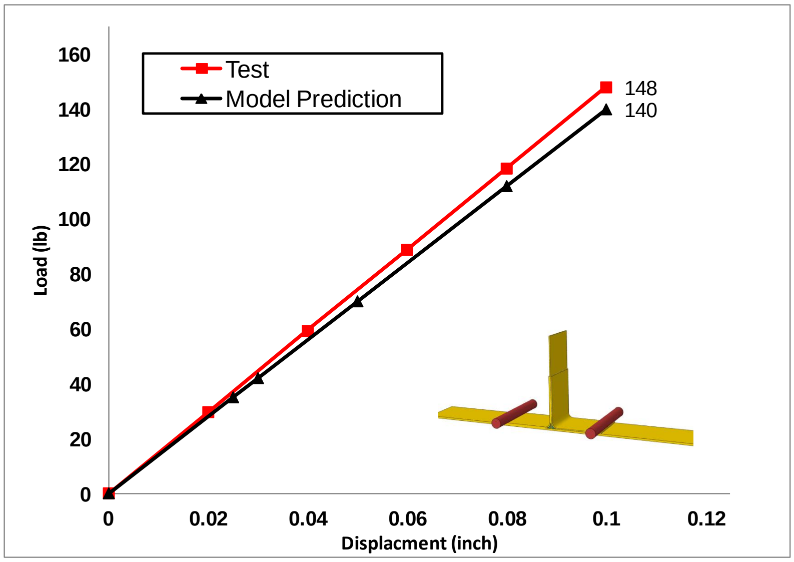

Figure 85. Correlation between the FEM and test for the simply supported specimen

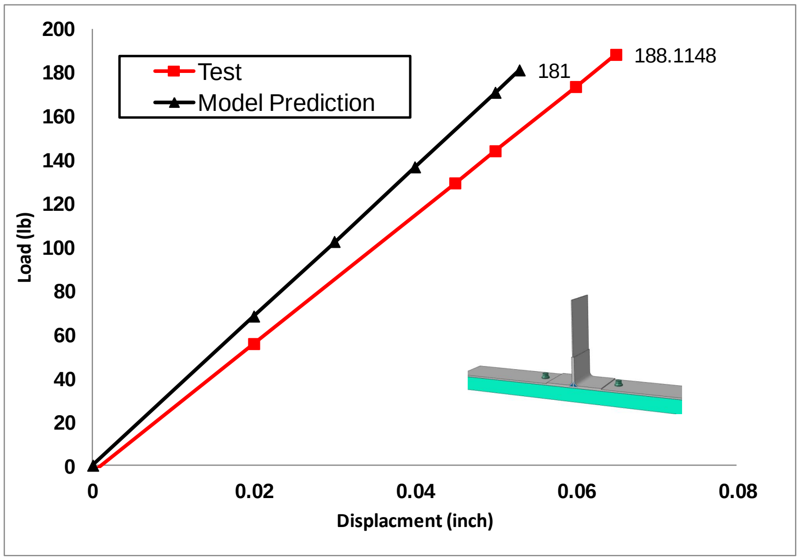

Figure 86. Correlation between the FEM and test for the clamped specimen

4.4. Composite Stringer Joints

After correlation to the experimental data, the next step is to create a comparatively larger detailed model with the same modeling methods. This larger model use a fine grid mesh (especially in the area of interest) to accurately capture the joint behavior under critical loading conditions. Two different types of stringer cross sections will be investigated in this study: a T section and a Hat section stringer. The reason for analyzing both is due to the fact that both are commonly used in aircraft and space structures and have different behaviors under different loading conditions.

To better understand the structural performance, several different damage scenarios and loading conditions are considered. Table 7 summarizes the different flaws and loading condition combinations considered in this study. A schematic diagram of the different flaw types is shown in Figure 87 and Figure 88 for the T section stringer and the Hat stringer, respectively. Comparisons between pure adhesive and adhesive with 1, 3, and 5 weight percent CNT are considered. It was previously found that the fracture toughness values significantly increase for adhesives that incorporate CNTs in their mixture (Kumar, S. et al. 2012), (Hsieh, T. et al. 2011), (Thakre, P. et al. 2011), which motivated the authors to consider that as an alternative to overcome some of the structural weaknesses in composite joints.

Table 7. Summary of the different flaws and loading condition combinations used in the analysis

Flaw Type	*Loading Condition*	*Tow Material*	*Case*
Flaw 1	Pull-off	Fabric	1
		Adhesive	2
	Pull-off + Axial	Fabric	3
		Adhesive	4
Flaw 2	Pull-off	Fabric	5
		Adhesive	6
	Pull-off + Axial	Fabric	7
		Adhesive	8
Flaw 3	Pull-off	Fabric	9
		Adhesive	10
	Pull-off + Axial	Fabric	11
		Adhesive	12

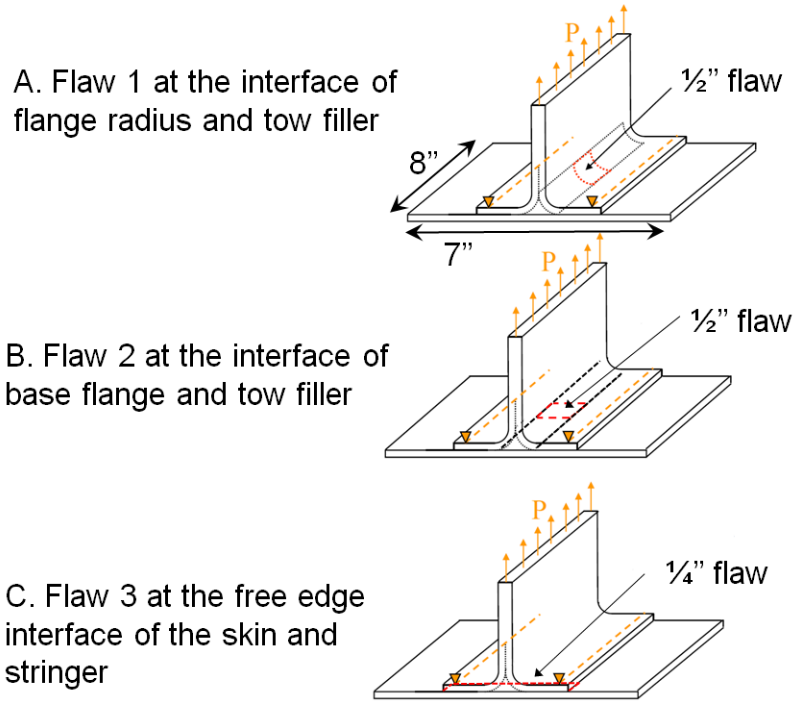

Figure 87. Schematic of T stringer configuration with the different flaws considered in the analysis

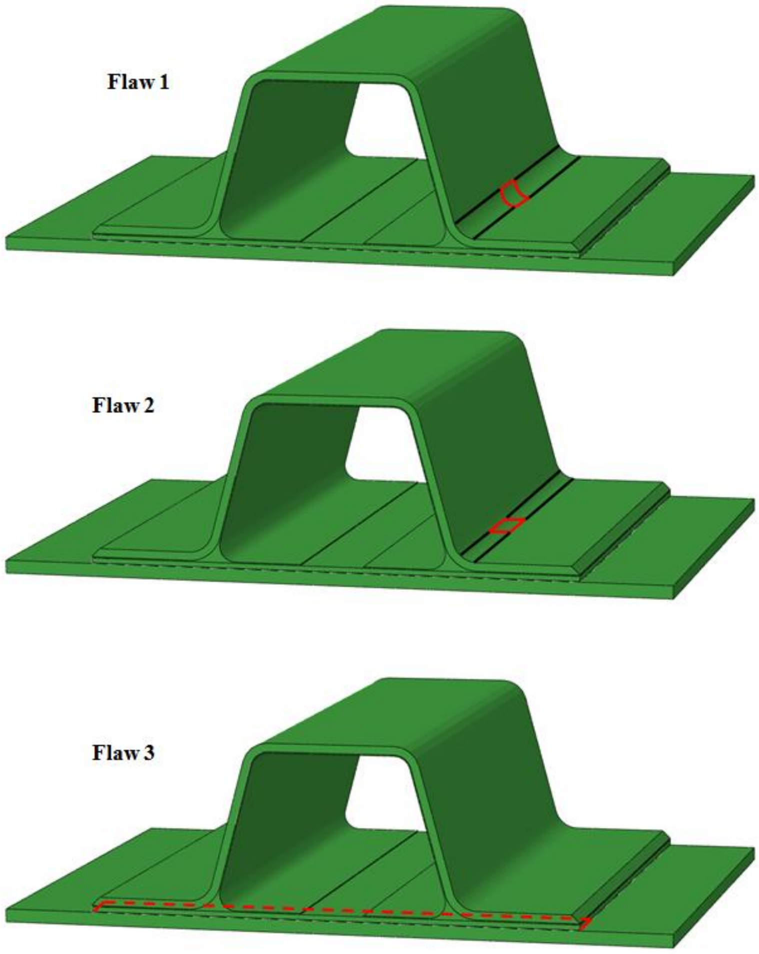

Figure 88. Schematic of Hat stringer configuration with the different flaws considered in the analysis

The detailed FEMs constructed are shown in Figure 89 and Figure 90. Initially, a baseline model is constructed that uses typical adhesive properties without any CNTs. In addition to the different flaw types, two designs are considered: one that uses adhesive to fill the tow region and another that uses fabric. Both were assessed because these materials are commonly used as fillers in the industrial manufacturing of T and Hat stringers. Moreover, the effect of having the composite laminates of the skin and stringer made using matrices that include CNTs is also studied. Note that all of the effective properties for the different nanocomposites are obtained from the multiscale analysis discussed in Chapter 2. The loading conditions considered are pull-off and combined axial/pull-off.

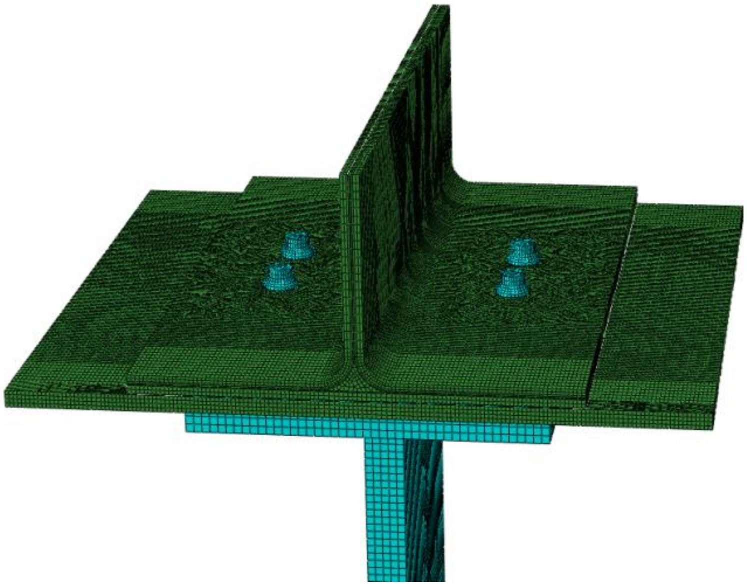

Figure 89. Schematic diagram of the T stringer

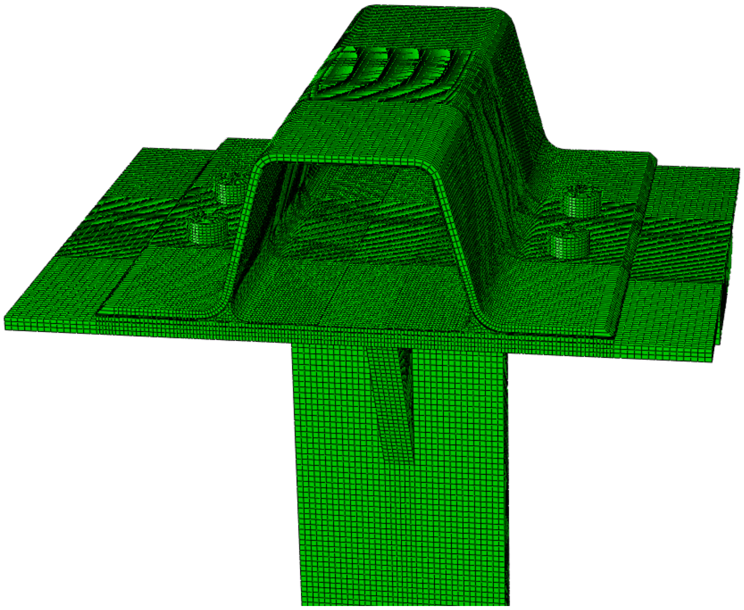

Figure 90. Schematic diagram of the Hat stringer

It is important to note that the value of the failure load depends on the location where the flaw is embedded in the structure. Figure 91 shows the running load of the stringer along its span-wise direction due to the applied pull-off load. As observed, the peak running load exists midway along the stringer; hence, both type 1 and 2 flaws are embedded in the T stringer in that location, whereas the type 3 flaw is inserted at the stringer termination between the stringer base and skin interface where there is an abrupt change in geometry and delamination is most likely to occur.

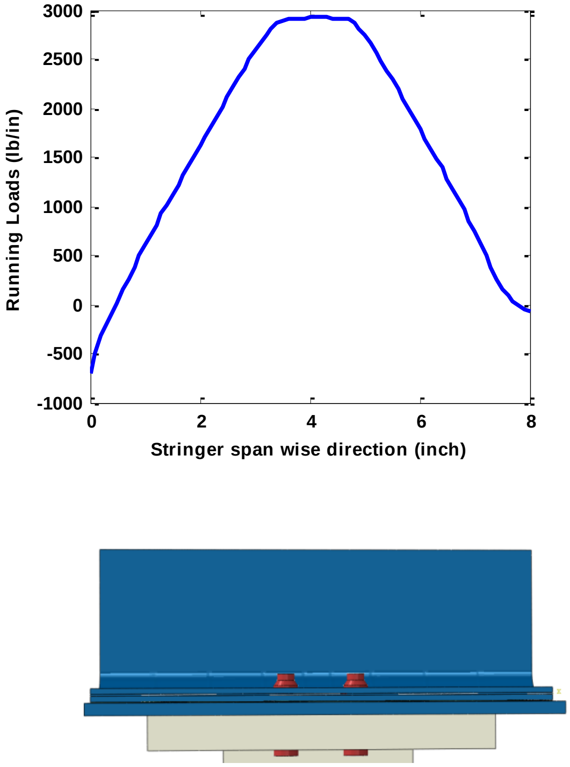

Figure 91. Running load plot along stringer span-wise direction

4.5. Analysis Results – T section Stringer

Figure 92– Figure 94 show the initial failure load by applying a pure pull-off load for the three different flaw types. Note that four different configurations regarding the use of CNT in the structure are considered and summarized in Table 8.

Table 8. Different configurations considered in the analysis

Configuration	Use of CNT
1	**Adhesive Tow**: CNT was used in the adhesive layer surrounding the tow filler and inside the tow filler itself. CNT was also used in the adhesive layer that exists between the skin and stringer interface.
2	**Adhesive Tow**: CNT was used in the adhesive layer surrounding the tow filler and inside the tow filler itself. CNT was also used in the adhesive layer that exists between the skin and stringer interface. In addition, CNT was used in the composite laminates of the stringer and skin.
3	**Fabric Tow**: CNT was used in the adhesive layer surrounding the tow filler and inside the tow filler itself. CNT was also used in the adhesive layer that exists between the skin and stringer interface.
4	**Fabric Tow**: CNT was used in the adhesive layer surrounding the tow filler and the inside tow filler itself. CNT was also used in the adhesive layer that exists between the skin and stringer interface. In addition, CNT was used in the composite laminates of the stringer and skin.

Figure 92 represents the pull-off failure load of a structure that incorporates a type 1 flaw. The general trend observed for both types of tow materials (fabric and adhesive) is the increase in failure load with greater CNT weight fraction due to the added through-thickness capability. It is also noticeable from the figure that for all values of CNT weight fractions, the failure load for the adhesive tow is considerably larger than that for the fabric tow. When examining the adhesive tow results, only the failure load is higher for the case when both the adhesive and composite contain CNTs, unlike the fabric tow design.

The type 1 flaw is noted to be mode I dominant, which relies on the angle opening of the radius where the pull-off load tends to open that radius, creating high energy release rates. Therefore, the use of CNTs provides additional through-thickness capability, thus preventing or delaying such an event from occurring. Figure 93 represents the pull-off failure load of the structure that incorporates a type 2 flaw. In this case, the failure load increases with greater CNT weight percentages for both types of tow materials. It can also be observed that the failure load for the adhesive tow is larger than that for the fabric tow. By considering only the adhesive tow results, the failure load is higher for the case where both the adhesive and composite contain CNTs. A similar observation can be made in the case of the fabric tow. A type 2 flaw is also found to be mode I dominant under pull-off loading, and the use of CNTs is shown to give additional through-=thickness capability. Figure 94 represents the pull-off failure load of a structure that incorporates a type 3 flaw. As in the previous two cases, the failure load increases with greater CNT weight percentages; however, for the fabric tow the failure load increases up until 5% CNT by weight, where it drops slightly. When examining the adhesive tow results, the failure load is higher for the case when both the adhesive and composite contain CNTs, but this statement does not hold true regarding the fabric tow. A type 3 flaw is found to have a mode mix of both I and II under pull-off loading, and the use of CNTs also provides additional through-thickness capability in this case.

From the previous results, it can be concluded that when considering a structure that is subject to pull-off loading (all aircraft structures fall under this category), the use of CNTs in the manufacturing process of such stringers in specific hot spot locations (e.g., the tow-stringer web interface or the bondline location between the skin and stringer) can prevent or delay the delamination that occurs in those locations. The study will continue by considering the combined loading effect. For the results shown next, it should be noted that both the axial and pull-off loads are applied simultaneously in the model; therefore, it cannot be determined whether the initial damage occurred due to pull-off load, axial load, or a combination of both.

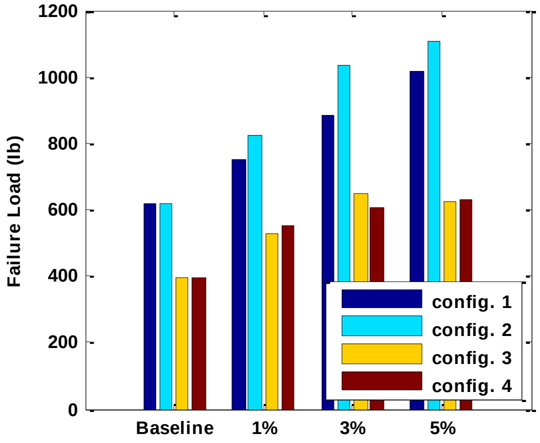

Figure 92. Pull-off failure load for flaw 1 considering different configurations

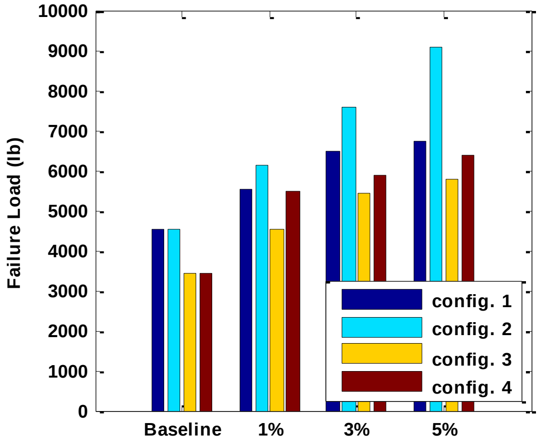

Figure 93. Pull-off failure load for flaw 2 considering different configurations

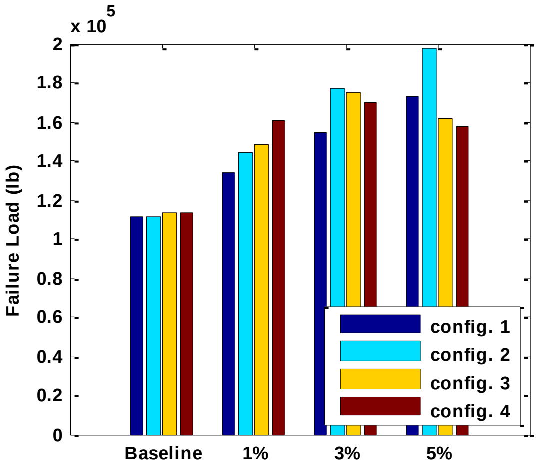

Figure 94. Pull-off failure load for flaw 3 considering different configurations

Figure 95−Figure 97 show results for a combined axial/pull-off load as applied to the structure for the same weight fractions, flaw types, and tow materials shown previously. In these figures, only the axial load at which initial failure occurred is reported. Figure 95 represents results for a type 1 flaw. The dominant trend observed is that the axial failure load increased with CNT weight fraction. Also, the axial failure load for the adhesive tow is always larger than that of the fabric tow for all cases. However, there is no substantial gain in failure load if the CNTs are used in the adhesive only or in both the adhesive and composite. Therefore, only using CNTs in the adhesive would reduce cost and manufacturing complexity while sustaining an almost similar failure load. Figure 96 represents the axial failure load of the structure that incorporates a type 2 flaw under combined axial/pull-off load. The general trend to be observed for both types of tow material is that failure load increases with the CNT weight fraction. It is also clear from the figure that for all values of CNT weight fractions, the failure loads for the adhesive tow are larger than those for the fabric tow. The failure loads for cases where

CNT is present are larger for the adhesive and composite configuration, except when the CNT is 5% by weight. Figure 97 shows the axial failure load of a structure that incorporates a type 3 flaw under axial/pull-off loading. For both types of tow materials, it can be observed that the failure load increases with CNT weight fraction. It is also obvious from the figure that for all values of CNT weight fractions, the axial failure load for the fabric tow is larger than that for the adhesive tow. In addition, the failure loads for cases where CNT was only in the adhesive are larger than those where CNT is used in both the adhesive and composite.

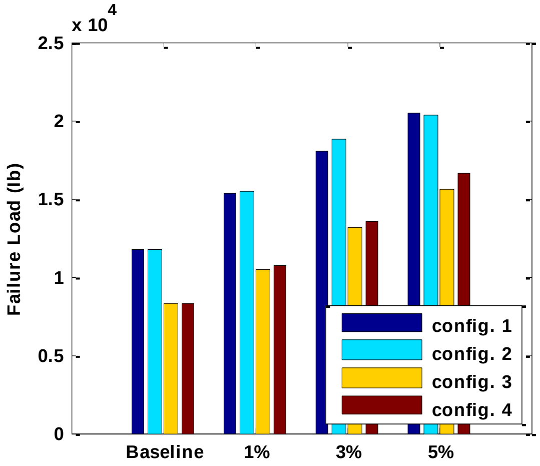

Figure 95: Axial failure load for flaw 1 by applying a combined axial/pull-off load for different configurations

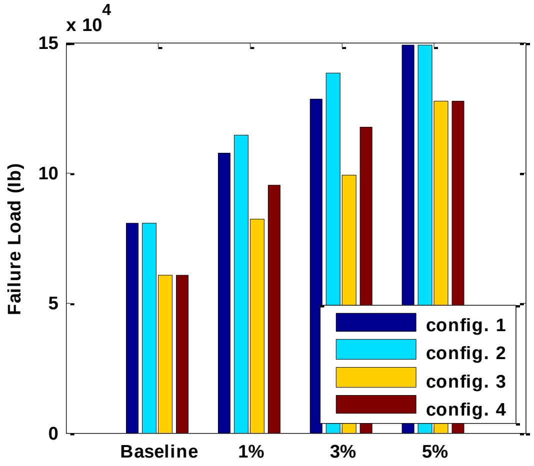

Figure 96. Axial failure load for flaw 2 by applying a combined axial/pull-off load for different configurations

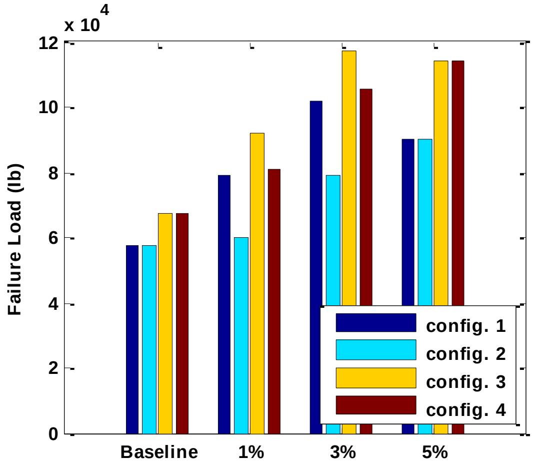

Figure 97. Axial failure load for flaw 3 by applying a combined axial/pull-off load for different configurations

Figure 98–Figure 100 show results for the same weight fractions, flaw types, tow design, and loading condition (combined axial/pull-off); however, the pull-off loads at which initial damaged occurred are also reported. Figure 98 shows the pull-off failure load from a combined axial/pull-off type load when considering a type 1 flaw. The

dominating trend is that the failure load increases with the CNT weight fraction, and the failure load is higher for the adhesive tow for all weight fractions less than 5% where the loads are higher for the fabric tow. In addition, there is no substantial gain in pull-off failure load if the CNT are in the adhesive only, or both the adhesive and composite. Therefore, only using CNTs in the adhesive would reduce cost and manufacturing complexity while sustaining an almost similar failure load. Figure 97 shows the initial pull-off failure loads for the same specimens; however, the flaws are type 2. It can be seen from the figure that the failure load is always higher for the adhesive tow for all cases. A dominant trend in which failure load increases with CNT weight fraction can also be observed, while the gap between the failure load for both the availability of CNT in the adhesive only and in both the adhesive and composite is reduced, while the CNT volume fraction increases. Figure 100 shows the results for a type 3 flaw. The fabric tow is capable of rendering a higher initial pull-off failure load than the adhesive one for all CNT weight fractions. It should be noted from the previous results that the axial failure load is much higher than the failure that occurred due to pull-off; therefore it can be concluded that such stringer designs are more tolerable to axial loading than pull-off. Moreover, combined loading consideration is an important part in the analysis and design process of such structures since, as observed from the results, the failure loads could be under- or overestimated, thereby providing a structure that might be less conservative or overly designed, respectively.

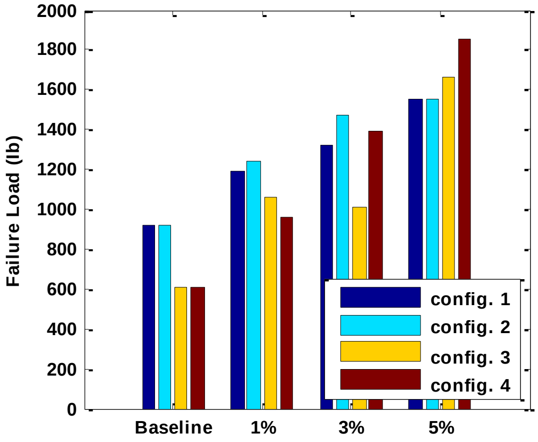

Figure 98. Pull-off failure load for flaw 1 by applying a combined axial/pull-off load for different configurations

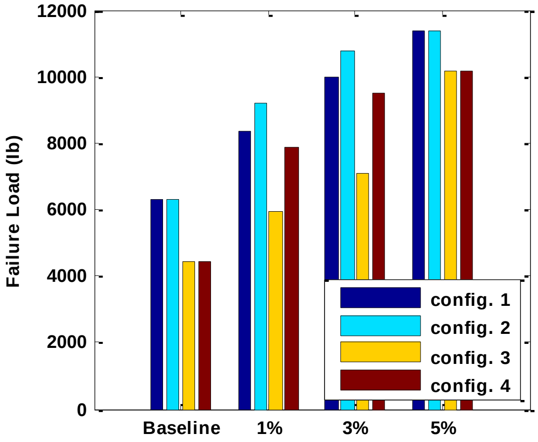

Figure 99. Pull-off failure load for flaw 2 by applying a combined axial/pull-off load for different configurations

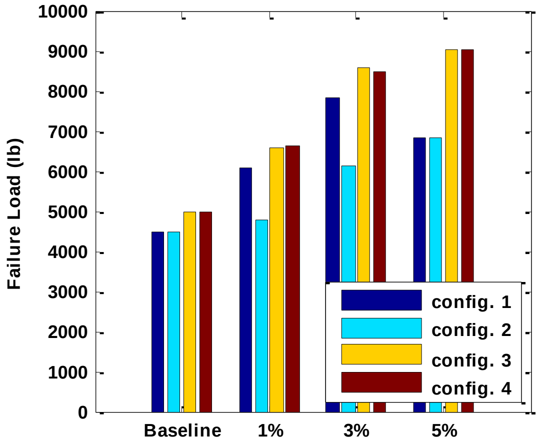

Figure 100. Pull-off failure load for flaw 3 by applying a combined axial/pull-off load for different configurations

4.6. Analysis Results – Hat Section Stringer

Figure 101–Figure 103 show the initial failure loads when applying a pure pull-off load for the three different flaw types. Figure 101 represents the pull-off failure load of the structure with a type 1 flaw. The general trend observed for both types of tow materials (fabric and adhesive) was an increase in failure load with greater CNT weight fraction due to the added through-thickness capability. It is also noticeable from the figure that for all values of CNT weight fractions, the failure load for the adhesive tow is considerably larger than that for the fabric tow. In addition, when examining the adhesive and fabric tow results, the failure load is higher for the case when both the tow material and composite contain CNTs. Flaw type 1 was noted to be mode I dominant, which relies on the angle opening of the radius where the pull-off load tends to open that radius, creating high energy release rates. Therefore the use of CNTs was shown to give additional though-thickness capability, thus preventing or delaying such an event from

occurring. Figure 102 represents the pull-off failure load of the structure that incorporates a type 2 flaw. In this case, the failure load increases with greater CNT weight percentages for both types of tow materials (fabric and adhesive). It can also be observed that the failure load for the adhesive tow is significantly larger than that for the fabric tow. By considering only the adhesive tow results, the failure load is higher for the case when only the adhesive tow contains CNTs; therefore, there is no additional benefit from using CNTs in the composite. On the other hand, when considering the fabric tow configuration, the failure load is higher for the case when both the tow material and composite contain CNTs. A type 2 flaw is also found to be mode I dominant under pull-off loading, and the use of CNTs provides additional though-thickness capability and prevents or delays such an event from occurring. Figure 103 represents the pull-off failure load of the structure that incorporates a flaw of type 3. As in the previous two cases, the failure load increases with greater CNT weight percentages; however, for the fabric tow, the failure load increases up until 5% CNT by weight, at which point it drops slightly. When examining the adhesive tow results, the failure load is higher for the case when both the adhesive and composite contain CNTs, and the same statement applies to the fabric tow. The type 3 flaw is found to have a mode mix of both I and II under pull-off loading, and the use of CNTs also provides additional though-thickness capability in this case. From the previous results, it can be concluded that when considering a structure that suffers from pull-off loading (all aircraft structures fall under this category) the use of CNTs in the manufacturing process of stringers in specific hot spot locations, such as the tow-stringer web interface or the bondline location between the skin and stringer, the delamination that occurs in those locations can be prevented or delayed. The study will continue by considering the combined loading effect. For the results shown next, it should be noted that both the axial and pull-off loading are simultaneously applied in the model. For this reason, it is not distinguished which loading was dominant in the failure; rather, both factors are considered as contributors.

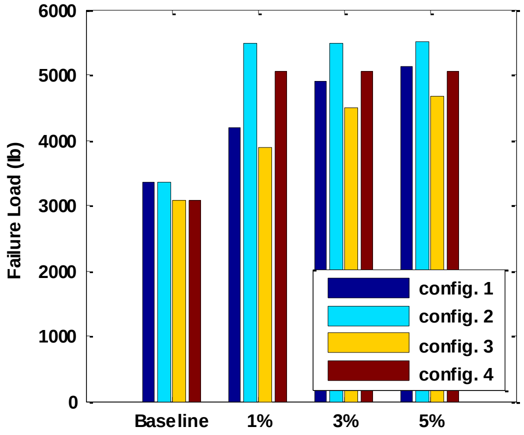

Figure 101. Pull-off failure load for flaw 1 considering different configurations

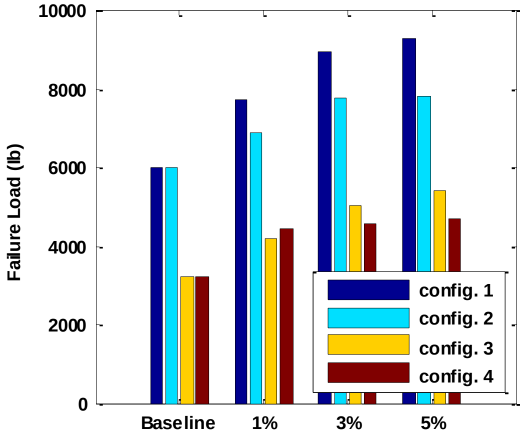

Figure 102. Pull-off failure load for flaw 2 considering different configurations

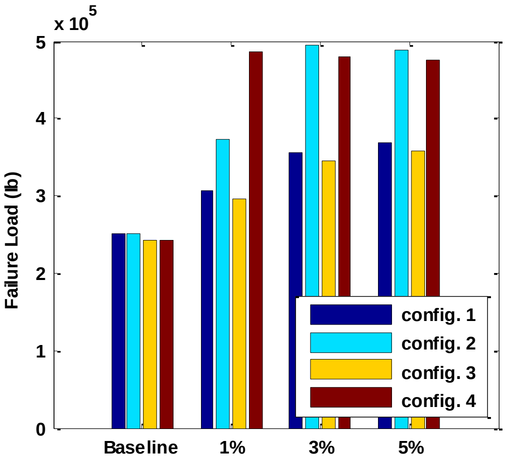

Figure 103. Pull-off failure load for flaw 3 considering different configurations

Figure 104–Figure 106 show the results for the same weight fractions, flaw types, and tow design as shown previously; however, combined axial/pull-off was applied to the structures, and only the axial load at which initial failure occurred was reported. Figure 104 represents results for a type 1 flaw. The dominant trend is that the axial failure load increased with CNT weight fraction. Also, the axial failure load for the fabric tow is always larger than that of the adhesive tow for all cases. There is, however, substantial gain in failure load if the CNTs were used in both the adhesive and composite. Figure 105 represents the axial failure load of the structure that incorporates a type 2 flaw under a combined axial/pull-off load. It can be observed for both types of tow materials (fabric and adhesive) that as the CNT weight fraction increases, so does the failure load. It is also clear from the figure that for all values of CNT weight fractions, the failure load for the adhesive tow is larger than that for the fabric tow. Moreover, the failure load is higher when CNTs are only used in the adhesive. This may be attributed to the location of the flaw and its interaction with the surrounding structure under the applied axial load. Figure

106 represents the axial failure load of the structure that incorporates a type 3 flaw under an axial/pull-off load. For both types of tow (fabric and adhesive), it can be observed that as the CNT weight fraction increases, so does the failure load. It is also obvious from the figure that for all values of CNT weight fractions, the axial failure load for the fabric tow is larger than that for the adhesive tow. In addition, the failure load for cases where CNT being present in the adhesive and composite laminates is larger than when it is only included in the adhesive. Note that a substantial increase in failure load is obtained for CNT weights of 3% and above for the design that incorporates the use of fabric tows and CNTs used in the adhesive and composite laminates.

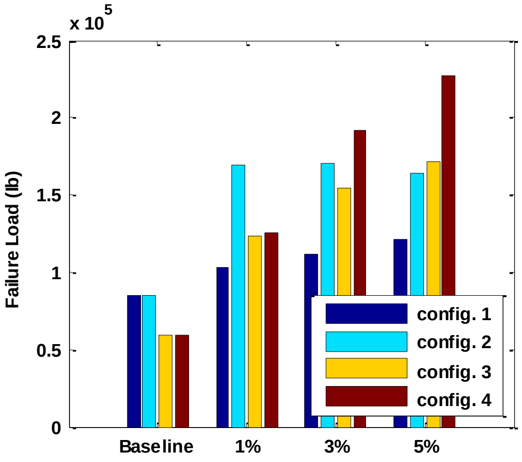

Figure 104. Axial failure load for flaw 1 by applying a combined axial/pull-off load for different configurations

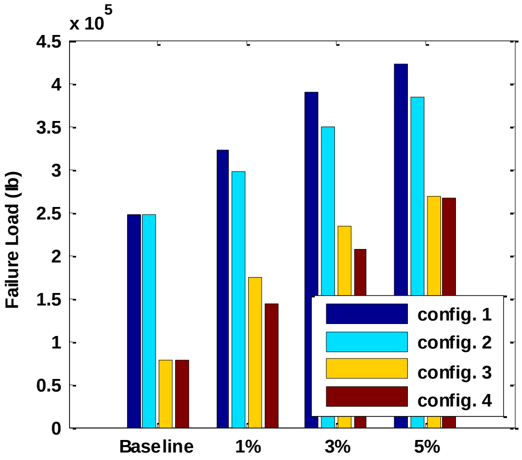

Figure 105. Axial failure load for flaw 2 by applying a combined axial/pull-off load for different configurations

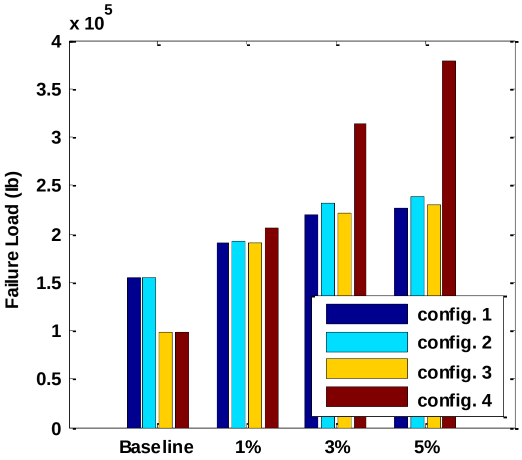

Figure 106. Axial failure load for flaw 3 by applying a combined axial/pull-off load for different configurations

In addition to the same weight fractions, flaw types, tow design, and loading condition (combined axial/pull-off), Figure 107–Figure 109 also depict the initial damaged that occurred due to the pull-off loading. Figure 107 shows the pull-off failure load from a combined axial/pull-off type loading. The dominant trend is that the failure load increases with CNT weight fraction, and the failure load is higher for the fabric tow for all weight fractions. In addition, there is substantial gain in pull-off failure load if CNTs are used in the adhesive and composite laminates. Figure 108 shows the initial pull-off failure loads for the same specimens with type 2 flaws. It can be seen from the figure that the failure load is always higher for the adhesive tow. A dominant trend of failure load increase with greater CNT weight fraction can also be observed, while the gap between the failure load for both the availability of CNT in the adhesive only and in both the adhesive and composite is relatively low. Therefore, only using CNTs in the adhesive would reduce cost and manufacturing complexity while sustaining a similar failure load. Figure 109 shows the pull-off failure load of a structure with a type 3 flaw under axial/pull-off load. For both types of tow (fabric and adhesive), it can be observed that as the CNT weight fraction increases, so does the failure load. It is also clear from the figure that the pull-off failure load varies with configuration. A substantial increase in failure load is obtained by having a CNT weight of at least 1% for the design that incorporates the use of fabric tows and CNTs used in the adhesive and composite laminates (configuration 4). It should be noted from the previous results that the axial failure load is much higher than the failure that occurs by pull-off. Moreover, combined loading consideration is an important part in the analysis and design process of such structures since the failure loads could be under- or overestimated, providing a structure that might be less conservative or overly designed, respectively.

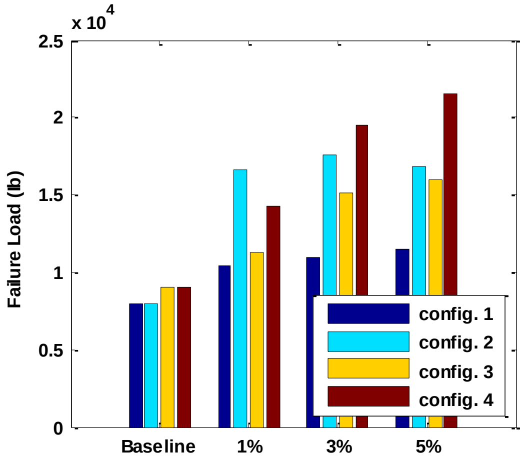

Figure 107. Pull-off failure load for flaw 1 by applying a combined axial/pull-off load for different configurations

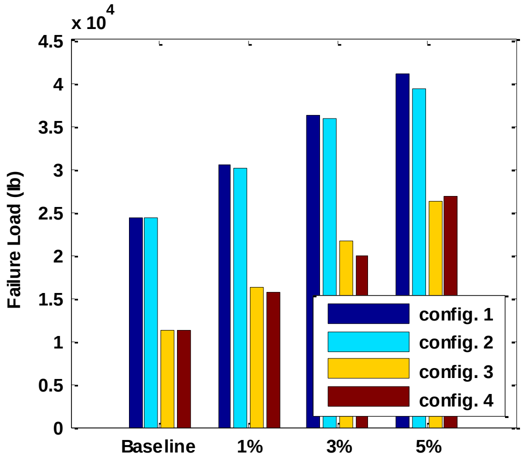

Figure 108. Pull-off failure load for flaw 2 by applying a combined axial/pull-off load for different configurations

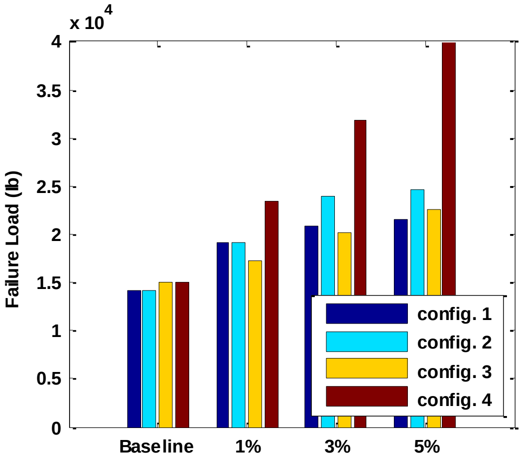

Figure 109. Pull-off failure load for flaw 3 by applying a combined axial/pull-off load for different configurations

By comparing the performance of the T section stringer to the Hat stringer, it is noted that both showed improvements when CNTs were used in the design, and the failure load increased, providing a more tolerant design. The Hat stringers tend to sustain higher loads than T section stringers, which is an interesting observation when considering alternatives for design purposes.

4.7. Influence of Non-Perfect CNT/Matrix Interface on the Failure Load

The effect of a non-perfect interface between the CNTs and epoxy on the failure load will be addressed next. As discussed in Chapter 2, the effective properties are computed assuming a non-perfect interface, and the properties vary depending on the stiffness of the interface layer. Table 9 shows the failure load for the different flaw types when the CNT content is 5% by weight. As noted, the interface stiffness has a clear influence on the failure load and depends on the flaw type. For type 1 flaws, it appears to have a smaller influence compared to type 2 and type 3 flaws, but that is due to the fact that type 1 flaws typically sustain a much lower failure load. For both type 1 and type 2 flaws, the value of the failure load decreases with lower stiffness whereas it increases for type 3 flaws.

Table 9. Different configurations considered in the analysis

Flaw Type	Failure Load, lbs (5% wt. CNT Perfect Bond)	Failure Load, lbs (5% wt. CNT 0.3 GPa interface Bond)	Percentage Difference
1	704	634	9%
2	5834	4273	26%
3	182836	206209	-12%

In an effort to understand the reason behind the different effects that the interface layer has on the failure load, several free body cuts are taken around the tow filler, which is considered the most critical spot in the structure, as shown in Figure 110.

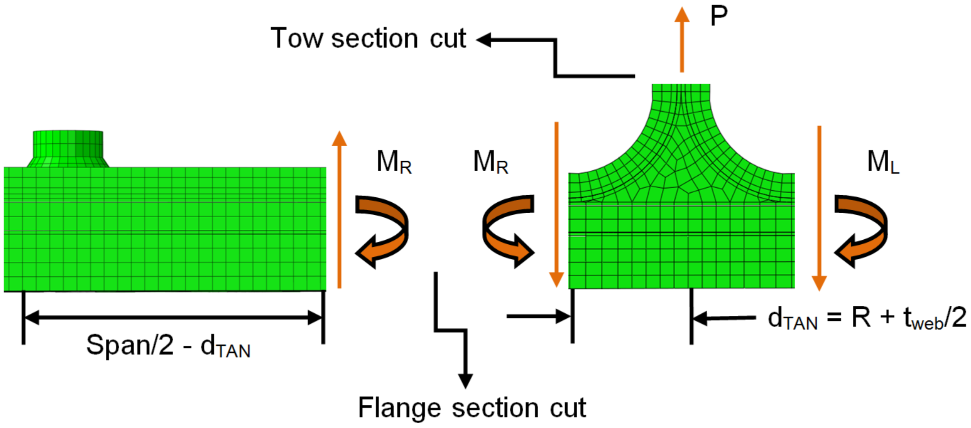

Figure 110. Section cuts to extract running loads around the tow filler

Figure 111 and Figure 112 show the running load and chordwise moment around the tow filler along the stringer span-wise direction for the case where the structure has a type 1 flaw with perfect bonding and non-perfect bonding, respectively. As shown, the value of the peak running load is higher for cases where non-perfect bonding exists, which describes why a lower initial failure load value was observed. On the other hand, the running moment does not differ between the two idealizations. Note that the "side bend moment" is the difference between both chordwise moments.

Figure 113 and Figure 114 show the running load and chordwise moment around the tow filler for type 2 flaws with perfect and non-perfect bonding, respectively. In this case, the value of the running load for the non-perfect interface is also higher and the location of the peak pull-off shifts compared to the perfect bonding case. Conversely, the running moments remain the same for both interface bonding types. This higher running load and the load redistribution that occurs explain the lower initial failure load value for the non-perfect bonding case.

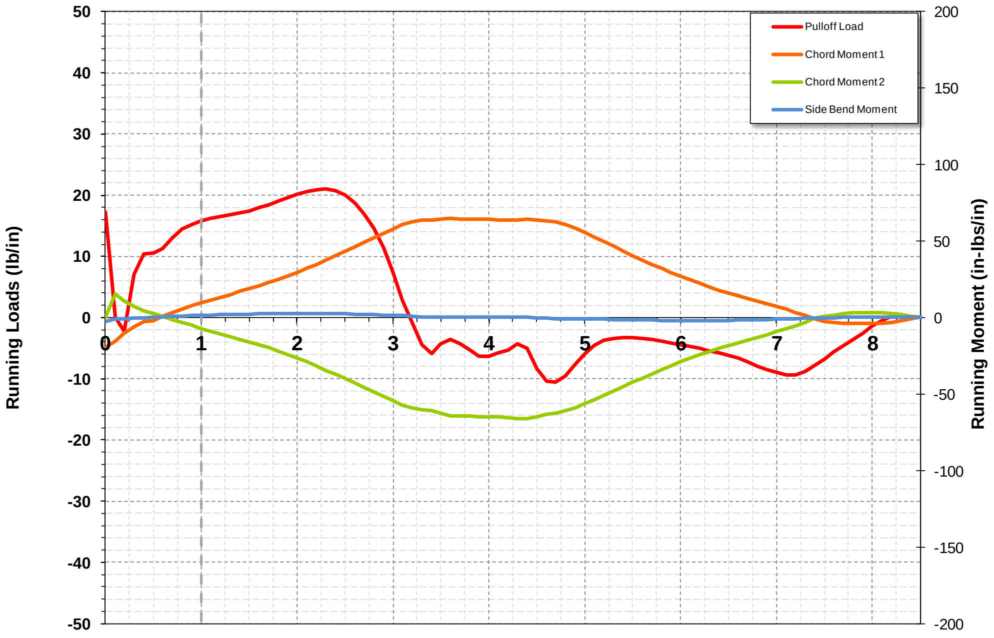

Figure 111. Running load and running moment for a structure with type 1 flaw and perfect interface

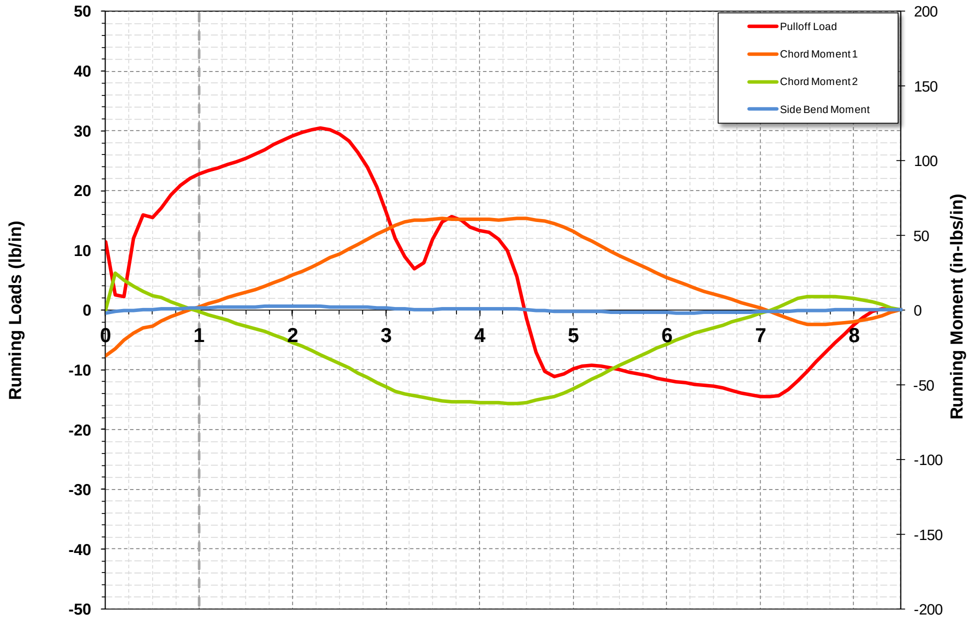

Figure 112. Running load and running moment for a structure with type 1 flaw and non-perfect interface

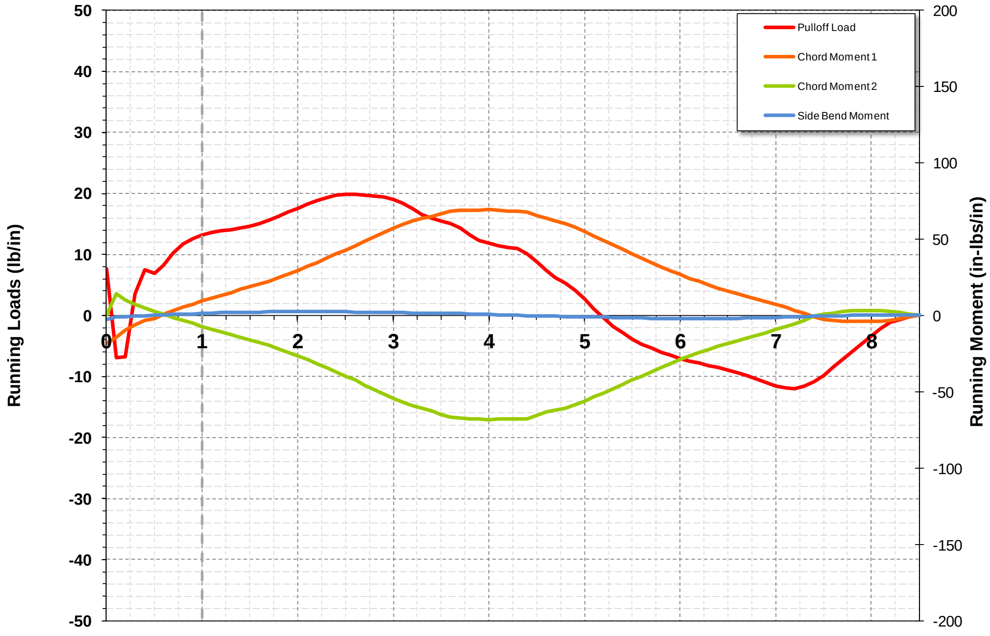

Figure 113. Running load and running moment for a structure with type 2 flaw and perfect interface

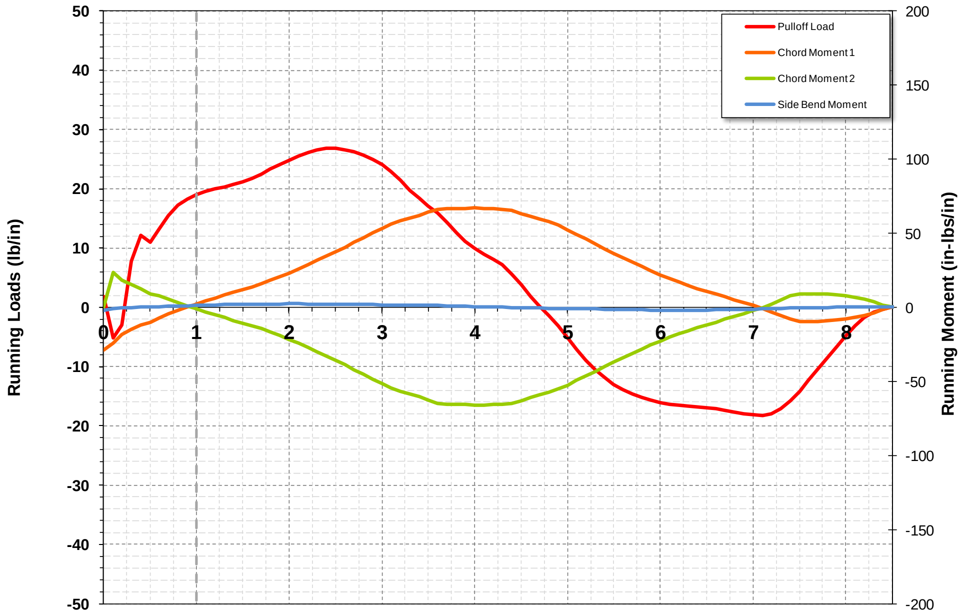

Figure 114. Running load and running moment for a structure with type 2 flaw and non-perfect interface

For type 3 flaws (skin-stringer bondline), the free body around the tow filler may not be relevant to understand the failure load, so another measure is considered. Free body loads and moments are extracted at the bondline interface. The specific load and moment components of interest are the pull-off load (in the global z direction in Figure 115) and the bending moment about the chordwise direction (in the global y direction in Figure 115). As shown in Figure 115, both the load and moment component can be used to understand the influence of the CNT/matrix interface of the failure load. As observed, the pull-off load and the chordwise moment are higher for perfect interface bonding. This is caused by the load redistribution occurring along the joint due to the difference in the structural stiffness. This in turn explains the lower initial failure load value for the perfect bonding case as shown in Table 9.

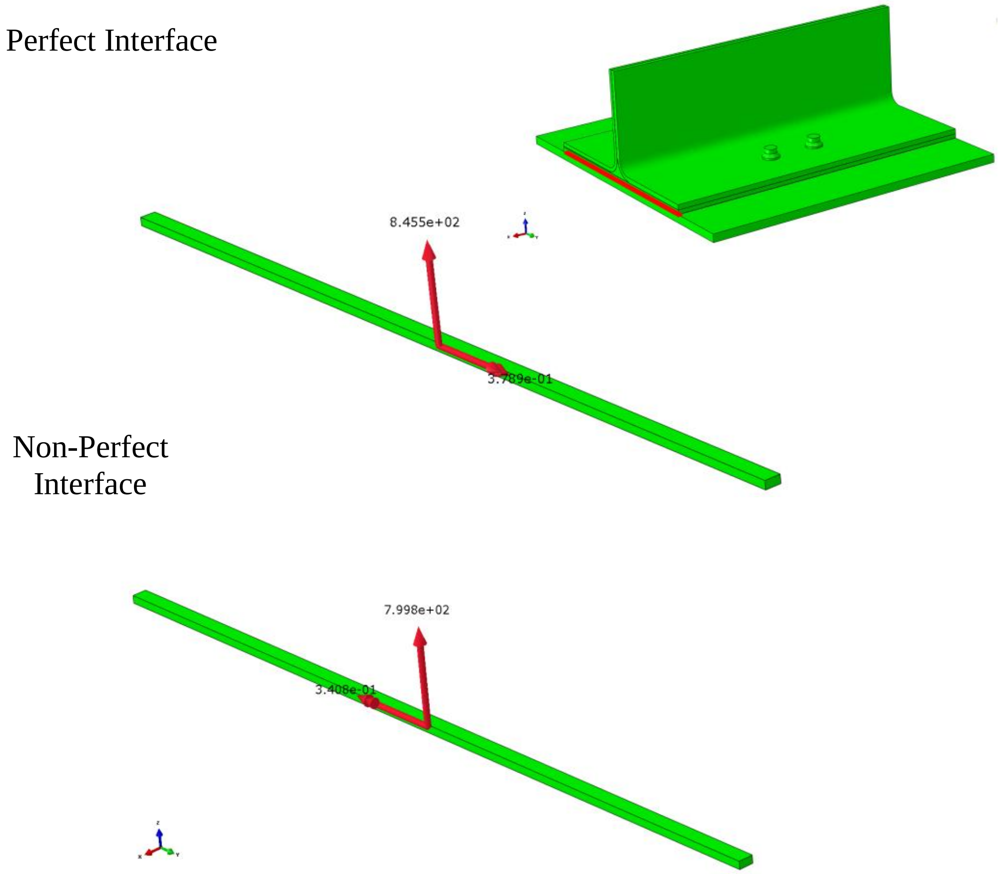

Figure 115. Free body loads and moments along the bondline interface for type 3 flaw

Chapter Summary

This chapter focused on the benefits of using nanocomposites in structural level components that are typically used in aerospace applications. Two examples of such structures were typical T and Hat section stringers. The multiscale approach discussed in Chapter 2 was used to determine the effective properties of the nanocomposite at different length scales when used in the detailed FEMs. Models were constructed to assess the use of nanocomposites at the structural level and to improve some of the weak spots in such structures. The VCCT was adopted to determine the initial damage of the structure, defined as the initial load drop in the load displacement curve. Different configurations, flaw types, and loading conditions were considered in this study. It was shown by comparing the initial failure loads that using CNTs in the manufacturing process of such stringers may improve the overall performance by up to 30%. It was also concluded that when considering a structure that undergoes pull-off loading, the delamination that typically occurs around the tow filler and skin stringer bondlines can be delayed by incorporating CNTs in those hot spot locations, thus providing a more robust structural design. Such a solution would help eliminate the usual fixes that are currently utilized in industry, such as adding local metallic fittings that are not desirable due to the added weight and manufacturing process complexity. Finally, the influence of non-perfect bonding between the CNT/matrix interface on the failure load was investigated. It was concluded that the bonding has a variable effect depending on the stiffness value at that interface and the flaw type considered.

CHAPTER 5

EXPERIMENTS

In this chapter the experiments conducted in support of this research will be discussed and the results will be shown. Initially a designed experiment is conducted to test specimens of T-section skin/stringer, replicating those used in composite panels as stiffeners. Two types of designs are considered: one that uses pure epoxy to fill the tow region and another that uses nanocomposite with 5 wt. % CNTs. The loading condition considered is pull-off loading. After obtaining the test results a multiscale simulation based on the analysis discussed in the previous chapters is used to help better understand the behaviour of composite structures that incorporate the use of nanocomposites and for additional validation purposes.

Several T-section composite stringers bonded to composite skins were manufactured and tested to verify the hypothesis that using CNTs during the manufacturing of composite structures can enhance their performance. The control factor in our experiment, as shown in Table 10, is the CNT weight percentage used in the epoxy matrix.

Table 10. Control factor and the corresponding low and high level

Control Factors	**Low Level (Coded Value: -1)**	**High Level (Coded Value: +1)**
CNT by weight (A)	0%	5%

5.1. Manufacturing

This section details the manufacturing of the test specimens. The epoxy resin used in the experiments was Epon 863 and the hardener was EPI-CURE 3290, shown in Figure 116. Two types of stiffeners were manufactured: one that used pure epoxy to fill the tow region of the stringer and another that had MWCNTs mixed into the epoxy. The key issue in nanocomposite fabrication is the need to disperse the MWCNTs uniformly in the epoxy. In this work a solvent assistance method was applied to disperse the MWCNTs in the epoxy. Acetone was used as the solvent. The experimental procedure was conducted as follows. First, the required amount of MWCNTs was weighed and dispersed in acetone (ratio of 1 mil acetone to every 20 mg nanotubes). The mixture was stirred at 500 rpm for 15 min as shown in Figure 117. Then, the mixture was sonicated using high-amplitude ultrasonication for 15 minutes in an ice bath.

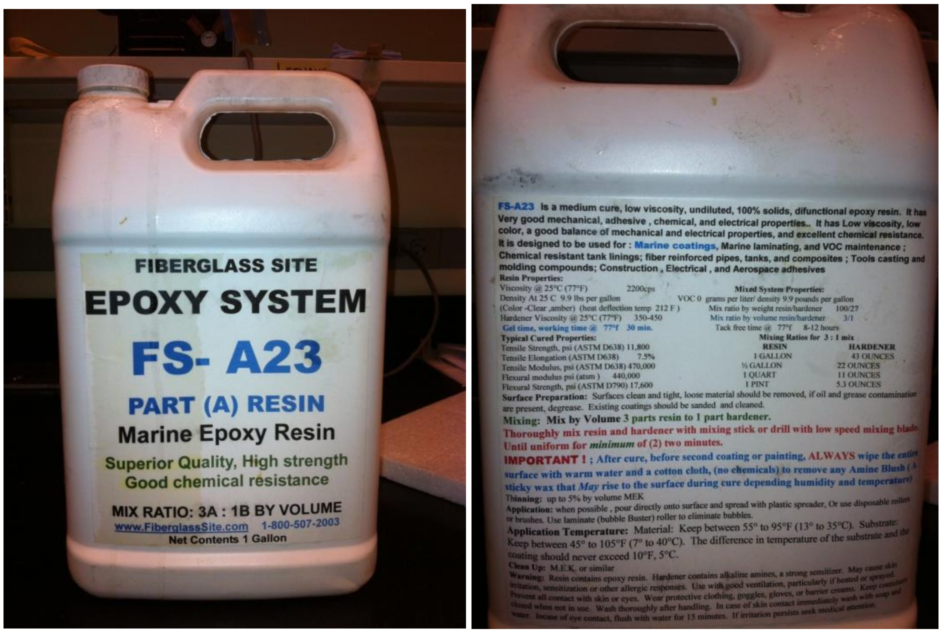

FS-A23 Is a medium cure, low viscosity, undiluted, 100% solids, difunctional epoxy resin. It has Very good mechanical, adhesive , chemical, and electrical properties.. It has Low viscosity, low color, a good balance of mechanical and electrical properties, and excellent chemical resistance. It is designed to be used for : **Marine coatings**, Marine laminating, and VOC maintenance ; Chemical resistant tank linings; fiber reinforced pipes, tanks, and composites ; Tools casting and molding compounds; Construction , Electrical , and Aerospace adhesives

Resin Properties:
Viscosity @ 25°C (77°F) 2200cps
Density At 25 C 9.9 lbs per gallon
(Color -Clear ,amber) (heat deflection temp 212 F)
Hardener Viscosity @ 25°C (77°F) 350-450
Gel time, working time @ 77°f 30 min.

Mixed System Properties:
VOC 0 grams per liter/ density 9.9 pounds per gallon
Mix ratio by weight resin/hardener 100/27
Mix ratio by volume resin/hardener 3/1
Tack free time @ 77°f 8-12 hours

Typical Cured Properties:
Tensile Strength, psi (ASTM D638) 11,800
Tensile Elongation (ASTM D638) 7.5%
Tensile Modulus, psi (ASTM D638) 470,000
Flexural modulus psi (atsm) 440,000
Flexural Strength, psi (ASTM D790) 17,600

Mixing Ratios for 3 : 1 mix

RESIN	HARDENER
1 GALLON	43 OUNCES
½ GALLON	22 OUNCES
1 QUART	11 OUNCES
1 PINT	5.3 OUNCES

Surface Preparation: Surfaces clean and tight, loose material should be removed, if oil and grease contaminatio are present, degrease. Existing coatings should be sanded and cleaned.

Mixing: Mix by Volume 3 parts resin to 1 part hardener.
Thoroughly mix resin and hardener with mixing stick or drill with low speed mixing blade Until uniform for *minimum* of (2) two minutes.

IMPORTANT ! ; After cure, before second coating or painting, ALWAYS wipe the entire surface with warm water and a cotton cloth, (no chemicals) to remove any Amine Blush (A sticky wax that *May* rise to the surface during cure depending humidity and temperature)

Thinning: up to 5% by volume MEK
Application: when possible , pour directly onto surface and spread with plastic spreader, Or use disposable rollers or brushes. Use laminate (bubble Buster) roller to eliminate bubbles.
Application Temperature: Material: Keep between 55° to 95°F (13° to 35°C). Substrate: Keep between 45° to 105°F (7° to 40°C). The difference in temperature of the substrate and the coating should never exceed 10°F, 5°C.
Clean Up: M.E.K. or similar
Warning: Resin contains epoxy resin. Hardener contains alkaline amines, a strong sensitizer. May cause skin irritation, sensitization or other allergic responses. Use with good ventilation, particularly if heated or sprayed. Prevent all contact with skin or eyes. Wear protective clothing, goggles, gloves, or barrier creams. Keep contai closed when not in use. Wash thoroughly after handling. In case of skin contact immediately wash with soap and water. Incase of eye contact, flush with water for 15 minutes. If irritation persists seek medical attention.

Figure 116. Epoxy resin system used to manufacture the specimens

Figure 117. Mixture stirring and mixture sonication

The epoxy resin was added to the solution, stirred at 500 rpm for 15 min, and sonicated for another 15 minutes. The acetone was removed by heating in an oil bath with a magnet stirring the mixture for 4 hours at 50 °C. To eliminate any remaining trace amount of acetone the mixture was placed in a vacuum oven for 12 hours at room temperature. The hardener was added and mixed using a magnet bar. The manufacturing process of the nanocomposite is summarized in Figure 118.

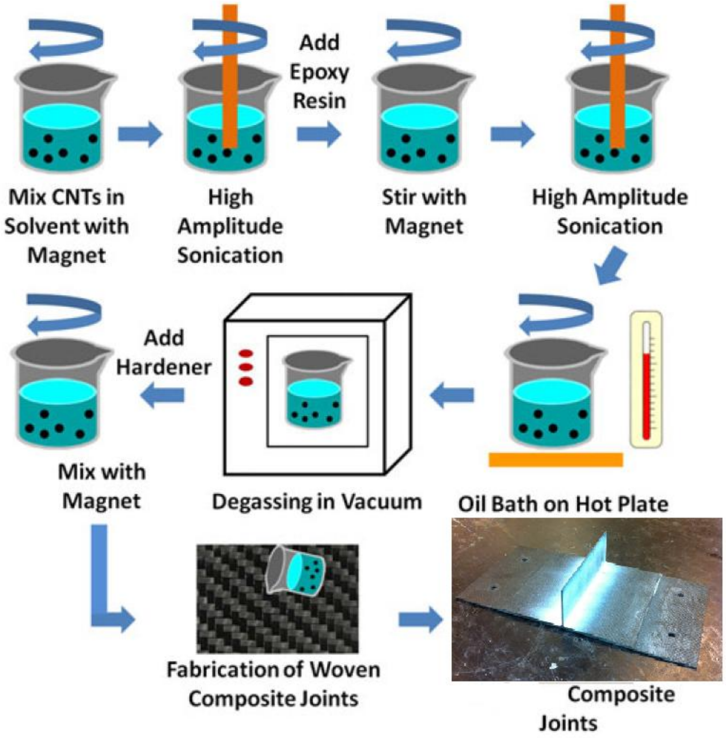

Figure 118. Solvent assistance methods for MWCNT dispersion and sample fabrication

To validate the dispersion of MWCNTs field emission scanning electron microscopy (FESEM) was used to scan the surface of the cured adhesive layer of the sample. The material used to manufacture the T-section stringers and skins was plain weave carbon fiber fabrics, as shown in Figure 119.

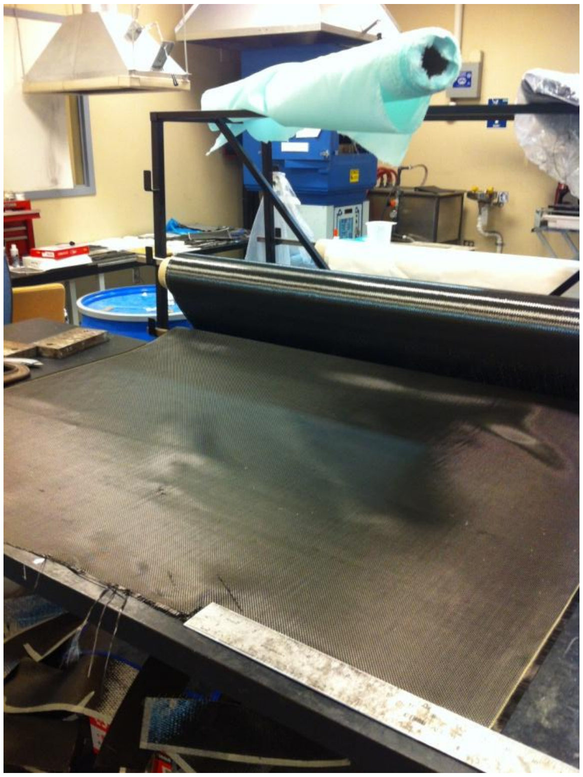

Figure 119. Plain weave carbon fiber fabrics used in manufacturing the specimens

A thermoset epoxy resin was used as the matrix material, similar to that used in the nanocomposite. The fabrication procedure for the composite joints is described as follows. (i) Three plies of plain weave carbon fiber fabric were stacked together using the wet lay-up method to form three pieces of $(0)_3$ CFRP laminate, used for the two web flanges and base flange as shown in Figure 120. Pure epoxy or the nanocomposite mix was used to fill the tow region depending on the design. The composite laminates were then cured using a compression/lamination press system (Terahedron Inc.) at the same temperature, pressure and cure time. (ii) The skin was made of six plies of plain weave carbon fiber fabric stacked together using the wet lay-up method to form a $(0)_6$ CFRP laminate, and was also cured using a compression/lamination press system (Terahedron

Inc.). iii) The stringer was then bonded onto the skin using pure epoxy resin and was cured to form the final specimen. (iv) The composite joints were cut into the designed geometries using a wet saw. Figure 121 show the steps followed to manufacture the skin section and Figure 122 show the steps followed to obtain the final skin/stringer sections prior to final trimming. The final manufactured specimen, including the fixture that was designed to hold the specimens during testing, is shown in Figure 123.

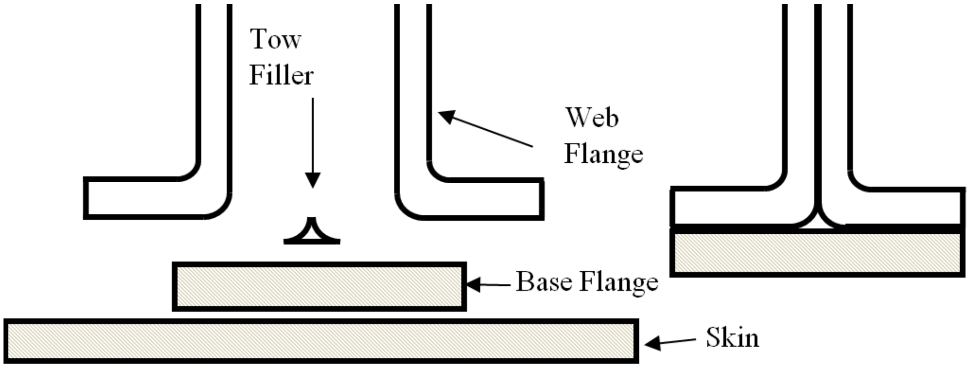

Figure 120. Schematic of the skin stringer composite joint

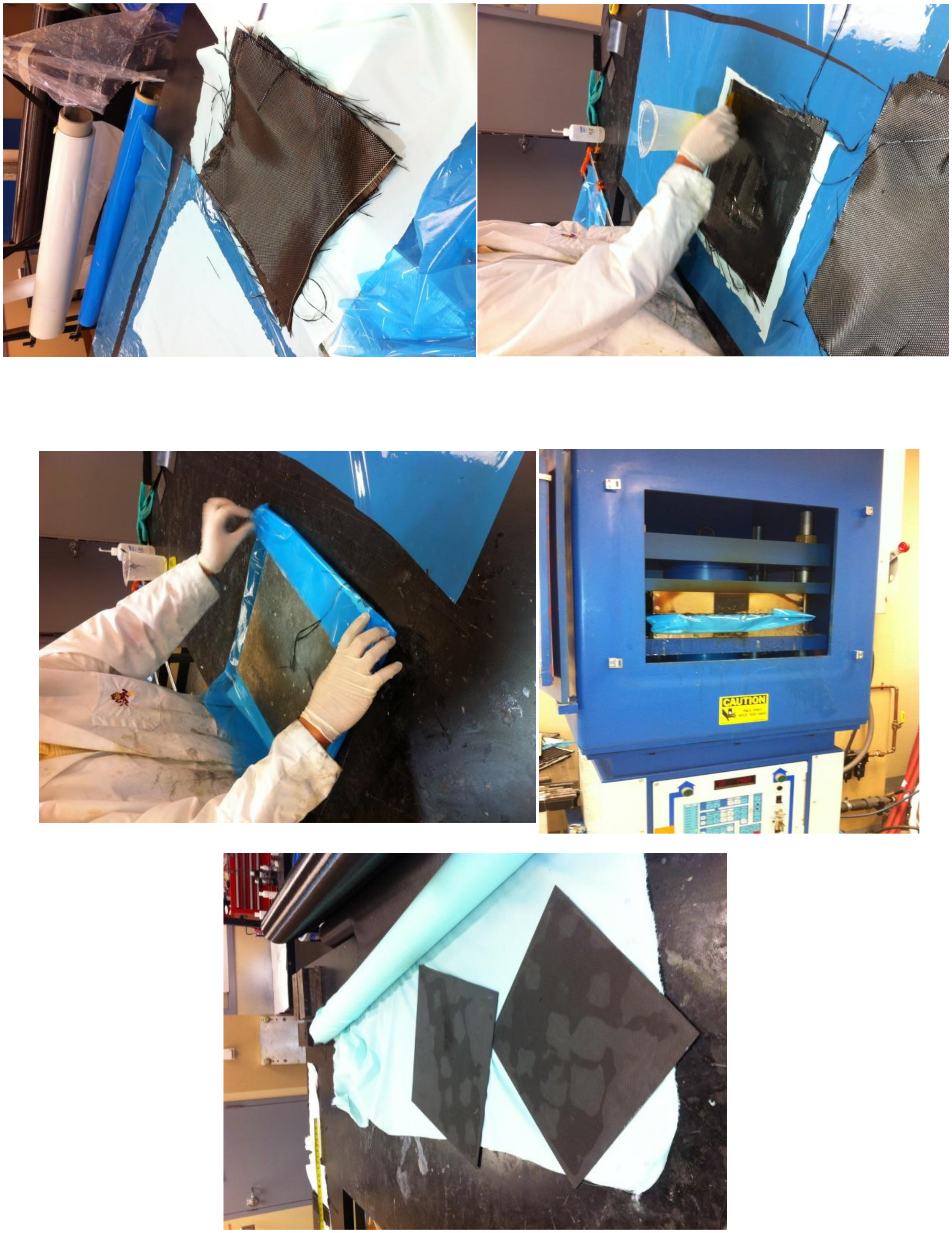

Figure 121. Steps followed to manufacture the skin section

Figure 122. Steps followed to manufacture the skin/stringer section

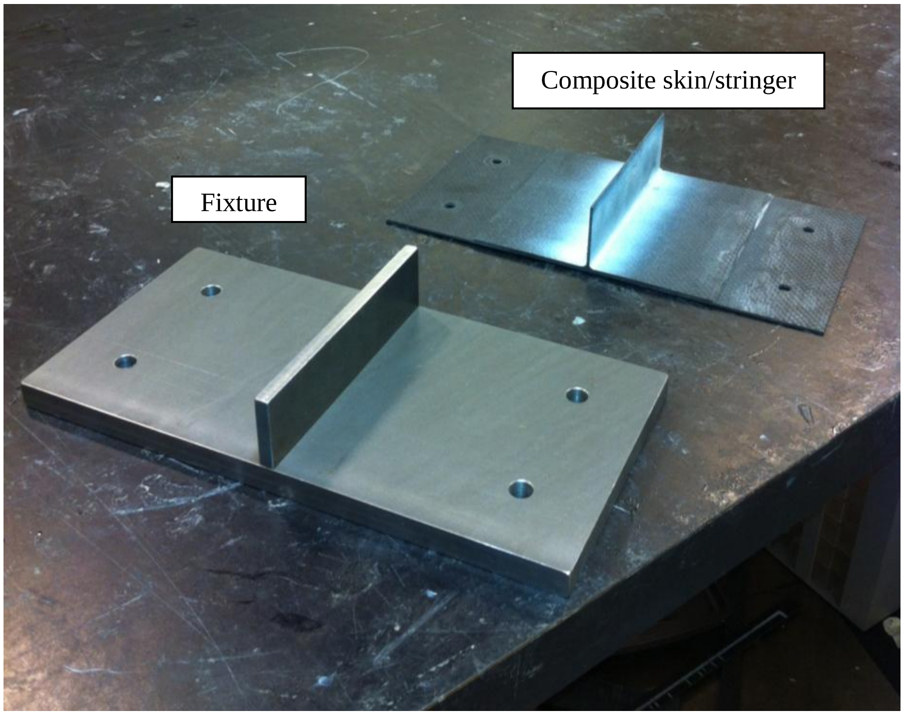

Figure 123. Manufactured specimen and fixture

5.2. Experimental Setup

The tests were conducted under quasi-static pull-off loading condition using an MTS test frame. A typical experimental setup is shown in Figure 124 and Figure 125. A three dimensional digital image correlation system (DIC, model ARAMIS 2M) was used to measure the strain field of the specimen area during the tests in real time.

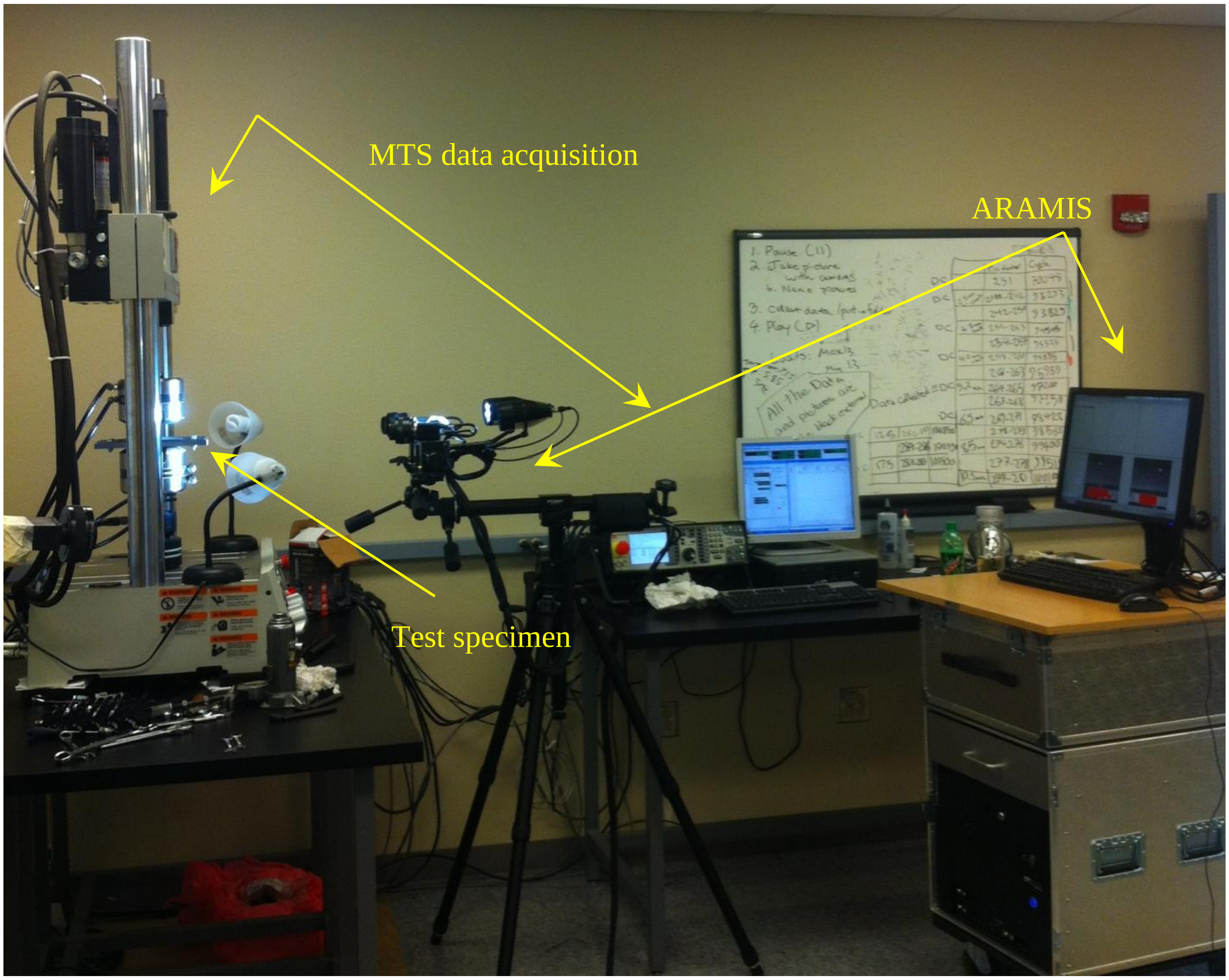

Figure 124. Experimental setup

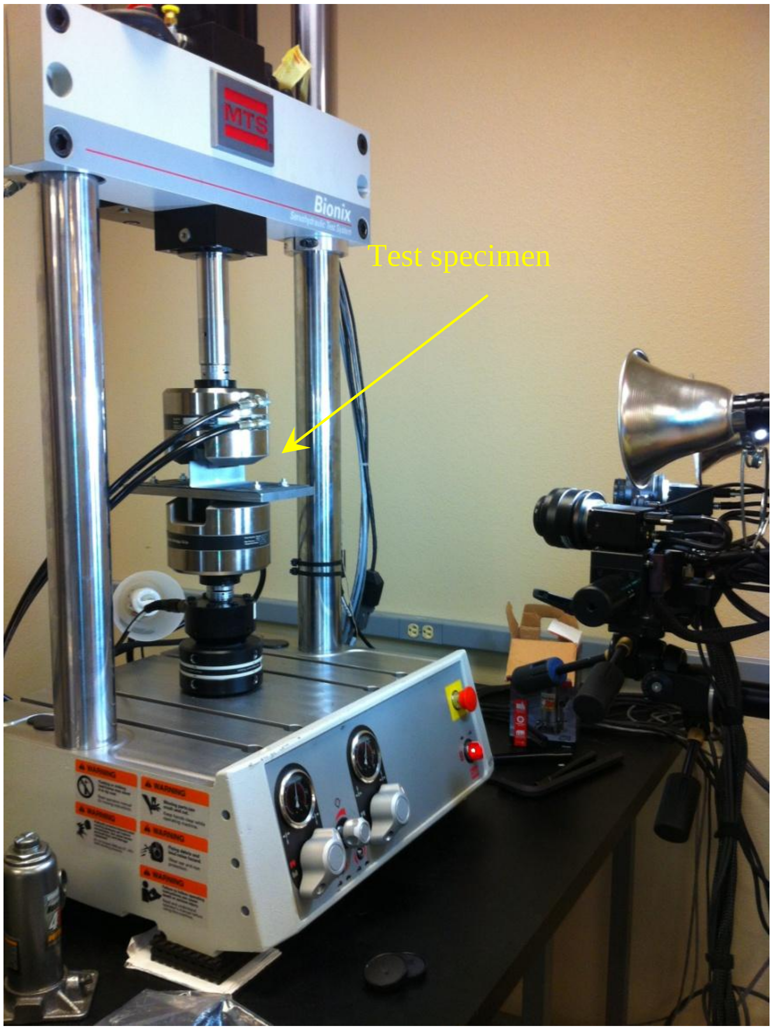

Figure 125. Test specimen

Cameras were used to take pictures of the joint area. These pictures were taken at constant intervals. The strain field can be calculated by tracking the pattern changes using DIC method. The experiment setup was designed to validate the hypothesis that using CNTs in critical hot spot locations in the structure will improve the initial damage. A total of 14 tests were conducted, of which seven had pure epoxy in the tow region and seven used nanocomposites to fill the tow region. Figure 126 shows the specimen while under loading. The tests were conducted under displacement control of 0.5 in/min. It is observed that the matrix cracking in the tow region is the primary damage introduced to the composite joints during the test. Typical FESEM images of the tow region, taken after final failure, are shown in Figure 127. The images show the damage around the critical region. In Figure 127a the crack surface of the tow area is displayed. The debonding between carbon fibers and matrix is shown in Figure 127b.

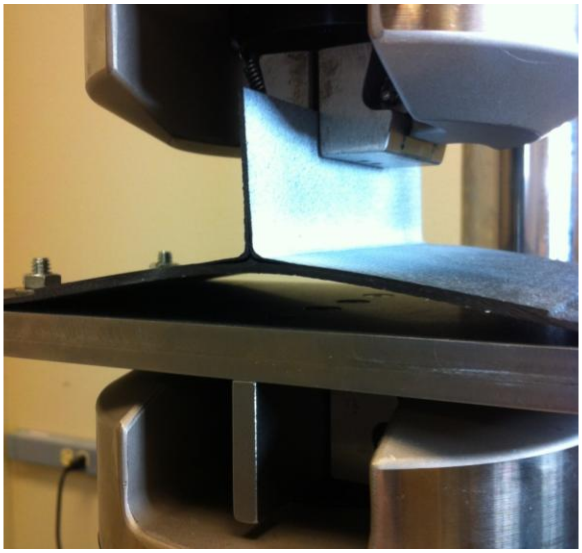

Figure 126. T-section stringer tow failure

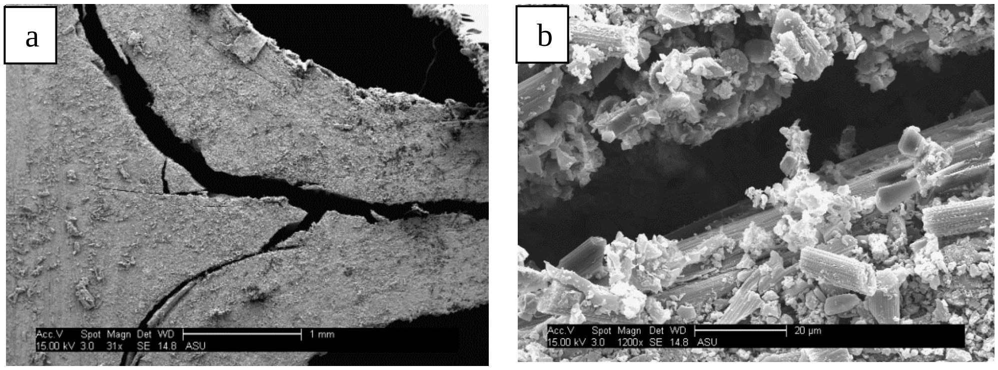

Figure 127. SEM images of failed specimen (a) crack surface of the tow area and (b) debonding between carbon fibers and matrix

5.3. Experimental Results and Discussion

The impact that nanocomposites had on the performance of composite joints is investigated using in-house fabricated composite joints. The samples were subject to pull-off and introduced matrix cracks in the tow filler area, which ultimately led to specimen failure. It is noted that the failure is considered to be mode I dominant, which relies on the angle opening of the radius where the pull-off load tends to open the radius creating high-energy release rates. Figure 128 shows the load displacement curves for the specimens that used pure epoxy in the tow region, while Figure 129 shows the load displacement curves for the specimens that had 5 wt. % nanotubes in the epoxy used to fill the tow region. The trend from the results provides evidence that the addition of CNTs did improve the initial damage load. Therefore, it was demonstrated that the use of CNTs would give additional through thickness capability, thus delaying such event from occurring. The initial failure loads obtained from the experiments are summarized in Table 11.

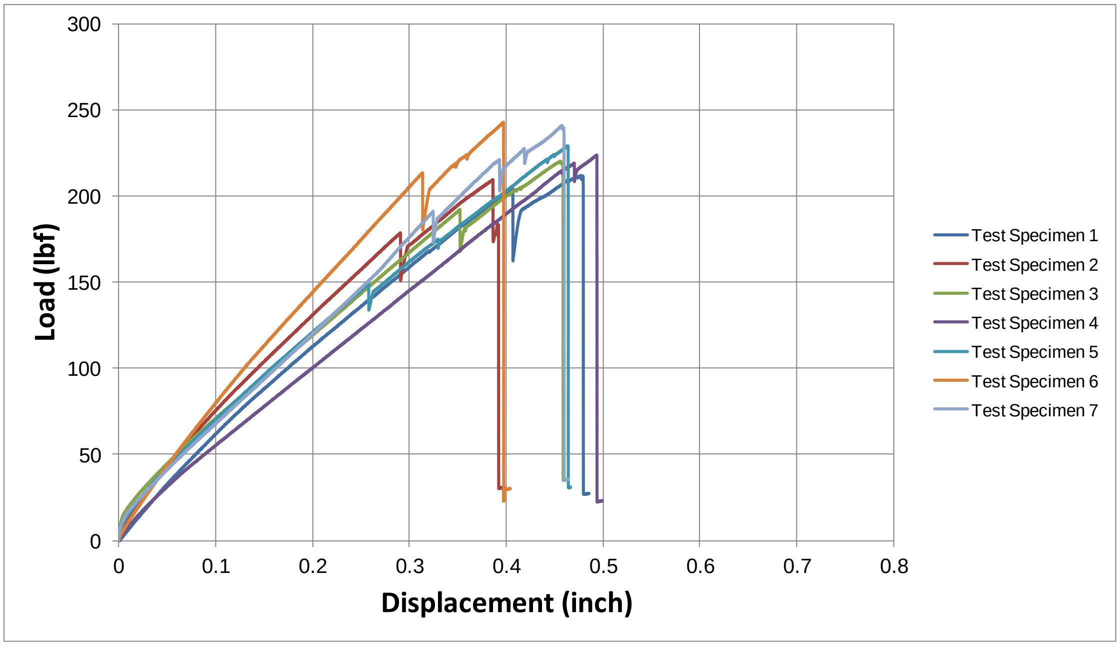

Figure 128. Load displacement curve for specimens with no CNT

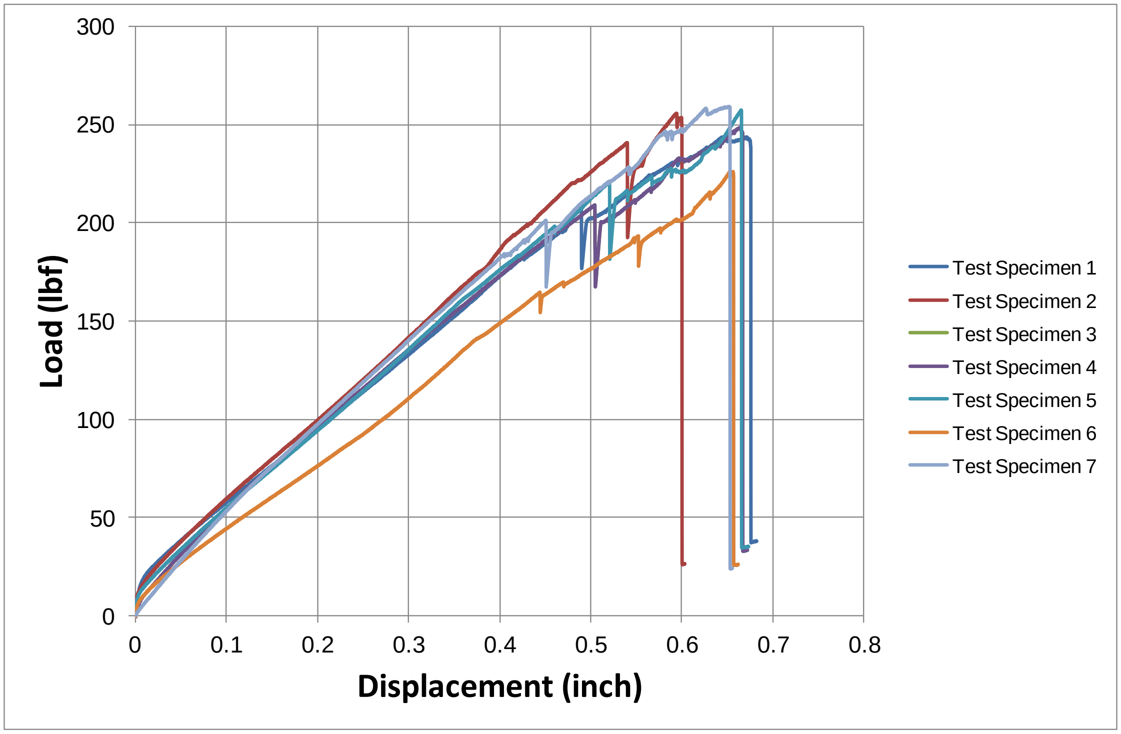

Figure 129. Load displacement curve for specimens with 5 wt. % CNT

Table 11. Initial damage obtained from the experiments

CNT Weight %	Observation (Initial Failure Load, lbf)							
	1	2	3	4	5	6	7	Average
0	172.75	171.7	190.38	214.7	149.5	213.2	188.89	185.8
5	222.8	210.8	238.9	218.85	216.8	189.4	201.26	214.1

Figure 130 and Figure 131 show the probability plot and the box plot for the test data respectively. As observed the data follow the normality assumption and the standard deviation of the data fall within a 95% confidence level, which provides confidence in the results and conclusions made in this study.

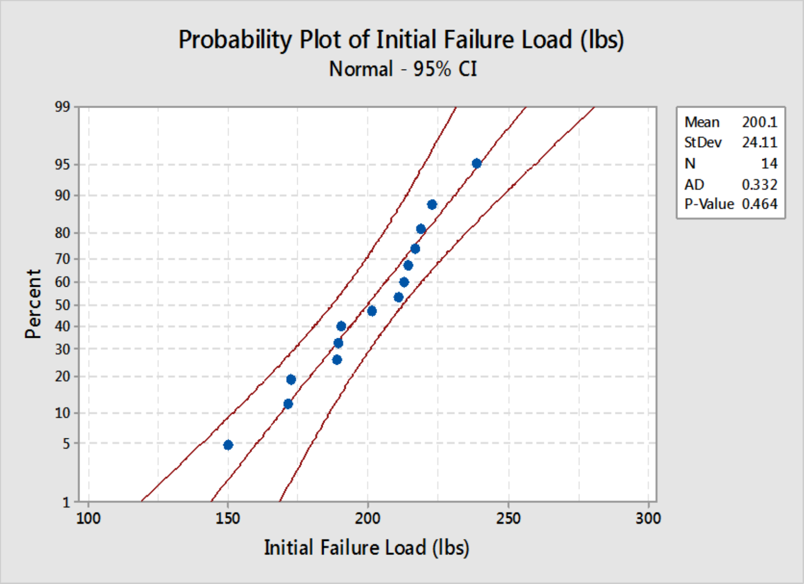

Figure 130. Probability plot for the test data

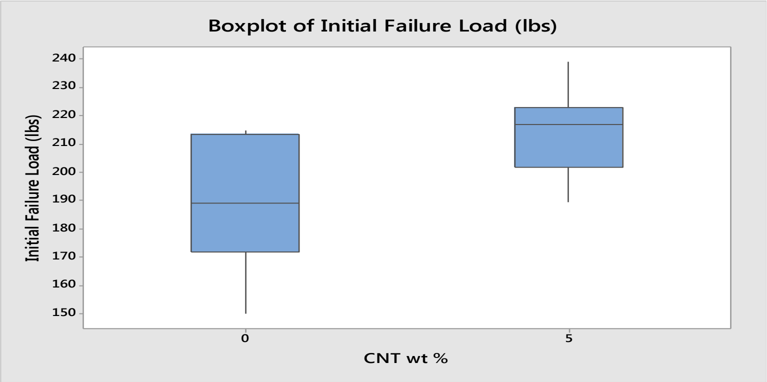

Figure 131. Box plot of the initial failure load

5.4. Numerical Results and Discussion

After investigating the applicability of using CNTs in composite joints experimentally and observing the improvements it provided on the initial failure load, the focus now lies on obtaining an analysis approach to investigate the performance by means of virtual testing using multiscale analysis and detailed FEMs. The multiscale approach used in the previous chapters will be used to correlate to the available experimental results. The effective properties obtained from the analytical solution are used as input into the models used to perform the failure analysis. The composite stringers will be modeled using pure epoxy and nanocomposites in order to quantity its effect on the structural performance and to correlate to the available experimental data.

In order to correlate to the available experimental data a model is created that replicates the specimens tested as shown in Figure 132. A flaw is inserted in the model based on the damage profile observed in test, typically found to initiate around the tow filler. It should be noted that pure epoxy resin toughness values are used in the analysis to predict the initial damage for the baseline model; however, for the other specimens epoxy with 5 wt. % CNTs is used.

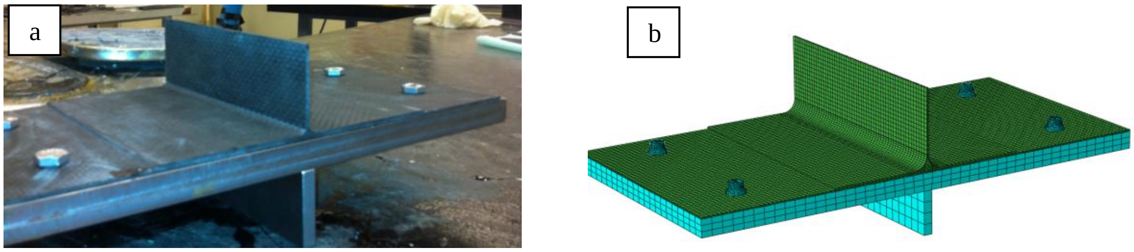

Figure 132. (a) Manufactured test specimen and fixture and (b) FEM with clamped BC

It is noted that the failure for this type of loading and structure is usually dominated by mode I, and the contribution of mode II and III is not as significant. Figure 133 and Figure 134 show the correlation between the FEM results and the experimental data for both the baseline model and the model that includes embedded CNTs respectively. The load displacement curve is only shown to the point of the initial damage state. It can be seen that the results from the FEMs fall within the range of the experimental results. The differences in behavior between the tests and the models can be attributed to the differences in stiffness, loading, and other anomalies that usually exist in a test environment, which are not typically captured by the models. The correlation obtained, however, is considered to be satisfactory. The results, from analysis and experiments, show improved failure characteristics when CNTs are embedded in the polymer matrix.

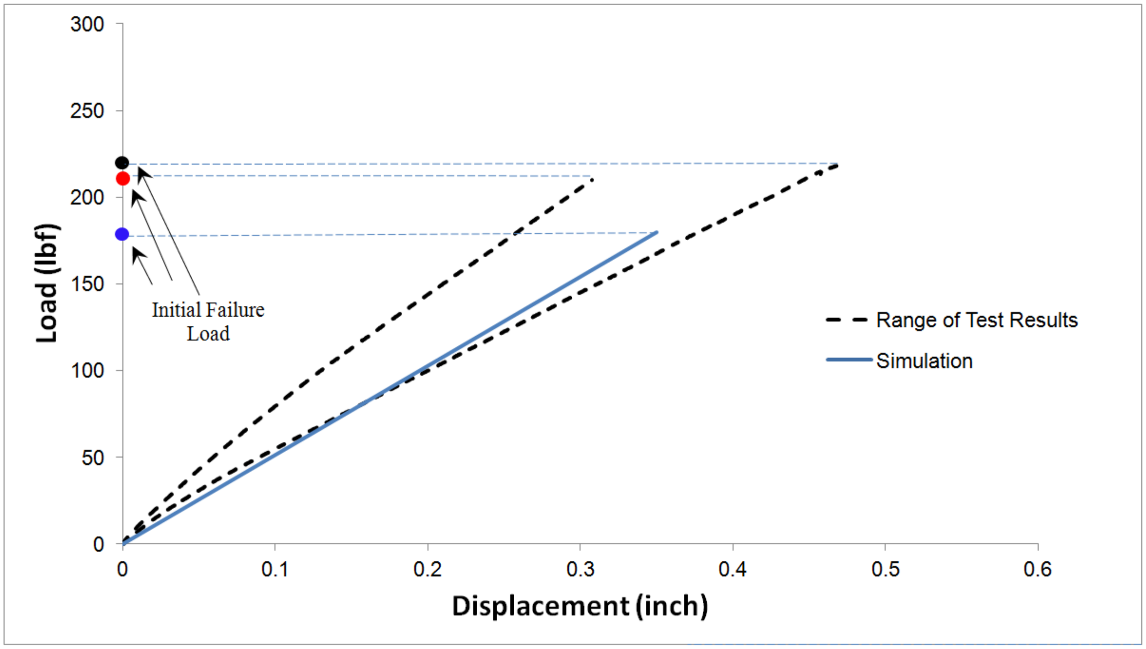

Figure 133. Comparison between test and simulation for specimen with no CNT

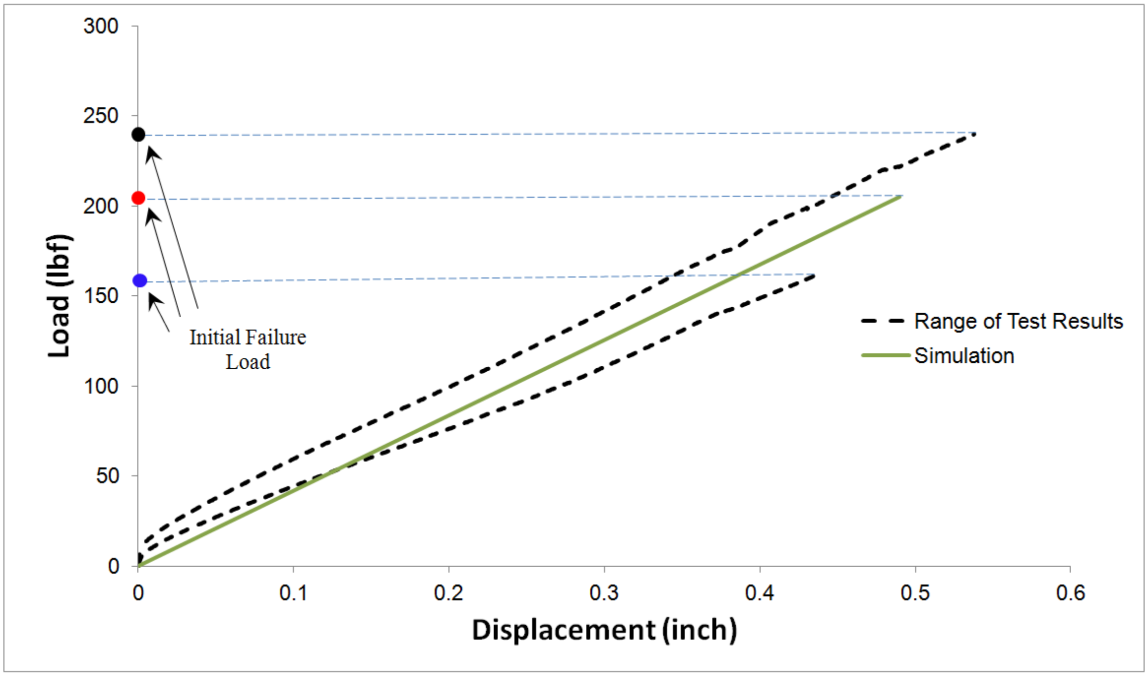

Figure 134. Comparison between test and simulation for specimen with 5 wt. % CNT

Chapter Summary

This chapter included a study that focused on an experimental procedure that was conducted to provide evidence to the hypothesis set forth that CNTs can improve the structural performance. Fourteen specimens were manufactured and tested under pull-off loading conditions. The response variable in all of the tests was the initial damage, defined as the first drop in the load displacement curve. It was shown that using CNTs in the manufacturing process of such stringers improves the overall performance when comparing the initial failure loads. It can be concluded that when considering a structure that undergoes pull-off loading, the delamination that typically occurs around the tow filler can be delayed by incorporating CNTs in local hot spot locations, thereby providing a more robust structural design. In addition, satisfactory correlation between the FEMs and test results were obtained. This provided a framework to analyze structural components that include CNTs, and further understand the performance of other designs without the need to conduct multitudes of experiments.

CHAPTER 6

THERMO-MECHANICAL ANALYSIS OF NANOCOMPSOITES

One important factor to be considered during the design phase of composite structures is the difference in the thermal properties of the parts being manufactured and assembled. Because the structure may contain hybrid metallic/composite joints, it is necessary to consider the differences in the thermal properties during the design to eliminate undesired distortions or stressing of the structure. In addition, the temperature at which the structure will operate must be taken into account to better understand the performance under different environmental conditions.

This chapter focuses on the coupled thermal-mechanical analysis and its influence on the performance of nanocomposites. A multiscale analysis is used to compute the effective thermal properties of the nanocomposite, which is similar to the method used for the mechanical properties. Those properties are then used in detailed FEMs to investigate the effect of operating temperature change on the structural behavior and failure load. In addition, progressive failure analysis will be conducted and the influence of nanocomposite on the delamination progression will be investigated.

6.1. Thermal Conductivity

The thermal conductivity behaviors of some composite materials, such as carbon fiber/polymer composites, have received wide attention from researchers over the past several decades and have been well established in recent years. The thermal conductivity properties of nanocomposites are far less known due to their novel composition, and many scientists are focusing their attention on investigating these properties using experimental, numerical, and analytical approaches. In recent years, many researchers have investigated the thermal properties of nanostructure materials. The results of this attempt consider the thermal conductivity of many nano-materials and their composites and are summarized in the following review articles published recently (Han, Z. and Fina, A. 2011), (Nejad, S.J. 2012). In this research, the effective thermal conductivities of the nanocomposites are computed by conventional micromechanical models taking into account the effect of the contact resistance on the interface between the CNT and epoxy matrix.

The effective thermal conductivity of the microscale RVE is calculated by averaging over all possible orientations of the CNTs, which are assumed to be randomly oriented in the matrix. In mathematical terms, the effective thermal conductivity is calculated as follows

$$k_{ij}^{eff} = k_{ij}^{m} + \frac{1}{4\pi}\int_0^{2\pi}\int_0^{\pi}\left[v_f\left(k_{im}^{m} - k_{im}^{f}\right)A_{mj}^{f}(\vartheta,\psi)\right]\sin(\vartheta)\,d\vartheta\,d\psi \tag{146}$$

where v_f is the total volume fraction of CNTs, ϑ and ψ define the CNT orientation, k^f is the CNT conductivity tensor, k^m is the matrix conductivity tensor, and A^f is the thermal gradient concentration tensor that accounts for the interactions of the randomly orientated CNTs in the composite. CNT thermal conductivity is determined using the generalized self-consistent composite cylinder method (Hashin, Z. 1990), which is applied to one composite cylinder assemblage at an arbitrary orientation with a local coordinate system and then expressed in the global microscale RVE coordinate system by a change of basis as follows

$$k_{ij}^{CC} = Q_{im}\tilde{k}_{mn}^{CC}Q_{jn} \tag{147}$$

where $\tilde{k}_{mn}^{CC}$ is the composite cylinder thermal conductivity expressed in the local coordinate system and Q is the rotation matrix defined with a 2-1-3 Euler angles sequence given as

$$[Q] = \begin{bmatrix} \cos(\psi)\sin(\vartheta) & \sin(\psi)\sin(\vartheta) & \cos(\vartheta) \\ -\sin(\psi) & \cos(\psi) & 0 \\ -\cos(\psi)\cos(\vartheta) & -\sin(\psi)\cos(\vartheta) & \sin(\vartheta) \end{bmatrix} \tag{148}$$

The thermal gradient concentration tensor can be calculated using the Mori-Tanaka method as follows

$$A_{ij}^{f} = Q_{im}\tilde{T}_{mn}^{MT}Q_{\ln}\left[\left(1-v_f\right)I_{jl} + \frac{v_f}{4\pi}\times\int_0^{2\pi}\int_0^{\pi}\left[Q_{lr}\tilde{T}_{rs}^{MT}Q_{js}\right]\sin(\vartheta)d\vartheta d\psi\right]^{-1} \tag{149}$$

where $\tilde{T}_{ij}^{MT}$ is given as

$$\tilde{T}_{ij}^{MT} = \left[\delta_{ij} + S_{jm}\left(k_{mn}^{m}\right)^{-1}\left(\tilde{k}_{ni}^{CC} - k_{ni}^{m}\right)\right]^{-1} \tag{150}$$

where δ_{ij} is the Kronecker delta and S_{ij} is the thermal equivalent of the Eshelby tensor. The effective axial and transverse conductivities for the total composite cylinder assemblage are obtained as

$$\tilde{k}_{11}^{CC} = \sum_{i=1}^{N}\tilde{k}_{11}^{i}\frac{\left(r_i^2 - r_{i-1}^2\right)}{r_N^2} \tag{151}$$

$$\tilde{k}_{22}^{CC} = \frac{1}{r_N^2 H_0^2}\sum_{i=1}^{N}\tilde{k}_{22}^{i}\left[\left(D_1^i\right)^2\left(r_i^2 - r_{i-1}^2\right) - \left(D_2^i\right)^2\left(\frac{1}{r_i^2} - \frac{1}{r_{i-1}^2}\right)\right] \tag{152}$$

Note that superscript *i* denotes the different phases considered in the composite cylinder assemblage. D_1^i and D_2^i are constants that can be found by solving the steady-state thermal energy equation expressed in cylindrical coordinates for spatially homogeneous, transversely isotropic materials as

$$\tilde{k}_{22}\frac{\partial^2 \tilde{T}}{\partial r^2}+\tilde{k}_{22}\left(\frac{1}{r^2}\frac{\partial^2 \tilde{T}}{\partial \theta^2}+\frac{1}{r}\frac{\partial \tilde{T}}{\partial r}\right)+\tilde{k}_{11}\frac{\partial^2 \tilde{T}}{\partial z^2}=0 \tag{153}$$

Eq. (153) has two solutions

$$\tilde{T}^i = D_1^i z + D_2^i \quad , \quad r_{i-1} \le r \le r_i \tag{154}$$

$$\tilde{T}^i = \left(D_1^i r + D_2^i \frac{1}{r}\right)\cos(\theta) \quad , \quad r_{i-1} \le r \le r_i \tag{155}$$

where $1 \le i \le N+1$, with $N+1$ being the effective material layer. The constants in Eq. (154) can be determined by applying boundary conditions corresponding to axial heat flow as follows

$$\begin{aligned} \tilde{T}^i\left(z=-\frac{L}{2}\right) &= \tilde{T}_0 \\ \tilde{T}^i\left(z=\frac{L}{2}\right) &= \tilde{T}_0+\Delta\tilde{T} \end{aligned} \tag{156}$$

The constants in Eq. (155) can be determined by applying the boundary conditions corresponding to transverse heat flow and insulated internal surface shown in Eq. (157), and the continuity of temperature and heat flux conditions across an ideal interface are given in Eq. (158)

$$\begin{aligned} &\tilde{T}^N\left(r=r_N,\theta\right)=\tilde{H}_0 r_N\cos(\theta) \\ &\tilde{q}_r^1\left(r=r_0,\theta\right)=0 \end{aligned} \qquad (157)$$

$$\begin{aligned} &\tilde{T}^j\left(r=r_j,\theta\right)=\tilde{T}^{j+1}\left(r=r_j,\theta\right) \\ &\tilde{q}_r^j\left(r=r_j,\theta\right)=\tilde{q}_r^{j+1}\left(r=r_j,\theta\right) \end{aligned} \qquad (158)$$

where $\tilde{H}_0$ and $\tilde{q}$ as are the heat intensity and heat flux, respectively. One of the important variables that must be considered in the determination of CNT thermal conductivities is an interface thermal resistance layer known as the Kapitza resistance, which is believed to be the source of the difference between the theoretical predictions of the effective medium approach and the measured data (Abdalla, M. et al. 2008). This effect was introduced into the effective medium approach through a proportional scaling of the axial and transverse CNT conductivities (Wu, F. and Cheng, H. 2005). The conductivity of the interphase layer representing the Kapitza resistance is given as follows (Wu, F. and Cheng, H. 2005).

$$\tilde{k}^{Kap}=\frac{\beta\left(D_1^{Kap}\left(r_{CNT}-r_{Kap}\right)+D_2^{Kap}\left(\frac{1}{r_{CNT}}-\frac{1}{r_{Kap}}\right)\right)}{D_1^{Kap}-\frac{1}{r_{CNT}^2}D_2^{Kap}} \qquad (159)$$

where β is the inverse of the Kapitza resistance. D_1^{Kap} and D_2^{Kap} are constants that are also determined by applying the boundary and continuity conditions in Eq. (156-158) to the composite cylinder assemblage. This results in a simplified expression of Eq. (160), which can be expresses as follows

$$\tilde{k}^{Kap} = \frac{\beta \tilde{k}^{CNT} t^{CNT} t^{Kap} \gamma_1}{\gamma_2 \left(t^{Kap}\right)^2 \beta + \gamma_3 t^{CNT} \tilde{k}^{CNT}} \tag{160}$$

where

$$\gamma_1 = \left(t^{CNT} - 2r_{CNT}\right)\left(t^{Kap} + 2r_{CNT}\right)$$
$$\gamma_2 = 2r_{CNT}^2 - 2r_{CNT} t^{CNT} + \left(t^{CNT}\right)^2$$
$$\gamma_3 = \left(2t^{CNT} - 4r_{CNT}\right)\left(t^{Kap} + r_{CNT}\right)$$

with t^{CNT} and t^{Kap} as the thickness of the CNT and Kapitza layers respectively. The thickness of the Kaptiza layer is selected to be less than 1% of the CNT thickness. The interphase thermal resistance end effect can also be accounted for in the model by including a lateral interface thermal resistance as a thin-interphase region that does not reflect the inclusion of the interface thermal resistance at the nanotube ends. By doing so, the expression for the effective axial conductivity can be attained as (Wu, F. and Cheng, H. 2005)

$$k_{11}^{eff} = \frac{k^{CNT} k^{Kap} L}{2k^{CNT} t^{Kap} + k^{Kap}\left(L - 2t^{Kap}\right)} \tag{161}$$

where L is the length of the CNT, and k^{Kap} is the value previously calculated from Eq. (160).

6.2. Thermal Expansion

Thermal expansion is another important property that must be accounted for during the design phase. Different models exist to calculate the thermal expansion of a composite from the properties of its components. The rule of mixtures can obtain a first approximation if the components have nearly equal elastic properties and if thermal stresses do not arise (Seidel, G. and Stephens, S. 2010). In this research, analytical and computational micromechanics techniques, based on the FE method and the composite cylinder method have been used to determine the effective coefficient of thermal expansion (CTE) of the nanocomposite containing aligned nanotubes. The effective thermal expansion coefficients are given as (Seidel, G. and Stephens, S. 2010)

$$\tilde{\alpha}_{11}^{eff} = \frac{1}{\tilde{E}_{11}^{eff}\,\Delta T}\cdot\left(\tilde{E}_{11}^{eff}\left\langle\tilde{\varepsilon}_{11}\right\rangle - \left\langle\tilde{\sigma}_{11}\right\rangle + 2\tilde{\nu}_{12}^{eff}\left\langle\tilde{\sigma}_{22}\right\rangle + 2\tilde{\nu}_{12}^{eff}G_{23}^{eff}\left(\left\langle\tilde{\varepsilon}_{33}\right\rangle - \left\langle\tilde{\varepsilon}_{22}\right\rangle\right)\right) \tag{162}$$

$$\tilde{\alpha}_{22}^{eff} = \frac{1}{2\tilde{E}_{11}^{eff}\kappa_{23}^{eff}\,\Delta T}\cdot\begin{pmatrix} 2\kappa_{23}^{eff}\left\langle\tilde{\sigma}_{11}\right\rangle - \left(E_{11}^{eff} + 4\left(\tilde{\nu}_{12}^{eff}\right)^2\kappa_{23}^{eff}\right)\left\langle\tilde{\sigma}_{22}\right\rangle \\ + \begin{pmatrix} E_{11}^{eff}\left(\kappa_{23}^{eff} + \tilde{G}_{23}^{eff}\right) \\ + 4\left(\tilde{\nu}_{12}^{eff}\right)^2\kappa_{23}^{eff}\tilde{G}_{23}^{eff} \end{pmatrix}\left\langle\tilde{\varepsilon}_{22}\right\rangle \\ + \left(E_{11}^{eff}\left(\kappa_{23}^{eff} - \tilde{G}_{23}^{eff}\right) - 4\left(\tilde{\nu}_{12}^{eff}\right)^2\kappa_{23}^{eff}\tilde{G}_{23}^{eff}\right)\left\langle\tilde{\varepsilon}_{33}\right\rangle \end{pmatrix} \tag{163}$$

where

$$\begin{aligned}\left\langle\tilde{\sigma}_{11}\right\rangle &= \left(2\tilde{\kappa}_{23}^{eff}\tilde{\nu}_{12}^{eff}\right)\cdot\left(\left\langle\tilde{\varepsilon}_{22}\right\rangle - \alpha_{22}^{eff}\Delta T\right) + \left(2\tilde{\kappa}_{23}^{eff}\tilde{\nu}_{12}^{eff}\right)\cdot\left(\left\langle\tilde{\varepsilon}_{33}\right\rangle - \alpha_{22}^{eff}\Delta T\right)\ldots \\ &\ldots + \left(E_{11}^{eff} + 4\left(\tilde{\nu}_{12}^{eff}\right)^2\tilde{\kappa}_{23}^{eff}\right)\cdot\left(\left\langle\tilde{\varepsilon}_{11}\right\rangle - \alpha_{11}^{eff}\Delta T\right)\end{aligned} \tag{164}$$

$$\begin{aligned}\left\langle\tilde{\sigma}_{22}\right\rangle &= \left(\tilde{\kappa}_{23}^{eff} + G_{23}^{eff}\right)\cdot\left(\left\langle\tilde{\varepsilon}_{22}\right\rangle - \alpha_{22}^{eff}\Delta T\right) + \left(\tilde{\kappa}_{23}^{eff} - G_{23}^{eff}\right)\cdot\left(\left\langle\tilde{\varepsilon}_{33}\right\rangle - \alpha_{22}^{eff}\Delta T\right)\ldots \\ &\ldots + \left(2\tilde{\kappa}_{23}^{eff}\tilde{\nu}_{12}^{eff}\right)\cdot\left(\left\langle\tilde{\varepsilon}_{11}\right\rangle - \alpha_{11}^{eff}\Delta T\right)\end{aligned} \tag{165}$$

In the equations above, <•> denotes volume averages of the stress and total strain over the composite cylinder assemblage expressed in Cartesian coordinates. The strain values that are input into Eq. (162–165) are volume averaged and are obtained from detailed RVE model of the nanocomposite. The effective properties $\tilde{\kappa}_{23}^{eff}, \tilde{G}_{23}^{eff}, \tilde{E}_{11}^{eff}, \tilde{\upsilon}_{12}^{eff}$ are determined using the composite cylinder method discussed in Chapter 2.

6.3. Effective Thermal Properties of Nanocomposites

6.3.1. Effective thermal conductivity of the nanocomposite

Figure 135 presents the effective thermal conductivity as a function of CNT volume fraction for the nanocomposite matrix without including the Kapitza effect. By incorporating the use of CNTs, the values of the axial and transverse conductivity increase compared to the baseline results. Figure 136 presents the effective thermal conductivity as a function of CNT volume fraction, but this time including the Kapitza effect. As can be observed, by incorporating the use of CNTs, the axial and transverse conductivity values increase compared to the baseline results, and the conductivity values that included the Kapitza resistance are much smaller than those without it. Hence, caution must be used when computing the effective thermal conductivity, and it is recommended to incorporate the effect of the Kapitza resistance because it aligns with results obtained from experiments (Nan, C. et al. 2004).

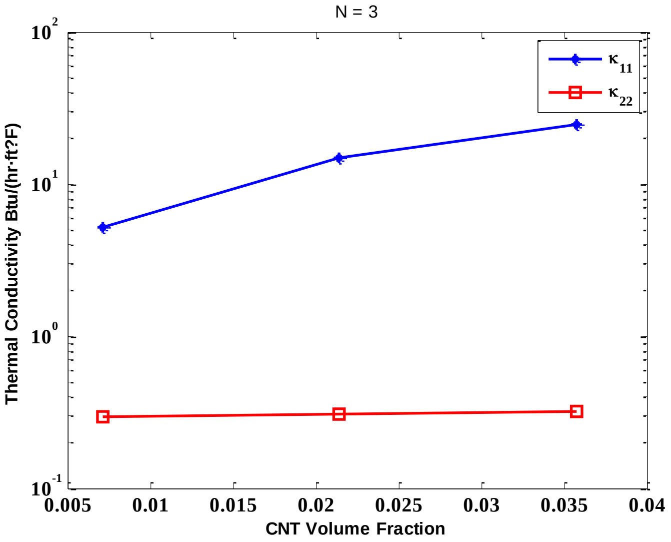

Figure 135. Effective thermal conductivity of nanocomposite as function of CNT volume fraction (No Kapitza effect)

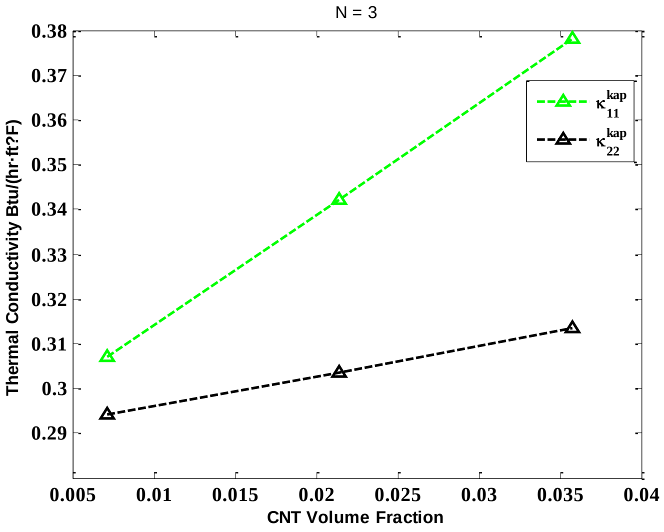

Figure 136. Effective thermal conductivity of nanocomposite as function of CNT volume fraction (Including the Kapitza effect)

6.3.2. Effective thermal expansion of nanocomposites

The computational micromechanics nanoscale RVE consists of a periodic hexagonal array of CNTs as shown in Figure 137. The boundary- and interface-matching conditions consist of stress-free internal CNT surfaces, constrained outer boundary displacements, and a continuity of displacements and tractions along interface boundaries between phases. Abaqus 6.11 is used to compute the displacement field in the RVE resulting from the application of a temperature variation (ΔT). The volume-averaged stress and total strain are then obtained from the post-processed data and are used to solve for the axial and transverse coefficients of thermal expansion using Eq. (156) and Eq. (157) in Cartesian coordinates.

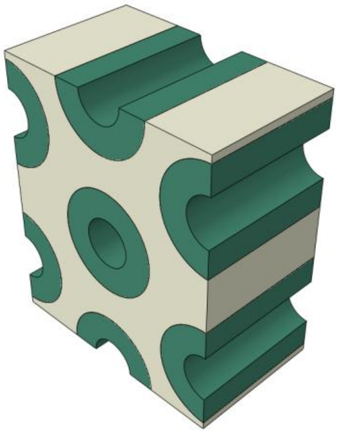

Figure 137. Detailed FEM model of the nanocomposite RVE

Figure 138 shows the axial and transverse thermal expansion coefficient for the nanocomposite. As observed, the values of the nanocomposite longitudinal and transverse effective thermal expansions are reduced compared to pure resin matrix, which will provide an enhanced overall performance of the structure, especially when it is expected to operate at higher temperatures.

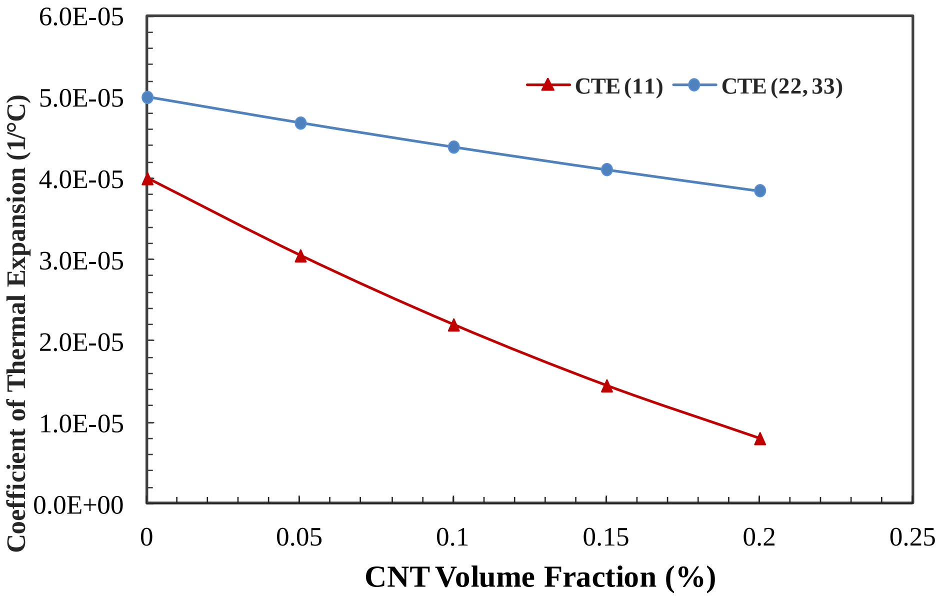

Figure 138. Effective thermal expansion of the nanocomposite as function of CNT volume fraction

Figure 139 shows the axial and transverse thermal expansions for the unidirectional nanocomposite. Both the longitudinal and transverse effective thermal expansions are reduced compared to pure resin matrix, which will provide enhanced overall performance of the structure especially when it is expected to operate at extreme thermal conditions.

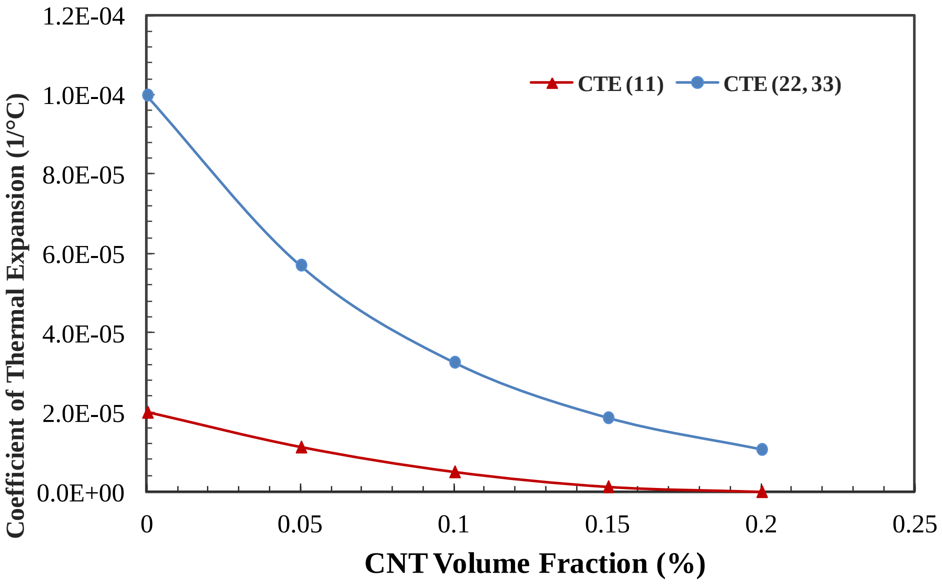

Figure 139. Effective thermal expansion of the nanocomposite as function of CNT volume fraction

6.4. Results and Discussion

The effective mechanical and thermal properties obtained are used to analyze a T section stringer using detailed FEMs. The influence of temperature variation on the structural performance is the main focus of this section. Figure 140 presents the pull-off failure load of the structure that incorporates a type 1 flaw for different CNT weight percentages and operating temperatures. It can be noted from the figure that the failure load increases with the increase in CNT weight percent in the composite. The trend holds for all the temperature conditions as shown in Chapter 2 for pure mechanical loading. The operating temperature seems to influence the failure load with the extreme cold (-40°F) and extreme hot condition (140°F) having the lowest and highest values, respectively, as observed in Figure 141. The rationale behind the failure load variation could be attributed to the additional thermal stresses induced in the tow region, creating additional opening or closing of the radius depending on the temperature, which affects the strain energy release rate at the critical location, which in turn influences the load at which failure occurs. A type 1 flaw is noted to be mode I dominant; this relies on the angle opening around the tow filler where the pull-off load tends to open that radius, creating high energy release rates. The use of CNTs is believed to provide additional through-thickness capabilities, delaying the failure from occurring.

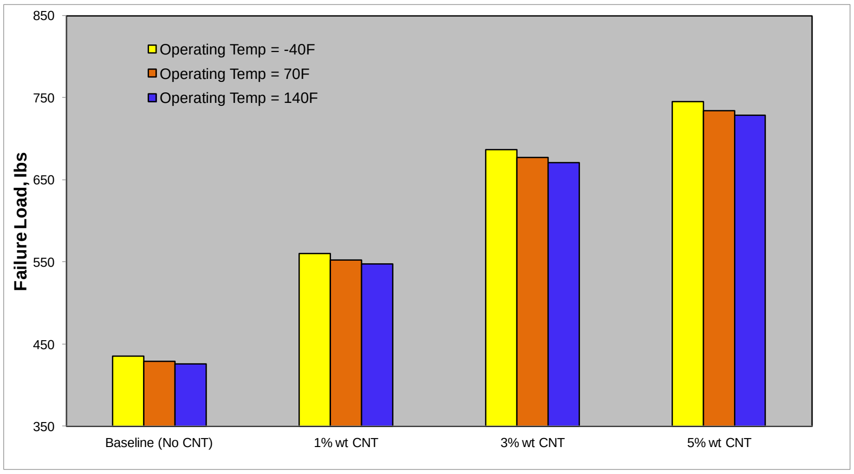

Figure 140. Pull-off failure load for flaw 1 at different temperatures

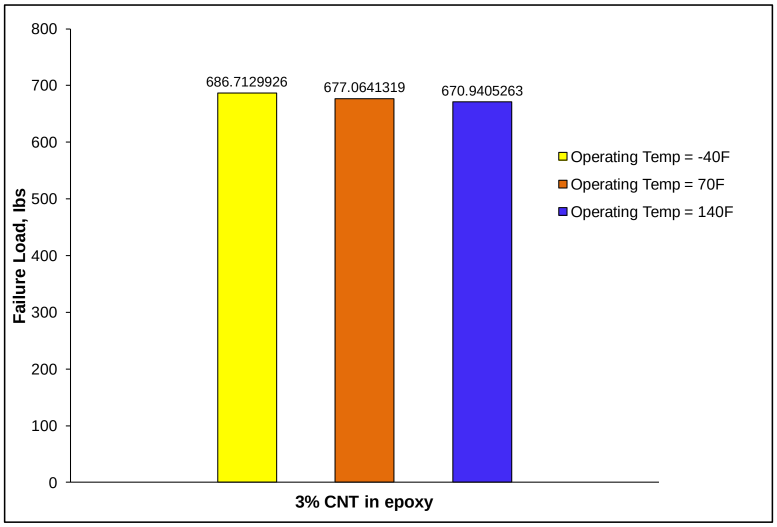

Figure 141. Failure load for type 1 flaw including temperature variation

Figure 142 represents the pull-off failure load of the structure that incorporates a type 2 flaw for different CNT weight percentages and operating temperatures. A similar trend to the previous flaw type is shown where the failure load increases with greater CNT weight percent in the composite for all the different operating temperature conditions. For this case, the maximum failure load occurs at the 140°F operating temperature condition, which is considered to be an extreme hot case at which the component is expected to operate. It is interesting to note that for different flaw types, different temperature conditions may become more critical than others, so caution must be taken during the design of those composite components. A type 2 flaw is also found to be mode I dominant under pull-off loading, and the use of CNTs is shown to provide additional through-thickness capability. Note that failure occurs at a higher value than that reported for type 1 flaw, which indicates that the risk of failure is smaller for this case.

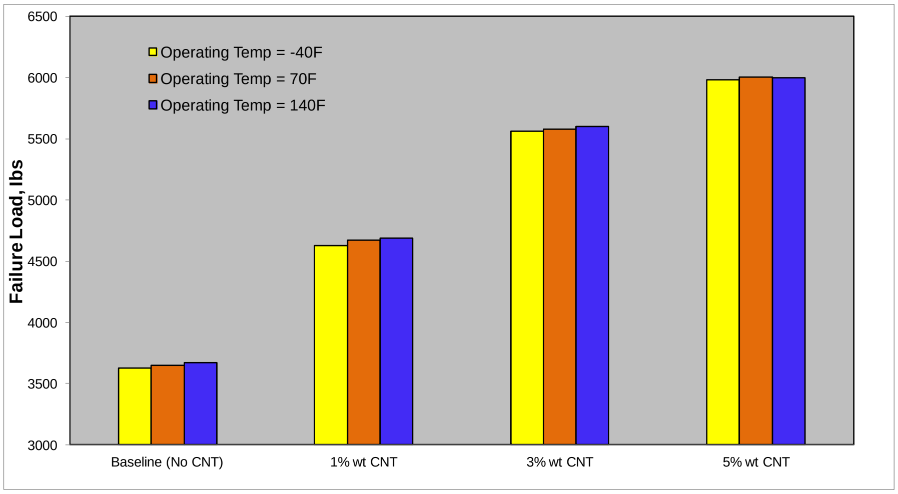

Figure 142. Pull-off failure load for flaw 2 at different temperatures

Figure 143 represents the pull-off failure load of the structure that incorporates a type 3 flaw for different CNT weight percentages and operating temperatures. It can be noted that the failure load increases with CNT weight percent, but the trend is not smooth as was observed in the previous two flaw types. For the 70°F temperature condition, it can be noted that the failure load increases in a steady manner with greater CNT weight fraction. However, for the -40°F temperature condition, there is a slight increase with 1% CNT, a significant increase with 3%, followed by a reduction for the 5% CNT. This indicates that there might be a threshold value for CNT weight percent; beyond this threshold value, any further increase in CNT may have a negative impact in terms of failure load. For the 140°F temperature condition, the failure load increases for 1% and is reduced slightly for 3%, while the highest value is obtained for the 5% CNT by weight. From here it is noted that a design optimization process might be necessary to determine the optimal CNT weight percent for the desired performance.

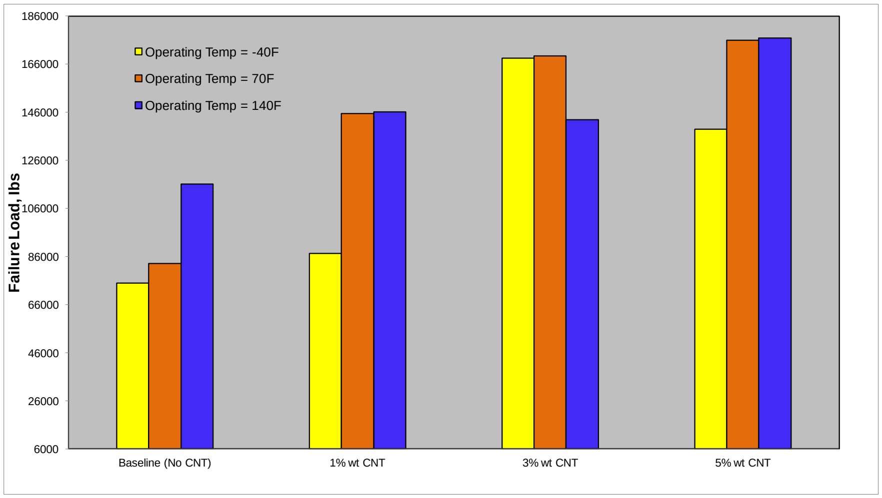

Figure 143. Pull-off failure load for flaw 3 considering different temperatures

Figure 144 a and b shows the damage index as the pull-off load increases for a model that includes a type 1 flaw and incorporates 0% and 5% CNT by weight in the adhesive material, respectively. It can be observed that the initial flaw increase in size as the pull-off load increases until the damage index exceeds the point where initial damage is assumed to occur. The damage size for the model that includes 5% CNT has a smaller final damage area compared to the baseline model, therefore providing a higher load-bearing capability structure that is able to sustain a higher failure load.

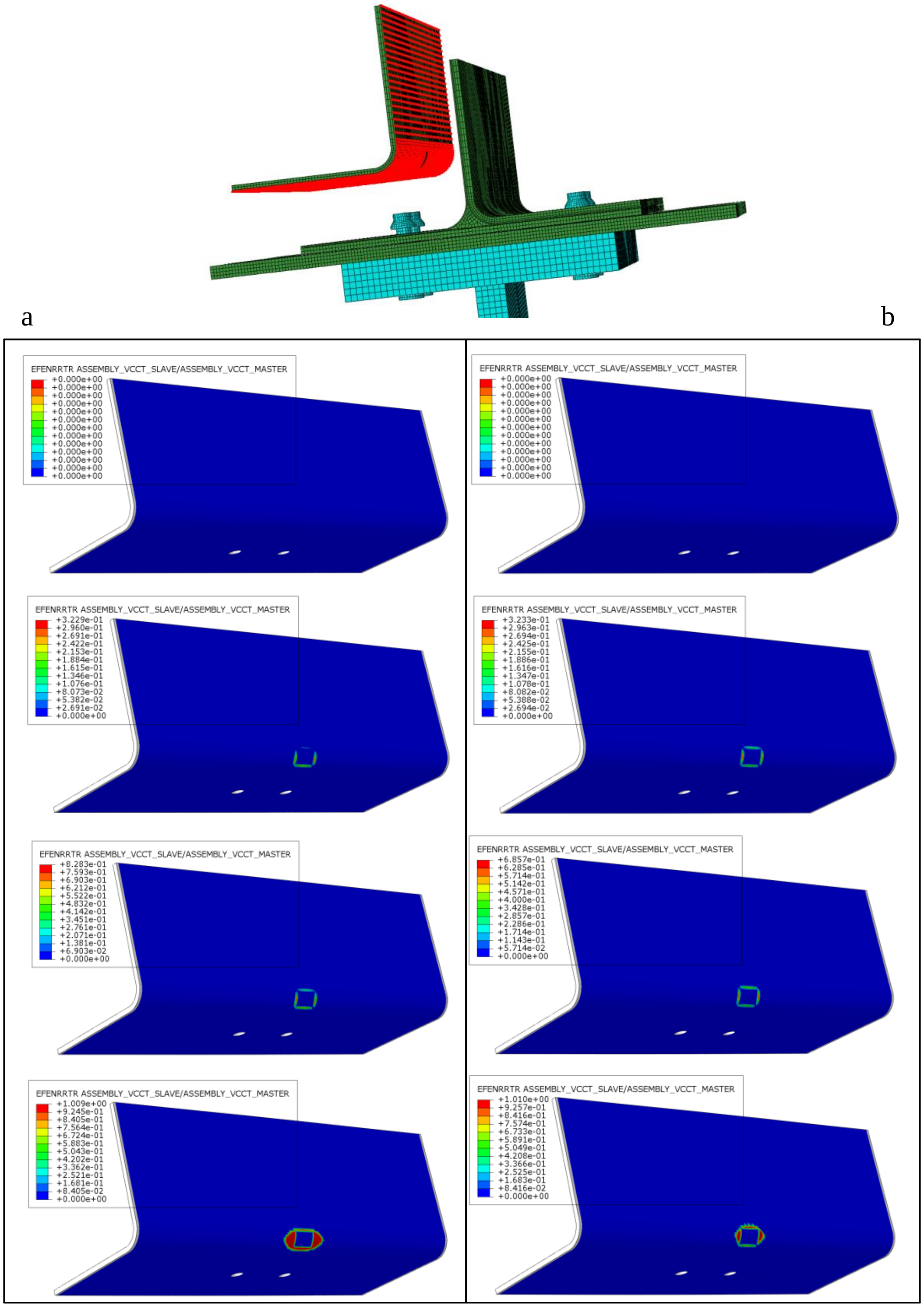

Figure 144. Damage indexes for models with (a) 0% CNT (b) and 5% CNT

6.5. Cure Cycle Effect

During the manufacturing process of composite structural components, such as T stringers, a cure process is required to solidify the stringer and skin. The stringer is first cured separately before being co-bonded (cured again) to the skin. The skin laminates are tailored to ensure the flattest post-cure shape possible. The curving of the stringer flanges during this cure process is detrimental to crack onset. The cure process produces a residual crack opening, which reduces the structural pull-off capabilities. During a cure cycle (350°F to 70°F temperature) stringers curl up. as shown in Figure 145, but are restrained by the skin, bagging, and pressure. This restraint creates crack openings. The stiffer the skin, the larger this induced moment. Even though the skin, bagging, and pressure restrain the curling of the stringers, these effects usually prevent the stringer from becoming flat. Flattening the stringer induces more crack-opening moments.

A comparison was made between the failure loads for models where the cure cycle effect is taken into account via a separate step in the analysis with another model where the cure step is neglected. As shown in Figure 146, the normalized failure load for the model with no cure cycle had a lower failure load for type 1 and 2 flaws while a type 3 flaw had a higher failure load. Therefore, it should be noted that depending on the flaw type, a conservative or less conservative failure load can be obtained. As such, the cure effect must be accounted for during simulations because it represents a realistic phenomenon and may have a dramatic impact on the failure predications.

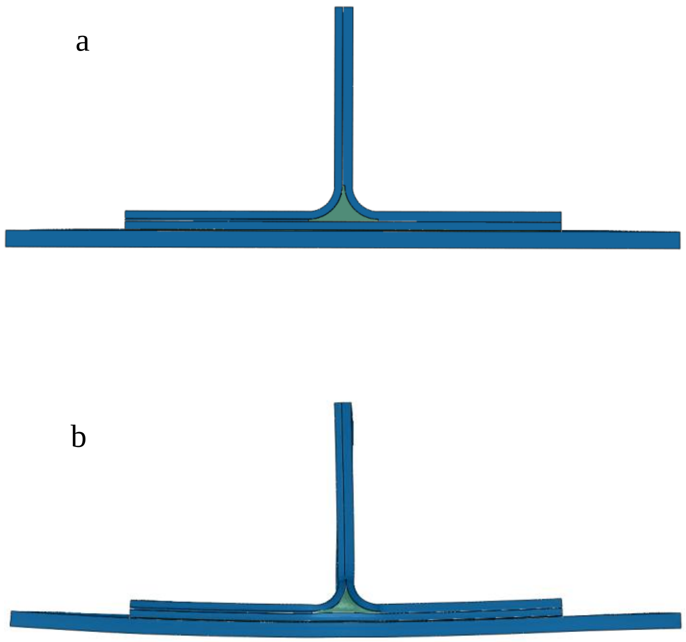

Figure 145. Cure cycle effect (a) before and (b) after the cure cycle (deformation is 10 times exaggerated)

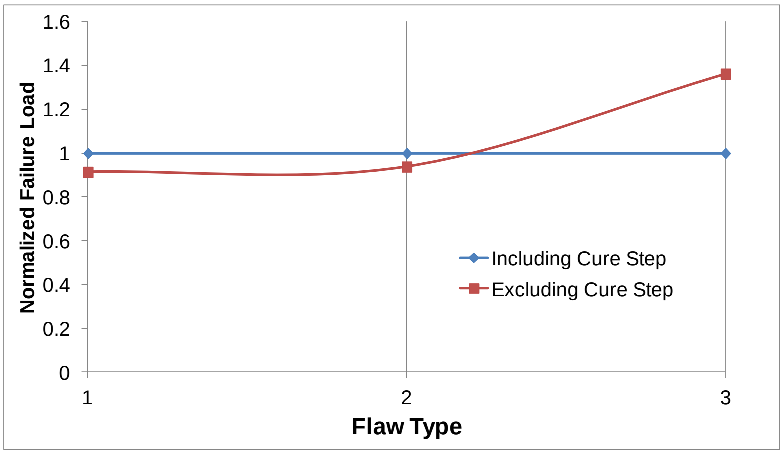

Figure 146. Pull-off failure load for different flaws considering the cure cycle effect

6.6. Flaw Propagation Analysis

This section discusses the effect of incorporating nanocomposites on delamination propagation of the different flaw types under the applied pull-off load condition. In order to allow the flaw to propagate in the simulation, the tolerance at which the damage index is allowed to exceed without terminating the analysis is increased. For initial damage, the simulation will terminate after the first node is released, while in the propagation simulation, the flaw continues to grow until either the final applied load is reached or the damage index exceeded the allowed tolerance. The size of the interlaminar crack propagating from the initial flaw and the rate of the damping energy are monitored during the simulation. The analysis is performed at the 70°F temperature condition to eliminate the contribution of thermal loading. A model that included 0% CNT (baseline) and another with 5% CNT are used to quantify the ability of the nanocomposite to reduce the amount of interlaminar crack propagation.

The flaw is driven both by the increasing load and by the unsymmetrical stiffness with respect to the four fastener tensile forces. When the flaw reaches a critical length, unstable growth occurs in the direction of the two more highly loaded fasteners. Figure 147 shows the crack length as a function of applied pull-off load for a type 1 flaw. As can be observed in the figure, the crack length is constant until a certain load level, at which point the crack begins to propagate. For this flaw type, the crack grows along the span-wise direction. The pull-off load at which the crack starts to grow is higher for the model that included CNTs, which can be attributed to the higher fracture toughness of the adhesive at that interface and the ability of the CNT to provide additional through-thickness capability. The final crack length for the baseline model is 7 inches, while the model that included 5% CNT is 4.3 inches and occurred at a higher load level.

Figure 148 shows the crack length as a function of applied pull-off load for a type 2 flaw. In this case, the crack for the model with CNTs grew only 0.075 inches, while the baseline model was growing unstably and a loss of stiffness was occurring. This can be observed from the reduction in the pull-off load at that crack length, indicating that the structure was approaching final failure. Regarding the type 3 flaws, Figure 149 shows the behavior of the structure. No stiffness loss was observed, but as in the previous two cases, the model with CNTs has the ability to sustain higher pull-off loads and smaller crack lengths. Figure 150 shows a comparison between the different flaw types by comparing their final crack lengths and associated pull-off loads. A type 3 flaw has the highest pull-off-to-crack length ratio, while a type 2 flaw has the highest difference in the final crack length between the baseline model and the one with 5% CNT. For a type 1 flaw, the pull-off load difference between the baseline and 5% CNT by weight is small, but the final crack length is more substantial. Figure 151 shows a visual comparison of the final crack lengths for the different flaw types. Overall, the use of nanocomposites in the structure reduced the propagation of the initial flaws in the models and therefore provides a more robust design. It can be concluded that incorporating nanocomposites in specific hot spot locations in the structure can significantly enhance the ability of that structure to sustain higher loads without growing unstable cracks, thereby allowing a higher residual strength. The results in this section also highlight the ability of the simulation to capture unstable crack growth and the attendant load decrease.

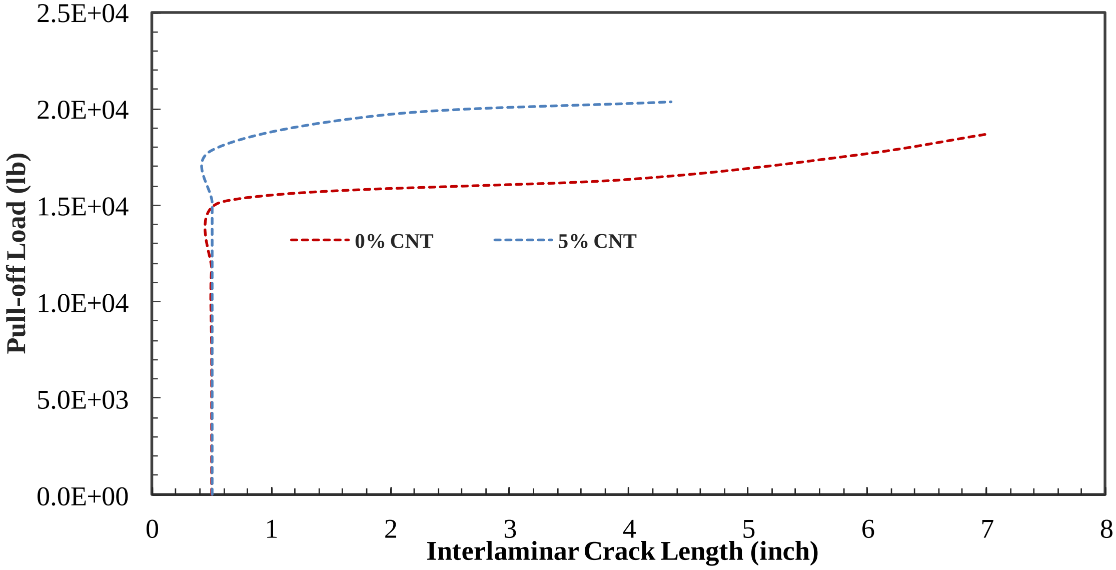

Figure 147. Pull-off load as function of crack length for type 1 flaws

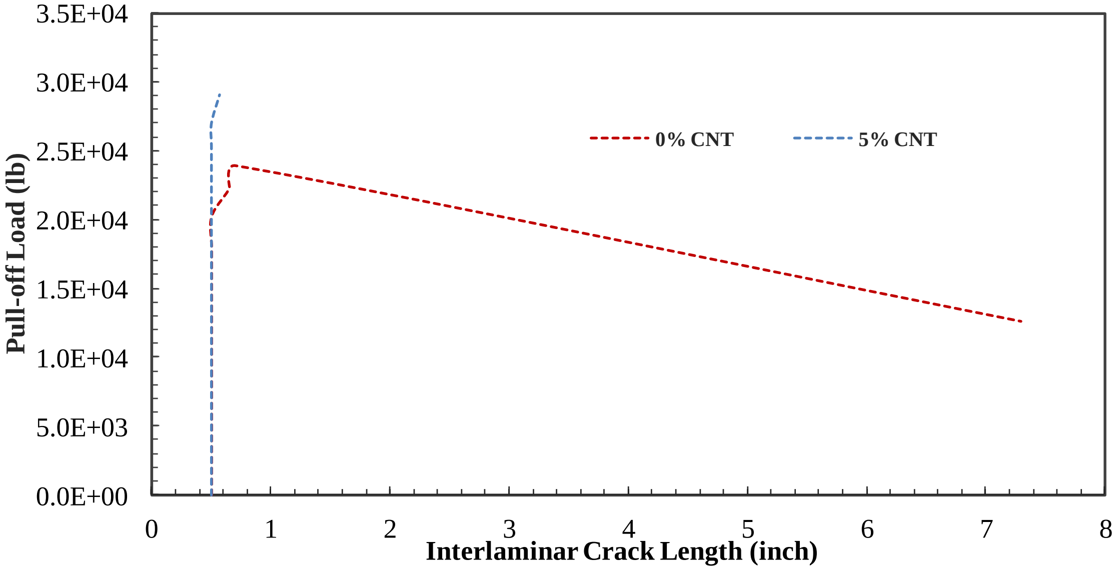

Figure 148. Pull-off load as function of crack length for type 2 flaws

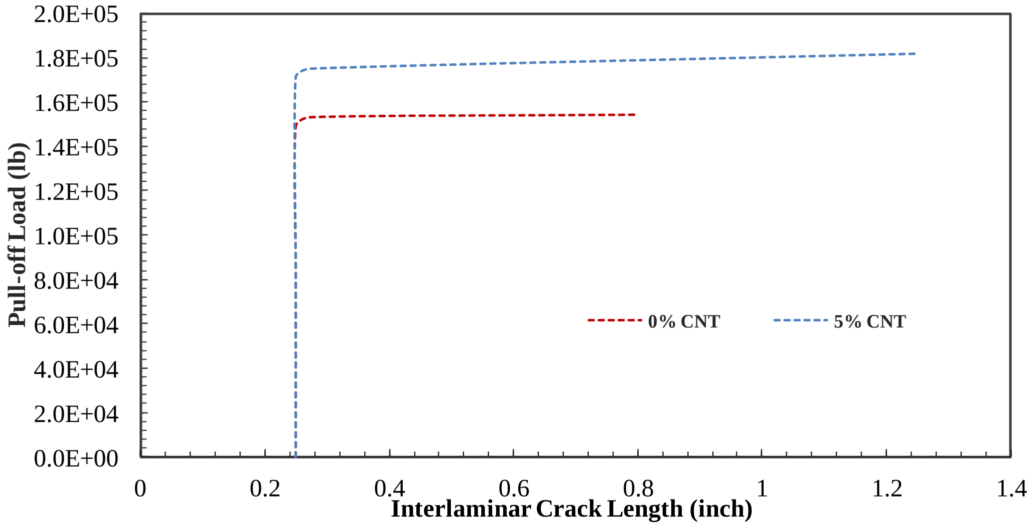

Figure 149. Pull-off load as function of crack length for type 3 flaws

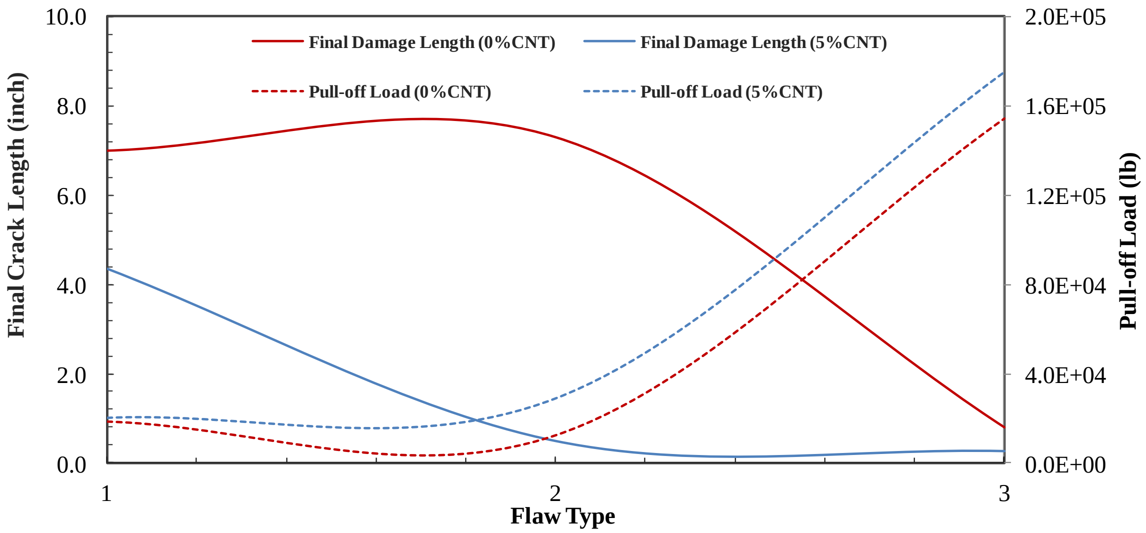

Figure 150. Comparison of the different flaw types

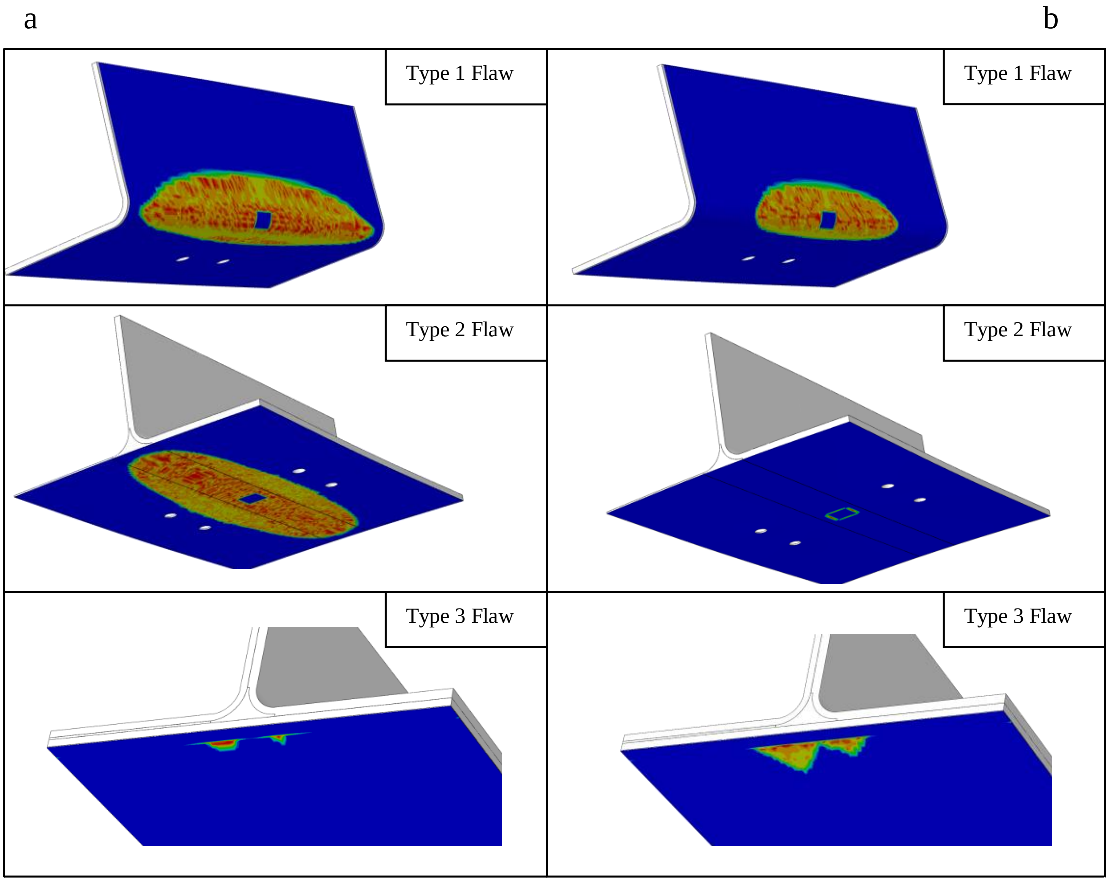

Figure 151. Crack propagation of the different flaws in the models with (a) 0% CNT and (b) 5% CNT by weight

Chapter Summary

This chapter discussed the thermal influence on the behavior of nanocompsoite structures. The results demonstrated that the consideration of different operating temperature conditions is an essential part of the design phase because the failure load may alter depending on the temperature. The three flaw types had different behaviors under the various temperature conditions; hence, the designer should be cautious and consider all possible damage scenarios and estimate the structural behavior to better understand the performance and gain confidence in the design. It was noted that by including the cure cycle affect in the analysis, the failure load changed for the different flaw types. Therefore, a more or less conservative failure load may be obtained if this effect was not considered in the analysis. Finally, the findings shed light on the ability of the nanocomposite to improve the interlaminar crack propagation, allowing the structure to sustain higher loads without growing cracks unstably and obtain a higher residual strength.

CHAPTER 7

CONCLUSIONS AND FUTURE WORK

7.1. Summary and Conclusion

The present research focused on the benefits of using nanocomposites in structural level components that are typically used in aerospace applications. Examples of such structures are T and Hat sections stringers. A multiscale approach based on micromechanics was used to determine the effective properties of the nanocomposite at different length scales. The effect of a non-perfect interface between the CNTs and epoxy matrix on the effective mechanical properties was investigated with detailed FEMs. The results revealed that a non-perfect interface has a notable influence on the mechanical properties, depending on the stiffness value that exists between the interfaces. The lower the stiffness values, the lower the effective mechanical properties.

An alternative approach in determining the effective mechanical properties was presented that is based on an estimation method using the Kalman filter. The results obtained using this method were compared with those obtained from the micromechanics approach. It was concluded that the Kalman filter can easily be utilized as a first method of system identification for estimating the material properties of nanocomposites using minimal strain measurements. The findings also underscore the validity of the micromechanic results.

Stress analysis of nanocomposites was also presented in this study. The stress and displacement fields were obtained via an analytical method, which adopted the Kelvin-Voigt viscoelastic constitutive relation to incorporate the time-dependent behavior of the composite. The effective properties of the CNTs were calculated using the composite cylinder micromechanics approach. It was concluded that the variation of axial stress over time is more pronounced for CNTs with larger aspect ratios, and the magnitude of the stress also increased. The shear stress distribution increased significantly for higher aspect ratios over time. In addition, the results showed that it is important to model the viscoelastic nature of the interface because higher shear stresses were obtained when considering the viscoelastic effect and this can lead to disbonding of the CNTs from the matrix jeopardizing the structural performance.

A detailed model of the T and Hat stringers bonded to a skin were constructed to assess the use of nanocomposites on structural level components and to improve some of the weak spots in such structures. The VCCT was employed to determine the initial damage to the structure, which is defined as the initial load drop in the load displacement curve. Different configuration, flaw types, and loading conditions were considered in this study. To validate both the modeling techniques and the analysis method, the results were first compared with available experimental data in the literature and showed acceptable correlation. It was found by comparing the initial failure loads that using CNTs in the manufacturing process of such stringers may improve the overall performance by up to 30%. It was also concluded that when considering a structure that undergoes pull-off loading, the delamination that typically occurs around the tow filler and skin stringer bondlines can be prevented or delayed by incorporating CNTs in those hot spot locations, thus providing a more robust structural design. Such a solution would help in eliminating the standard fixes that are currently utilized in industry, such as adding local metallic fittings that are not desirable due to the added weight and manufacturing process complexity.

Several experiments were conducted in support of this research. Initially, a designed experiment was conducted to test specimens of a T section skin/stringer by replicating those used in composite panels as stiffeners. Two types of designs were considered: one that used pure epoxy to fill the tow region and another that used 5% CNT by weight nanocomposite. The samples were subjected to pull-off loading and introduced matrix cracks in the tow filler area, which ultimately led to specimen failure. The trend from the results provided evidence that the addition of CNTs did improve the initial damage load. Therefore, it was demonstrated that the use of CNTs would provide additional through-thickness capability, thus preventing or delaying such events from occurring.

Multiscale analysis was used to compute the thermal effective properties of the nanocomposite. The thermal properties were then used in detailed FEMs to investigate the effect of operating temperature change on the structural behavior and the failure load. It was noticed that the failure load increases with greater CNT weight percents in the composite. This trend held for all the temperature conditions, which indicates that there is no induced thermal effect that reduces the failure load for any flaw type. A comparison was made between the failure loads for models where the cure cycle effect was taken into account via a separate analysis step with another model where the cure step was neglected. The normalized failure load for the model with no cure cycle had a lower failure load for type 1 and 2 flaws, while type 3 had a higher failure load. Therefore, it was noted that, depending on the flaw type, a conservative or less conservative failure load can be obtained. This leads to the conclusion that the cure effect must be accounted for during simulations because it represents a realistic phenomenon and may have a dramatic impact on the failure predications.

7.2. Future Work

The history of airplane development has shown a steady progression from lightweight, flexible materials toward heavier, stiffer materials more capable of handling large payloads and high speeds, as shown in Figure 152.

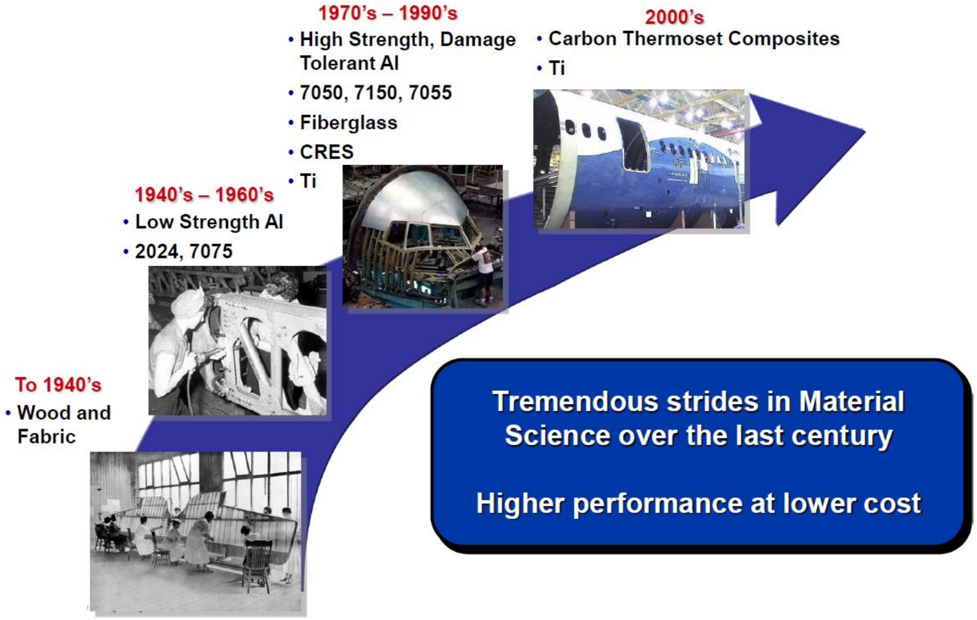

Figure 152. History of material advancements in aerospace application

With the advent of polymer science and the subsequent development of advanced polymer composite systems with tremendous strength-to-weight ratios, many speculated that there would be an exponential growth in the amount of composite materials used in aircraft. However, the growth has been significantly slower than expected due to the development of lightweight alloys, advanced joining techniques, low-cost castings, and high-speed machining, thereby extending the use of traditional materials in aircraft design (Baughman, R.H. et al. 2002). In addition, the uncertainty involving the fatigue life of polymer materials, the typically poor fracture toughness, and compression-after-impact (CAI) strength of those materials have further mired the growth of polymer composite systems in structural applications.

In the last two decades, tremendous resources have been pushed toward the development of multifunctional nanocomposite materials using CNTs as a reinforcing agent within a polymer matrix. Multifunctional composite materials promise to simultaneously decrease weight, increase strength, and allow for improved performance over a range of mechanical, thermal, and electrical properties, but several obstacles remain to be overcome.

In this work, the static capabilities of nanocomposite structures were investigated; however, neither fatigue nor have damage tolerance aspects been addressed, which are essential elements for such materials to be considered in future military and commercial aircrafts. In addition, the coupled thermo-electro functionality of nanocomposites and their application in aerospace structures needs to be investigated. Moreover, much experimental work needs to be conducted to provide experimental evidence indicating that incorporating CNTs in structural elements can improve composite repairs, specifically in oversized and misallocated holes, which occur often in production. The current solution to this issue is expensive, and its influence on the static and durability margins of safety is high. Based on the preliminary analysis conducted here, CNTs might help overcome such weaknesses.

Several challenges still exist for nanomaterials. One of the basic features of a CNT is that it has an atomically smooth surface. Due to the hybridized bonds between the carbon atoms on the graphitic shells, there are no reactive groups available to form bonds with a matrix material. Because there is no effective bond that will promote compatibility with a matrix material, a group must be added to the surface of the CNTs to promote a sidewall reaction. Another problem is that the high aspect ratio promotes an extremely high free surface energy. In order to minimize the energy of the system, CNTs are attracted to each other and form bundles and ropes held together by van der Waals (vdW) forces.

Another challenge is the dispersion of CNTs, which tend to self-assemble into insoluble bundles of parallel nanotubes due to strong inter-CNT vdW interaction and π-stacking. Aqueous suspensions of mostly debundled CNTs can be prepared through extensive chemical functionalization, but this technique compromises electrical performance due to extensive structural degradation. Surfactant-assisted exfoliation by ultrasonication and ultracentrifugation is a common approach that does not damage the structure, but it is limited to a very low yield (less than 5% with most common surfactants) and reduces electrical conductivity because of the physical separation of CNTs by the insulating surfactant layer. Control over the degree of CNT exfoliation has not been demonstrated by either of the above methods.

The second problem with the implementation of CNTs into a matrix material is poor interfacial adhesion. The atomically smooth and non-reactive surface characteristics of the CNTs restrict any degree of interfacial bonding between the nanotubes and the matrix material. This is shown in failure mechanisms where CNTs were pulled out of the epoxy material without breaking, limiting their reinforcement effect.

The final consideration with regard to the properties of a CNT filler material to a matrix material is alignment. Tremendous research efforts have sought to utilize the magnetic and electrical properties of CNTs to orient them toward the creation of conductive pathways. The most common methods have sought to align the CNTs via ambient electrical or magnetic currents while they are suspended in a viscous medium. All the above issues and many others need to be overcome to enable effective real-world nanocomposite use. Table 12 shows some potential uses of nanocomposites in future applications.

Table 12. Potential applications of nanocomposites for future research considerations

FUTURE APPLICATIONS OF NANOMATERIALS	
Electrically conductive composite materials Reduced Weight and Cost for EME Protection	**Material characterization and quality-assurance method**
Thermally resistant composite materials Increase Resistance to Fire and Higher Service Temperatures for Low Cost Polymers.	**Hydrophobic/ice-phobic coatings** Allow Certification of Clean Wing
Acoustically enhanced composite materials Elimination of Parasitic Noise Damping and Absorbing Materials	**Nano sensors and electroactive coatings for integrated health monitoring of systems and structures** Nano Sensor Film to Eliminate BVID Criteria
Structural enhanced composite materials Higher Strength, Stiffness, Durability	**Transparent nanocomposite materials** Nanofibers are below diffraction limits of visible light
Enhanced adhesives and bonded-repair methods	**Nanoscale power sources and embedded conductors**
Design tools and modeling of nano morphology from mixing to structure	**Resin Infusion with Nano Additives**

BIBLIOGRAPHY

Abaqus. 2012. "Abaqus: Version 6.11." Providence, RI.

Abdalla, M. et al. 2008. "Cure behavior of epoxy/MWCNT nanocomposites: The effect of nanotube surface modification." *Polymer:* 3310–3317.

Aboudi, J. et al. 2012. *Micromechanics of Composite Materials: A Generalized Multiscale Analysis Approach.* Oxford: Elsevier.

Ahmed, J. and Ebrary, I. 2012. *Starch-based polymeric materials and nanocomposites chemistry, processing, and applications.* Boca Raton, FL: CRC Press.

Ajayan, P.M. et al. 2003. *Nanocomposite science and technology.* Weinheim, Germany: Wiley-VCH.

Arai, M. et al. 2008. "Mode I and mode II interlaminar fracture toughness of CFRP laminates toughened by carbon nanofiber interlayer." *Composites Science and Technology* 68 (2): 516-525.

Bal, S. 2010. "Experimental study of mechanical and electrical properties of carbon nanofiber/epoxy composites." *Materials & Design* 31 (5): 2406-2413.

Banks-Sills, L. 1991. "Application of the finite element method to linear elastic fracture mechanics." *Applied Mechanics Reviews* 44: 447-461.

Baughman, R.H. et al. 2002. "Nanotubes--the Route Toward Applications." *Science* 297(5582): 787-792.

Benveniste, Y.,. 1987. "A new approach to the application of Mori-Tanaka's theory in composite materials." *Mechanics of Materials* 6 (2): 147-157.

Blackman, B.R. et al. 2003. "The use of a cohesive zone model to study the fracture of fibre composites and adhesively-bonded joints." *International Journal of Fracture* 119 (1): 25-46.

Bouvard, J. L. et al. 2009. "Review of Hierarchical Multiscale Modeling to Describe the Mechanical Behavior of Amorphous Polymers." *Journal of Engineering Materials and Technology* 131(4): 041206-1 - 041206-15.

Broek, D. 1982 . *Elementary Engineering Fracture Mechanics.* New York: Springer.

Brown, R.T. and Crow Jr, E.C. 1992. "Automatic through-the-thickness braiding." *37th International SAMPE Symposium and Exhibition.* Anaheim, CA. : 832-842.

Bryning, M.B. et al. 2005. "Thermal conductivity and interfacial resistance in single-wall carbon nanotube epoxy composites." *Applied Physics Letters* 87 (16): 161909-1 - 161909-3.

Buchholz, F. G. 1988. "2D- and 3D- Applications of the Improved and Generalized Modified Crack Closure Integral Method." *Computational Mechanics* : 387-390.

Camacho, G.T. and Ortiz, M. 1996. "Computational modelling of impact damage in brittle materials." *International Journal of Solids and Structures* 33 (20-22): 2899-2938.

Camanho, P.P. et al. 2003. "Numerical simulation of mixed-mode progressive delamination in composite materials." *Journal of Composite Materials* 37 (16): 1415-1438.

Camargo, P.H. et al. 2009. "Nanocomposites: Synthesis, Structure, Properties and New Application Opportunities." *Materials Research* 12(1): 1-39.

Chang, P. et al. 2007. "Flexural properties of z-pinned laminates." *Composites Part a-Applied Science and Manufacturing* 38 (2): 244-251.

Chen, J.Y. et al. 2009. "Prediction of delamination in braided composite T-piece specimens." *Composites Science and Technology* 69 (14): 2363-2367.

Chen, T.Y. et al. 2005. "Effect of Kapitza contact and consideration of tube-end transport on the effective conductivity in nanotube-based composites." *Journal of Applied Physics* 97 (10): 104312-1 - 104312-4.

Chen, W. et al. 2003. "Exact solution of cross-ply laminates with bonding imperfections." *AIAA Journal* 41 (11): 2244 - 2250.

Chow, W. T. and Atluri, S. N. 1997. "Stress intensity factors as the fracture parameters for delamination crack growth in composite laminates." *Composites, Part B* 21(1): 375-384.

Christensen, R. and Lo, K. 1979. "Solutions for effective shear properties in three phase sphere and cylinder models." *Journal the Mechanics and Physics of Solids* 27: 315–330.

Clancy, T.C. and Gates, T.S. 2006. "Modeling of interfacial modification effects on thermal conductivity of carbon nanotube composites." *Polymer* 4 (16): 5990-5996.

Claydon, P. W. 1992. "Maximum Energy Release Rate Distribution From a Generalized 3D Virtual Crack Extension Method." *Engineering Fracture Mechanics* 42(6): 961-969.

Cope, R.D. and Pipes, R.B. 1982. "Design of the composite spar-wing skin joint." *Composites* 13 (1): 47-53.

Courage, W. M. et al. 1990. "Estimation of mechanical parameter values of composites with the use of finite element and system identification techniques." *Computers and Structures* 34(2): 231-237.

Delorenzi, H. G. and Shih, C. D. 1983. "3-D Elastic-plastic investigation of fracture parameters in side-grooved compact specimen." *Int. J. Fracture* 21(3): 195-220.

Delorenzi, H. G. 1985. "Energy Release Rate Calculations by the Finite Element Method." *Eng. Fracture Mech.* 21(1): 129-143.

Delorenzi, H. G. 1982. "On the energy release rate and the J-integral for 3-D crack configurations." *Int. J. Fracture* 19(3): 183-193.

Dereli, G. and Ozdogan, C. 2003. "Structural stability and energetics of single-walled carbon nanotubes under uniaxial strain." *Physical Review B.* 67 (3): 035416-1 - 035416-6.

Doltsinis, J. et al. 1985. *Fracture Mechanics.* User Manual, Stuttgart: Publication No. 226, Rev. C.

Dransfield, K.A., et al. 1998. "On the effects of stitching in CFRPs - I. Mode I delamination toughness." *Composites Science and Technology* 58 (6): 815-827.

Dresselhaus, M.S. et al. 1996. *Science of Fullerenes and Carbon Nanotubes: Their Properties and Applications.* Waltham, MA: Academic Press.

Durham, S.D. and Padgett, W.J.,. 1997. "Cumulative damage models for system failure with application to carbon fibers and composites." *Technometrics* 39 (1): 34-44.

Elliott, J. A.,. 2011. "Novel approaches to multiscale modelling in materials science." *International Materials Reviews* 56(4): 207-225.

Eshelby, J.D. 1957. "The Determination of the Elastic Field of an Ellipsoidal Inclusion, and Related Problems." *Proceedings of the Royal Society of London Series a-Mathematical and Physical Sciences.* London. 376-396.

Fan, H., and Wang. G. 2003. "Interaction between a screw dislocation and viscoelastic interfaces." *International Journal of Solids and Structures* 40: 763-776.

Fisher, F.T. et al. 2003. "Fiber waviness in nanotube-reinforced polymer composites-1: Modulus predictions using effective nanotube properties." *Composites Science and Technology* 63(11): 1689-1703.

Fu, S.Y., et al. 2008. "Effects of particle size, particle/matrix interface adhesion and particle loading on mechanical properties of particulate-polymer composites." *Composites Part B-Engineering* 39 (6): 933-961.

Gaggar, S. and Broutman, L.J. 1977. "Fracture toughness of random glass fiber epoxy composites: an experimental investigation." *ASTM STP 631, American Society for Testing and Materials* : 310-330.

Gao, X.L. and Li, K. 2005. "A shear-lag model for carbon nanotube-reinforced polymer composites." *International Journal of Solids and Structures* 42 (5-6): 1649-1667.

Gao, Y.F. and Bower, A.F. 2004. "simple technique for avoiding convergence problems in finite element simulations of crack nucleation and growth on cohesive interfaces." *Modelling and Simulation in Materials Science and Engineering* 12 (3): 453-463.

Gary D.S. and Dimitris C.L. 2006. "Micromechanical analysis of the effective elastic properties of carbon nanotube reinforced composites." *Mechanics of Materials* 38: 884–907.

Gojny, F.H. et al. 2006. "Evaluation and identification of electrical and thermal conduction mechanisms in carbon nanotube/epoxy composites." *Polymer* 47 (6): 2036-2045.

Gosz, M. and Moran, B. 2002. "An interaction energy integral method for computation of mixed-mode stress intensity factors along non-planar crack fronts in three dimensions." *Engineering Fracture Mechanics* 69: 299-319.

Guthy, C. et al. 2007. "Thermal conductivity of single-walled carbon nanotube/PMMA nanocomposites." *Heat Transf.-Trans. ASME* 129 (8): 1096-1099.

Han, Z. and Fina, A. 2011. "Thermal conductivity of carbon nanotubes and their polymer nanocomposites: A review." *Progress in Polymer Science* 36(7): 914–944.

Hashin, Z. and Rosen, B. 1964. "The elastic moduli of fiber-reinforced materials." *Journal Applied Mechanics* 31: 223–232.

Hashin, Z. 1990. "Thermoelastic Properties and Conductivity of Carbon/Carbon Fiber Composites." *Mech. Mater.* 293–308.

He, L. H. and Jiang, J. 2003. "Transient mechanical response of laminated elastic strips with viscous interfaces in cylindrical bending." *Composites Science and Technology* 63: 821-828.

Helenon, F. et al. 2012. "Numerical investigation into failure of laminated composite T-piece specimens under tensile loading." *Composites Part a-Applied Science and Manufacturing* 43 (7): 1017-1027.

Hellen, T. K. 1975. "On the Method of Virtual Crack Extension." *Int. J. Num. Meth. Eng.* 9: 187-207.

Hillerborg, A. et al. 1976. "Analysis of crack formation and crack growth in concrete by means of fracture mechanics and finite elements." *Cement and Concrete Research* 6 (6): 773-781.

Hojo, M. et al. 2006. "Modes I and II interlaminar fracture toughness and fatigue delamination of CF/epoxy laminates with self-same epoxy interleaf." *Journal of Fatigue* 28 (10): 1154-1165.

Hoyt, D.M. et al. 2002. "Strength and fatigue life modeling of bonded joints in composite structure." *Journal of Composites Technology & Research* 24 (3): 188-208.

Hsieh, T. et al. 2011. "The effect of carbon nanotubes on the fracture toughness and fatigue performance of a thermosetting epoxy polymer,." *Journal Materials Science* 46" 7525-7535.

Huxtable, S.T. et al. 2003. "Interfacial heat flow in carbon nanotube suspensions." *Nature Materials* 2 (11): 731-734.

Hwang, C. G. et al. 1998. "On the virtual crack extension method for calculation of the rates of energy release rate." *Engineering Fracture Mechanics* 59: 521-542.

Iijima, S. 1991. "Helical microtubules of graphitic carbon." *Nature* 354 (6348): 56-58.

Irwin, G. R. 1958. "Fracture I." *Handbuch der Physik VI* : 558-590.

Ishikawa, H. 1980. "A Finite Element Analysis of Stress Intensity Factors for Combined Tensile and Shear Loading by Only a Virtual Crack Extension." *Int. J. Fracture* 16: 243-246.

Jansson, S. 1992. "Homogenized nonlinear constitutive properties and local stress concentrations for composites with periodic internal structure,." *International Journal of Solids and Structures* 29(17): 2181–2200.

Jin, Y. and Yuan, F.G. 2003. "Simulation of elastic properties of single-walled carbon nanotubes." *Composites Science and Technology* 63 (11): 1507-1515.

Keller, T.,. 2001. "Recent all-composite and hybrid fibre-reinforced polymer bridges and buildings." *Progress in Structural Engineering and Materials* 3 (2): 132-140.

Knauth, P. and Schoonman, J. 2008. *Nanocomposites ionic conducting materials and structural spectroscopies.* New York: Springer.

Krueger, R. et al. 2000. "Testing and analysis of composite skin/stringer debonding under multi-axial loading." *Journal of Composite Materials* 34 (15): 1263-1300.

Krüger, R. et al. 1993. "Computation of Local Energy Release Rates Along Straight and Curved Delamination Fronts of Unidirectionally Laminated DCB- and ENF-Specimens." *Proceedings of the 34th AIAA/ASME/ASCE/AHS/ASC SSDM Conference.* La Jolla, CA: American Institute of Aeronautics and Astronautics. 1332-1342.

Kumar, S. et al. 2012. "Fracture Toughness of Multi Walled Carbon Nano Tubes Modfied Polymer Composite in Mode – I." *Journal Materials Science Research* 1(3): 117-123.

Kumari, S. and Sinha, P.K. 2002. "Finite element analysis of composite wing T-joints." *Journal of Reinforced Plastics and Composites* 21 (17): 1561-1585.

Li, J. 2002. "Pull-off Tests and Analyses of Composite Skin and Frame T-Joint Presented test data for several pull-off specimens." *Proceedings of American Society for Composites Conference.* West Lafayette, IN.

Li, J.A. et al. 1997. "Test and analysis of composite hat stringer pull-off test specimens." *Journal of the American Helicopter Society* 42 (4): 350-357.

Liao, K. and Li, S. 2001. "Interfacial characteristics of a carbon nanotube-polystyrene composite system." *Applied Physics Letters* 79 (25): 4225-4227.

Linderoth, M. et al. 2011. "Initialization of the Kalman Filter without Assumptions on the Initial State." *IEEE International Conference on Robotics and Automation*. Shanghai, China.

Lin, S. C. and Abel, J. F. 1988. "Variational aproach for a new direct-integration form of the virtual crack extension method." *International Journal of Fracture* 38(3): 217-235.

Liu, Y. J. and Chen, X. L. 2003. "Evaluations of the effective material properties of carbon nanotube-based composites using a nanoscale representative volume element." *Mechanics of Materials* 35 (1-2): 69-81.

Mai, Y.W. et al. 2006. *Polymer nanocomposites.* Cambridge, MA: Woodhead Publishing.

Martin, R.H. 1996. "Local fracture mechanics analysis of stringer pull-off and delamination in a post-buckled compression panel." *Applied Composite Materials* 3 (4): 249-264.

Marzari, N. and Ferrari, M. 1992. "Textural and micromorphological effects on the overall elastic response of macroscopically anisotropic composites." *Journal of Applied Mechanics* 59: 269–275.

Miloh, T. and Benveniste, Y. 1988. "A generalized self-consistent method for the effective conductivity of composites with ellipsoidal inclusions and cracked bodies." *Journal of Applied Physics* 63: 789–796.

Moes, N., J. et al. 1999. "A finite element method for crack growth without remeshing." *International Journal for Numerical Methods in Engineering* 46 (1): 131-150.

Montazeri, A. et al. 2010. "Mechanical properties of multi-walled carbon nanotube/epoxy composites." *Materials & Design* 31 (9): 4202-4208.

Montazeri, A. et al. 2010. "Viscoelastic properties of multi-walled carbon nanotube/epoxy composites using two different curing cycles." *Materials & Design* 31 (7): 3383-3388.

Moore, D.R. et al. 2001. *Fracture Mechanics Testing Methods for Polymers, Adhesives and Composites.* Elsevier.

Mori, T. and Tanaka, K. 1973. "Average stress in matrix and average elastic energy of materials with misfitting inclusions." *Acta Metallurgica* 21 (5): 571-574.

Mouritz, A.P. 2007. "Review of z-pinned composite laminates." *Composites Part a-Applied Science and Manufacturing* 38 (12): 2383-2397.

Mukhopadhyay, P. et al. 2013. *Graphite, graphene, and their polymer nanocomposites.* Boca Raton, FL: CRC Press.

Mura, T. 1987. *Micromechanics of Defects in Solids.* Amsterdam, Netherlands: Springer Netherlands.

Nan, C. et al. 2004. "Interface effect on thermal conductivity of carbon nanotube composites." *Applied Physics Letters* 85 (16): 3549–3551.

Nan, C.W. et al. 2003. "A simple model for thermal conductivity of carbon nanotube-based composites." *Chemical Physics Letters* 375 (5-6): 666-669.

Nan, C.W. et al. 1997. "Effective thermal conductivity of particulate composites with interfacial thermal resistance." *Journal of Applied Physics* 81 (10): 6692-6699.

nanowerk. 2014. *nanowerk.com.* http://www.nanowerk.com/spotlight/spotid=23934.php.

Nejad, S.J. 2012. "A review on modeling of the thermal conductivity of polymeric nanocomposites ." *e-Polymers* 12(1): 253–288.

Nishikawa, M. et al. 2007. "Numerical simulation of interlaminar damage propagation in CFRP cross-ply laminates under transverse loading." *International Journal of Solids and Structures* 44 (10): 3101-3113.

Odegard, G. M. et al. 2001. "Constitutive modeling of nanotube-reinforced polymer composite systems." NASA Technical Memorandum.

Odegard, G.M. 2003. "Constitutive modeling of nanotube-reinforced polymer composites." *Composites Science and Technology* 63 (11): 1671-1687.

Odegard, G.M. et al. 2005. "Effect of nanotube functionalization on the elastic properties of polyethylene nanotube composites." *AIAA Journal* 43 (8): 1828-1835.

Odegard, G.M. et al. 2002. "Equivalent-continuum modeling of nano-structured materials." *Composites Science and Technology* 62 (14): 1869-1880.

Odegard,G. and Gates, T. 2002. "Constitutive modeling of nanotube/polymer composites with various nanotube orientations." *SEM Annual Conference on Experimental and Applied Mechanics.*

Ostergaard, M., et al.,. 2011. "Virtual testing of aircraft structures." *An Official Journal of the Council of European Aerospace Societies* 1 (1): 83-103.

Owen, M.J. and Bishop, P.T. 1979. "Critical Stress Intensity Factors Applied to Glass Reinforced Polyester Resin." *Journal of Composite Materials* 7 (April): 146-159.

Panigrahi, S. and Pradhan, B. 2009. "Development of Load Coupler Profiles of Spar Wingskin Joints with Improved Performance for Integral Structural Construction of Aircraft Wings." *Journal of Reinforced Plastics and Composites* 28 (6): 657-673.

Park,O. and Sankar, B. V. 2002. "Crack-tip force method for computing energy release rate in delaminated plates." *Composite Structures* 55(4): 429-434.

Parks, D. M. 1977. "The Virtual Crack Extension Method For Nonlinear Material Behaviour." *Comput. Methods Appl. Mech. Eng* 12(3): 353-364.

Parks, D. M. 1978. "Virtual Crack Extension: A General Finite Element Technique for J-Integral Evaluation." *Numerical Methods in Fracture Mechanics* 464-479.

Parks, D. M.,. 1974. "A stiffness derivative finite element technique for determination of crack tip stress intensity factors." *Int. J. Fracture* 10(4): 487-502.

Potluri, P. and Manan, A.,. 2007. "Mechanics of non-orthogonally interlaced textile composites." *Composites Part a-Applied Science and Manufacturing* 38 (4): 1216-1226.

Qian, D. et al. 2000. "Load transfer and deformation mechanisms in carbon nanotube-polystyrene composites." *Applied Physics Letters* 76 (20): 2868-2870.

Ragosta, G. et al. 2005. "Epoxy-silica particulate nanocomposites: Chemical interactions, reinforcement and fracture toughness." *Polymer* 46 (23): 10506-10516.

Raju, I. S. and Shivakumar, K. N. 1990. "An Equivalent Domain Integral Method in the Two-Dimensional Analysis Mixed-Mode Crack Problems." *Engineering Fracture Mechanics* 37(4): 707-725.

Raju, I. S. 1987. "Calculation Of Strain-Energy Release Rates With Higher Order And Singular Finite Elements." *Eng. Fracture Mech* 28(3): 251-274.

Reddy, J.N. 2004. *Mechanics of laminated composite plates and shells : theory and analysis.* Boca Raton, FL: CRC Press.

Rispler, A.R. et al. 1997. "Failure analysis of composite T-joints including inserts." *Journal of Reinforced Plastics and Composites* 16 (18): 1642-1658.

Rosso, P. et al. 2006. "A toughened epoxy resin by silica nanoparticle reinforcement." *Journal of Applied Polymer Science* 100 (3): 1849-1855.

Rybicki, E. F. and Kanninen, M. F. 1977. "A Finite Element Calculation of Stress Intensity Factors by a Modified Crack Closure Integral." *Eng. Fracture Mech* 9(4): 931-938.

Segurado, J. and Llorca, J. 2004. "A new three-dimensional interface finite element to simulate fracture in composites." *International Journal of Solids and Structures* 41 (11-12): 2977-2993.

Seidel, G. and Stephens, S. 2010. "Analytical and computational micromechanics analysis of the effects of interphase regions on the effective coefficient of thermal expansion of carbon nanotube-polymer nanocomposites." *51st AIAA/ASME/ASCE/AHS/ASC Structures, Structural Dynamics, and Materials Conference.* Orlando, FL: AIAA. 1-10.

Seidel, G. D. . 2007. "Micromechanics modeling of multifunctional nature of carbon nanotube-polymer composites,." College Station, Texas: PhD dissertation submitted to Texas A&M University.

Seidel, G. D. and Lagoudas, D. C. 2006. "Micromechanical analysis of the effective elastic properties of carbon nanotube reinforced composites,." *Mechanics of Materials* 38(8–10): 884–907.

Sha, G. T. 1984. "On the Virtual Crack Extension Technique for Stress Intensity Factors and Energy Release Rate Calculations for Mixed Fracture Mode." *Int. J. Fracture* 25(2): 33-42.

Shivakumar, K. N. and Raju, I. S. 1992. "An Equivalent Domain Integral Method for Three-Dimensional Mixed-Mode Fracture Problems." *Engineering Fracture Mechanics* 42(6): 935-959.

Song, P.C. et al. 2006. "Improving the thermal conductivity of nanocomposites by increasing the length efficiency of loading carbon nanotubes." *Applied Physics Letters* 88 (15): 153111-1 - 153111-3.

Song, Y.S. and Youn, J.R. 2006. "Evaluation of effective thermal conductivity for carbon nanotube/polymer composites using control volume finite element method." *Carbon* 44 (4): 710-717.

Steinhauser, M. and Hiermaier, S. 2009. "A Review of Computational Methods in Materials Science: Examples from Shock-Wave and Polymer Physics." *International Journal of Molecular Sciences* 5135-5216.

Sun, L.Y. et al. 2009. "Energy absorption capability of nanocomposites: A review." *Composites Science and Technology* 69 (14): 2392-2409.

Thakre, P. et al. 2011. "Investigation of the effect of single wall carbon nanotubes on interlaminar fracture toughness of woven carbon fiber–epoxy composites,." *Journal of Composite Materials* 48 (18): 1-17.

Thostenson, E.T. and Chou, T.W. 2003. "the elastic properties of carbon nanotube-based composites: modelling and characterization." *Journal of Physics D-Applied Physics* 36 (5): 573-582.

Tong, L. et al. 2002. *3D fibre reinforced polymer composites.* Boston, MA: Elsevier.

Unnikrishnan, V.U. and Reddy, J.N. 2005. "Characteristics of silicon-doped CNT-reinforced nanocomposites." *International Journal for Multiscale Computational Engineering* 3 (4): 437-450.

Winzen, A. 2006. "Simulation of stringer stiffened CFRP panels in consideration of skin-stringer separation." Master Thesis.

Wu, F. and Cheng, H. 2005. "Structure and thermal expansion of multi-walled carbon nanotubes before and after high temperature treatment." *J. Phys. D: Appl. Phys* 38: 4302–4307.

Xu, X.P. and Needleman, A.,. 1994. "Numerical simulations of fast crack growth in brittle solids." *Journal of the Mechanics and Physics of Solids* 42 (9): 1397–1434.

Yakobson, B.I. et al. 1996. "Nanomechanics of carbon tubes: Instabilities beyond linear response." *Physical Review Letters* 76 (14): 2511-2514.

Yang, Q.D. and Cox, B. 2005. "Cohesive models for damage evolution in laminated composites." *International Journal of Fracture* 133 (2): 107-137.

Yokozeki, T. et al. 2009. "Fracture toughness improvement of CFRP laminates by dispersion of cup-stacked carbon nanotubes." *Composites Science and Technology* 69 (14): 2268-2273.

Zhang, G. and Li, B. 2005. "Thermal Conductivity of Nanotubes: Effects of Chirality and Isotope Impurity." *Journal of Physical Chemistry B* 109: 23823-23826.

Zhang, H. et al. 2006. "Property improvements of in situ epoxy nanocomposites with reduced interparticle distance at high nanosilica content." *Acta Materialia* 54 (7): 1833-1842.

Zhang, T.F. et al. 2011. "A Two-Parameter Model of FRP Laminates Stiffness Reduction." *Advanced Materials Research* 236: 1187-1194.

Zhao, Q.Z. et al. 2002. "Ultimate strength of carbon nanotubes: A theoretical study." *Physical Review B* 65 (14): 144105-1 - 144105-6.

Zimmermann, K. et al. 2010. "Testing and analysis of ultra thick composites." *Composites Part B-Engineering* 41 (4): 326-336.

BIOGRAPHICAL SKETCH

Zeaid Hasan received his Bachelor of Science degree in aeronautical engineering from Jordan University of Science and Technology, Jordan in June 2009. During that time he worked at the Royal Jordanian Air force as a maintenance engineer supporting both military and commercial aircrafts. He entered the mechanical engineering program at Texas A&M University in September 2009 and worked under the supervision of Dr. Anastasia Muliana for his thesis titled "*Controlling Performance of Laminated Composites using Piezoelectric Materials*." He received his Master of Science degree in December 2010. During that period he also worked at the space engineering research center in Bryan, Texas supporting the analysis of heat exchangers for nuclear power plants. In January 2011, he started working for Boeing Defense Space and Security in Mesa, Arizona as a structural engineer supporting several products under research and development, including the Apache Helicopter, Boeing 787 -8, -9 and -10 commercial aircrafts, AH 6i and A-160 (unmanned flying vehicle). He enrolled at Arizona State University and obtained a Master's degree in Aerospace Engineering in December 2013, and a PhD in Aerospace Engineering in July 2014 under the supervision of Prof. Aditi Chattopadhyay. Zeaid also holds a degree in applied mathematics from the University of Washington and is a registered professional engineer in the state of Arizona. During his time in Arizona, he worked part time as an adjunct faculty in the mathematics department at Chandler Gilbert Community College. He currently works as a Liaison engineer in Boeing Commercial Aircraft's in Charleston, South Carolina. Zeaid can be reached via email at zeadnws@hotmail.com.